2006

Magnetic, thermodynamic and transport properties of the magnetic semiconductor Fe_1 -xCoxS$_2$ and superconducting LaSb$_2$

Song Guo
Louisiana State University and Agricultural and Mechanical College, sguo1@lsu.edu

MAGNETIC, THERMODYNAMIC AND TRANSPORT PROPERTIES OF THE MAGNETIC SEMICONDUCTOR $FE_{1-X}CO_XS_2$ AND SUPERCONDUCTING $LASB_2$

A Dissertation

Submitted to the Graduate Faculty of the
Louisiana State University and
Agricultural and Mechanical College
in partial fulfillment of the
requirement for the degree of
Doctor of Philosophy

in

The Department of Physic and Astronomy

by
Song Guo
B.S. Beijing Normal University, 1992
M.S. Louisiana State University, 2001
August 2006

Acknowledgements

There are many people that I want to say thanks here. I could not possibly complete this thesis work without their help and encouragement.

First, I would like to thank John. F. DiTusa, my thesis advisor, for his help, encouragement, guidance and patience in mentoring me toward the Ph.D. degree in physics. I have learned from him a great deal of low temperature experimental techniques and methods in conducting cutting-edge research.

I would like to thank David Young for making the crystals used in this thesis work and for his encouragement and guidance.

I would like to thank Julia Chan and her student Robin Macaluso for determining the crystal structure and lattice constants by X-ray diffraction measurements. I also benefited a great deal from Julia Chan's class in Solid State Chemistry.

I would like to thank Dana Browne and Richard Kurtz for serving on my thesis committee, for their advice and encouragement, and for inspiring teaching in the Solid State Physics classes.

I would like to thank Roy Goodrich, Ilya Vekhter, Cigdem Capan, Monica Moldovan, Philip Adams, and Philip Sprunger for their advice and encouragement.

I would like to thank Paul Kirk for his lucid and inspiring teaching in his Quantum Mechanics class.

I would like to thank Allen Young, Donnie Olano, Duane Cambre, Randy Gould, Marcus Nauman, Philip Nurse, Ronald Depew and Hortensia Valdes for their numerous technical support.

I would like to thank Arnell Dangerfield, Beverly Rodriguez, Rochelle Grayer, Karen Richard, Ophelia Dudley and Robert Dufrene for the numerous ways they have provided assistance.

I would like to acknowledge the teaching assistantship I received from the Department of Physics and Astronomy and the research assistantship from Dr. John F. DiTusa.

My greatest thanks go to my wife, Jian Guan, for her love, encouragement, and for taking care of our two sons most of the time. I also want to thank my parents-in-law, Zhengting Guan and Dehua Kong, for coming here all the way from China to help us take care of our children in our most needed time, despite their poor health and their inability to speak English. I also want to thank my two sons, Michael and Gabriel, for the happiness and inspiration they bring to me.

Table of Contents

List of Tables

List of Figures

Abstract

In recent years magnetic semiconductors have attracted a great deal of attention because it is thought that they can be used to generate spin polarized current in spintronics, an emerging field where the spin degree of freedom of charge carriers is utilized in microelectronic devices. In this dissertation work, we investigate the magnetic, thermodynamic, and transport properties of the magnetic semiconductor $Fe_{1-x}Co_xS_2$ for x less than 0.14, the doping range where Insulator-to-Metal and paramagnetic-to-ferromagnetic transitions occur. We discovered that the Kondo effect is an important ingredient in the paramagnetic region of magnetic semiconductor $Fe_{1-x}Co_xS_2$. Disorder that comes with doping, coupled with the Kondo effect and the RKKY interaction between the local moments, leads to the observed features of spin clusters and the Griffiths phase. This inhomogeneous magnetic state can be used to explain the resulting physical properties, including the NFL behavior as evidenced by the increase of C/T at very low temperature in proximity to the zero-T critical point.

A second system, $LaSb_2$, is found to have a very inhomogeneous superconducting transition at low temperatures. We have discovered that the application of pressure induces a much more homogeneous superconducting ground state in this highly layered compound.

Chapter 1 Introduction

1.1 Motivation

Traditional semiconductor devices usually take advantage of the charge degree of freedom of electrons or holes for information processing and communication. On the other hand, the spin degree of freedom is used for storage of information in ferromagnetic (FM) materials. Recently, an emerging field of electronics utilizing both the charge and the spin degree of freedom of electrons, spintronics [1.1], is gaining more and more attentions. Successful manipulation of the spin states in semiconductors has been envisioned to enhance the performance of current devices and to create new spin-based devices. For example, the giant magnetoresistive effect (GMR) [1.2] observed in thin film sandwiches of FM/Non-FM/FM has been used in magnetoresistive random access memory (MRAM) and in read heads for hard drives [1.1]. One important challenge in spintronics is to find a carrier-mediated ferromagnetic semiconductor with a Curie temperature T_c well above room temperature. Major progress in this direction was made by the growth of the magnetic semiconductor (Ga,Mn)As by MBE with Curie temperature (T_c)as high as 110K [1.3]. However, the fundamental problem of how a paramagnetic insulator evolves into a ferromagnetic metal is not well understood. Our investigation in the Co doped FeS_2 pyrite series was designed to shed new light on this problem.

1.2 Background and Previous Investigations of $Fe_{1-x}Co_xS_2$

FeS_2 (fool's gold) is a paramagnetic semiconductor with a van Vleck-like temperature independent magnetic susceptibility and an energy gap of ~ 1ev [1.4] [1.5] [1.6], while CoS_2 is an itinerant ferromagnet with Curie temperature ~ 120K and ~ 95%

carrier spin polarization [1.4] [1.5]. Both FeS_2 and CoS_2 crystallize in the cubic pyrite structure which can be described as the NaCl structure with one sublattice occupied by iron atoms and the other by the center of mass of the sulfur atom pairs. These sulfur dumbbells are oriented along the <111> axes [1.6]. The solid solutions $Fe_{1-x}Co_xS_2$ can be formed over the entire doping range $0 < x < 1$. The crystal field splits the 3*d* bands into octahedral t_{2g} and e_g levels, where FeS_2 and CoS_2 have the configurations $t_{2g}^6e_g^0$ and $t_{2g}^6e_g^1$ respectively [1.4]. It was predicted that for most of the concentration range ($0.25 \leq x \leq 0.9$) $Fe_{1-x}Co_xS_2$ is a half metal which is robust with respect to disorder [1.7]. Experimentally, for $0.1 \leq x \leq 0.95$, the saturation magnetization in Bohr magnetons (μ_B) is equal to the Co concentration, indicating full spin polarization or half metallic behavior [1.4]. For $x < 0.1$, a previous investigation showed that ferromagnetism occurs at x as low as 0.05, as indicated by a sharp peak in zero field AC magnetic susceptibility [1.4].

1.3 Outline of Our Work

We have investigated the magnetic, thermodynamic, and transport behavior in $Fe_{1-x}Co_xS_2$ for $x \leq 0.14$ by measuring the DC magnetization, AC magnetic susceptibility, specific heat, resistivity, magnetoresistance, and the Hall effect. For x as low as 0.001, we found that the resistivity displays metallic behavior ($\sigma(T \rightarrow 0) > 0$). With further doping, at $x > 0.01$, we observed a peak in the zero field AC susceptibility, indicating the emergence of ferromagnetic ordering. Further Co doping increases the Curie temperatures as determined by both the zero field susceptibility and an Arrott analysis as shown in the phase diagram of Fig. 1.1.

From the saturation magnetization and the Hall effect measurements, we find a Hall carrier density that is smaller than the saturation magnetization, indicating that the

magnetism likely results from the formation of local magnetic moments. Further evidence for local moments comes from transport measurements where in the $x \leq 0.01$ samples, the zero field resistivity displays a Kondo-like increase with cooling and a magnetoresistance (MR) that obeys a single-ion Kondo scaling form at $T \geq 1.8$ K. For $x > 0.01$ samples, with decreasing temperature, the zero field resistivity displays a maximum or a shoulder, indicative of magnetic ordering caused by the RKKY interaction.

The electronic contribution to the specific heat of metals is linear-in-T for Landau Fermi liquids with a slope of γ proportional to the density of electron states. In $Fe_{1-x}Co_xS_2$, γ exhibits a power law increase with decreasing temperature over one and a half decades from ~ 6K down to 0.1 K for our $x \sim 0.01$ samples, a clear indication of a departure from the Fermi-Liquid (FL) behavior. For $x = 0.003$, γ increases from ~ 1K down to our lowest temperature 0.1 K. For higher x, γ first increases, then saturates or slightly decreases into a Fermi-Liquid like (constant γ) behavior. Increasing magnetic fields tend to recover the FL behavior at higher temperature. The Non-Fermi-Liquid (NFL) behavior observed here is reminiscent of the NFL behavior often observed in heavy fermion metals [1.8] where the Kondo effect and the RKKY interaction are competing against each other. In Fig. 1.1, we plot the phase diagram for $Fe_{1-x}Co_xS_2$ and display the phase region where this NFL behavior occurs. The red line in the plot indicates the Curie temperature, the blue line indicates the temperature below which C/T increases with decreasing T, and the green line indicates the temperature below which C/T decreases slightly into a Fermi-Liquid like (constant γ)behavior. We can see that NFL behavior, as evidenced by the

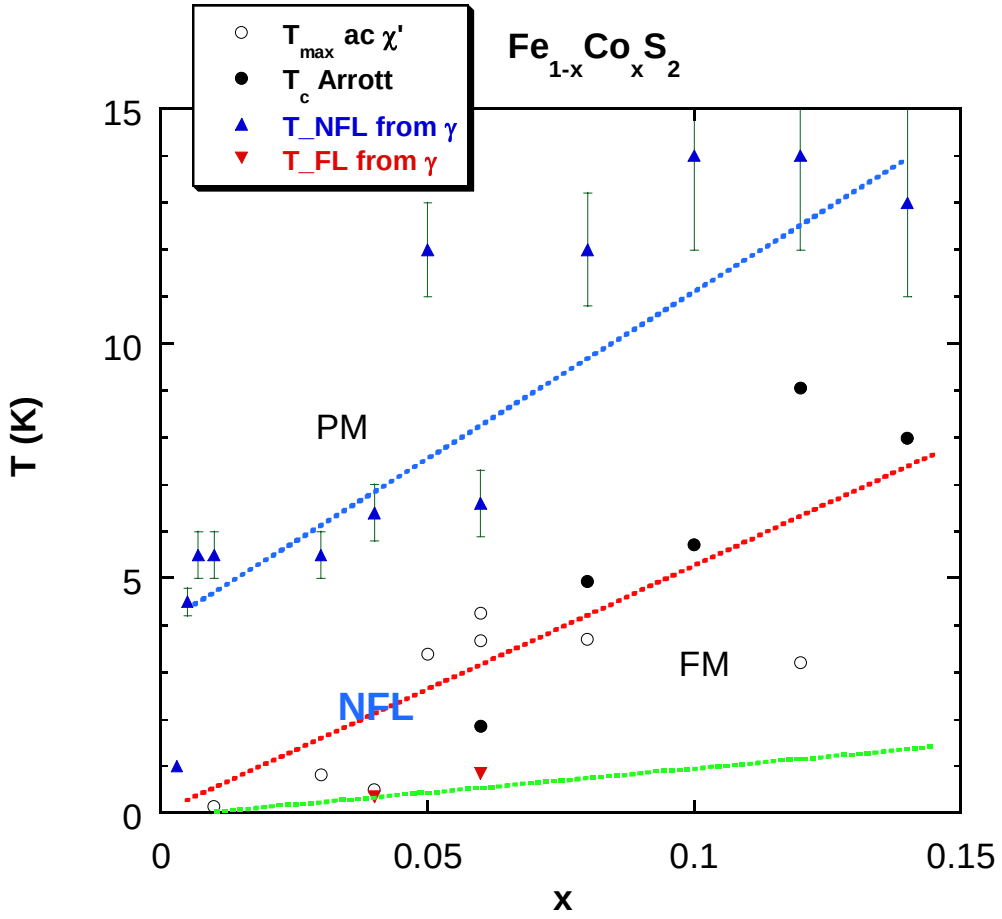

Figure 1.1 Phase diagram of $Fe_{1-x}Co_xS_2$ ($0 \leq x \leq 0.14$)

The red line indicates the Curie temperature, the blue line indicates the temperature below which C/T increases with decreasing T, and the green line indicates the temperature below which C/T decreases to a Fermi-Liquid like behavior.

increase of C/T with decreasing T, persists in both the paramagnetic (PM) and the ferromagnetic (FM) phases. This phenomenon is consistent with the formation of a Griffiths phase which will be introduced and discussed later.

In recent years, there has been a renewed interest in the Griffiths phases in the field of strongly correlated electron systems. For example, the Griffiths phase was invoked to explain the NFL behavior in doped heavy fermion metals close to a quantum critical point [1.9] [1.10]. In doped manganite $La_{1-x}Sr_xMnO_3$, the sharp downturn of inverse susceptibility at low-T was explained by the formation of the Griffiths phase above the Curie temperature [1.11] [1.12] [1.13]. It is also predicted [1.14] that the Griffiths phase exists in the strongly localized regime of a dilute magnetic semiconductor as magnetic polarons percolate close to the Curie temperature. In our pyrite series, $Fe_{1-x}Co_xS_2$, we found evidence for the formation of the Griffiths phase in the magnetic susceptibility. In particular, we find that the magnetic susceptibility is suppressed significantly by small magnetic fields at low-T. In addition, we find that the inverse susceptibility displays a sharp downturn as the temperature is lowered near T_c for our x = 0.06 sample, clearly indicating the formation of a Griffiths phase.

Chapter 2 Experimental Details

In this Chapter, I will present some of the experimental details of the specific heat measurements, the magnetic susceptibility measurements in high pressure, and several other measurements and crystal growth techniques.

2.1 Experimental Details for Millikelvin Specific Heat Measurements of Small Samples (a Few Milligrams) in a Dilution Refrigerator

2.1.1 Introduction to Specific Heat Measurement

The traditional technique to measure the specific heat of solids is the adiabatic method which directly utilizes the definition of specific heat, i.e.,

$$C_p = \lim_{dT \to 0} \left(\frac{dQ}{dT} \right)_p . \tag{2.1}$$

Here, a heat input dQ is used to raise the temperature of an otherwise thermally isolated sample from T to T + dT. Thus measuring dT and dQ can give the specific heat. One common problem for realizing this simple method at low temperature is that when the sample size is small (< 200mg [2.1]), it is difficult to adequately thermally isolate the sample. Thus the effect of stray heat leads to large uncertainties.

The steady state AC method [2.2] and thermal relaxation method [2.1] were thus developed to measure small sample specific heats below 1K. For both methods, the heater, the thermometer, the substrate, and the sample are considered thermally coupled together as a lumped element via the internal time constant τ_2, while the lumped elements are considered thermally coupled to the heat bath via time constant τ_1. Both heater and thermometer are usually implemented as resistors.

In the AC method [2.2], a current of frequency 1/2ω is driven through the heater. Using lock-in techniques, the AC temperature variation of the sample at a frequency ω can be detected through the thermometer as

$$T_{AC} = \frac{Q}{2\omega C_P}\left[1 + \frac{1}{\omega^2\tau_1^2} + \omega^2\tau_2^2 + \frac{2\kappa_b}{3\kappa_s}\right]^{-\frac{1}{2}} \quad . \tag{2.2}$$

Here κ_s is the thermal conductance of the sample, κ_b is the thermal conductance between the lumped elements and the heat bath, and C_P is the heat capacity of the sample. The AC method has the advantage of measuring the specific heat continually and can be very sensitive to small changes. However, for it to work correctly, the condition $\omega\tau_1 >> 1 >> \omega\tau_2$ must be rigorously satisfied [2.3]. Unfortunately, when the temperature is below 1K, τ_2 can be quite large due to the high thermal contact resistance [2.4] between heater, thermometer, substrate and sample. This has the effect of reducing the working frequency, ω, to less than 1Hz which may be difficult for lock-in amplifier detection. This can make the AC method inaccurate at the lowest temperatures of a dilution refrigerator.

The thermal relaxation method [2.1] also has the necessary condition $\tau_1 >> \tau_2$. However we have avoided the low frequency problem by the use of low thermal conductivity wire connecting the sample and bath. This has the effect of increasing τ_1, thus satisfy the condition $\tau_1 >> \tau_2$. With this method the temperature of the sample can be raised above the constant bath temperature and then allowed to decay exponentially to the bath temperature [2.4],

$$T_s = T_0 + \Delta T \times \exp(-\frac{t}{\tau_1}) \quad . \tag{2.3}$$

Here T_s is the sample temperature; T_0 is the bath temperature, ΔT is the initial temperature difference between sample and bath, and t is the time. The time constant τ_1 can thus be determined by fitting the time dependence of the sample temperature. The thermal conductance κ_b can be determined by measuring the input heating rate dQ/dt and the temperature change ΔT from the relation

$$dQ/dt = \kappa_b \Delta T \ . \qquad (2.4)$$

And finally heat capacity can be calculated from the relation

$$C_p = \tau_1 \kappa_b \qquad . \qquad (2.5)$$

2.1.2 Experimental Details of the Specific Heat Measurements

In our realization of the thermal relaxation method the thermometer and the heater are fabricated from a single commercial RuO chip 1K ohm resistor. One side of the rectangular alumina substrate is covered by the RuO resistor. We thinned the substrate with sand paper in order to reduce the thickness of the chip to less than 0.25 mm. This reduces the addenda's heat capacity. The chip is then notched lengthwise on the resistor side with fine diamond wire saw to split the resistor into two resistors both having a resistance of roughly 3.2 KΩ. Either of the resisters can be used as heater or thermometer (see Fig. 2.1). The sample is glued to the resistors' side of the chip with GE varnish. We use GE varnish because it is a good electrical insulator and has a high thermal conductivity (~ $9*10^{-3}$ Watts/cm K at T = 1K from reference [2.5]). The surface of the sample was made to be as flat and smooth as possible to reduce the thermal contact resistance between sample and the substrate, and thus reduce τ_2.

The experiment is conducted in an Oxford 200 top loading dilution refrigerator with a 9T superconducting magnet. Four resistive wires connecting thermometer and

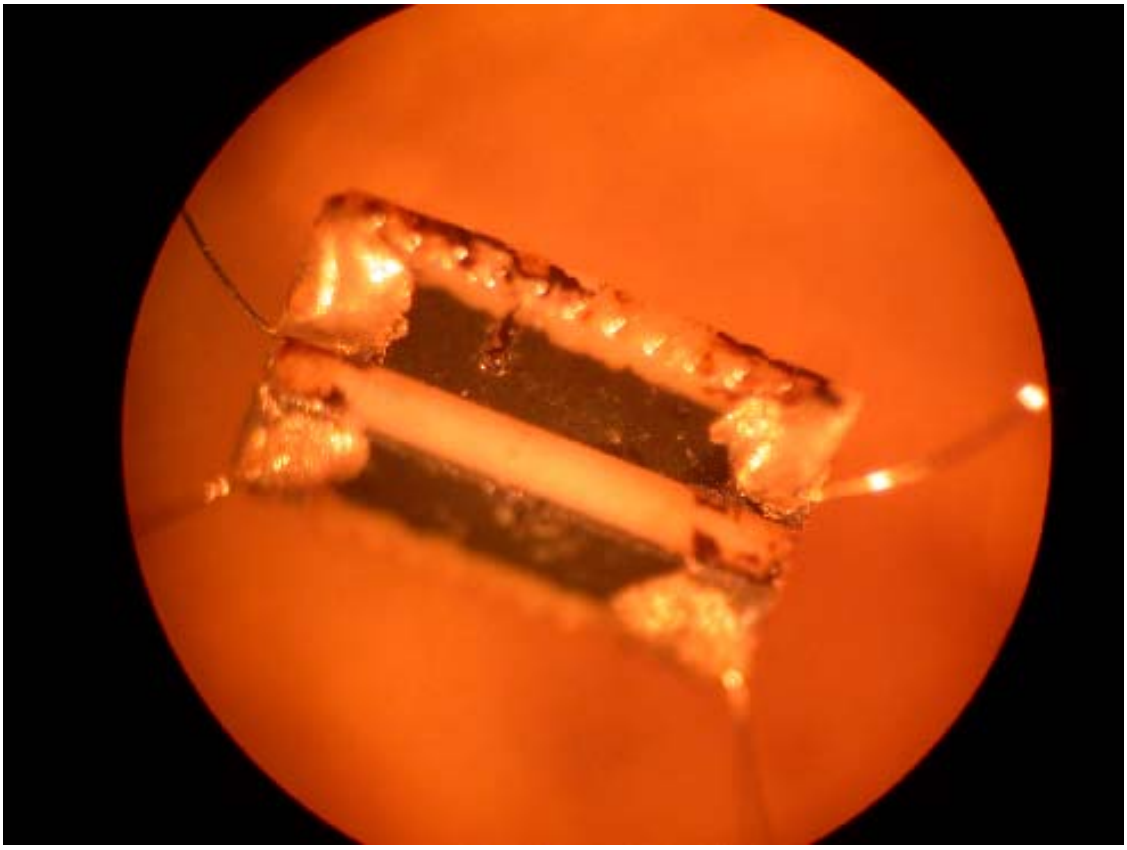

Figure 2.1 Picture of RuO chip resistor after cutting into a thermometer and heater

heater to the top-loading slug are the only thermal link between the lumped elements (sample and resistors) with the heat bath, giving a large τ_1 to meet the condition $\tau_1 >> \tau_2$.

When the experiment is carried out a small amplitude pulsed current from a pulse generator, SRS DC345, is driven through the heater (see Fig.2.2 for schematic circuit). We have been careful to assure that the time of heating and cooling phase are long enough ($> 6*\tau_1$) for the sample, thermometer and heater to reach thermal equilibrium. During each cycle of heating and cooling, the temperature of the mixing chamber was kept extremely stable (± 0.05% of temperature). This reduces error in the extracted time constant τ_1. The resistance of thermometer R_{Th} is measured and recorded at small fixed time intervals by standard lock-in techniques at 1 kHz. The current driven through the thermometer R_{Th} is ~10 nA, and the heating power by this current on the thermometer is ~1 nW. The voltage across the heater is measured with a high precision voltmeter, HP3457. Since the driving current is known from the voltage divided by the current limiting resistor, the resistance of the heater and the heat input rate dQ/dt can be easily calculated from the measured voltage across the heater. A Labview program is developed to control the various instruments via GPIB interface so that data can be taken continually and automatically with the aid of a computer.

2.1.3 Data Reduction and Analysis for Specific Heat Data

At each temperature, we have measured the sample temperature through 10 cycles of heating and cooling in order to reduce noise level. It is found that averaging over 10 cycles significantly reduces the scatter in specific heat data. The averaged data is used to extract τ_1 and ΔT. We combine this information with the measured heating rate dQ/dt to calculate the heat capacity of the sample and the addenda. The addenda's heat capacity

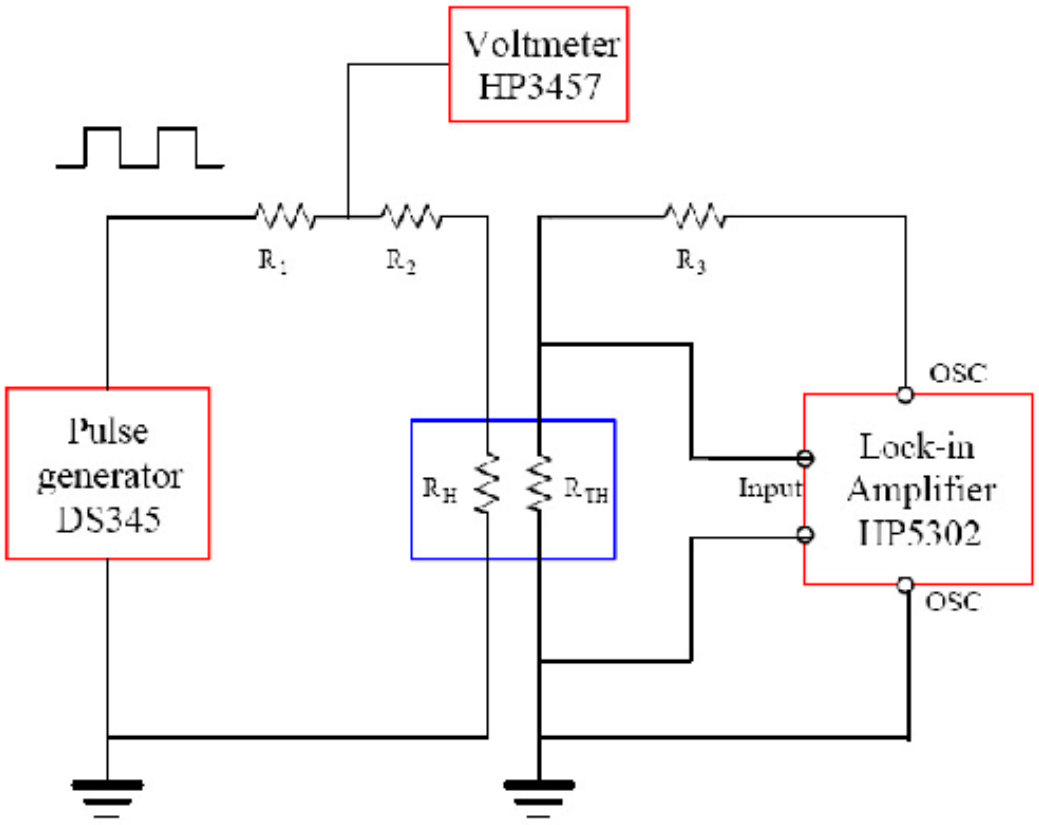

Figure 2.2 Schematic circuit of specific heat measurement

(R_1 = 11.6 MΩ
R_2 = 98.5 Ω
R_3 = 11.67 MΩ)

was measured separately and subtracted from the data to calculate the heat capacity of the sample. At zero magnetic field the addenda's heat capacity is in the order of 10^{-8} J/K for temperature less than 1.8 K. For most of the measurements the addenda's heat capacity is less than 20% of the total heat capacity, while for large crystal masses it was reduced to less than 10%. In one measurement of $Fe_{0.997}Co_{0.003}S_2$, at low temperatures, $T < 1$K, the addenda's contribution is of order 50% of the total heat capacity.

2.1.4 An Example of Extracting the Heat Capacity from the Raw Data

In the following example we show how we acquire values of the heat capacity for a particular temperature. In Fig. 2.3 we plot how the resistance of the thermometer changes during one cycle of heating and cooling. We can extract the time constant τ_1 and ΔR_{Th} from the exponential fit during the cooling cycle:

$$\boldsymbol{R_{Th}}(\boldsymbol{t}) = \boldsymbol{R_{Th}}(0) - \Delta\boldsymbol{R_{Th}} \times \exp(-\frac{\boldsymbol{t}}{\boldsymbol{\tau}_1}), \tag{2.6}$$

where t is the time elapsed after the heater stops heating or the cooling cycle is started.

From the schematic in Fig. 2.2, we can easily get

$$\frac{\boldsymbol{V_p}}{\boldsymbol{R}_1 + \boldsymbol{R}_2 + \boldsymbol{R_H}} = \frac{\boldsymbol{V_m}}{\boldsymbol{R}_2 + \boldsymbol{R_H}}, \tag{2.7}$$

where V_p is the pulse voltage and V_m is the measured voltage in HP3457. From this equation, we can get

$$\boldsymbol{R_H} = \frac{\boldsymbol{R}_1 \times \boldsymbol{V_m}}{\boldsymbol{V_p} - \boldsymbol{V_m}} - \boldsymbol{R}_2 \tag{2.8}$$

and

$$\boldsymbol{I} = \frac{\boldsymbol{V_m}}{\boldsymbol{R}_2 + \boldsymbol{R_H}}, \tag{2.9}$$

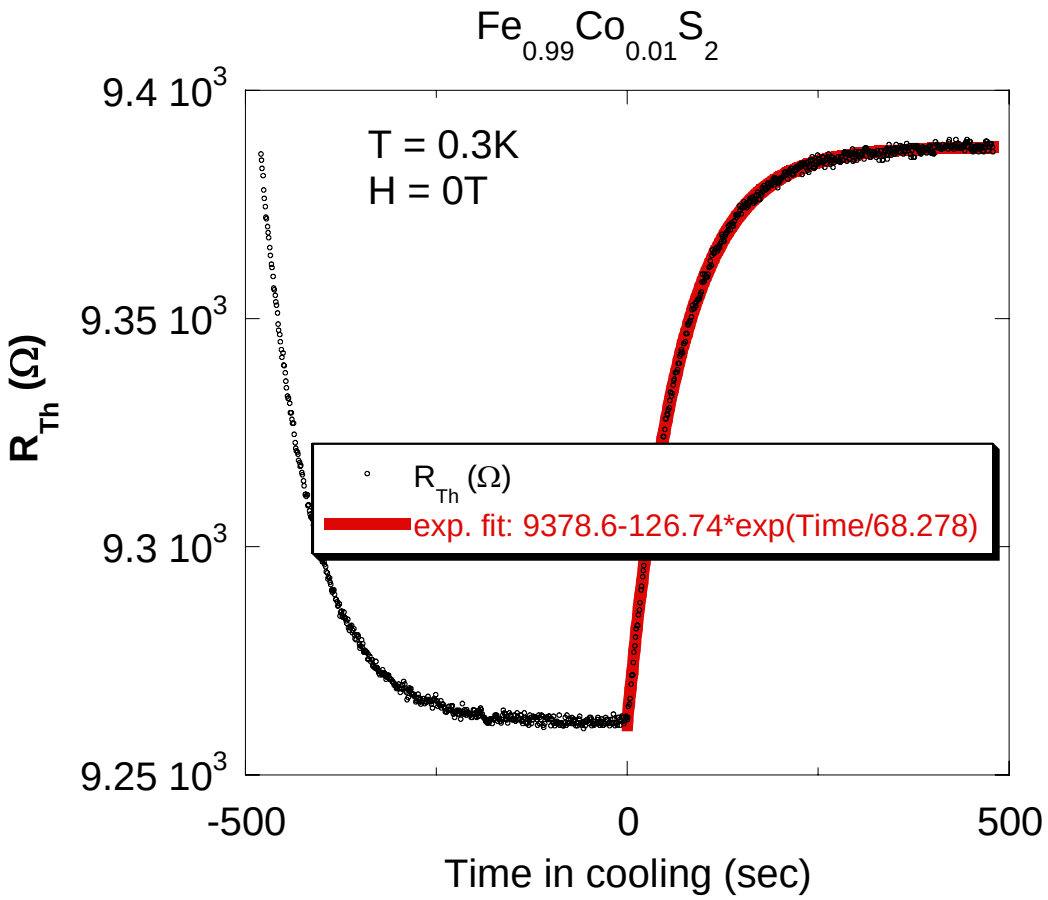

Figure 2.3 Changes in the resistance of the thermometer during one cycle of heating and cooling

where I is the current flowing through the heater. Therefore we have

$$\frac{dQ}{dT} = I^2 \times R_H = \left(\frac{V_m}{R_2 + R_H} \right)^2 \times R_H \quad . \tag{2.10}$$

Next, we need to convert ΔR_{Th} to ΔT. The RuO thermometer we use has a resistance that is well fit by the Mott variable range hopping [2.6] form,

$$R_{Th} = m_1 \times \exp\left(\left(\frac{m_2}{T} \right)^{1/4} \right), \tag{2.11}$$

where m_1 and m_2 are two parameters. We extract m_1 and m_2 from fits to the quiescent temperature dependence of the thermometer. From equation (2.11), we have

$$T = \frac{m_2}{\left(\ln\left(\frac{R_{Th}}{m_1} \right) \right)^4}, \tag{2.12}$$

and thus

$$\Delta T = \Delta R_{Th} \times \frac{-4 m_2}{R_{Th}} \left[\ln\left(\frac{R_{Th}}{m_1} \right) \right]^{-5} . \tag{2.13}$$

Now that dQ/dT and ΔT are known from equations 2.10 and 2.13, we can calculate κ_b from equation 2.4. Finally, we can calculate the heat capacity from equation 2.5 using the time constant τ_1 extracted from the equation 2.6.

2.2 Experimental Details of Magnetic Susceptibility Measurements in a Nonmagnetic Pressure Cell

2.2.1 Introduction to Susceptibility Measurements in High Pressure

Pressure has been widely used in recent years to study novel properties of correlated electron systems. For example, pressure can be used to tune the ordering temperature of ferromagnets or antiferromagnets to zero, providing a clean method (without introducing disorder as in chemical doping) for reaching a quantum critical point

(QCP). In contrast to chemical doping, applying pressure provides an opportunity to fine tune towards a QCP. Pressure can also induce superconducting phases in a solid. For instance, the heavy fermion compounds $CePd_2Si_2$ and $CeIn_3$ can be tuned by pressure into superconducting phase close to an anitiferromagnetic QCP [2.7]. Another interesting example is organic Mott insulator $(BEDT\text{-}TTF)_2X$ with a similar a phase diagram to high-T curates superconductors when chemical doping is replaced by pressure [2.8].

2.2.2 Pressure Cell for Use in a SQUID Magnetometer (Quantum Design MPMS)

Based on previous literature [2.9] [2.10] [2.11], we designed and manufactured a nonmagnetic piston-cylinder pressure cell for use in a commercial Quantum Design SQUID magnetometer. The pressure range obtained was up to 7 kBar (0.7 GPa).

The cell consists of a long cylindrical cell body, a piston seat and screws as shown in Fig. 2.4 – 2.10. They are all made of commercial beryllium-copper alloy 25. This material is nonmagnetic and has exceptional mechanical properties at low temperatures, so that it has been widely used in the design of piston-cylinder pressure cells. After the cylinder cell body has been manufactured, it is age hardened at 335°C for 2 hours and subsequently cooled in air to room temperature. The long uniform cylindrical geometry (see Fig. 2.6) is employed to ensure that the background signal caused by BeCu cell can be canceled or minimized in the SQUID magnetometer signal.

The pistons are made of high purity zirconia or quartz rods (see Fig. 2.5). We found that most of the temperature dependent part (diamagnetic) of the background signal is caused by the paramagnetic property of zirconia. Initially, when we used McMaster 8750k33 zirconia rods, the background magnetization measured at 50 Gauss and 1.8 K is about 1.4e-4 emu. Instead, high purity Technox 3000 zirconia rods from Dynamic

Ceramic are used, so that the background can be reduced by more than one order of magnitude, to about -7e-6 emu at 50 Gauss and 1.8 K. The background can vary according to the space between the two paramagnetic zirconia rods. The less space between the zirconia rods, the smaller the diamagnetic background signal will be.

The edges of the pistons can experience higher pressure than the interior, leading to possible chipping at the edges. To solve this problem, the edges of the zirconia rods are rounded with sand paper before they are inserted into the cell body.

The sample is located inside the Teflon container (see Fig. 2.4 and 2.10), which is sealed with a BeCu cap and a BeCu retainer on opposite sides of the container. To maintain large hydrostatic pressure inside the Teflon container, silicone oil (Dow Corning 704) is used as a pressure transmitting medium. Although the oil freezes at room temperature at approximately 10kBar, it remains an isotropic deformable glass [2.12].

The pressure around the sample was determined by placing a small piece of $(V_{0.99}Ti_{0.01})_2O_3$ (mass <0.5mg) in the sample container for use as manometer. It has previously been reported that the Metal-Insulator Transition (MIT) temperature of this material changes linearly with pressure up to 10 kBar [2.12]. The MIT temperature at ambient pressure is 141K and decreases at the rate of 5.8 Kelvin per kBar [2.12] and can be easily measured by the SQUID magnetometer. The size of the change in magnetization at the MIT for our $(V_{0.99}Ti_{0.01})_2O_3$ crystal is measured to be ~ $2.5*10^{-5}$ emu at H = 1T.

2.2.3 Applying Pressure

A carbide rod is inserted from the top screw in contact with the piston seat as in Fig. 2.4. It is pressed in a hydraulic press and the top screw is locked to maintain the

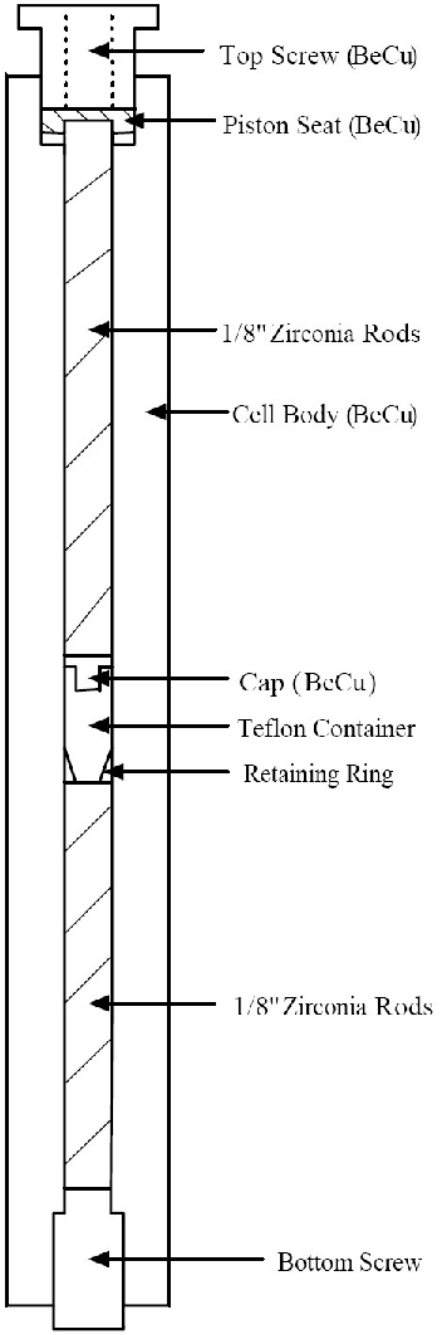

Figure 2.4 Schematic diagram for pressure cell after assembly

Figure 2.5 Picture of pressure cell parts

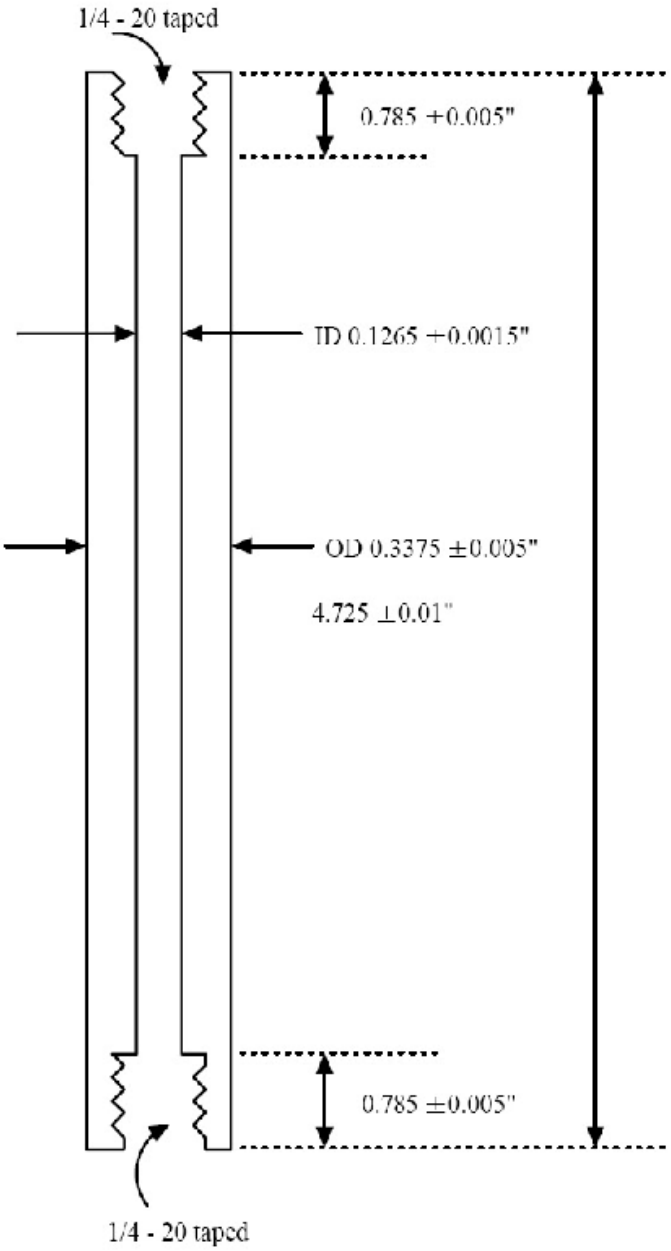

Figure 2.6 Cell body (BeCu)

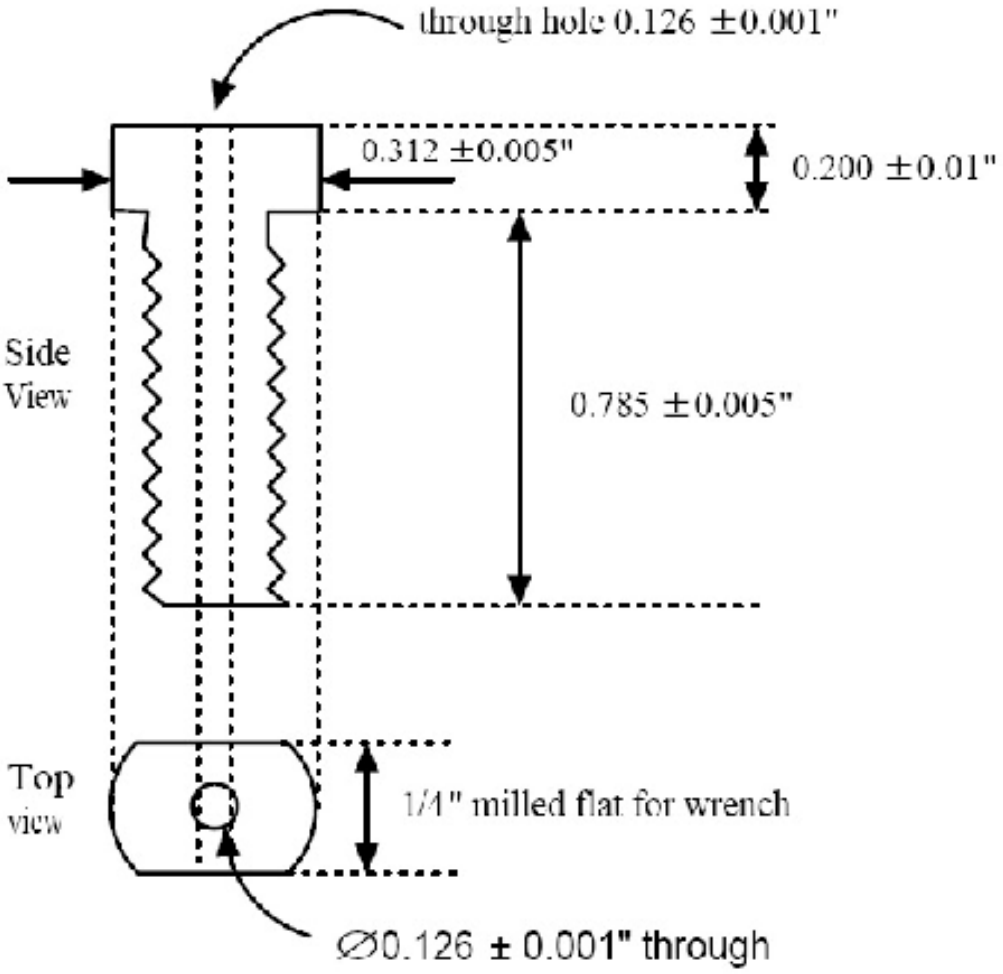

Figure 2.7 Top screw (BeCu)

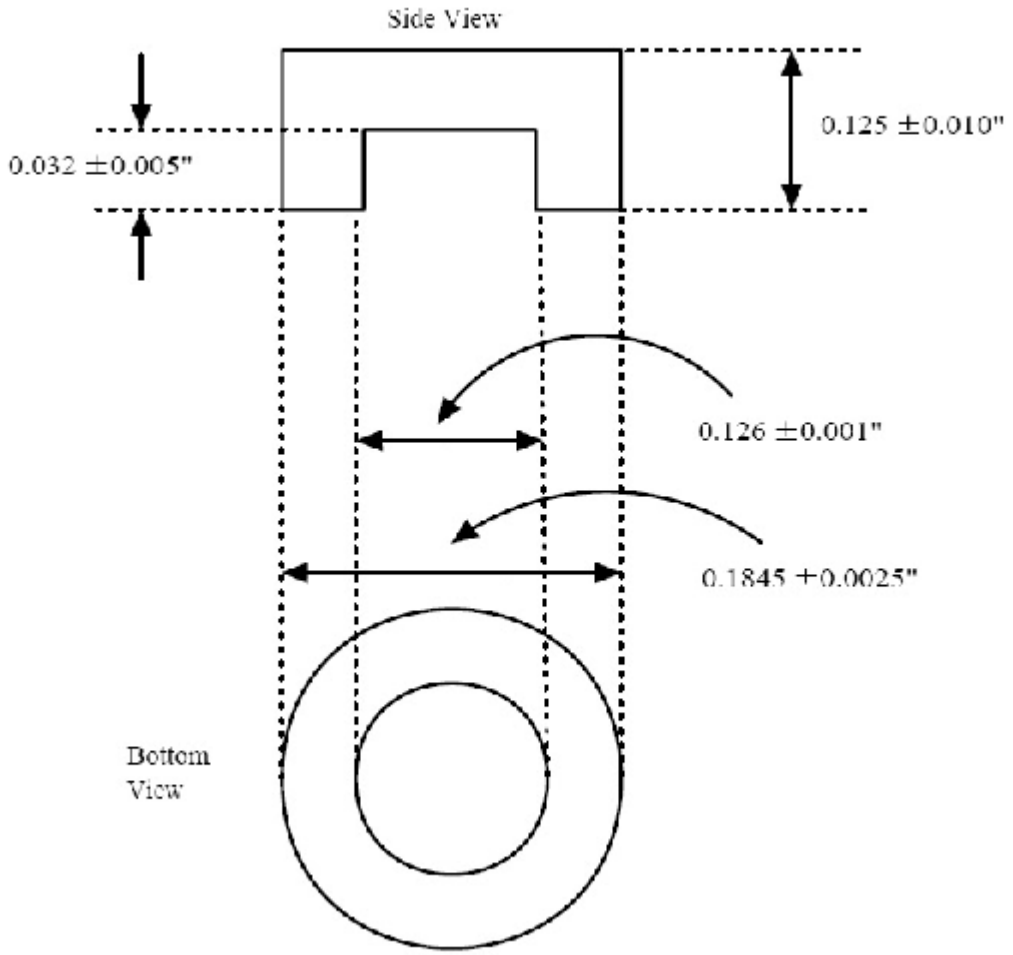

Figure 2.8 Piston seat (BeCu)

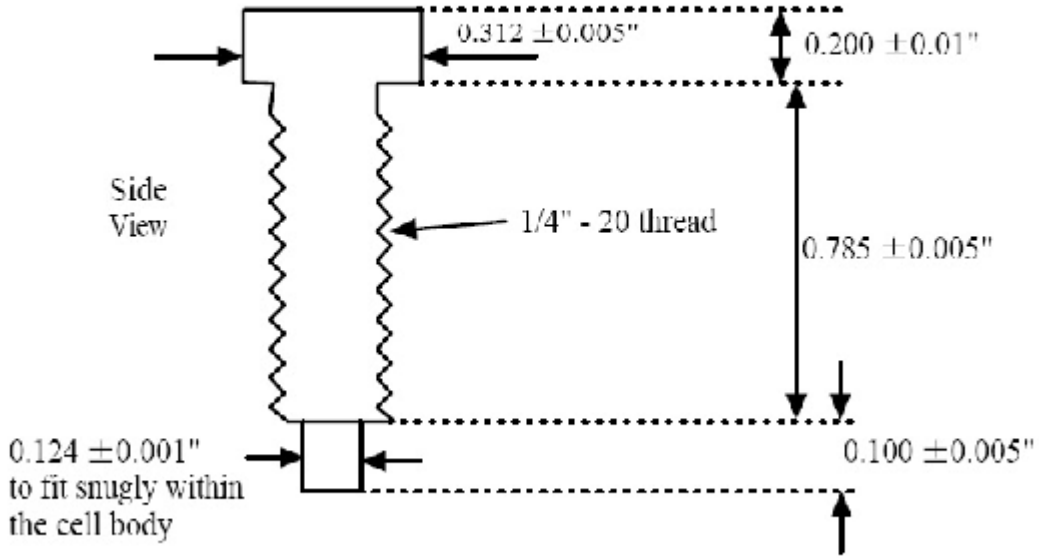

Figure 2.9 Bottom screw (BeCu)

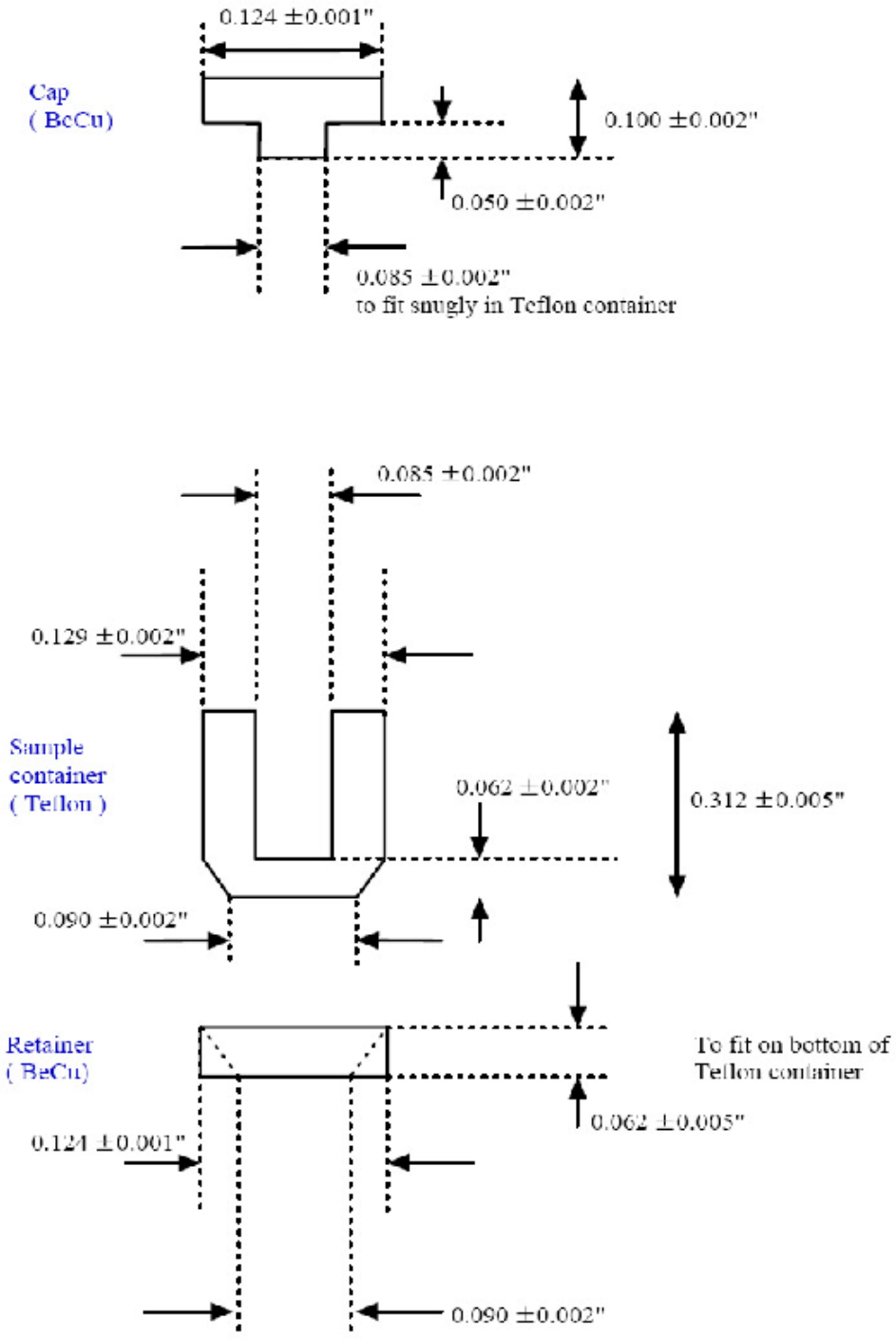

Figure 2.10 Cap, sample container and retainer

pressure. We increased the pressure in the intervals of 1/2 to 1 kBar in each step, tightening the top screw after each pressure increase. After each pressure increase, we waited for two minutes in order to let the pressure relax throughout the whole pressure cell. Applying pressure is a frustrating process, especially for inexperienced hands. Besides the danger of catastrophic explosion or breakup of the carbide rod, the zirconia rods can crack or break down. During the process of applying pressure it is very important to listen for any sound emitted. Except for the normal sounds from the hydraulic press just about any sound emanated from the apparatus indicates that pressing should be immediately stopped. Usually sounds like clicks indicate that the zirconia rods might be chipped or cracked. Another danger is that when a good seal is not achieved the pressure-transmitting liquid can seep out and the Teflon cap and the sample will be crushed. In our current setup, when we did not observe an increase in the pressure indicator after compressing 4mm, then it was considered likely that the liquid was escaping from the Teflon cap. Again compression should be terminated. In that case, the sample should be taken out and the pressure cell reassembled.

2.3 Other Experimental Details

Our samples for the pyrite series $Fe_{1-x}Co_xS_2$ are single crystals synthesized by standard iodine vapor techniques from high purity starting elements provided by Alfa AESAR. The typical dimension for a single sample is about a few tenths of a millimeter. The samples are then etched in hydrochloric acid to remove the remaining flux. Lattice constants for these samples were determined by X-ray diffraction measurements. In Fig. 2.11, we notice that the lattice constant tends to increase with the nominal Co concentration although there is significant scatter in the data indicating possible sample-

to-sample dependence. Comparing with previous investigations [2.13], we found that the true Co concentration of our samples is likely to be about 0.62 ± 0.1 of the nominal Co concentration. This is consistent with x determined by the saturation moment per formula unit from measurements of the magnetization in 5T fields. In Fig. 2.12, we plot the saturation moment per formula unit vs. the nominal Co concentration. We can see that the scatter is smaller in this plot than in the plot of the lattice constant. Therefore, we conclude that the saturation moment per formula unit is a good indicator of the true Co concentration. For clarity, we will continue to use the nominal Co concentration for the rest of this thesis, but it must be noted that the probable Co concentration is about 2/3 of this nominal value.

The DC magnetization and AC susceptibility above 1.8 K are measured in a Quantum Design Superconducting Quantum Interference Device (SQUID) magnetometer. The AC susceptibility below 1.8 K is measured in Oxford 200 top loading dilution refrigerator, and normalized against SQUID data for the same sample with the same frequency, 1kHz, and the same excitation field 1.47 G.

Resistivity, ρ, and magnetoresistance (MR) are measured by the standard four contact method. The Hall Effect is also measured using four contacts, with the two Hall contacts carefully aligned perpendicular to both the field and the current directions. For both the MR and the Hall Effect measurements, the sample is attached with thin Pt wires using silver paste or silver epoxy. Standard lock-in techniques are used to take data at 17Hz or 19Hz. We obtain the Hall voltage from the asymmetric part of the change in voltage with magnetic field, $V_H = (V(H) - V(-H))/2$, to avoid the problem of contamination of the data from field symmetric MR due to misalignment of the contacts.

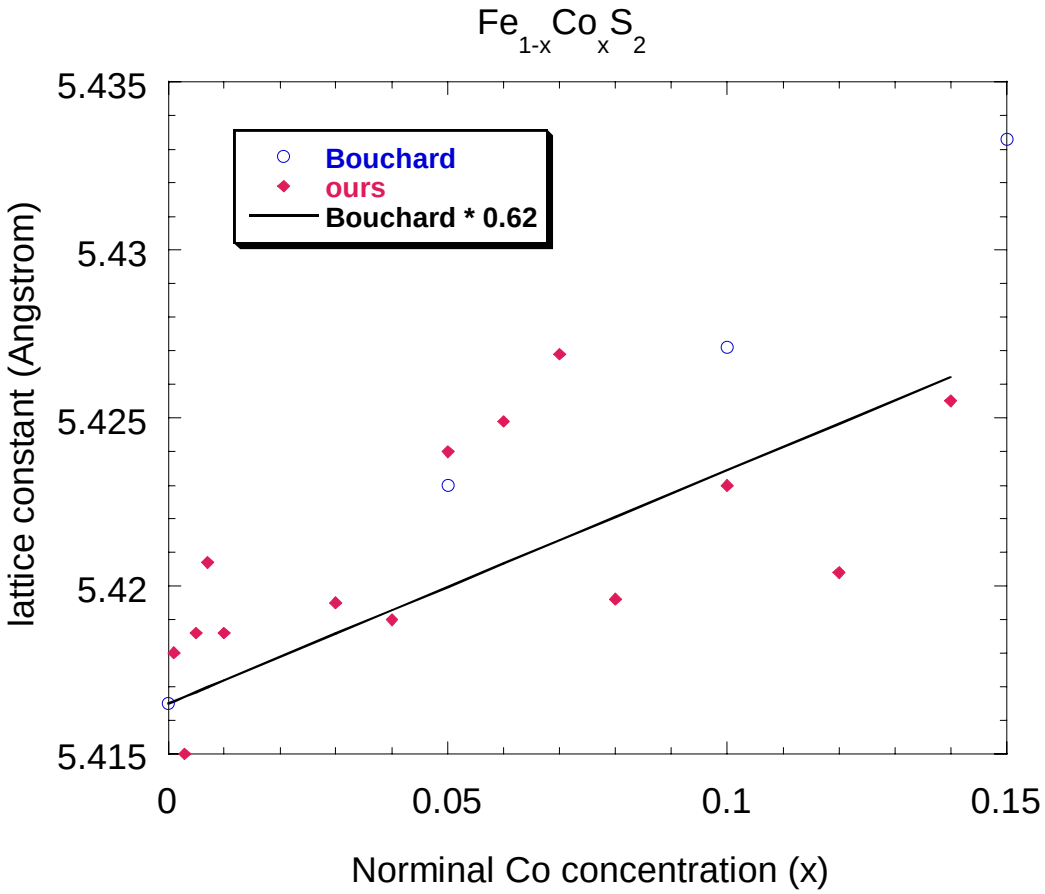

Figure 2.11 Lattice constant vs. nominal Co concentration in $Fe_{1-x}Co_xS_2$

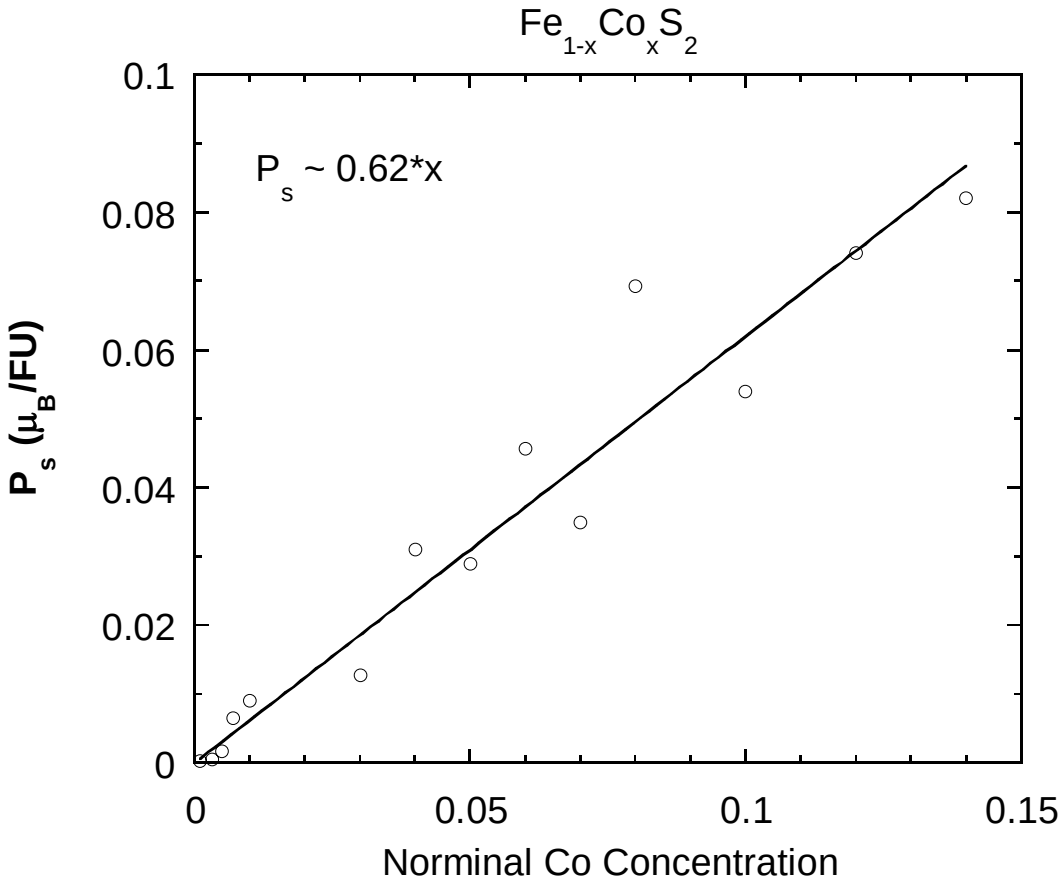

Figure 2.12 The saturation moment per formula unit vs. nominal Co concentration

Chapter 3 Magnetization and Magnetic Susceptibility Measurements in $Fe_{1-x}Co_xS_2$

3.1 Introduction

Magnetization and magnetic susceptibility measurements are important tools in characterizing materials. Usually, for a paramagnetic or a ferromagnetic metal above its Curie temperature, the magnetic susceptibility is composed of two terms [3.1]. The first is the temperature-dependent Curie-Weiss term for fluctuating moments

$$\chi_{cw} = \frac{C}{T - \theta_W}, \tag{3.1}$$

where C is the Curie constant, and θ_W is the Weiss temperature. The second is the temperature-independent Pauli term for free carriers,

$$\chi_P = \mu_B^2 D(\varepsilon_F) \tag{3.2}$$

where μ_B is Bohr Magneton, and $D(\varepsilon_F)$ is the density of states at the Fermi energy, ε_F [3.1].

From the Curie constant, C, we can calculate the density of magnetic moment, n_c, [3.1] via

$$C = \frac{n_c p^2 \mu_B^2}{3k_B}, \tag{3.3}$$

where $p^2 = g^2 J(J+1)$ and k_B is the Boltzmann's constant. From n_c, we can calculate the Curie moment per formula unit P_c.

In the same fashion the magnetization of paramagnetic metals also has a linear in field term for free carriers ($M(H) = \chi_P H$), and a nonlinear term [3.1]

$$M(H) = ngJ\mu_B B_J\left(\frac{gJ\mu_B H}{k_B T}\right) \tag{3.4}$$

where $B_J(x)$ is the Brillouin function which is defined as

$$\boldsymbol{B}_J(\boldsymbol{x}) = \frac{2\boldsymbol{J}+1}{2\boldsymbol{J}}\boldsymbol{ctnh}\left[\frac{(2\boldsymbol{J}+1)\boldsymbol{x}}{2\boldsymbol{J}}\right] - \frac{1}{2\boldsymbol{J}}\boldsymbol{ctnh}\left[\frac{\boldsymbol{x}}{2\boldsymbol{J}}\right] \quad . \tag{3.5}$$

Here J is the angular momentum quantum number and g is the g-factor, a constant that characterizes the coefficient between J and the associated magnetic moment M ($M = -g \mu_B J$).

3.2 AC Susceptibility

The Alternating Current (AC) susceptibility at zero field is measured in a Quantum Design SQUID magnetometer for $T > 1.8$ K and in a dilution refrigerator with an astatic coil for 0.05 K < T < 1.8 K. The temperature dependence of the AC susceptibility of $Fe_{1-x}Co_xS_2$ is plotted in Fig 3.1. We can see that there are systematic changes with cobalt concentration in both the magnitude and the peak temperature. The saturation at low-T, below ~ 0.1 K, for our 0.7% and 1% samples evolve into a peak with further Co doping. Further Co doping increases the peak temperature and at the same time increases the values of AC susceptibility by almost three orders of magnitude in going from our 0.7% sample to our 6% sample. We have measured the AC susceptibility at frequencies from 1Hz to 1kHz at $T \geq 1.8$ K in the SQUID magnetometer. We find only a very small frequency dependence and a small difference between the field cooled and zero field cooled susceptibility (see Fig. 3.2). Similarly, the excitation fields were varied from 0.1 G to 1.5 G, with little variation of the AC susceptibility. Although we can not rule out the possibility of spin glass formation, it is likely that these samples are highly disordered ferromagnets. We base this conclusion on the observation of a positive Curie-Weiss temperature for these samples and a smooth variation of the Curie temperature with x. At large x the behavior is more clearly ferromagnetic. In order to

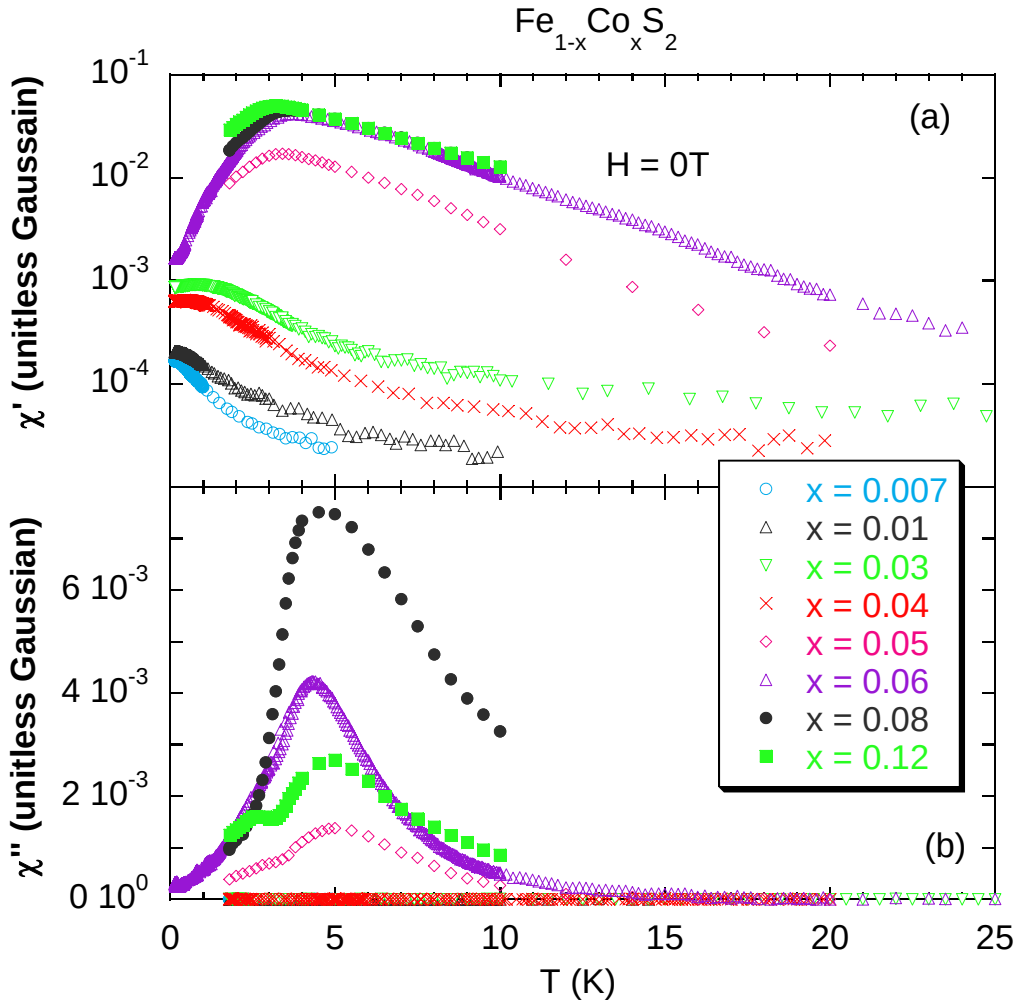

Figure 3.1 Temperature dependence of AC susceptibility at $H = 0$ for $Fe_{1-x}Co_xS_2$

Excitation field 1.5 G, frequency 1kHz for $x = 0.007$, 0.01, 0.03, 0.04, and 0.06; excitation field 1G, frequency 10Hz for $x = 0.05$ and 0.12; excitation field 1G, frequency 100Hz for $x = 0.08$.

Double peaks in χ"(T) for $x = 0.12$ are most likely due to sample variations for the data were taken on several crystals from the same batch.

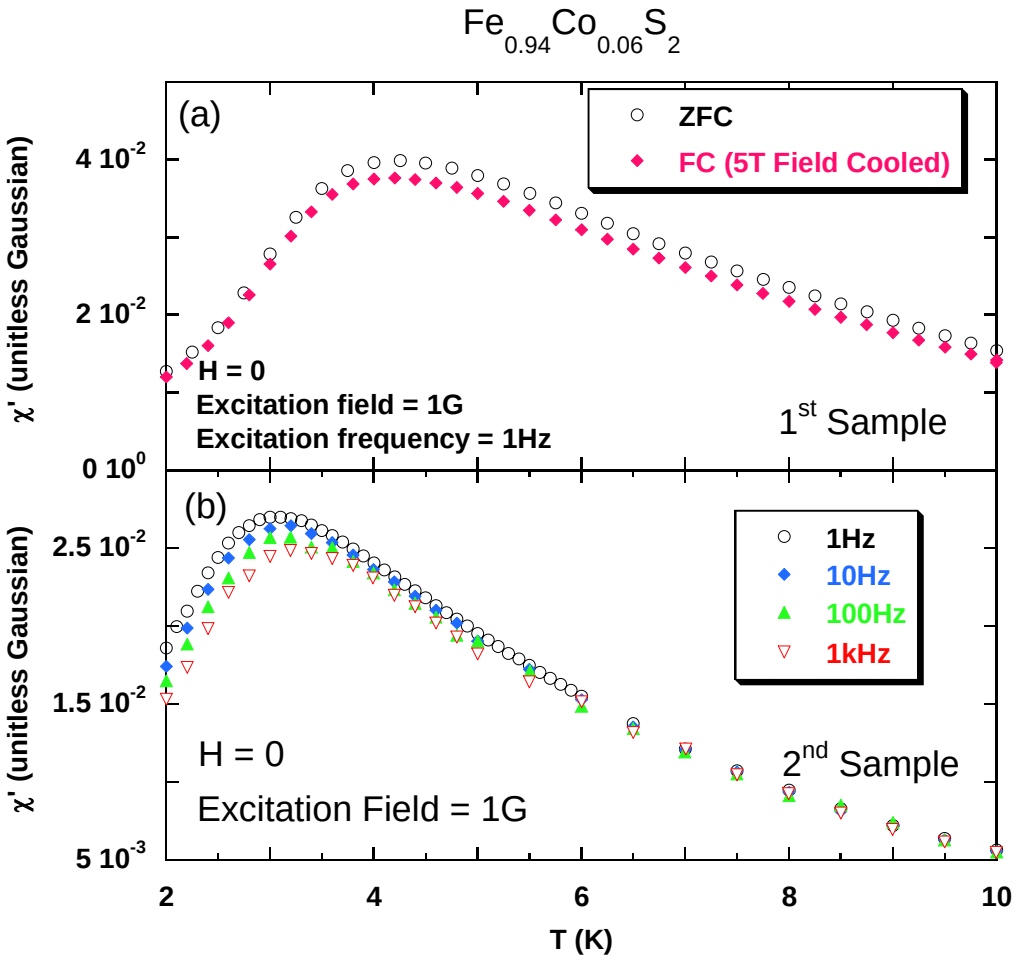

Figure 3.2 Zero field $\chi'(T)$ measured at zero field cooled (ZFC) and field cooled (FC) conditions and at excitation frequencies from 1Hz to 1kHz for two $Fe_{0.94}Co_{0.06}S_2$ crystals

differentiate between a disordered FM state and spin glass formation, neutron scattering measurements are needed to probe the long range magnetic order.

We conclude from Fig. 3.1 and 3.2 that below ~ 1% nominal cobalt concentration, the system is strongly paramagnetic down to our lowest temperature ~ 0.1 K. For samples with x larger than $x_c \sim 1\%$, a disordered FM state develops as evidenced from the peak in AC susceptibility. Further cobalt doping tends to increase the Curie temperature (T_c) as plotted in Fig 3.3.

3.3 DC Magnetization and Susceptibility

We plot our low field (H = 50G) Direct Current (DC) susceptibility as measured in the Quantum Design SQUID Magnetometer in Fig 3.4(a). The common feature is a Curie-Weiss like temperature dependence especially evident in samples with Co concentration above 4% for $T < 20$K. Broad peaks begin to show up for samples above 6% Co concentration, indicating magnetic ordering is occurring in this temperature range. Comparing with the zero field AC susceptibility, we notice that both the magnitude of magnetic susceptibility and the peak temperature are suppressed. This behavior is more evident in Fig. 3.4(b), where both AC and DC susceptibilities are measured in the same x = 0.06 sample.

In order to get a fuller picture of the magnetic state of these materials, the field dependence of the magnetization was measured and the results are presented in Fig 3.5. What this figure makes clear is that increased Co doping increases the magnetic moment in a systematic fashion. In Fig. 3.6, we plot $g\mu_B M/k_B\chi_0$ as a function of $Jg\mu_B H/k_B T$ at T = 1.8 K together with the Brillouin function for comparison, where $g = 2$, $J = 1/2$, and χ_0 is the initial susceptibility from linear fits in field from 500G to 1kG. From this plot, we can

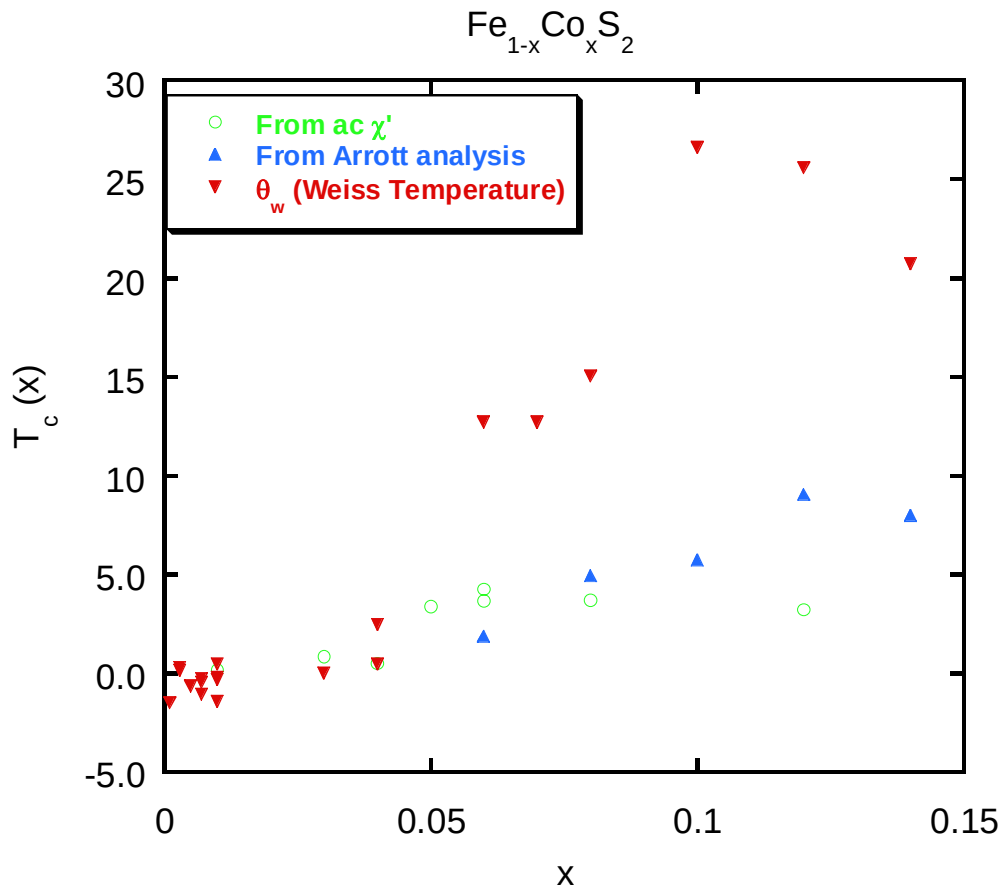

Figure 3.3 Curie temperature vs. Co concentration

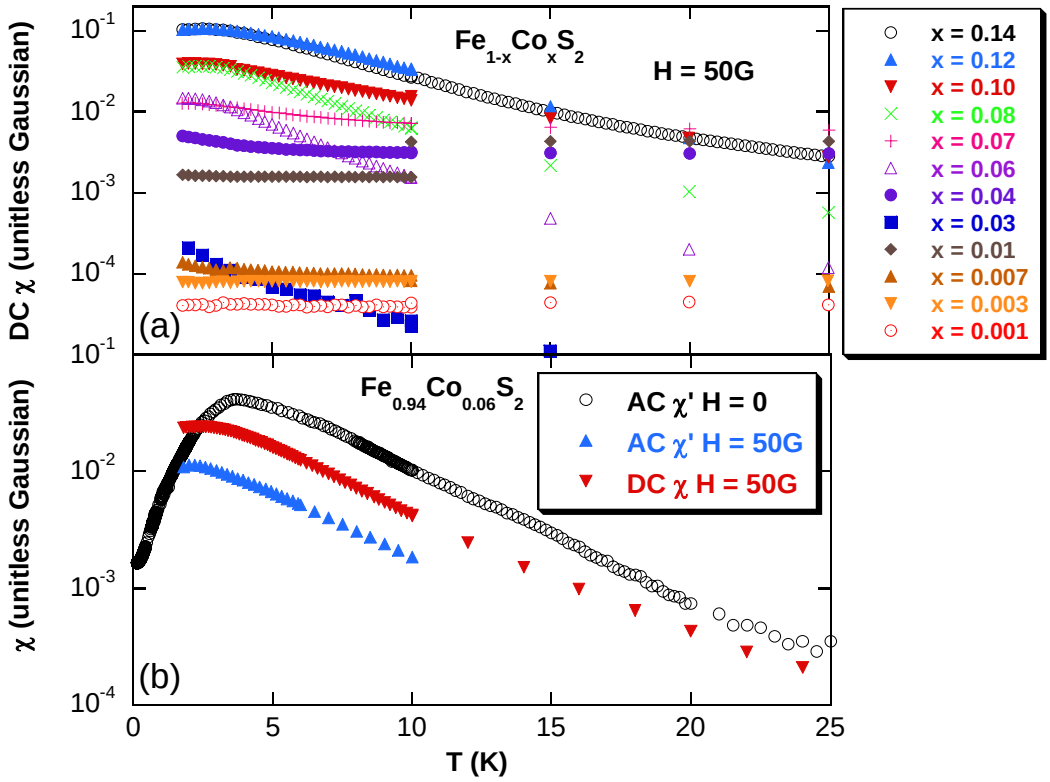

Figure 3.4 *T* dependence of DC susceptibility at $H = 50$G for $Fe_{1-x}Co_xS_2$ and *T* dependence of DC and AC susceptibility for the same $Fe_{0.94}Co_{0.06}S_2$ sample

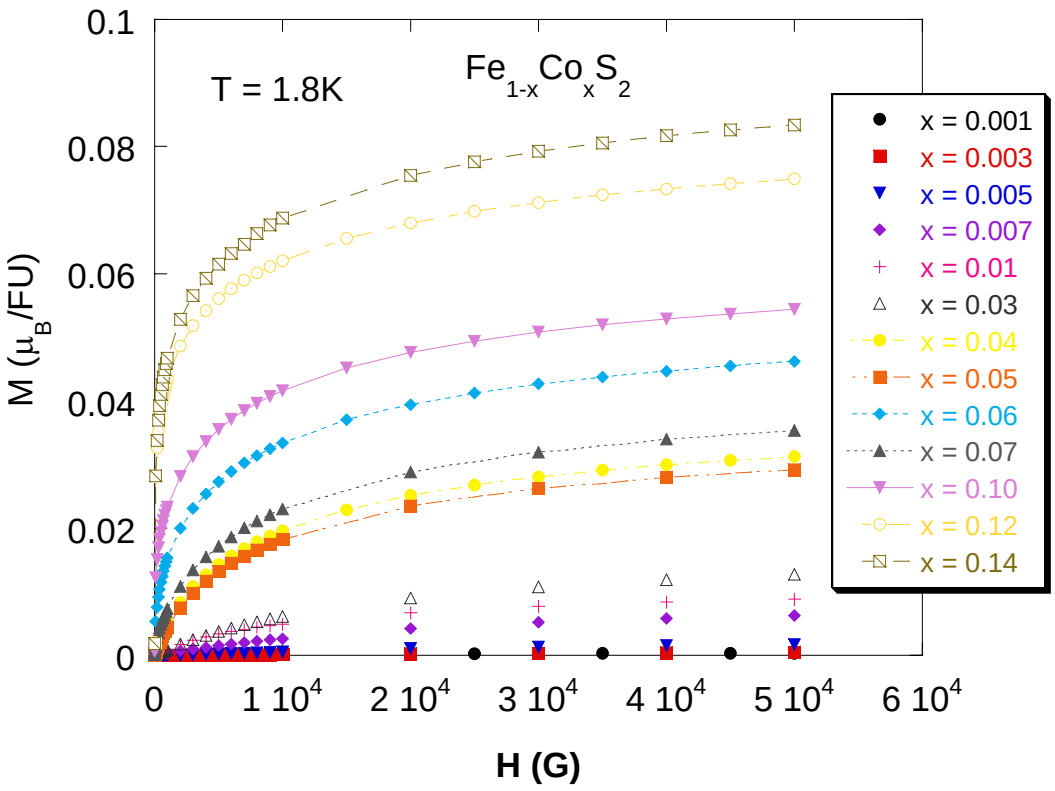

Figure 3.5 Field dependence of Magnetization at $T = 1.8$ K for $Fe_{1-x}Co_xS_2$

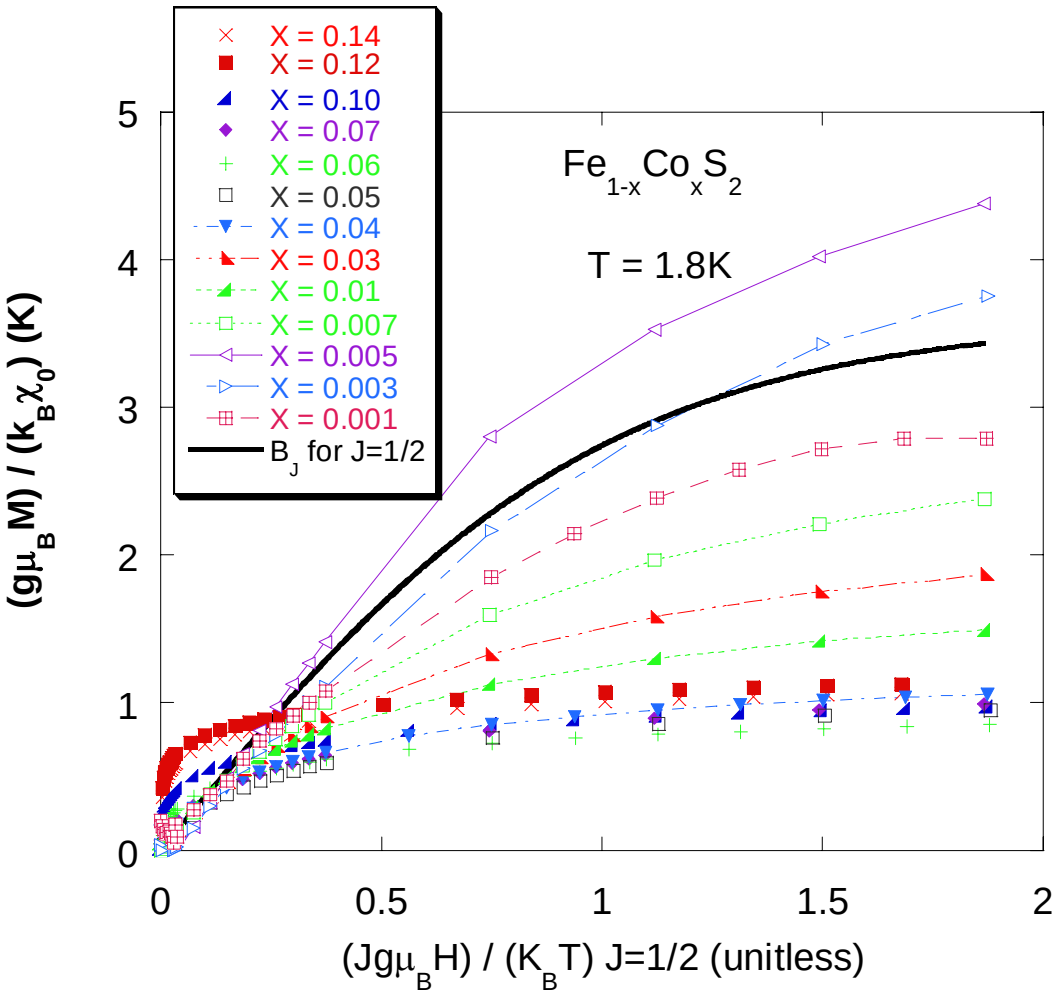

Figure 3.6 M/χ_0 vs. H/T for $Fe_{1-x}Co_xS_2$ at $T = 1.8$ K

see that for $x \leq x_c$ (~ 0.01) the magnetization is Brillouin-like. With increasing Co concentration the magnetization curves deviate from the Brillouin function and become more ferromagnetic-like. For x above ~ 0.03, it is clear that a spontaneous magnetic moment develops at low fields.

The magnetic moment at low temperature (T = 1.8 K) and large field (H = 5T) is referred to as the saturated moment or spontaneous moment. In Fig. 3.7(a), the saturated moments are plotted as a function of x as well as the moments from high T Curie-Weiss behavior. The ratio of the Curie-Weiss moment (P_c) to this saturated moment (P_s), referred to as the Rhodes-Wohlfarth ratio, is usually an indication of the degree of itinerancy of the magnetic moment [3.2]. It is found to be close to 1 for local moment magnets such as Gd. On the other hand, and it can be very large for itinerant magnets [3.2]. For our pyrite series $Fe_{1-x}Co_xS_2$ when $x \geq x_c$ (~ 0.01), the Rhodes-Wohlfarth ratio is larger than one and increases with x (see Fig 3.7(b)), although there is considerable scatter in the data indicating sample-to-sample dependence. The increasing Rhodes-Wohlfarth ratios may be an indication of the increasing itinerant nature of the ferromagnetic order at low T [3.3] [3.4] [3.5], or alternatively, the formation of spin clusters above the Curie temperature T_c. We believe the latter to be more appropriate for our pyrite series after considering our other measurements. According to equation 3.3, the Curie constant C is proportional to $n_c J(J+1)$. And since the saturation moment is proportional to $n_c J$, a large Curie constant C and a subsequently large Rhodes-Wohlfarth ratio could be the result of a small density n_c of large J spin clusters. As an example, large values of Curie moment, and therefore large Rhodes-Wohlfarth ratios, were

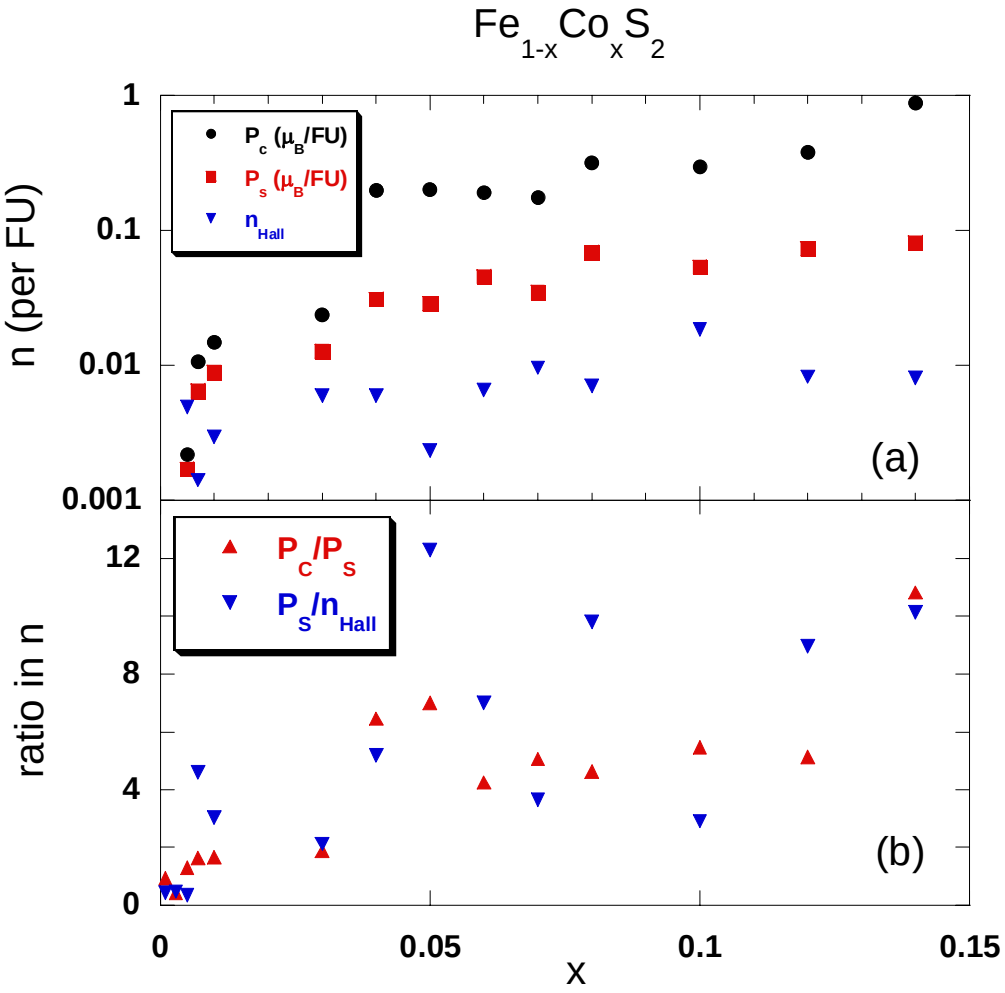

Figure 3.7 Curie moment (P_c), Saturation moment (P_s), Hall carrier density (n_{Hall}), P_c/P_s and P_s/n_{Hall} vs. Co concentration in $Fe_{1-x}Co_xS_2$

observed in doped manganites and interpreted in the context of the Griffiths phase [3.6]. The formation of spin clusters with large J will be further discussed in Chapter 4.

For an itinerant magnet, such as CoS_2, the degree of spin polarization can be estimated as the ratio of P_s, in units of μ_B per FeS_2 formula unit, to the number of charge carriers. In the case of 100%, or full spin polarization, the so-called half metals, each carrier can contribute 1 μ_B to the magnetization, and the number of carriers is equal to P_s. The magnetic moment per formula unit at low temperature and high field (H = 5T and T = 1.8 K) for our $Fe_{1-x}Co_xS_2$ series follows the nominal Co concentration for $x > x_c$ (~0.01) as shown in Fig 3.7(a), indicating most of the Cobalt atoms contributes a spin ½ moment. On the other hand, if we compare P_s with the Hall carrier density as shown in Fig. 3.8 and Fig. 3.7(b), we notice that P_s is larger than the Hall carrier density by a substantial amount for $x > 0.01$, and with increasing Co concentration, P_s tends to increase faster than the Hall carrier density. We interpret this as the result of the formation of local magnetic moments, and that a small number of carriers may be responsible for the coupling of a large number of local magnetic moments.

3.4 The Arrott Analysis

The Arrott analysis of the magnetization is often used to extract the thermodynamic Curie temperature T_c for a weakly ferromagnetic material from $M(H)$ curves [3.7].

In the mean field theory of ferromagnets, the field dependence of magnetization can be expressed as

$$\boldsymbol{M(H) = ngJ\mu_B B_J\left(\frac{gJ\mu_B(H+\lambda M)}{k_B T}\right)}, \qquad (3.6)$$

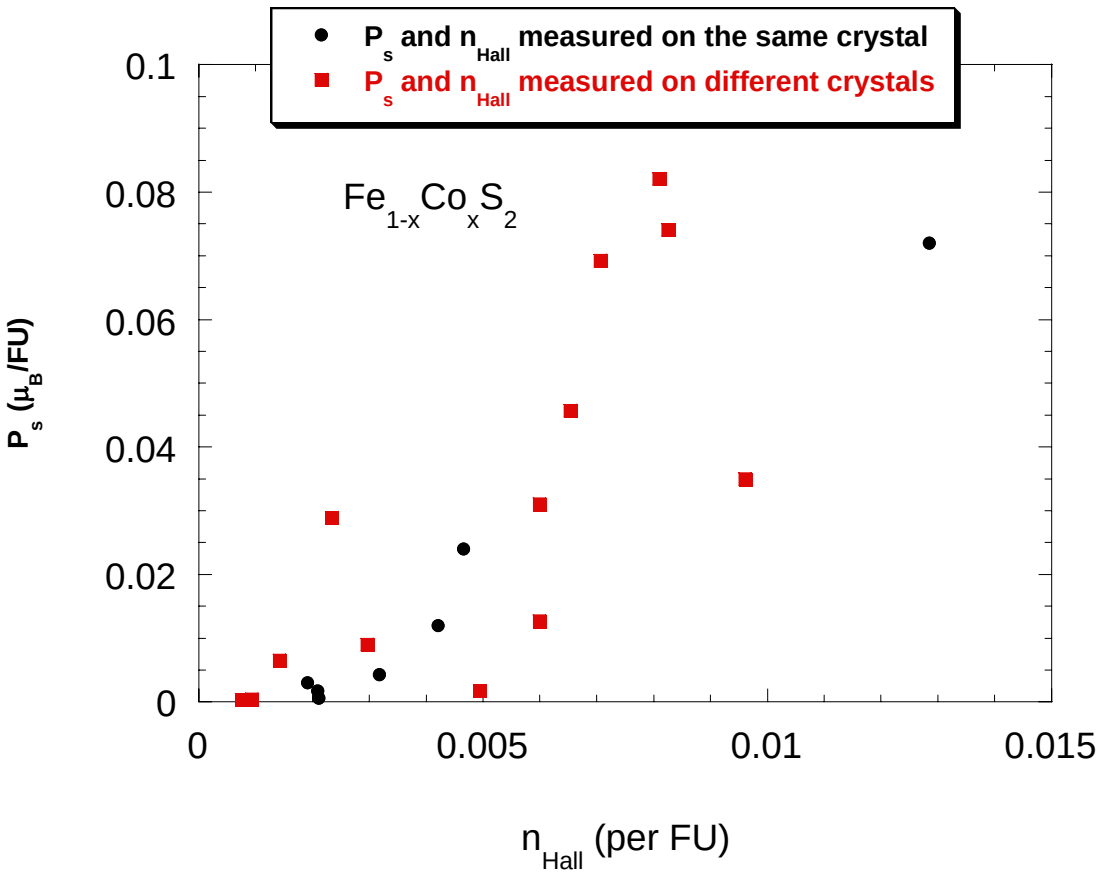

Figure 3.8 Saturation moment P_s vs. Hall carrier density n_{Hall} for $Fe_{1-x}Co_xS_2$

where $B_J(x)$ is the Brillouin function, and λ is a constant that parameterizes the strength of the molecular mean field. From this relation, the field, H, can be expanded in a power series in M, leading to the expression [3.7]

$$\boldsymbol{H} = \left(1/\chi_0\right)\boldsymbol{M} + \beta\boldsymbol{M}^3 + \gamma\boldsymbol{M}^5 + \cdots \quad , \tag{3.7}$$

where χ_0 is the initial magnetic susceptibility for fields close to zero. Therefore, a M^2 vs. H/M plot (Arrott plot) for a fixed temperature should be a straight line if we can ignore the higher order terms in M. The intercept on the H/M axis is the zero magnetization interpolation of inverse susceptibility $(\chi_0)^{-1}$. At $T = T_c$, the mean field value should be zero, and thus the plot of M^2 vs. H/M should go through zero. In Fig 3.9 we show the Arrott plot for our 8% sample as an example. The dashed lines are linear fits to the high field behavior at temperatures indicated in the figure. The reason that high field data are used in Arrott analysis is to avoid the issue of averaging over domains with different directions of the magnetization vector.

Based on the Arrott analysis, the Stoner-Edwards-Wohlfarth model [3.8] for weak itinerant ferromagnets further predicts that the inverse susceptibility $(\chi_0)^{-1}$ from Arrott analysis is a linear function of T^2. In Fig 3.10, we plotted $(\chi_0)^{-1}$ against T^2 for several samples. We can make a linear fit to the data, giving us the intercept on the T^2 axis, which should be equal to T_c^2. Note that for $x = 0.04$, we get a negative intercept on the T^2 axis indicating paramagnetic behavior down to $T = 0$ which is at odds with experimental observation of a peak in susceptibility at finite temperature. This is most likely due to the failure of mean field theory when the Curie temperature is close to zero. In Fig. 3.3, The Curie temperatures obtained from the Arrott analysis are plotted along with the peak temperatures in the zero field AC susceptibility.

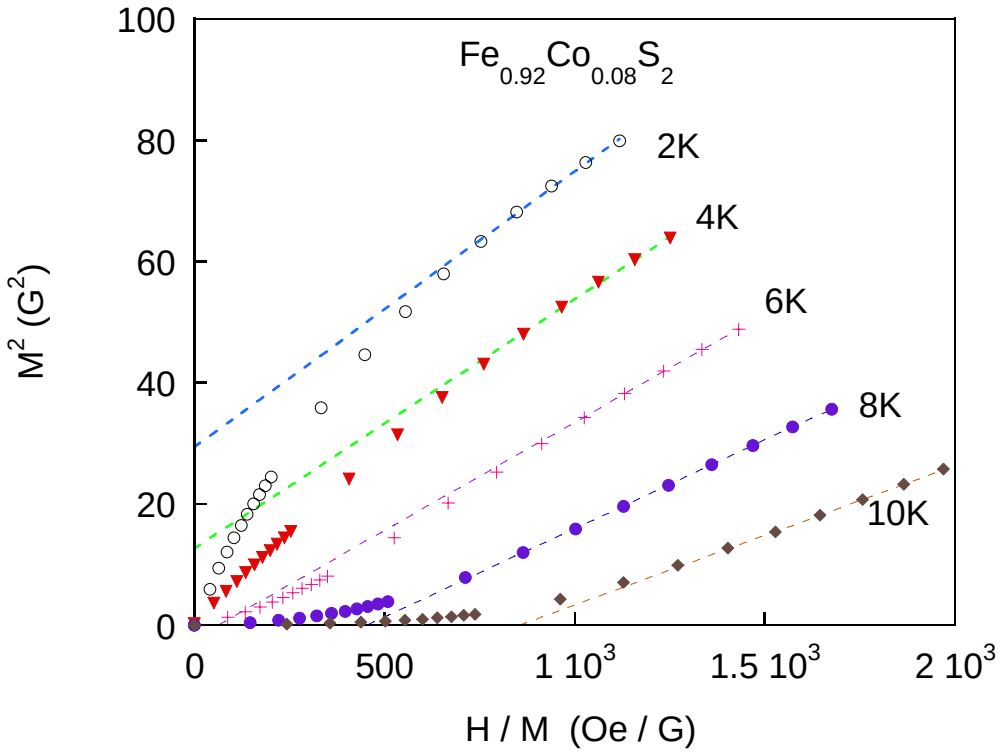

Figure 3.9 Arrott plot for $Fe_{0.92}Co_{0.08}S_2$

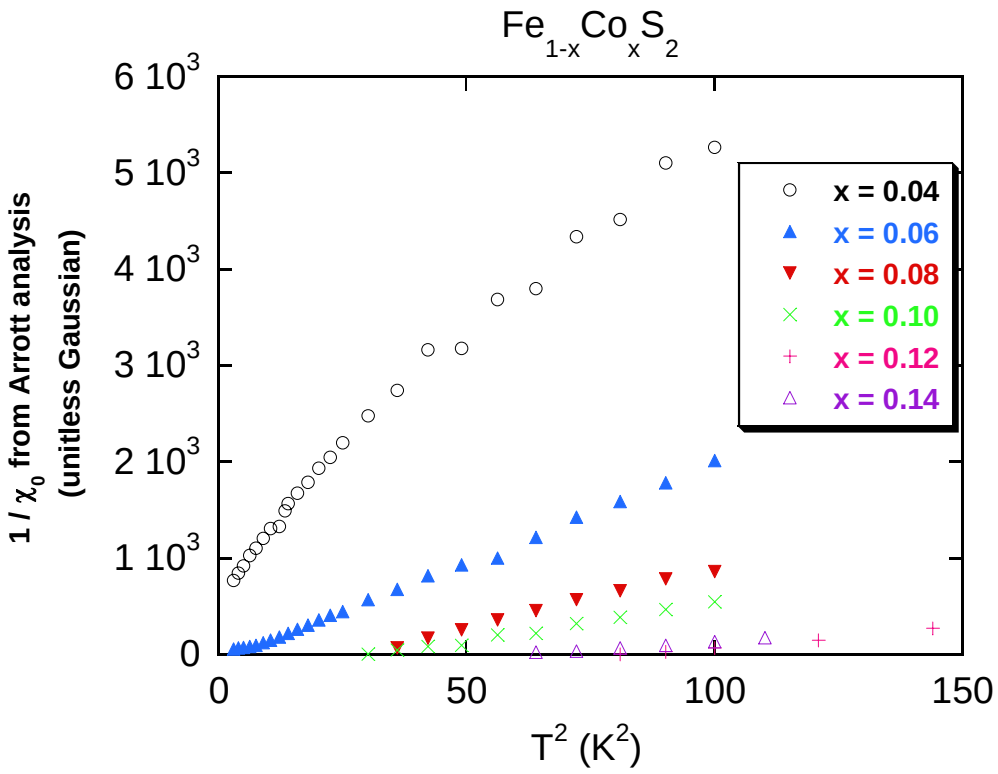

Figure 3.10 T^2 dependence of χ_0^{-1} from Arrott analysis in $Fe_{1-x}Co_xS_2$

3.5 Evidence for the Griffiths Phase

In recent years the possible existence of the Griffiths phase has gained renewed interest in strongly correlated electron systems [3.9]. For example, the Griffiths phase was invoked to explain the non-Fermi-liquid behavior in doped heavy fermion metals close to a quantum critical point [3.10][3.11]. In the doped manganite, $La_{1-x}Sr_xMnO_3$, the Griffiths phase was observed by electron spin resonance and magnetic susceptibility above the Curie temperature [3.12] [3.13] [3.14]. In the strongly localized regime of a diluted magnetic semiconductor, the Griffiths phase is also thought to occur as magnetic polarons percolate near the Curie temperature [3.15].

The original discovery of the Griffiths phase was found when investigating the problem of a random ferromagnet where only a fraction p (≤ 1) of the lattice sites were occupied with Ising spins, whereas the rest were left vacant [3.16]. The exchange interaction is taken to only exist between the nearest neighbors of occupied spins and the probability p of the occupancy is assumed to be independent of H and T. When $p = 1$, the ferromagnetic transition occurs at a temperature T_G, which is called the Griffiths temperature. For $p < 1$, the ferromagnetic transition temperature T_c is suppressed below T_G and it was shown that the free energy and the magnetization are not an analytic function of H and therefore the susceptibility is divergent at $H = 0$ in the temperature range between T_c and T_G. This is caused by the accumulation of spin clusters whose local ferromagnetic transition temperatures are higher than T_c. Bray and Moore [3.17] [3.18] extended this theory to all systems in which disorder suppresses the magnetic transition temperature from its maximal value T_G to the disordered value T_c. In this temperature

range, the system is in a Griffiths phase with divergent magnetic susceptibility at zero magnetic field.

The observation of Non-Fermi-Liquid behavior in many *d*- and *f*-electron alloys has generated much interest in recent years [3.9]. For many doped systems where disorder may be important, the Griffiths phase theory proposed by Castro Neto et al [3.10] has been invoked to explain a large body of experimental data [3.9] [3.11]. According to this theory, the NFL behavior is caused by the competition of RKKY interactions and the Kondo effect in the presence of disorder and magnetic anisotropy. The disordered Kondo lattice problem is mapped into the random Ising model in a random transverse magnetic field where the disorder is correlated. The result is the coexistence of two electronic fluids: one is the paramagnetic metallic phase quenched by the Kondo effect and the other is the granular or spin cluster magnetic phase dominated by the RKKY interactions. At low *T*, rare strongly coupled magnetic clusters can be thought of as giant spins which can quantum-mechanically tunnel over classically forbidden regions. The thermodynamic properties are predicted to follow the power-law behavior:

$$\gamma \equiv C/T \propto \chi \propto T^{-1+\lambda} \quad , \tag{3.8}$$

with a nonuniversal positive exponent $\lambda < 1$. Experimentally, λ is usually between 0.7 and 1, and always larger than 0.5 for doped heavy fermion metals [3.9] [3.19]. Our specific heat data for $x \sim 0.01$ follow the power law at low T with $\lambda \sim 0.3$, while the susceptibility displays saturation at lowest temperatures (see chapter 4 on the specific heat).

Griffiths phases were also observed in $La_{0.7}Ca_{0.3}MnO_3$ as evidenced in the sharp downturn of the inverse susceptibility above the Curie temperature [3.13], as shown in Fig. 3.11. It was argued that this downturn alone identifies the transition as a Griffith

singularity, characterized by $\chi^{-1}(T) \propto (T - T_c^{rand})^{1-\lambda}$, with λ = 0.32 as shown in the inset of Fig. 3.11.

We have also found evidence in the susceptibility measurements for the Griffith phase in our pyrite series. In Fig. 3.12, we show the temperature dependence of the AC susceptibility at zero and small magnetic fields for a 6% sample containing tens of crystals. We can see that a small field of 5G can suppress the value of the maximum susceptibility by ~ 60%. In the insets (a) and (b) of Fig. 3.12, the magnetic field dependence of the AC susceptibility at T = 4K is displayed on linear and logarithmic scales respectively. We notice that from H = 1G to 50G, the AC susceptibility at T = 4K can be fitted by a power law form ($\chi' \sim H^{0.62}$). This large suppression of the susceptibility by the small magnetic field is the first indication of the formation of spin clusters as in the Griffiths phase. To further test the existence of the Griffiths phase, we plot the temperature dependence of inverse AC susceptibility in Fig. 3.13. In the inset of this figure, we observe a sharp downturn of the zero field inverse AC susceptibility below ~30k. Notice that a small field of 10G will destroy this downturn and restore the Curie-Weiss behavior above T_c. In the case of heavy fermion systems doped close to a quantum critical point, Castro Neto argues that the formation of Griffith phases lead to a power law increase of susceptibility $\chi \propto T^{-1+\lambda}$ as the consequence of quantum tunneling of spin clusters [3.10]. In general, the relaxation rate of Griffiths clusters is expected to be proportional to its inverse susceptibility, so $\chi^{-1}(T) \propto (T - T_c^{rand})^{1-\lambda}$ may hold in general for the Griffiths phase [3.13] [3.14], leading to the downturn of the susceptibility as the Curie temperature is approached. In Fig. 3.14, we plot the logarithm of inverse susceptibility as the function of $\log(T / T_c^{rand} - 1)$, with T_c^{rand} = 24.881 K obtained by the

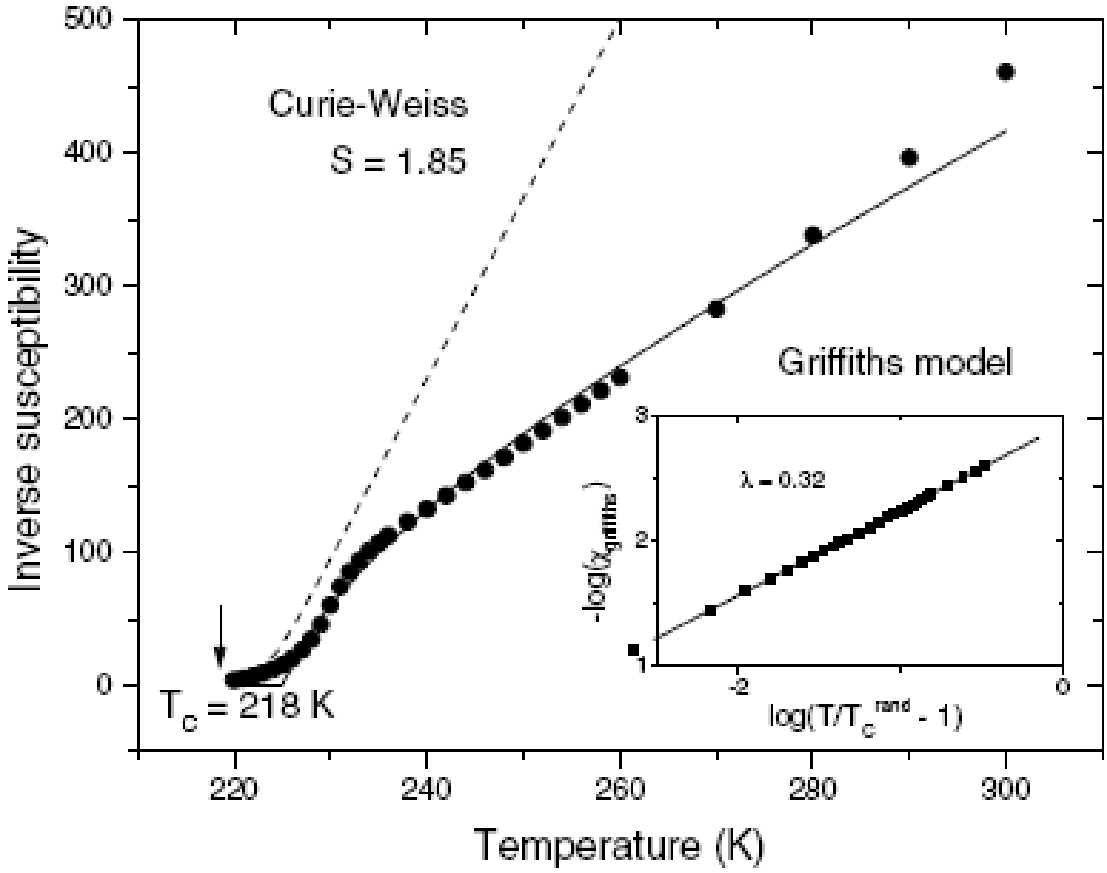

Figure 3.11 *T* dependence of DC inverse susceptibility for $La_{0.7}Ca_{0.3}MnO_3$ measured at *H* = 1kG (From reference 3.13)

(The dashed line is the expected Curie-Weiss behavior for *S* = 1.85, and the solid line is based on the calculation of the Griffiths phase.)

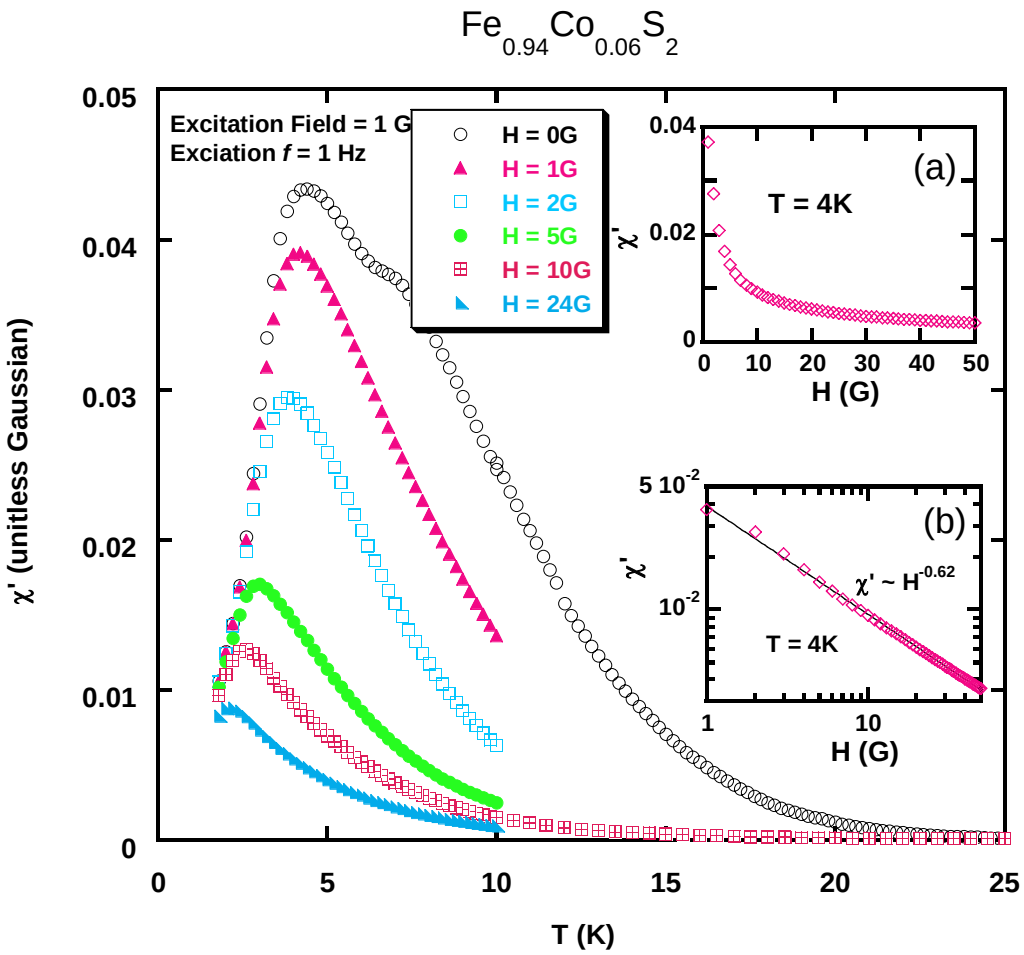

Figure 3.12 *T* dependence of AC susceptibility at magnetic fields indicated in the figure for $Fe_{0.94}Co_{0.06}S_2$

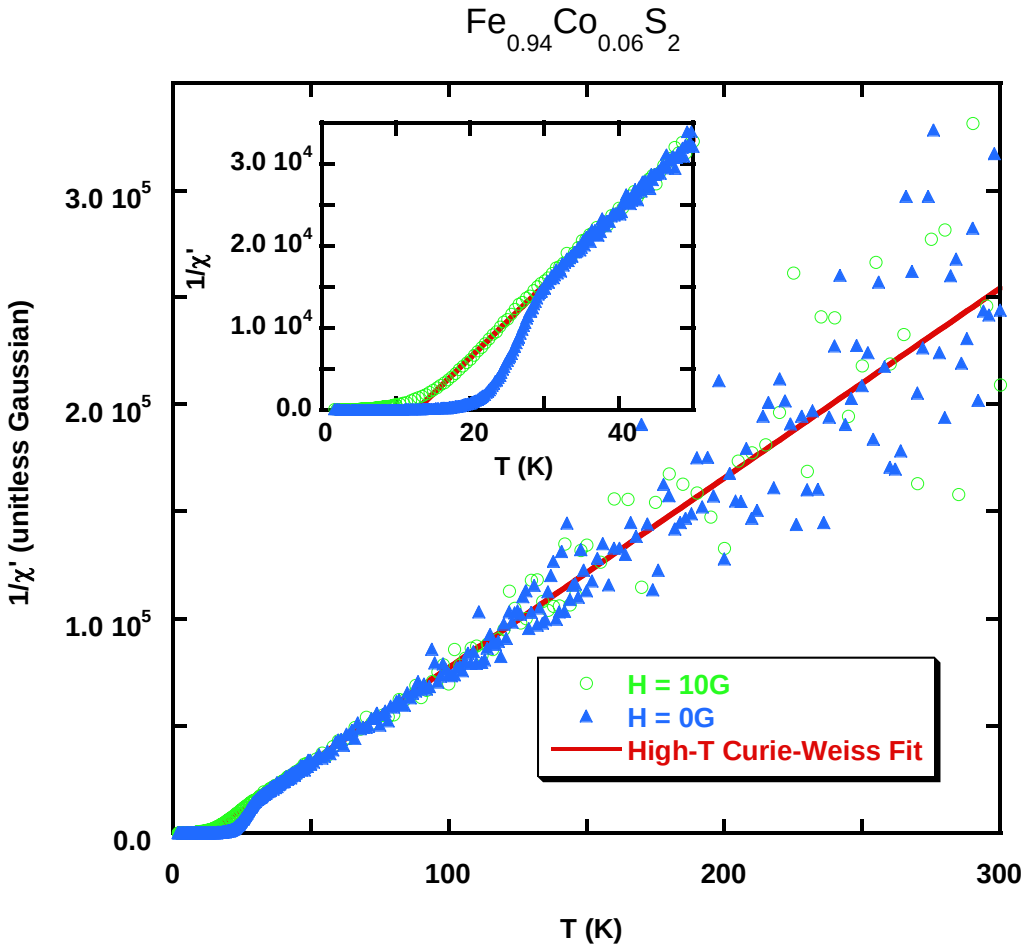

Figure 3.13 *T* dependence of inverse AC susceptibility for $Fe_{0.94}Co_{0.06}S_2$

best fitting of the data. The slope of the plot, 1-λ, is found to be 0.45, therefore the exponent λ is equal to 0.55.

3.6 Susceptibility and Magnetization under Pressure

The AC susceptibility in hydrostatic pressure for our 5%, 6% and 8% samples are plotted in Fig. 3.15 and Fig. 3.16 (a). For all the three samples we find that pressure suppresses the magnitude of susceptibility significantly. This pressure suppression is nonlinear in the sense that the lower pressures have bigger effect on reduction of susceptibility than higher pressures. The temperature of the peak in susceptibility slightly decreases from 3.7 K to 3.1 K with pressure for our 8% sample, while our 6% and 5% samples show no measurable change of the peak temperature with pressure (see Fig. 3.17).

The DC magnetization measured in 50G exhibits similar behavior to the AC susceptibility as shown in Fig. 3.16(b). Pressure has the effect of significantly reducing DC magnetization and has seemingly little effect on peak temperature.

3.7 Conclusions

Cobalt substitution of iron in paramagnet FeS_2 induces magnetic ordering at Co concentration higher than $x_c \sim 1\%$ as evidenced by a peak in the AC magnetic susceptibility. The Curie temperature increases with further Co doping as determined by the susceptibility peaks and the Arrott analysis. The magnitude of susceptibility sharply increases by more than two orders of magnitude, from our 0.7% sample to our 6% sample. For x larger than x_c, the ratio of the Curie moment to the saturation moment is larger than 1 and tends to increase with Co concentration, indicating either an itinerant nature of the low-T ferromagnetic state or the formation of spin clusters above T_c, which we think is

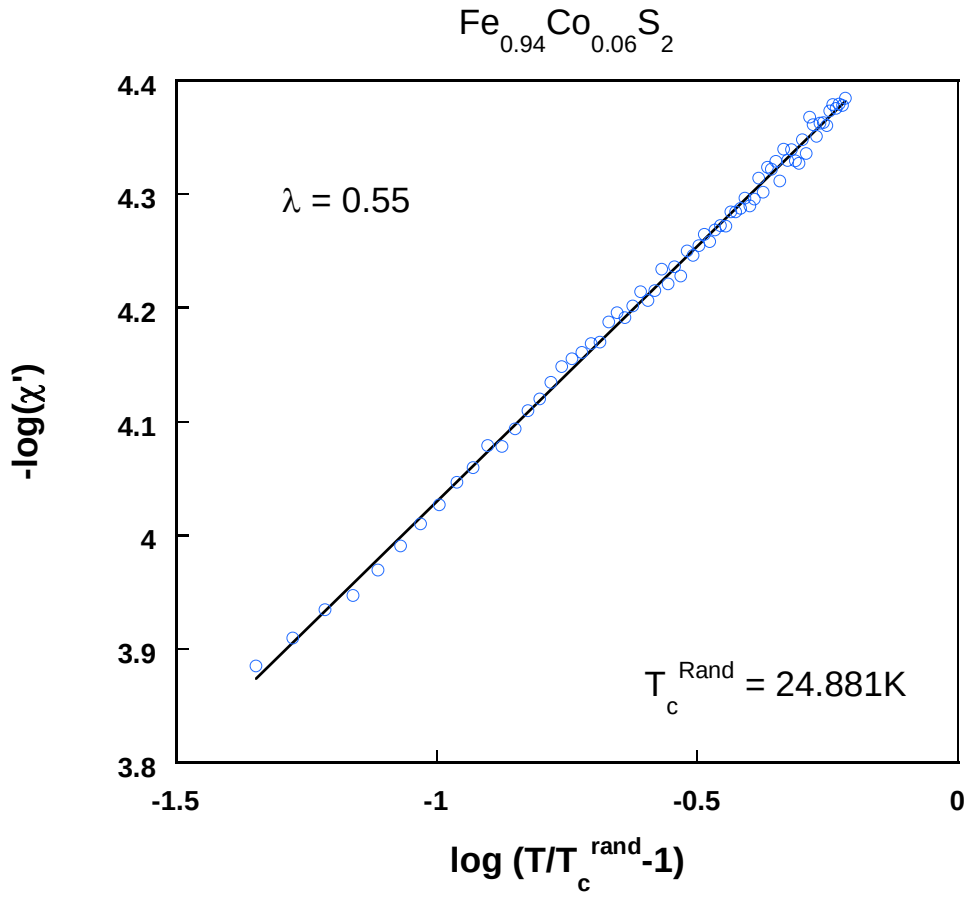

Figure 3.14 Logarithm of the AC inverse susceptibility vs. the logarithm of reduced temperature (T/T_c^{rand}-1) for $Fe_{0.94}Co_{0.06}S_2$

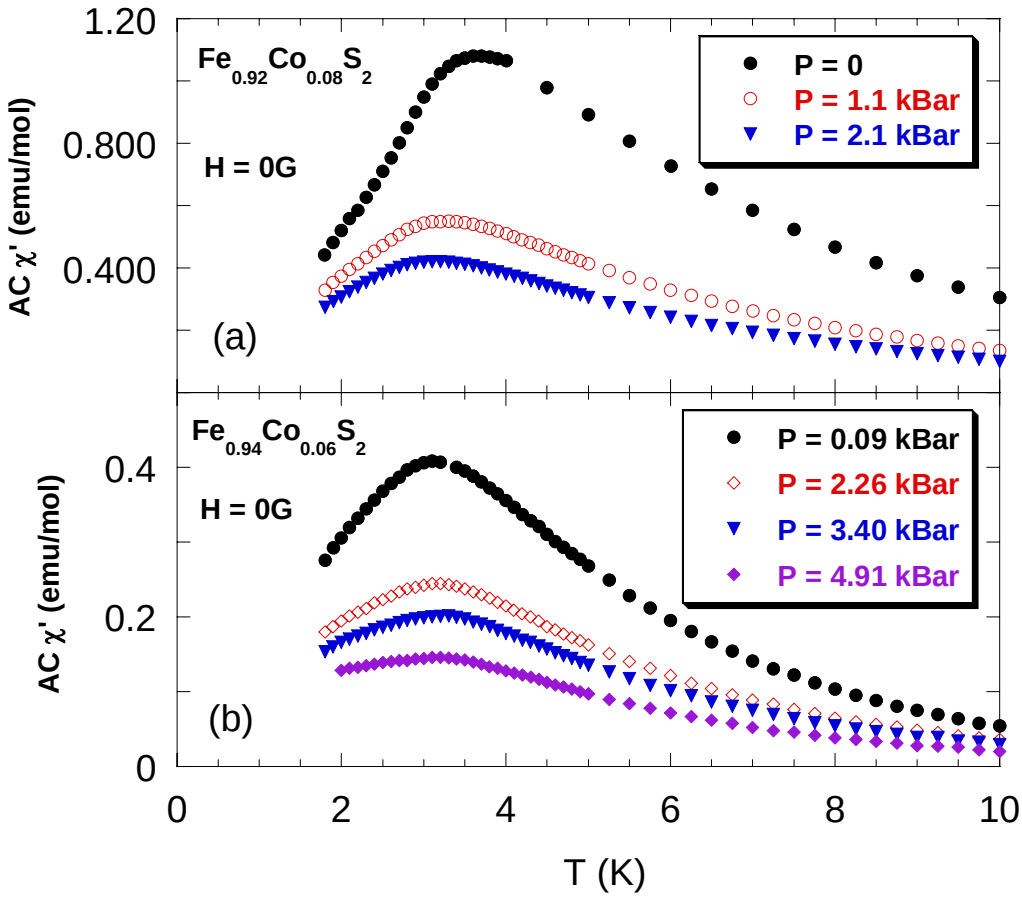

Figure 3.15 Temperature dependence of AC susceptibility χ' for $Fe_{0.92}Co_{0.08}S_2$ and $Fe_{0.94}Co_{0.06}S_2$ at pressures indicated in the figure

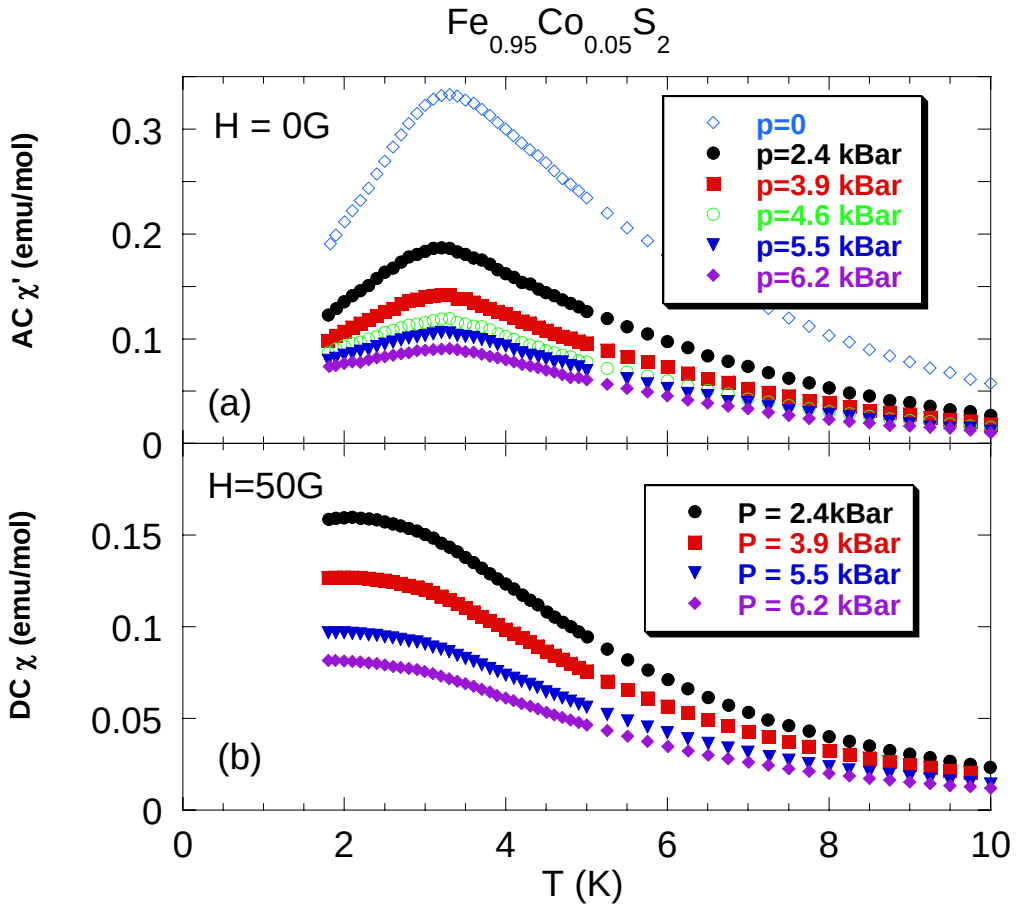

Figure 3.16 Temperature dependence of AC susceptibility, χ', and DC susceptibility, χ, for $Fe_{0.95}Co_{0.05}S_2$ at pressures indicated in the figure

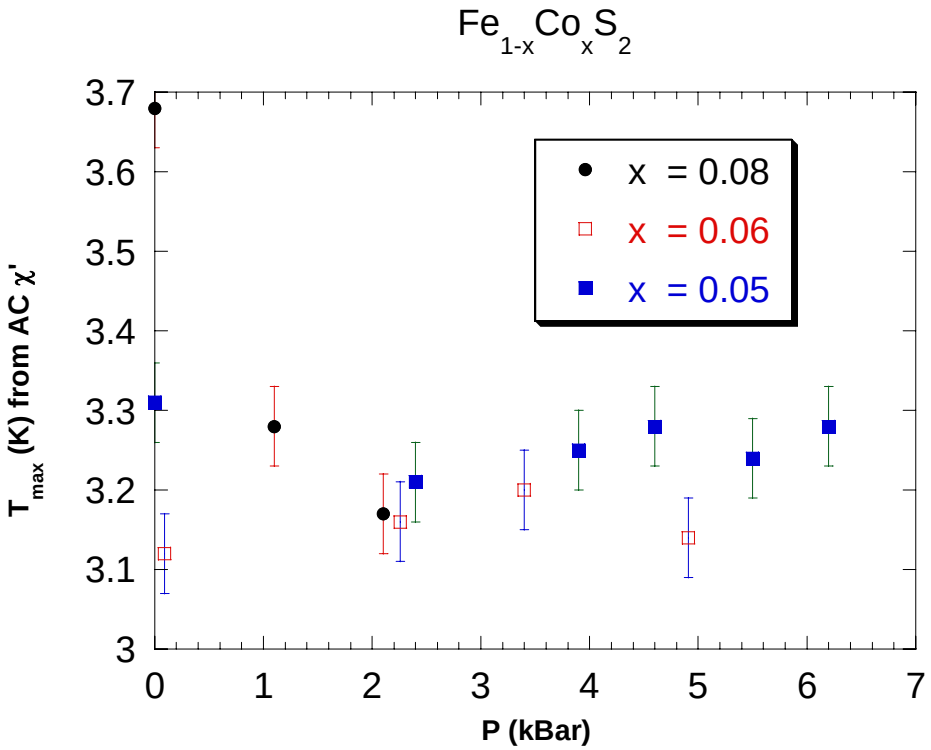

Figure 3.17 Pressure dependence of the temperature at which the AC susceptibility peaks in $Fe_{1-x}Co_xS_2$

more appropriate considering that we have a small concentration of charge carriers compared to our saturation magnetization. The magnetic moments per formula unit in high magnetic field and low temperature (H = 5T and T = 1.8 K) is close to the cobalt concentration, indicating that Cobalt atoms are effectively doped into the crystals and contributes a spin ½ magnetic moment. The Hall carrier density is smaller than the saturation moment, indicating the formation of local moments and suggesting that a small number of carriers couple a large number of magnetic moments.

The strong suppression of susceptibility by small magnetic fields at low temperatures suggests the formation of spin clusters as in the Griffiths phase. For our x = 0.06 sample, the sharp downturn of inverse susceptibility below ~ 30K is also strong evidence for the formation of the Griffiths phase above the Curie temperature.

Pressure suppresses the magnitude of susceptibility while having little or no effect on the peak temperature.

Chapter 4 Specific Heat Measurement and Wilson Ratio in $Fe_{1-x}Co_xS_2$

4.1 Introduction

The low temperature specific heat is often used to probe the electronic properties of materials. For an ordinary metal, it is proportional to the absolute temperature, with the coefficient γ proportional to the density of states at the Fermi level, $D(E_F)$ [4.1].

The density of states can be parameterized in terms of the carrier density and m^*, the effective mass [4.1]. The effective mass can be enhanced by electron-phonon interaction and electron-electron interactions or other mechanisms such as exchange enhanced spin fluctuations [4.2]. One particular example is the heavy Fermion system, where the interaction between conduction electrons and the local *f* moments can lead to an effective mass as large as 1000 times that of the bare electron [4.1]. In the following paragraphs, I will briefly discuss some possible contributions to the specific heat at low temperatures.

4.1.1 Specific Heat of Metals

Since for most metals $E_F >> k_BT$ for all reasonable temperatures, only the electrons within the range of k_BT of the Fermi energy can be excited thermally. Since each of these electrons has a thermal energy of the order of k_BT, the total electronic kinetic energy U is of the order of [4.1]

$$U \sim (NT/T_F)k_BT. \tag{4.1}$$

Here, N is the total number of electrons, and T/T_F is the fraction of electrons contributing to thermal excitations. Therefore the electronic heat capacity of N electrons is of the order of $Nk_B(T/T_F)$. Rigorous calculation of electronic specific heat for a parabolic band of carriers gives the result [4.1]

$$C_{el} = \frac{\pi^2}{2} N k_B T / T_F = \frac{\pi^2}{3} D(E_F) k_B{}^2 T \,. \tag{4.2}$$

If we take into account electron-electron interactions, in Landau's Fermi liquid theory where quasiparticles are low lying single particle excitations, we would have a one-to-one correspondence with free electrons having an enhanced effective mass m^*.

At low temperatures ($T < \theta/50$), the phonon contribution to specific heat is

$$C_{ph} = \frac{12\,\pi^4}{5} N k_B \left(\frac{T}{\theta}\right)^3 , \tag{4.3}$$

where θ is the Debye temperature and indicates the temperature above which all phonon modes begin to be excited [4.1].

The sum of electron and phonon contribution to specific heat can be expressed as

$$C = \gamma T + \beta T^3 \quad , \tag{4.4}$$

where γ is known as the Sommerfield constant. To extract the value of γ and β from the experimental data, it is often useful to plot C/T versus T^2. For typical metals which obey equation 4.4 this plot is linear with a slope β and an intercept equal to γ.

4.1.2 The Schottky Anomaly

We consider a system of N non-interacting magnetic moments, and calculate the specific heat as a function of T and H. In $H = 0$ the ground state of each moment will be degenerate with $(2J+1)$ states, where J is the quantum number associated with the magnetic moment. In magnetic field, this degeneracy in energy will be lifted and we have $(2J+1)$ energy levels associated with the m_z quantum number of the magnetic moments and the magnetic field direction.

Let us consider the simplest case for a spin-½ system where there are only two possible spin states, spin up and spin down, with respect to external magnetic field. At

low temperatures, most of the spins will be in the lower energy spin state. As we increase the temperature, some of them will be excited into the higher energy spin states. The heat capacity associated with this process is calculated as [4.3],

$$C_m = k_B N \left(\frac{\Delta E}{k_B T} \right)^2 \frac{e^{\Delta E / k_B T}}{\left(1 + e^{\Delta E / k_B T}\right)^2} \quad , \tag{4.5}$$

where ΔE is the energy splitting $g\mu_B B$ and N is the number of spins. This contribution of specific heat is known as the Schottky anomaly, and has a broad maximum in the temperature dependence of the specific heat. The peak temperature is determined by the energy splitting ΔE, which is proportional to the magnetic field. The maximum value of the specific heat is independent of the energy splitting and is only a function of the number of degrees of freedom $(2J+1)$ [4.3].

For magnetic moments of arbitrary J, the specific heat per mole is calculated as

$$C = R\left\{(y/2)^2 \sinh^{-2}(y/2) - \left[y(2J+1)/2\right]^2 \sinh^{-2}\left[y(2J+1)/2\right]\right\}, \tag{4.6}$$

where $y = (\mu_B g B)/(k_B T)$ [4.3].

4.1.3 Local Moment Contribution and Two Fluid Model in Doped Semiconductors

Phosphorous doped silicon (Si:P), a prototypical doped semiconductor, has been studied intensively since 1980's to probe the metal-insulator (MI) transition in disordered electron systems. According to the scaling theory of localization [4.4] [4.5] [4.6], which takes into account e-e interactions to all orders and disorder to lowest order, the MI transition is considered to be a zero temperature second order phase transition at critical impurity concentration, with diverging correlation length and vanishing energy scale [4.7]. The square root dependence of the conductivity on T and H at low temperatures is predicted for 3-D system and confirmed experimentally in Si:P [4.8].

In the insulating phase of Si:P, the donor ion P^+ and the localized electron form a hydrogen-like atom with a large effective Bohr radius *a*. The weak overlap of the neighboring electron wave functions lead to an antiferromagnetic (AF) interaction between these localized electron moments [4.7]. In the Bhatt-Lee model [4.9] a system of spatially random quantum Heisenberg spins-1/2 with exponential AF interactions at low impurity density ($na^3 << 1$) is calculated numerically and leads to a power-law behavior in the magnetic susceptibility, $\chi \sim T^{-\alpha}$, and specific heat coefficient, $C/T \sim T^{-\alpha}$, with the same exponent α. It also shows that the freezing of the moments into inert local spin singlets prevents long range spin ordering down to zero temperature.

In the metallic phase, surprisingly, the local moment contribution to specific heat also dominates at low temperatures [4.7]. In order to model this, the specific heat in Si:P has been consistently explained in terms of the phenomenological two fluid model [4.7] [4.10] [4.11] [4.12] [4.13]. Here the localized moments and itinerant electrons contribute independently to the thermodynamic properties, i.e. the specific heat and magnetic susceptibility. The local moments in the metallic phase are thought to originate from the random distribution of P-atoms which give rise to rare regions in the sample where a doped electron is only weakly interacting with the neighboring states and thus forms a local moment [4.7]. The following formulas give the results of the two fluid model,

$$\gamma / \gamma_0 = m^* / m_0 + (T / T_0)^{-\alpha} \quad , \tag{4.7}$$

$$\chi / \chi_0 = m^* / m_0 + \beta (T / T_0)^{-\alpha} \quad . \tag{4.8}$$

Here γ_0, χ_0, and m^* are the Fermi liquid parameters for the specific heat coefficient, magnetic susceptibility and electron effective mass, and α and $\beta \approx 3.1e^{0.4\alpha}/(1-\alpha)^2$ the

susceptibility exponent and Wilson ratio in the Bhatt-lee model for the random quantum Heisenberg spin-1/2 antiferromagnet.

In high magnetic field, $g\mu_B B/k_B T > 10$, the local moment contribution to the specific heat has a power law dependence on field, $C/T \sim B^{-\alpha}$ [4.12]. In a magnetic field, Schottky-like peaks appear in the data and are reproduced by this model. The peak temperature is proportional to the magnetic field, while the peak specific heat values are described by the formula [4.12],

$$\frac{C_1}{C_2} = \left(\frac{B_1}{B_2} \right)^{1-\alpha} . \qquad (4.9)$$

4.1.4 Kondo Effect and Heavy Fermion Metals

In a nonmagnetic metal with magnetic impurities, the antiferromagnetic exchange interaction between conduction electrons and local moments leads to interesting behavior at low temperatures [4.1] [4.14]. When the temperature is cooled below T_K, a characteristic temperature known as the Kondo temperature, the conduction electrons tend to form opposite spin clouds around the local spins, resulting in the screening of the local spins and the formation of virtual bound state. The resonant scattering of the conduction electrons by local spins will lead to a significant increase in the density of states, which can be detected by strong enhancement of specific heat coefficient γ and a ln$T$ increase of resistivity at low temperatures [4.1] [4.14].

In several *f*-electron compounds, extraordinary specific heat coefficients, $\gamma > 400$ mJ/mol.K^2, are observed [4.15]. These materials are called Heavy Fermion metals because the effective mass of electrons can be as large as 1000 times that of the bare electrons. Some of the Cerium based Heavy Fermion systems show a rapid increase of C/T at low temperatures [4.15], which can be suppressed by magnetic field[4.16] [4.17],

in contrast to U-based Heavy Fermion systems such as UBe_{13} and UPt_3 [4.18], where *C/T* is slightly increased by a magnetic field. In particular, for $CeCu_6$, a magnetic field of 24T can completely suppress the Heavy Fermion ground state by decreasing *C/T* from 1500 at zero field to 350 mJ/mol K^2 at 24T for temperatures approaching zero. The magnetic field dependence of *C/T* for $CeCu_6$ has been qualitatively fit (see Fig. 4.1) by one form of the resonant level model (RLM) [4.19], which treats $CeCu_6$ as a dilute Kondo system with crystal-field effects taken into consideration. This model is basically a one electron approximation, where the specific heat is calculated from the enhanced density of states around the Fermi energy. Another attempt to explain the drastic reduction of *C/T* by field at low temperatures is done by using lattice Anderson model on a small cluster [4.20]. Narrow dense manifold of states which are mostly spin rearrangements of *f*-electrons lead to a large specific heat at low temperatures. Although the ground state is the spin singlet state, the manifold contains states with different spins which can be Zeeman split under magnetic field, resulting in a decrease of the specific heat at low temperatures, and increase of the specific heat at higher temperatures.

4.1.5 Specific Heat Close to a Quantum Critical Point

Non-Fermi-Liquid (NFL) behavior, characterized by the low temperature increase of the specific heat linear coefficient γ, and the quasi-linear temperature dependence of the resistivity, has been studied intensively in the last decade. Theories to explain these phenomena include the single-impurity multichannel Kondo model for the case of overcompensation of local moments [4.21], disorder induced distribution of Kondo temperatures [4.21], and theories of Quantum Critical Points (QCP).

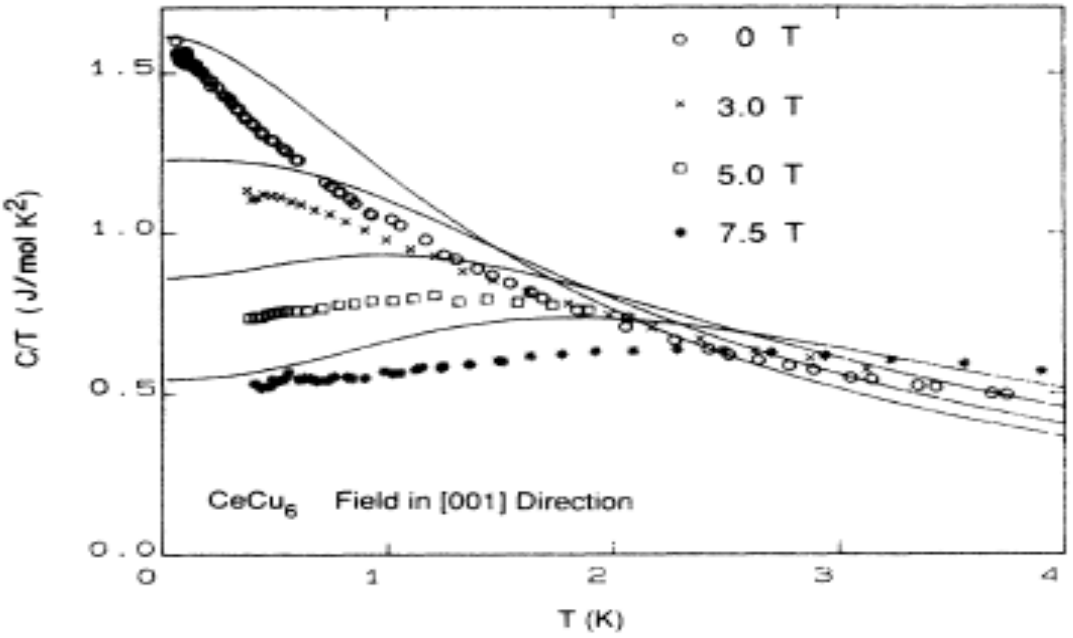

Figure 4.1 Temperature dependence of C/T for $CeCu_6$ at magnetic fields indicted in the figure (from ref. 4.19)

The lines are fits from one form of the resonant level model (RLM), which treats $CeCu_6$ as a dilute Kondo system with crystal-field effects taken into considerations (see text for details).

Since a large number of systems exhibiting NFL behavior are experimentally found close to a magnetic ordered phase, theories emphasizing quantum phase transitions have been developed in the last few years [4.21]. A quantum phase transition, as opposed to a classical one, is driven by a control parameter other than temperature, such as pressure, doping, or magnetic field, at absolute zero temperature [4.22]. It is quantum mechanical fluctuations, instead of thermal fluctuations, that are dominant at quantum phase transitions. An important conclusion that makes this quantum phase transition experimentally relevant is that for a large portion of the phase diagram, the physical properties of a material are influenced by the quantum critical point [4.22].

For 3-D ferromagnetic quantum phase transitions, diverging correlation time and length in spin fluctuations close to quantum critical point lead to NFL behavior as the temperature is cooled toward zero. Currently, there are three spin fluctuations theories for quantum phase transition, by Millis and Hertz, by Moriya, and by Lonzarich [4.21]. All three theories are for clean systems and therefore disorder is ignored. They all predict logarithm divergence of C/T ($C/T \sim -\log T$) [4.21]. For resistivity, the Millis Hertz theory predicts a linear dependence on temperature, $\rho = \rho_0 + cT$, while the other two theories predict $\rho = \rho_0 + cT^{5/3}$ [4.21]. For susceptibility, the Millis Hertz theory does not give an explicit prediction, and the other two theories predict $\chi = \chi_0 - \chi_1 T^{3/4}$. Experimentally, Ni doped Pd [4.23] has been measured to follow the predictions of Moriya and Lonzarich quite well as it approaches a ferromagnetic quantum critical point.

Castro Neto et al [4.24] proposed that Non-Fermi-Liquid behavior in *f*-electron systems could arise from disorder and the competition between the RKKY and Kondo effects, leading to the equivalent Griffiths phase of dilute magnetic systems. In this

picture, the presence of disorder leads to coexistence of two electronic fluids. One is quenched by the Kondo interaction, behaving as a Fermi liquid. The other is dominated by the RKKY interaction, leading to rare regions of ordered clusters of local moments, which are strongly coupled at low temperatures. At low temperatures, these clusters of moments can be thought of as giant spins which can tunnel over classically forbidden regions, giving rise to singularities in thermodynamic properties. It predicts both a γ (= C/T) and a susceptibility, χ, that diverge at low temperatures with a power law of the same small exponent. This theory has been invoked to model a large number of heavy fermion systems exhibiting NFL behavior at low temperatures [4.21].

4.2 Specific Heat of $Fe_{1-x}Co_xS_2$

The results of our specific heat measurement for samples with various Co concentrations are displayed as C/T vs. T^2 in Fig 4.2. The most interesting aspect of this data is the low temperature upturn in C/T, which, of course, cannot be attributed to Fermi liquid behavior. In this plot, the high temperature data can be fit by a linear function to extract phonon contribution to the specific heat, via the equation $C/T = \gamma + \beta T^2$. The values for β that best fit our data are within ± 2.5% of 2.17 J/(mole K^4) for all the samples. In the following discussions, we will subtract the phonon contribution to the specific heat and focus on understanding the remaining specific heat.

In Fig 4.3, we plot C/T versus T on a log-log scale for $T < 10$K. We observe an increase of C/T with decreasing temperature over a wide concentration range from x = 0.14 to $x = 0.003$. For $x = 0.06$ and $x = 0.04$, C/T below $T \sim 6$K increases with cooling and then eventually becomes saturated or decreasing slightly to a Fermi-Liquid like behavior at the lowest temperatures. We contrast this behavior to that in the classical

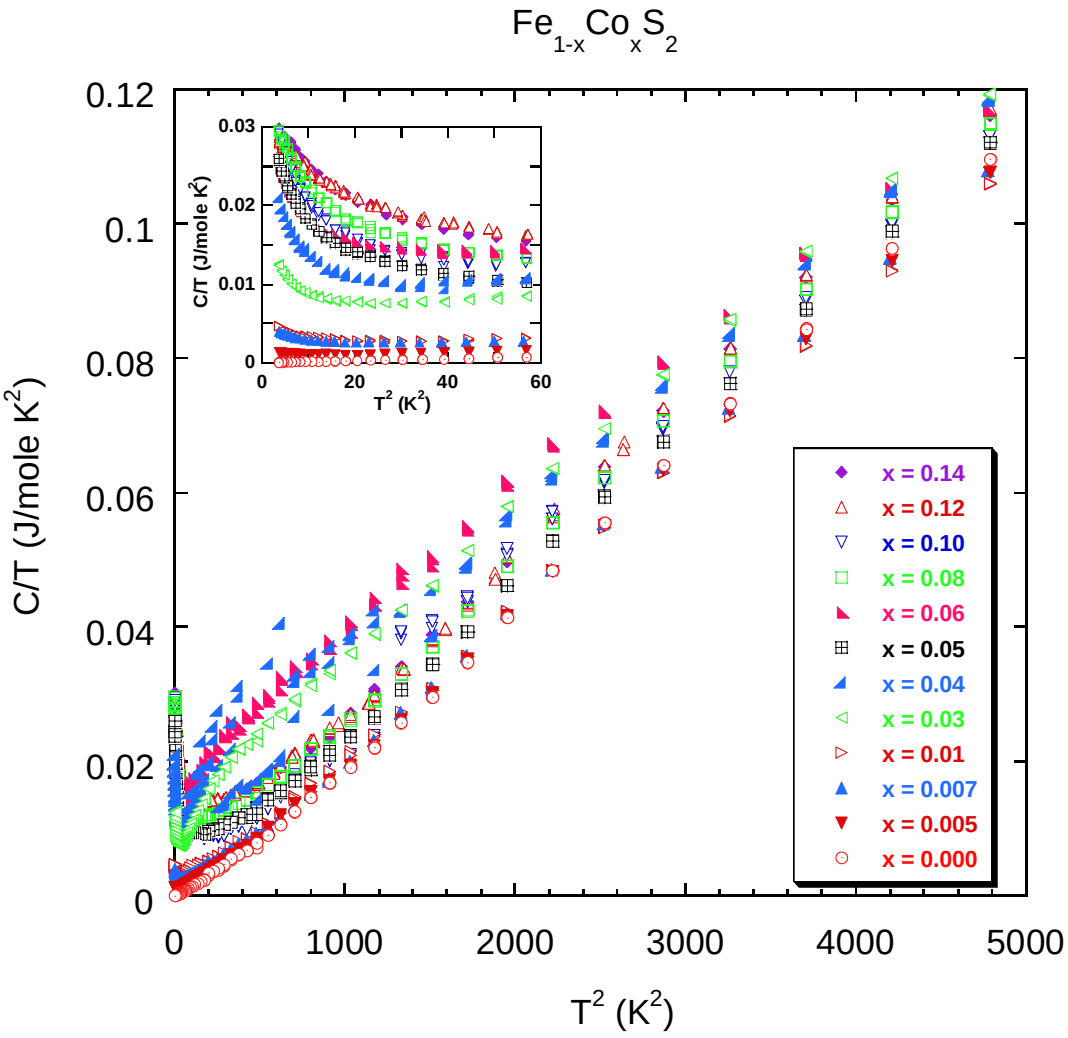

Figure 4.2 *C/T* vs. T^2 for $Fe_{1-x}Co_xS_2$

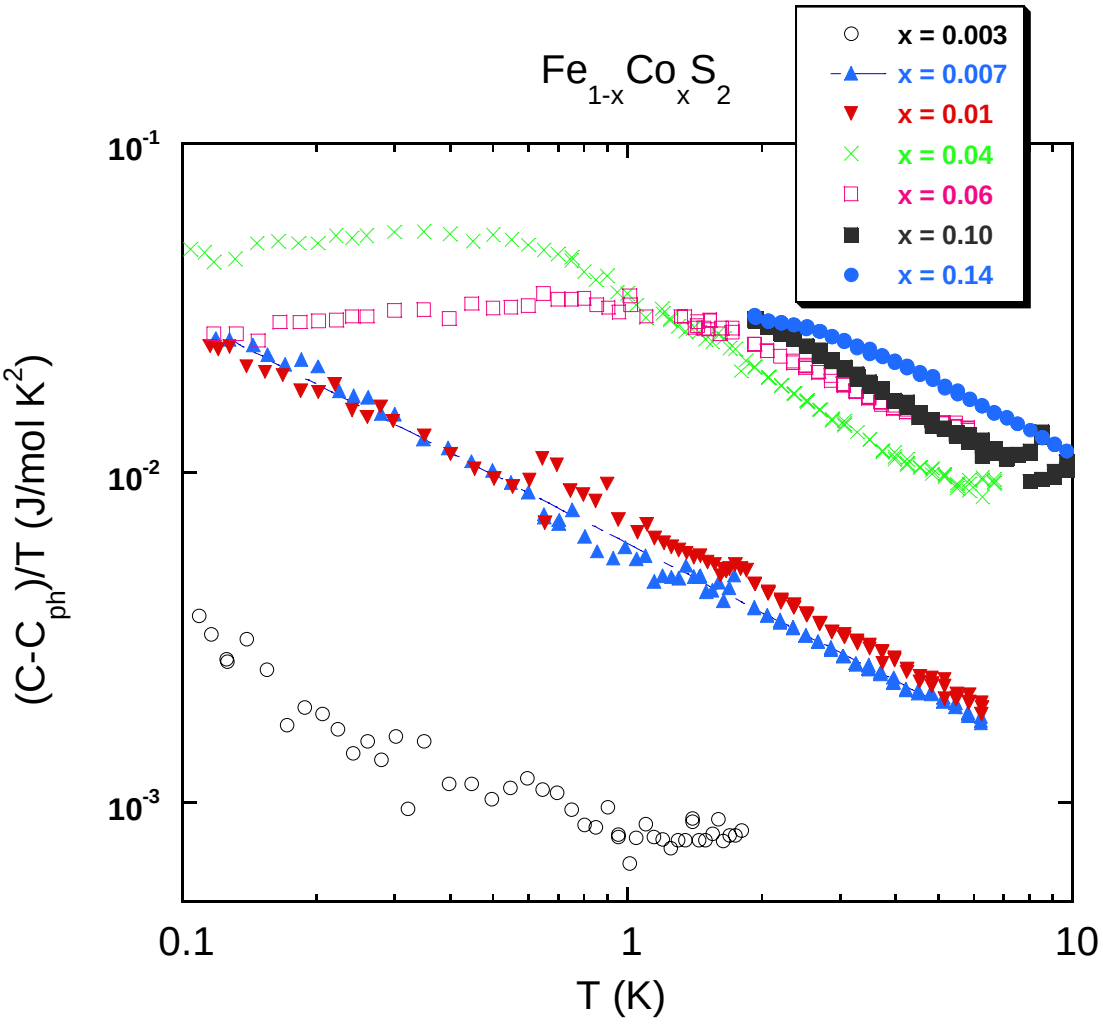

Figure 4.3 Temperature dependence of $(C\text{-}C_{ph})/T$ for $Fe_{1-x}Co_xS_2$

doped semiconductor Si:P, where the low temperature anomaly is a simple power law divergent C/T. For smaller x, C/T continues to rise at lower temperatures with our x = 0.007 and 0.01 samples showing no saturation down to our lowest T measured (0.1 K). A fit to a power law ($C/T \sim T^{\alpha}$) behavior for x = 0.007, shown by the dashed line in the figure, yields an exponent of $\alpha = -0.69 \pm 0.03$. For x = 0.003, we observe that C/T is flat for T above ~ 1K, and increases roughly as a power law as the temperature is decreased below 1K. Note that our susceptibility measurements have already established that the 0.7% and 1% Co doping levels are very near the concentration for the appearance of magnetic ordering.

The power law divergence we measured in C/T extends over more than one decade of temperature for samples close to this ferromagnetic instability. We believe this is a very interesting and significant discovery. We notice that in Castro Neto's Griffiths phase picture [4.24] for disordered Heavy Fermion compounds close to a quantum critical point, the competition between the Kondo effect and the RKKY interactions in the presence of disorder may lead to coexistence of a Kondo quenched paramagnetic phase and the rare strongly coupled giant spin clusters dominated by the RKKY interactions. At low temperatures, both C/T and χ [4.24] are predicted to follow a power law divergence with the same exponent. In Fig. 4.4, we present our C/T and χ data for x = 0.007 in the same plot. We notice that the susceptibility χ follows a power law with the same exponent as C/T within experimental error for T above 0.8 K. However, the susceptibility below 0.8 K begins to saturate while C/T continues to increase as a power law. Similar features are observed for x = 0.01, 0.04 and 0.06 as shown in Fig. 4.5, 4.6 and Fig. 4.7, respectively, where C/T continues to increase with cooling after the

susceptibility saturates or peaks. Therefore we conclude that the NFL behavior, as evidenced by increase of C/T with cooling, persists into the FM ordered phase. NFL behavior within the FM phase had been observed before in $URu_{2-x}Re_xSi_2$ [4.25] close to a FM quantum critical point (see Fig. 4.8 for a phase diagram). In Fig. 4.9, the logarithmic divergence of C/T is shown for several doping concentrations of $URu_{2-x}Re_xSi_2$. Notice that for $x \leq 0.6$, a C/T divergence exists inside the FM phase. It was argued [4.25] [4.26] that for the Griffiths phase model, even in the FM phase the contribution to the critical behavior from the local magnetic clusters may exceed that of the infinite cluster which describes the long range order of the FM phase, hence it is possible for NFL behavior to exist within the FM phase.

To further test the idea of Griffiths phase and spin clusters in our $Fe_{1-x}Co_xS_2$ crystals, we assume, as a first order approximation, that all the spin clusters are of the same size, i.e. we are dealing with the problem of non-interacting magnetic moments all with the same quantum number J. At high temperatures, we can fit the temperature dependence of the specific heat by the sum of contributions from itinerant electrons γT and the contribution from the local moments of quantum number J (see equation 4.6). The density of the moments n and J are constrained such that $nJ(J+1)$ is a constant proportional to the Curie constant from the high temperature susceptibility data. In Fig. 4.10, we show the fits on the specific heat data for $x = 0.007$, 0.04 and 0.06 samples. The fitting parameters that result, n and J vs. x, are presented in Fig. 4.11(a) and (b) respectively. (The temperature range for fitting is between 2K and 6K. We also assume the g-factor to be 2.) We notice that J increases with x from ~ 2.5 for $x = 0.007$ to ~ 8 for $x = 0.14$. The value of J is much larger than ½, consistent with the picture of spin clusters.

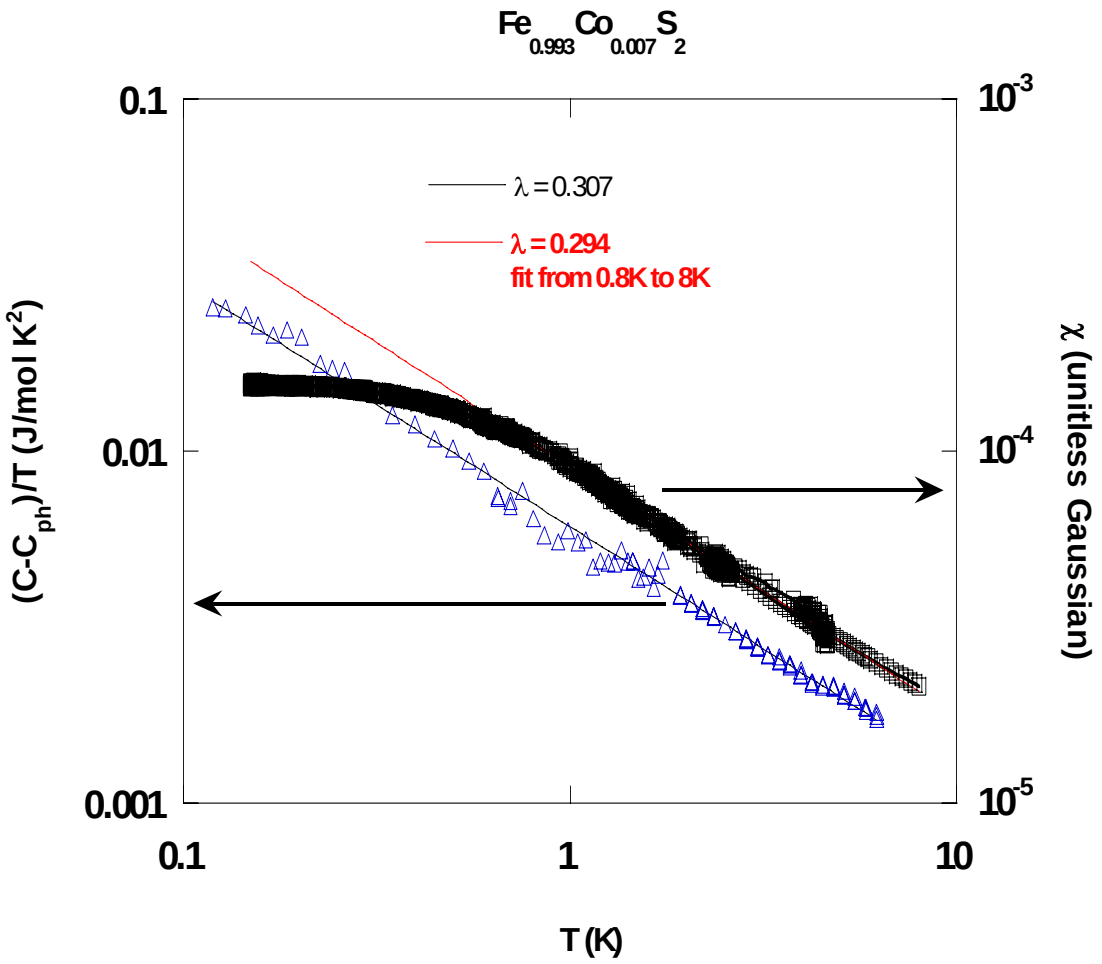

Figure 4.4 Temperature dependence of $(C\text{-}C_{ph})/T$ and χ, and the power law fit $T^{-1+\lambda}$ for $Fe_{0.993}Co_{0.007}S_2$

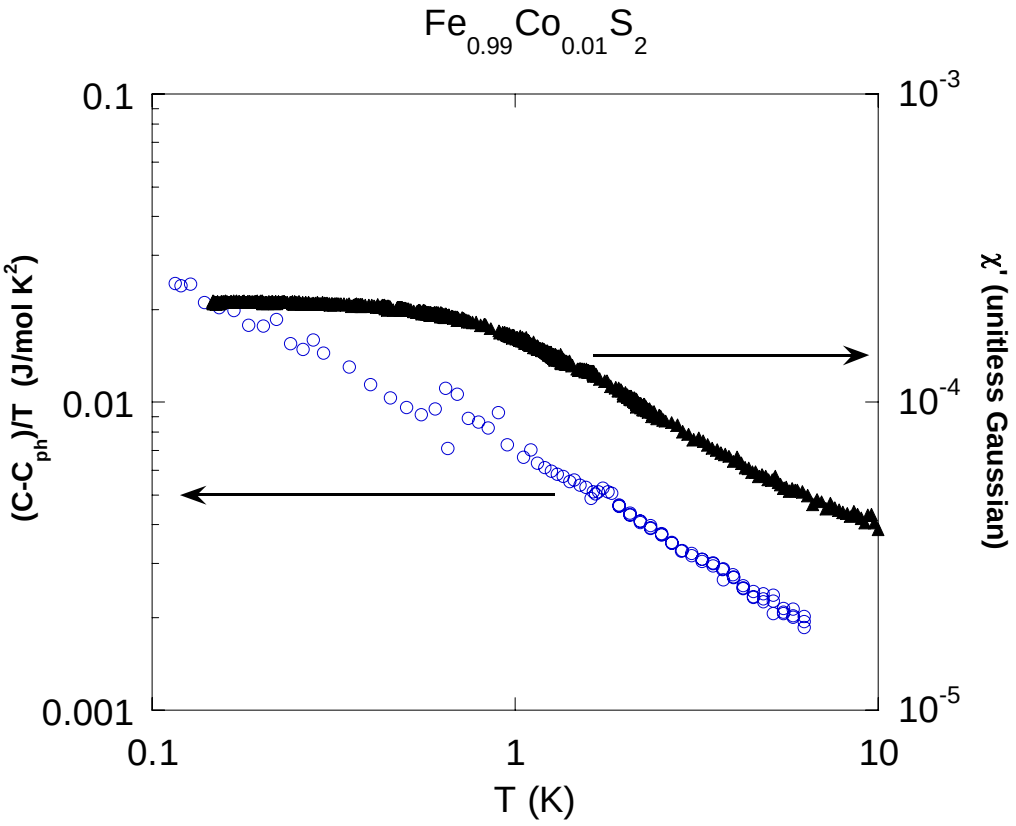

Figure 4.5 Temperature dependence of $(C\text{-}C_{ph})/T$ and χ for $Fe_{0.99}Co_{0.01}S_2$

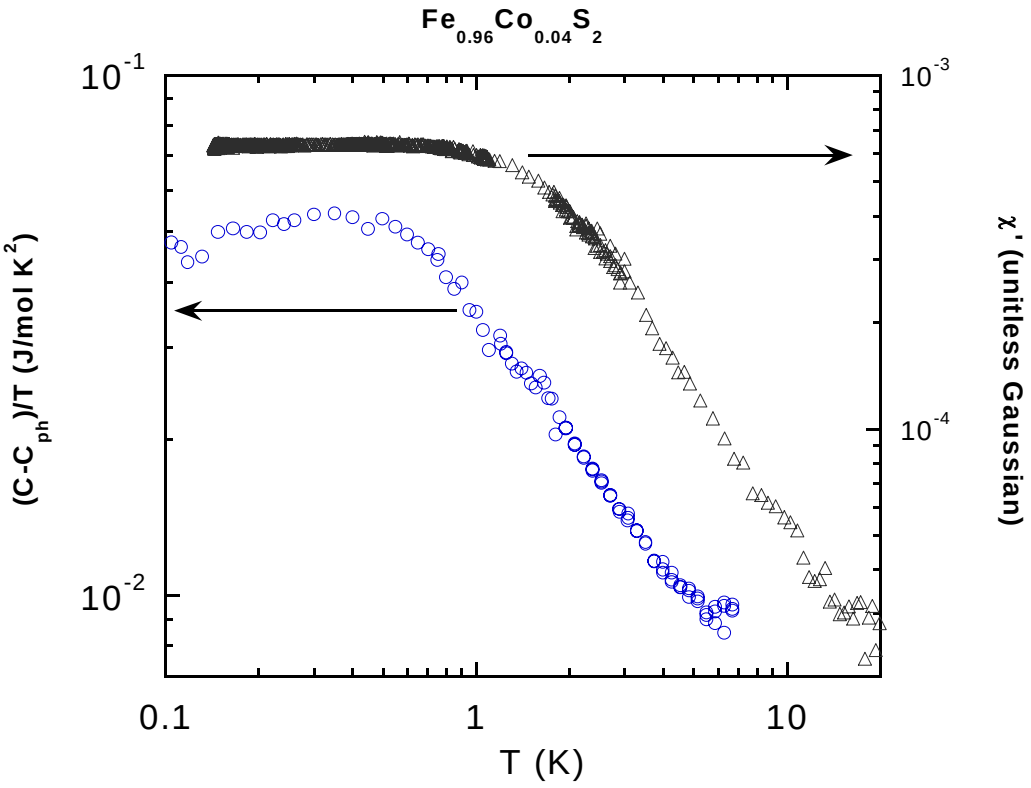

Figure 4.6 Temperature dependence of $(C\text{-}C_{ph})/T$ and χ for $Fe_{0.96}Co_{0.04}S_2$

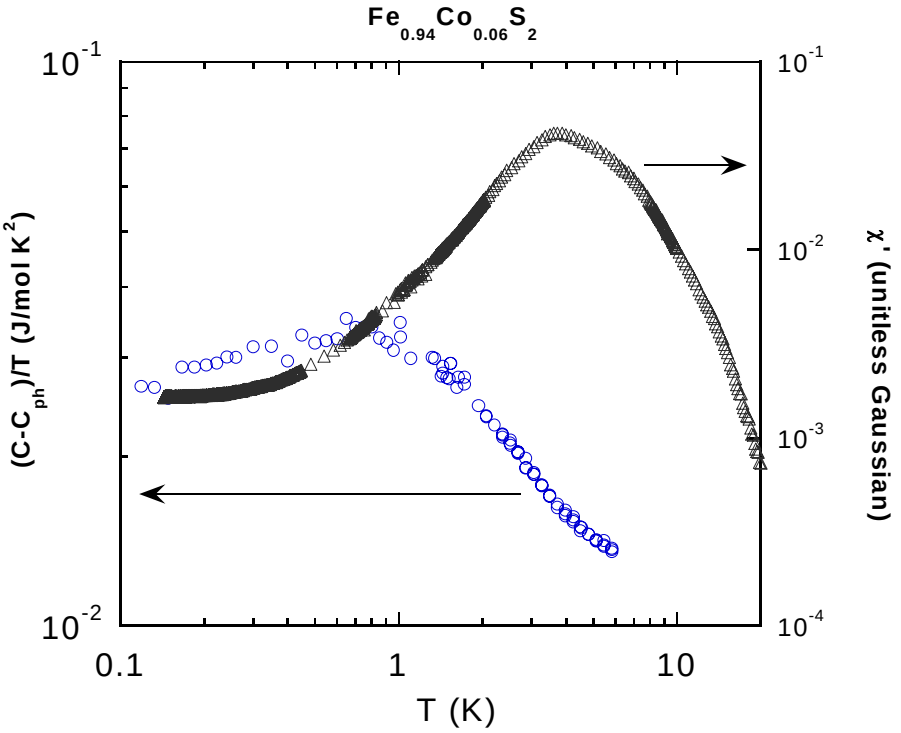

Figure 4.7 Temperature dependence of $(C\text{-}C_{ph})/T$ and χ for $Fe_{0.94}Co_{0.06}S_2$

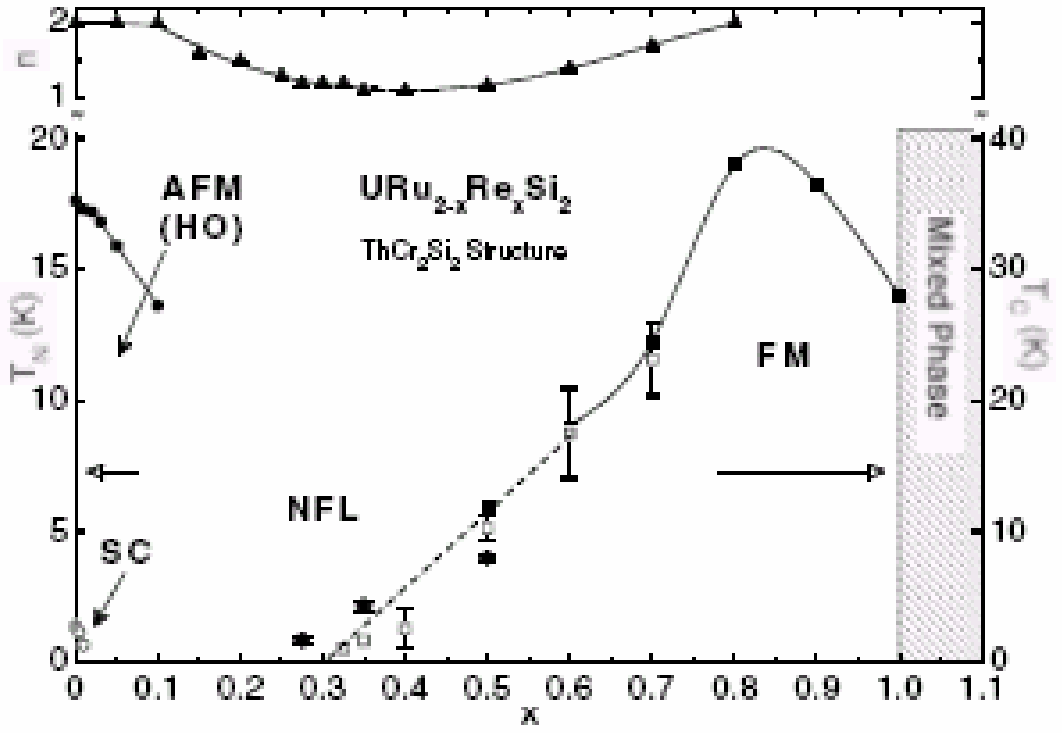

Figure 4.8 Magnetic phase diagram of $URu_{2-x}Re_xSi_2$ (from Ref. 4.25)

(Filled squares: Arrott plot analysis; filled diamonds: modified Arrott plots; open squares: low-field $\chi(T)$ data; n is from power law fit of $\rho(T) \sim T^n$)

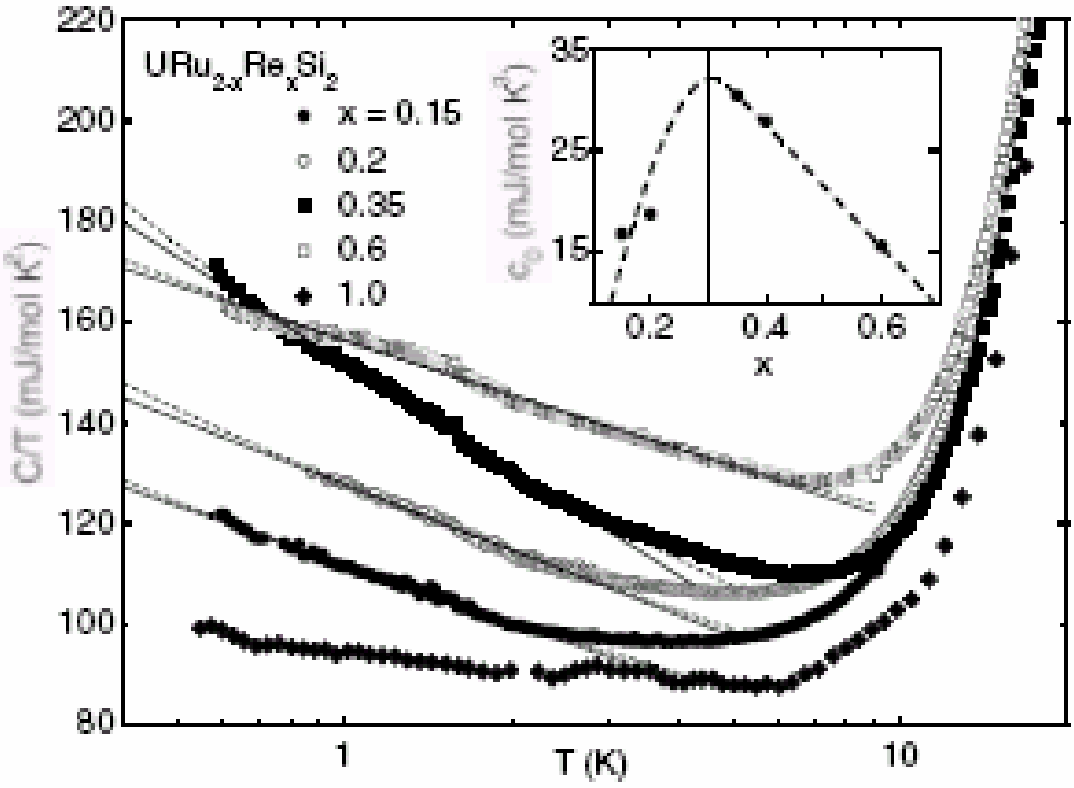

Figure 4.9 C/T vs. T for $URu_{2-x}Re_xSi_2$ (from Ref. 4.25)

(Solid line: logarithmic fit; Dashed line: power-law fit;
c_0 are from fit $C/T = \gamma_0 - c_0\ln(T)$)

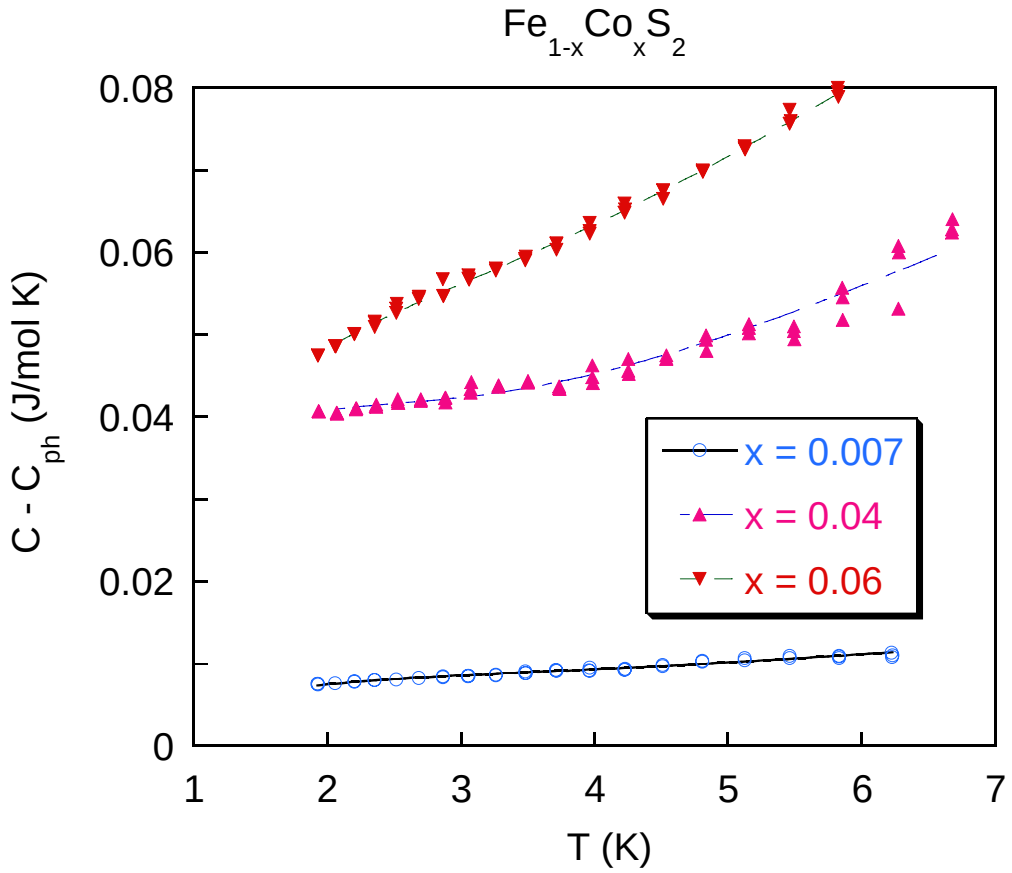

Figure 4.10 *T* dependence of C-C_{ph} for x = 0.007, 0.04 and 0.06 with fits of (γT + large-*J* Schottky Anomaly)

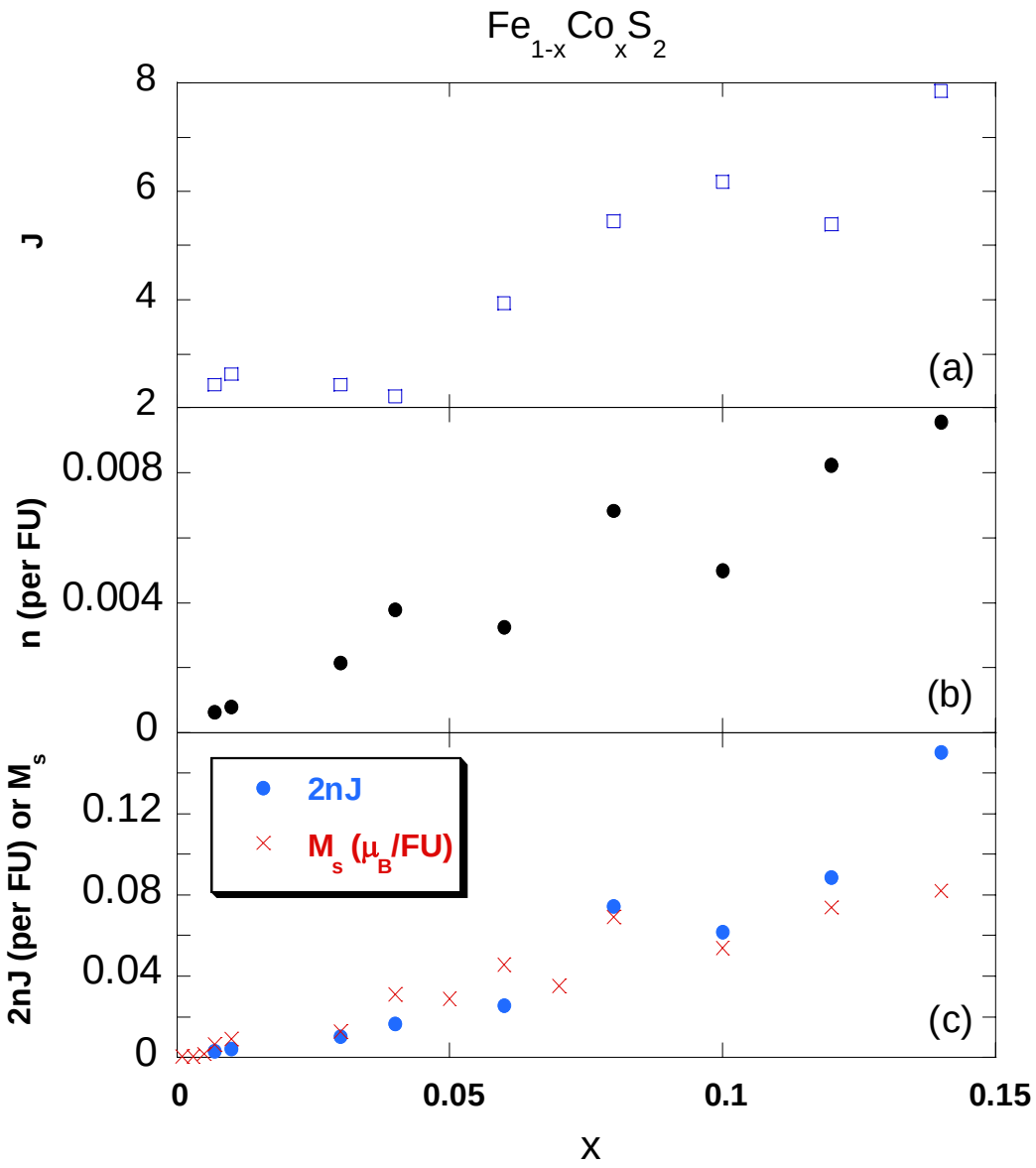

Figure 4.11 Results of the fitting and fitting parameters for $Fe_{1-x}Co_xS_2$

(J is the quantum number for local moments, n is the density of local moments per FU, and both of them are extracted from the temperature dependent specific heat data between 2K and 6K)

We also notice that n is only about 8% of x. In Fig. 4.11(c), we display $2nJ$ and M_s (the saturation moment per Formula Unit M_s) as a function of x, and we observe that both of these two quantities are roughly about 70% of nominal Co concentration x. That $2nJ$ is roughly equal to M_s is consistent with the idea that most of the doped electrons form local moments. In summary, our naive model of spin clusters of a large J can fit both the high temperature Curie-Weiss behavior of susceptibility, the high temperature specific heat and is consistent with our measured saturation magnetization, leads to the conclusion that there are a small number of large spin clusters in our crystals.

The magnetic field significantly suppresses the specific heat at the lowest temperatures for all samples, as is evident in Figure 4.12. We can see that increasing magnetic fields recover the low-T Fermi-Liquid-like behavior to higher temperature. The large electronic contribution due to the interaction of local moments and itinerant electrons can be suppressed as magnetic field is turned on and resulting in simple FL plus Schottky-like behavior. The field dependence of C/T at $T = 0.1$ K is shown in Fig 4.13 and Fig 4.14, which is simply a log-log replot of nonzero field data of Fig 4.13. Again we can fit the H-dependent C/T by a power law form $C/T = c_1 H^{c2}$ for H from 1T to 3T. We find exponent of -0.68 for our 4% sample, -0.95 for our 0.7% and 1% sample and -0.76 for the 0.3% sample at $T = 0.1$ K.

Thus far, we have only described the measured specific heat data without significant data manipulation. We can further examine the temperature evolution of the entropy ΔS, with the assumption $\Delta S = 0$ for $T = 0.1$ K. For all the samples, ΔS resembles the expected form for the combination of local and itinerant electrons, as can be seen in Fig. 4.15. We do not observe a strong discontinuity in either $C(T)$ as in Fig. 4.16 or

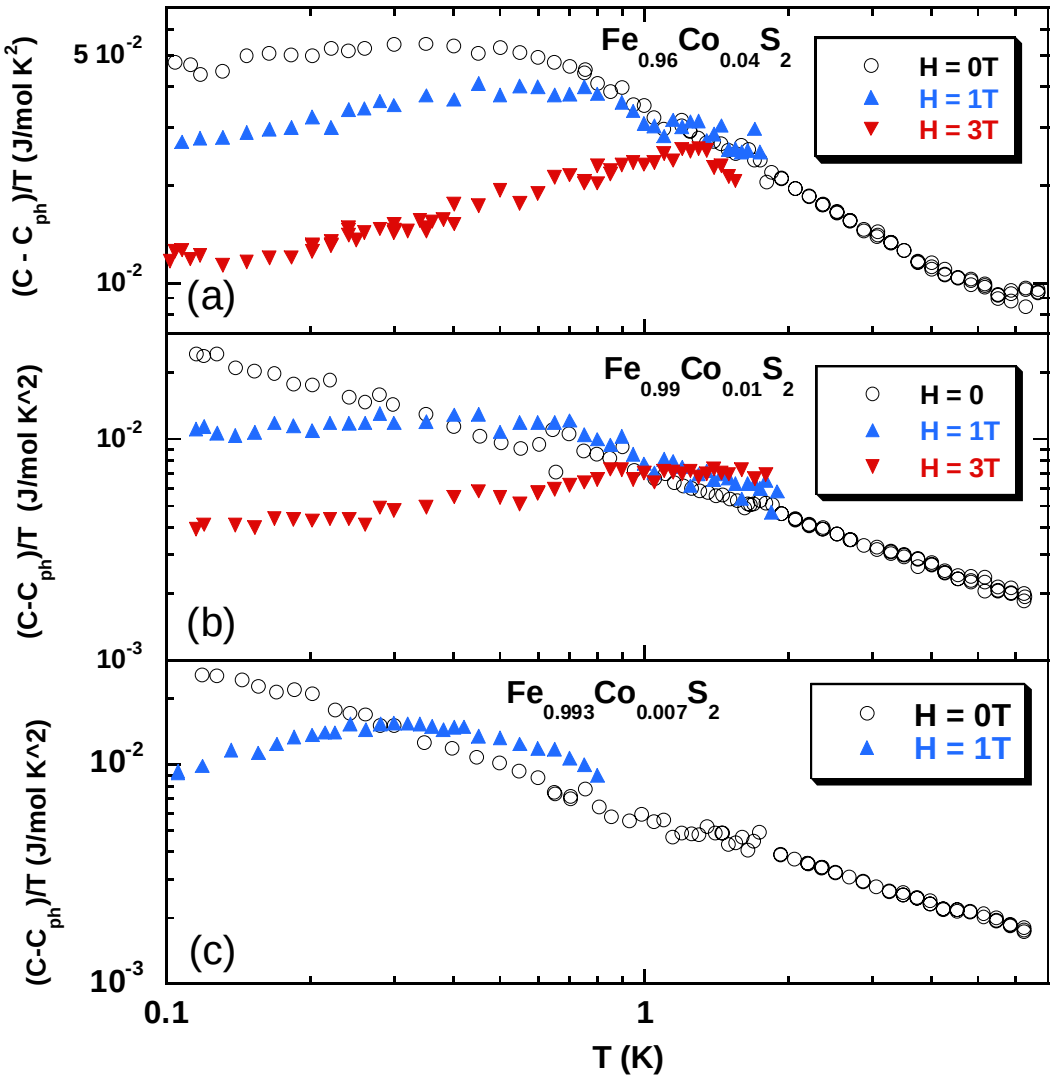

Figure 4.12 Temperature dependence of $(C\text{-}C_{ph})/T$ for $Fe_{1-x}Co_xS_2$ (x = 0.04, 0.01 and 0.007) in magnetic fields indicated in the figure

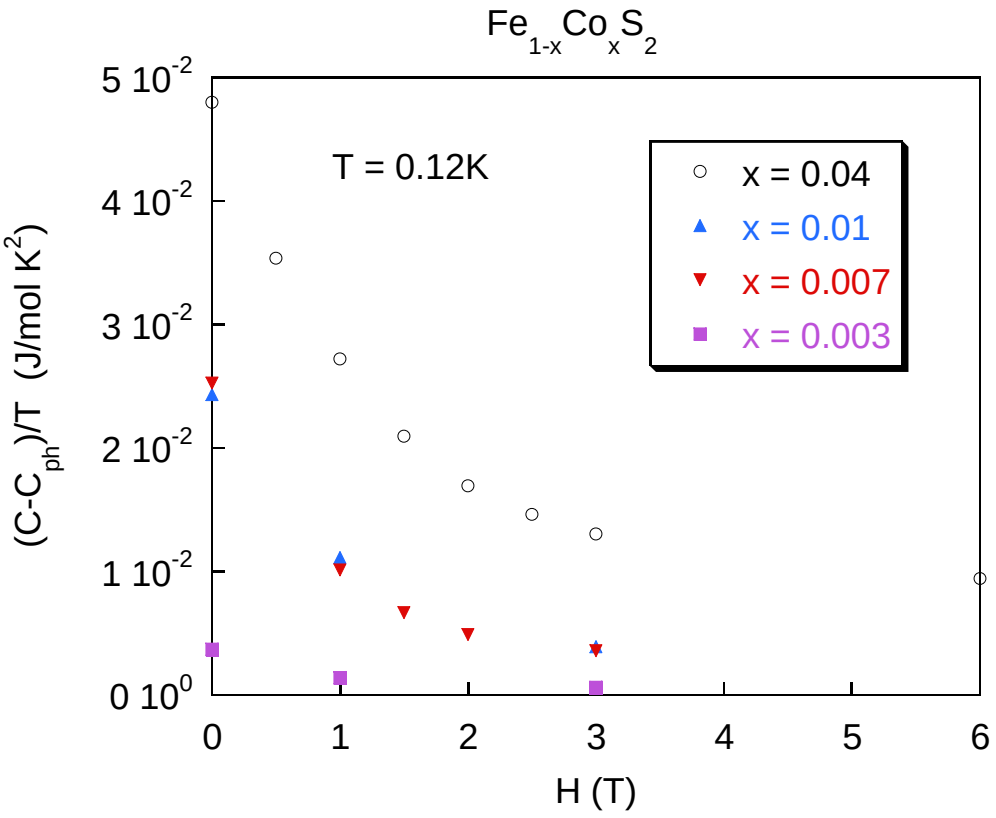

Figure 4.13 Magnetic field dependence of $(C\text{-}C_{ph})/T$ for $Fe_{1-x}Co_xS_2$ at $T = 0.12$ K

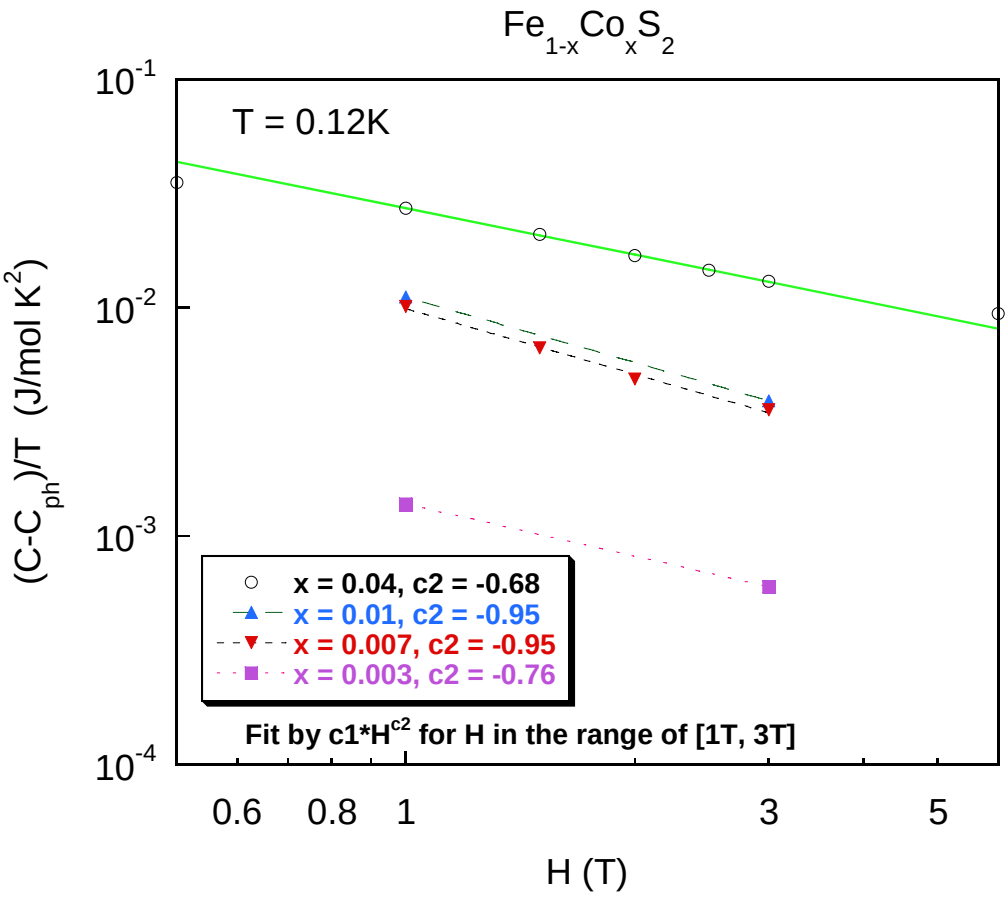

Figure 4.14 Magnetic field dependence of $(C\text{-}C_{ph})/T$ for $Fe_{1-x}Co_xS_2$ at $T = 0.12$ K on a logarithmic scale

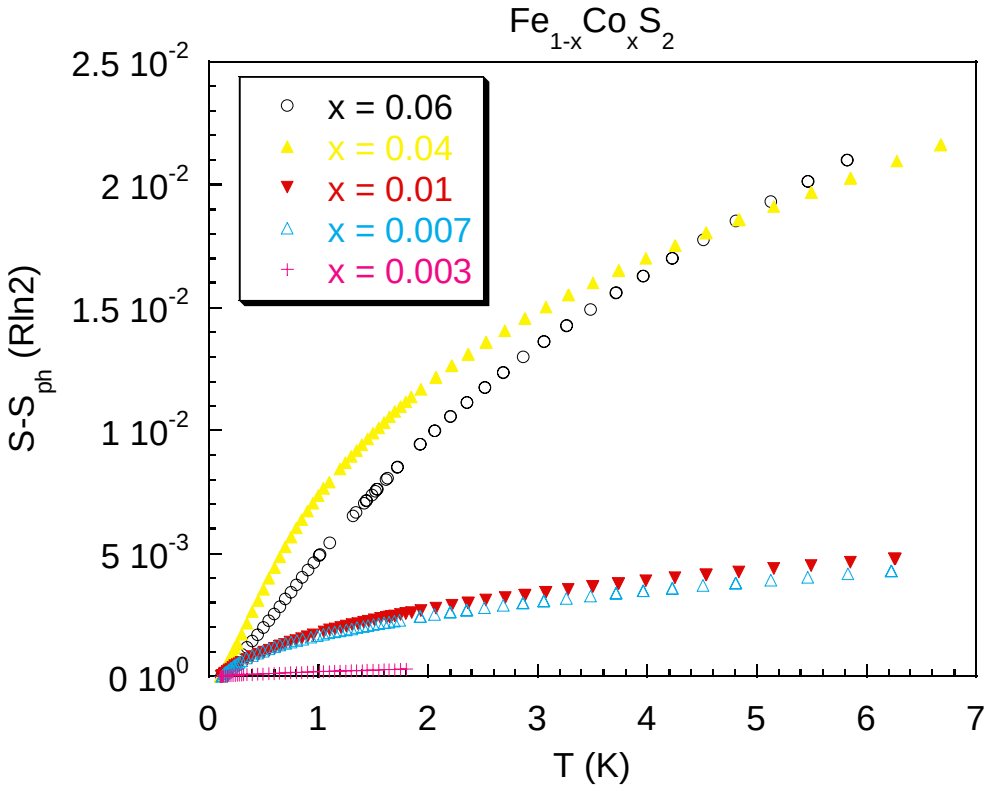

Figure 4.15 Temperature dependence of entropy for $Fe_{1-x}Co_xS_2$

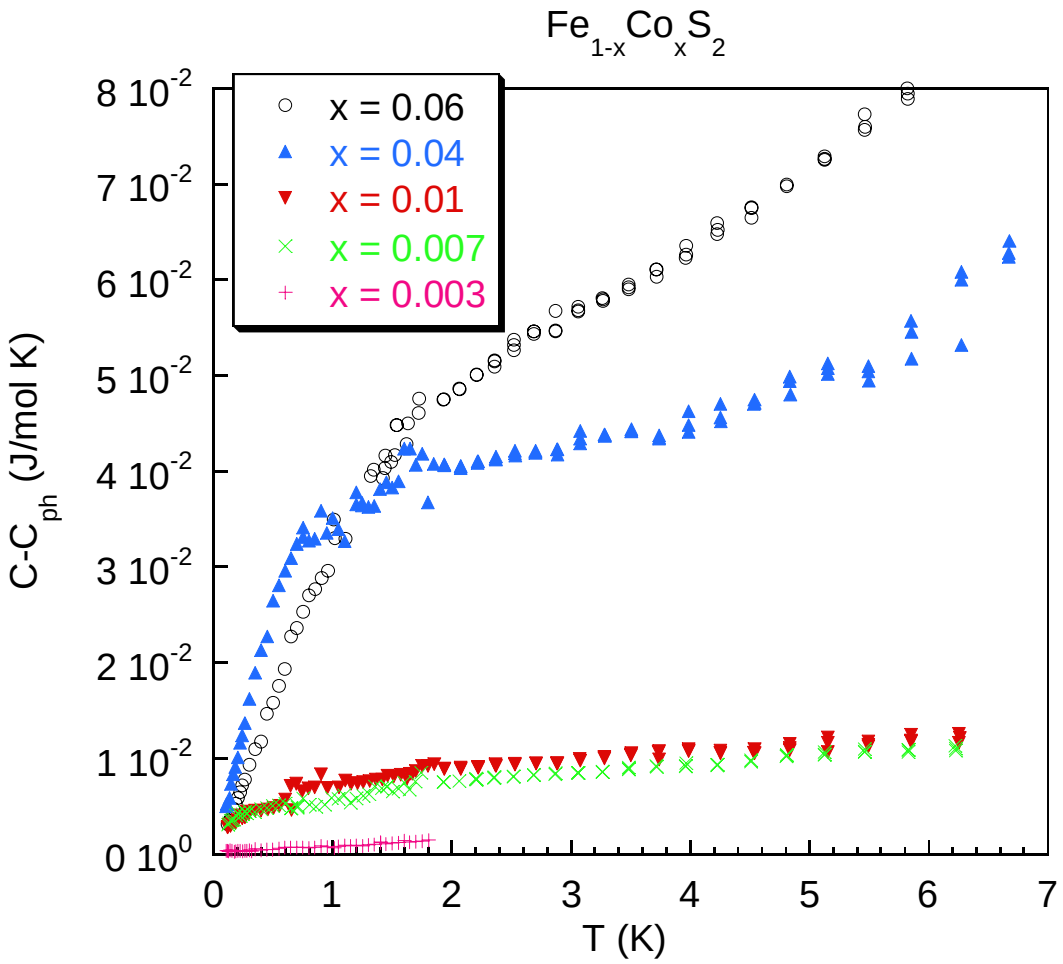

Figure 4.16 Temperature dependence of (C-C_{ph}) for $Fe_{1-x}Co_xS_2$

consequently *S(T)* at the temperature where the material becomes ferromagnetic as evidenced by a peak in $\chi(T)$.

If we propose that the low temperature anomaly in specific heat is electronic in origin, the effective mass calculated from the maximum value in *C/T* assuming a parabolic band can be two orders of magnitude larger than that of bare electrons, as shown in Fig. 4.17. Also plotted for comparison is the effective mass calculated from γ obtained from high temperature (30K to 70K) *C/T* vs. T^2 linear fit.

4.3 The Wilson Ratio of $Fe_{1-x}Co_xS_2$

The Wilson Ratio is often used to compare thermodynamic properties of materials. The Wilson Ratio is the ratio between magnetic susceptibility χ and specific heat coefficient γ normalized to the free electron value:

$$R_W = \frac{\chi / \chi_0}{\gamma / \gamma_0} = \frac{\gamma_0}{\chi_0}\frac{\chi}{\gamma} = \frac{\pi^2}{3}\frac{k_B^2}{\mu_B^2}\frac{\chi}{\gamma} \quad . \tag{4.9}$$

Here

$$\chi_0 = \mu_B^2 D(E_F) \tag{4.10}$$

and

$$\gamma_0 = \frac{\pi^2}{3} k_B^2 D(E_F) , \tag{4.11}$$

are the free electron magnetic susceptibility and specific heat respectively. $D(E_F)$ is the electronic density of states at the Fermi energy.

The Wilson ratio for a non-magnetic Fermi-liquid is generally 1 and large values of the Wilson ratio often indicate the dominance of spin excitations. In the Brinkman-Rice treatment for interacting electrons in a Hubbard model without disorder, the Wilson ratio saturates to 4 as a MI transition is approached [4.13] [4.27]. On the other hand, the

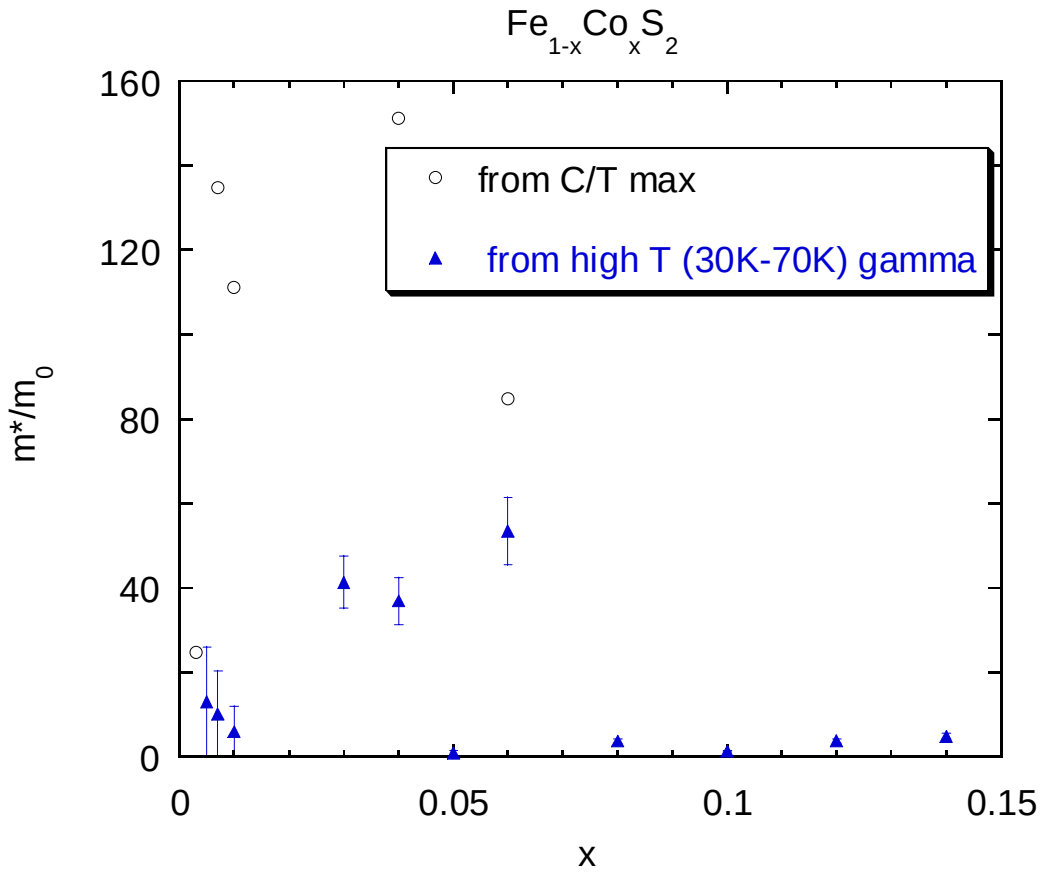

Figure 4.17 Doping dependence of effective mass for $Fe_{1-x}Co_xS_2$

scaling theory of localization [4.4] [4.5] for disordered electrons predicts a divergent Wilson ratio ($\sim T^{-0.2}$) [4.6] as $T \rightarrow 0$ close to MI critical concentration for 3-D systems. For the two fluid model of Paalanen and Bhatt [4.6], the Wilson ratio increases smoothly from the Fermi-liquid value to the local moment saturation value $\beta \approx 3.1e^{0.4\alpha}/(1-\alpha)^2$. The value $\beta = 10.5$ for $\alpha = 0.62$ gives a good fit of data for Si:P [4.7][4.13]. For the two spin fluctuations theories proposed by Moriya and Lonzarich for 3-D FM quantum phase transition suitable for clean systems and ignoring the effect of disorder [4.21], the predicted logarithm divergence of C/T ($C/T \sim -\log T$), and the saturation of susceptibility as $\chi = \chi_0 - \chi_1 T^{3/4}$ will immediately lead to the decrease of Wilson ratio at low temperatures. The data for Ni_xPd_{1-x} [4.23] are consistent with these predictions. In addition, for a heavy fermion material close to a antiferromagnetic quantum critical point, such as $CeCu_{5.9}Au_{0.1}$, the measured data [4.28] show $C/T \sim -\log T$ and $\chi = \chi_0(1 - T^{1/2})$, which also leads to decreasing of Wilson ratio with cooling.

The temperature dependence of the Wilson ratio for our samples is plotted in Fig 4.18. The first feature worth noticing is that we have an enormous (10 to 50) values for samples with $x \leq 0.04$, indicating very strong spin fluctuations. The Wilson ratio is usually large in nearly ferromagnetic metals due to the Stoner enhancement. For example, the Wilson ratio is 6 - 8 for Pd, 12 for $TiBe_2$ and 40 for Ni_3Ga [4.29]. Another interesting observation is that, for the samples close to a ferromagnetic instability, $x = 0.007$ and $x = 0.01$, the Wilson ratio decreases with cooling at low temperatures, which is at odds with two fluid model for Si:P, but consistent with spin fluctuation theory close to a ferromagnetic quantum critical point [4.21]. In this figure, the measured data for $CeCu_{5.9}Au_{0.1}$ [4.28] and Ni_xPd_{1-x} [4.23] are also plotted for comparison. For Ni_xPd_{1-x} close

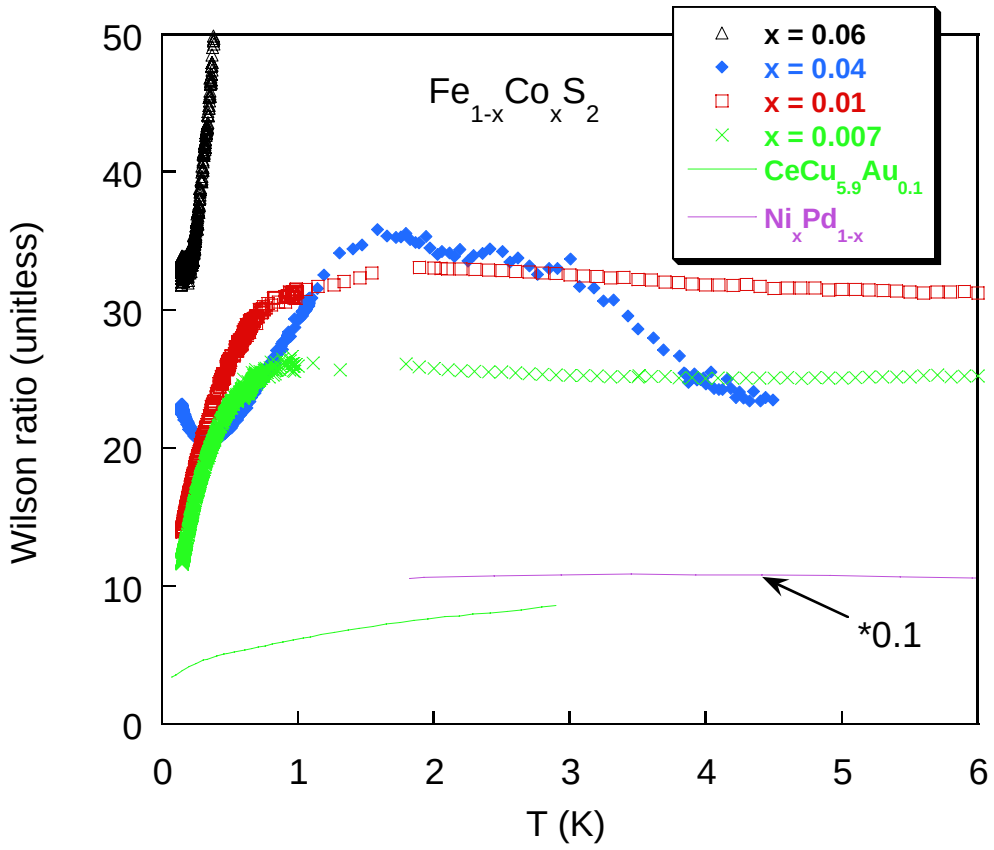

Figure 4.18 Temperature dependence of the Wilson ratio for $Fe_{1-x}Co_xS_2$, $CeCu_{5.9}Au_{0.1}$ [4.28], and Ni_xPd_{1-x} [4.23]

to a FM quantum critical point, the Wilson ratio is above 100 and slightly decreases with cooling from ~ 3K to lowest measured temperature 1.8K, while for $CeCu_{5.9}Au_{0.1}$ close to a AFM quantum critical point, the Wilson ratio is below 10 and decreases continuously with cooling from 3K to 0.1 K.

4.4 Conclusions

We have measured the specific heat in low temperatures for Co doped FeS_2, across the magnetic transition or crossover close to a Co doping level 1%. For all our samples, the low temperature data show strong deviations from the free electron contribution γT. The large values of γ we measure are consistent with effective masses two orders of magnitude larger than the bare electron mass. Above the critical concentration, C/T at first increases with cooling, then becomes saturated or decreases slightly to a Fermi-liquid like behavior. Close to the critical concentration of $x \sim 1\%$, C/T can be fit by a power law over almost two decades in temperature from 6K down to 0.1 K, with an exponent of -0.69 ± 0.03, clearly a Non-Fermi-liquid behavior. Below the critical concentration, for example, $x = 0.003$, C/T is smaller in magnitude compared to the $x = 0.01$ sample, and also shows a low temperature divergence below 1K.

Castro Neto's theory of Griffiths phase proposed for disordered heavy fermion metals has many features in common with our data. This theory predicts a power law divergence of both C/T and $\chi(T)$ close to a QCP, similar to what we measure in our pyrite system, where C/T increases as a power law with cooling even below the temperature where susceptibility saturates or peaks. Thus we find NFL behavior also within the FM phase that is consistent with this theory. We compare this behavior with $URu_{2-x}Re_xSi_2$ where NFL behavior within FM phase was discovered close to a FM QCP. It was argued

that contributions to the critical behavior from local magnetic clusters may exceed that of the infinite cluster which describes the long range order of the FM phase, and therefore it is possible to observe NFL behavior within the FM phase. A simple model of fluctuating magnetic moments with large J can be used to fit the high temperature susceptibility and specific heat data. The results from our fits reveal that both n and J increase with x, and that a small number of large magnetic moments form above the Curie temperature.

The measured Wilson ratios are in the range of 10 to 50 for $x \leq 0.04$ suggesting the dominance of spin fluctuations at low temperatures. The decrease in Wilson ratio with cooling for samples close to critical concentration are favorably compared with spin fluctuation quantum critical theories and experimental data in $CeCu_{5.9}Au_{0.1}$ and Ni_xPd_{1-x}, which also show decreases of the Wilson ratio with cooling.

Chapter 5 Resistivity and Magnetoresistance in $Fe_{1-x}Co_xS_2$

5.1 Introduction

Resistivity and magnetoresistance (MR) measurements are important tools in extracting information on scattering processes in metals or semiconductors. Since our Co doped FeS_2 samples undergo MI (metal-insulator) and PM to FM transitions, disorder and Coulomb interactions will clearly be important in determining the magnetotransport properties. In the following sections, I will briefly review various contributions identified in highly correlated electron materials which may be relevant and serve as a background for discussion on our data in $Fe_{1-x}Co_xS_2$.

5.1.1 MR in the Semiclassical Description of Metals

In the Drude theory or free electron model, the magnetic field has no effect on the resistivity of a metal. However, within the band theory of metals, a positive transverse MR is predicted. When a metal is placed in a magnetic field, the electrons are restricted to move along curves in k-space given by the intersection of surfaces of constant energy with planes perpendicular to the magnetic field [5.1] [5.2]. In the limit of strong magnetic field satisfying the condition $\omega_c\tau>>1$, where the cyclotron frequency $\omega_c = (eH)/(mc)$, the electrons can travel many cycles in these orbits before being scattered. A positive transverse MR has been calculated in this high field limit and is summarized here. If the orbits are closed, the MR will increase as H^2 and then become saturated at high field, unless the material is compensated with equal density of electrons and holes, in which case it grows without limit. On the other hand, if there is at least one band with open orbits, the MR will also increase as H^2 without limit [5.1] [5.2]. In disordered metals these contributions are often very small.

5.1.2 Coherent Quantum e-e Interaction Contribution to the MR in Disordered Metals ——— The Effect of Disorder and the Coulomb Interaction between Carriers Near MI Transitions

For a disordered metal close to a MI transition, at low temperatures, electrons can be elastically scattered many times before their quantum mechanical phase changes by 180 degrees, resulting in coherent interference of the scattered electron wave functions. This quantum contribution to the resistivity is known to result in a square root dependence of the conductivity in T and H for 3D material such as P doped Si at low temperatures [5.3] [5.4]. This singular behavior arises from the enhancement of effective Coulomb interaction between electrons for diffusive carrier motion, giving rise to square root singularity in the density of states at the Fermi level [5.3][5.4]. This is in contrast to Landau's idea that in a Fermi Liquid the Coulomb interaction renormalizes the density of states, but leaves it a smooth function of energy.

In 3D, the correction to low T conductivity, $\Delta\sigma$, is given by

$$\Delta\sigma = \frac{e^2}{\hbar}\frac{1}{4\pi^2}\frac{1.3}{\sqrt{2}}\left(\frac{4}{3}-\frac{3}{2}\tilde{F}_\sigma\right)\sqrt{\frac{K_B T}{\hbar D}} \quad , \qquad (5.1)$$

where $D = v_F l/3$ is the diffusion constant, and $\tilde{F}_\sigma$ is a dimensionless number that sets the strength of the relevant part of electron-electron interaction [5.3] [5.5]. Magnetic fields have a significant effect on this correction to conductivity. We can consider the total interference amplitude to be composed of spin singlet and triplet amplitudes. While the magnetic field has no effect on spin singlet interference amplitude, it will split the $j = 1$ states by $g\mu_B H$. The precession of the spins in a magnetic field will decrease the interference probability, effectively cutting off the spin triplet terms for $g\mu_B H > k_B T$. The resulting negative magnetoconductance (MC) has the form [5.3] [5.5]

$$\Delta\sigma(H) = -\frac{e^2}{\hbar}\frac{\tilde{F}_\sigma}{4\pi^2}\sqrt{\frac{k_B T}{2\hbar D}}g_3(h) \tag{5.2}$$

where $h = g\mu_B H/k_B T$, and $g_3(h)$ has the limiting behavior

$$g_3(h) = \begin{cases} \sqrt{h} - 1.3, & h >> 1 \\ 0.053h^2, & h << 1 \end{cases}. \tag{5.3}$$

Therefore, at low fields, the MC varies as H^2, while for high fields it grows as the square root of H.

5.1.3 Spin Fluctuation Scattering in Ferromagnetic Metals

In ferromagnetic metals, spin fluctuations scatter electrons through the exchange interaction. At temperatures well below T_c, spin fluctuations in nearly or weakly ferromagnetic metals add an additional T^2 contribution [5.6] to the usual Fermi liquid electron-electron scattering

$$\rho = \rho_0 + \rho_2 T^2 + \ldots \tag{5.4}$$

In weak ferromagnets at low temperatures,

$$\rho_2 \propto [M(0)]^{-1} \propto (\alpha - 1)^{-1/2} \tag{5.5}$$

where $M(0)$ is the zero temperature magnetization and α is the exchange enhancement factor for susceptibility. α is close to 1 for ferromagnets near T_c and in nearly ferromagnetic metals at low temperatures. Therefore, the smaller the magnetization at T = 0, the larger the T^2 term coefficient ρ_2, which is consistent with experimental result for weak ferromagnet Sc_3In and $ZrZn_2$ ($\rho_2 \sim 0.05$ μΩ cm K^{-2}), and normal ferromagnetic metals Fe, Co and Ni ($\rho_2 = 1 \sim 2$ μΩ cm K^{-2}). As the quantum critical point is approached ($T_c \rightarrow 0$), the temperature range of the T^2 dependence become smaller, beyond which the resistivity follows a $T^{5/3}$ dependence [5.6]. The resistivity shows no discontinuity, but its

temperature derivative usually displays a small discontinuity proportional to $[M(0)]^2$ at T_c, which is small in weakly ferromagnetic metals. The external magnetic field suppresses the amplitude of the spin fluctuations, resulting in a negative MR, which is a maximum near T_c.

5.1.4 Contribution to the Resistivity Due to a Dilute Concentration of Magnetic Impurities: The Kondo Effect

Nonmagnetic impurities in metals usually result in a temperature independent residual resistivity at low temperatures, above which the resistivity increases with temperatures monotonically. On the other hand, a metal containing a small density (ppm order of magnitude) of magnetic impurities, a logarithmic increase of the resistivity with decreasing temperature is observed, which when combined with phonon scatting at high temperatures, results in a minimum in the T-dependence of resistivity. This was explained by second order perturbation theory and is known as the Kondo effect [5.7]. The antiferromagnetic exchange interaction between the local moments and conduction electrons leads to spin flip scattering of the itinerant electrons by a local moment and the subsequent screening of the local moment.

For dilute magnetic alloys the magnetic field dependence of the resistivity can be divided into two cases, both of which give negative MR (see Fig. 5.1). In the first case, as in Cu with dilute Fe impurities, the magnetic field depresses the saturation value of the resistivity as T goes to zero [5.8]. In the second case, as in Cu with dilute Mn, a maximum appears in the temperature dependence of resistivity in magnetic field, and the maximum temperature, T_M, increases with field [5.8]. For both cases, the absolute value of the resistance increases as the square of magnetization [5.8]. These experimental results have been explained in 3rd-order perturbation calculation on the s-d exchange

model in the second Born approximation which in principle is only valid for $T >> T_k$, where T_k is the Kondo Temperature [5.9]. In the regime for $g\mu_B H/k_B T < 2$ [5.9], the physical picture is the freezing out of the impurity's spin degree of freedom by a Zeeman splitting of allowed energy levels by the magnetic field. When combined with the exclusion principle, this results in a decrease of the spin flip scattering amplitude. The leading term in MR is calculated to be proportional to the square of the magnetization, consistent with the experimental results of ref. [5.8]. In the high field regime, $g\mu_B H/k_B T >> 1$, the magnetization is close to saturation, the field and temperature dependence of the scattering amplitude is the dominant mechanism for negative MR, compared to freezing out of spins. Third-order perturbation theory predicts a $\ln H$ dependence of resistivity [5.10], consistent with infinite order perturbation summation for $J/E_f << 1$ [5.11], and the experimental measurement in CuCr alloys [5.12]. However, third-order perturbation theory [5.10] also predicts an increase of the resistivity with field in this high field regime if the impurity magnetization is close to saturation, which seems to be at odds with experimental result in CuCr alloys [5.12].

In the second case of dilute magnetic alloys mentioned above, such as CuMn [5.8], AuMn [5.13], and AgMn [5.14], as the magnetic field or the impurity concentration is increased, the low-T resistivity displays a deviation from a simple logarithmic increase and a maximum is observed above T_K [5.15]. The maximum temperature T_M is found to be proportional to the impurity concentration [5.13], and usually thought as an effect of the interaction between impurity spins and formation of a spin glass. There have been three theoretical approaches to this problem.

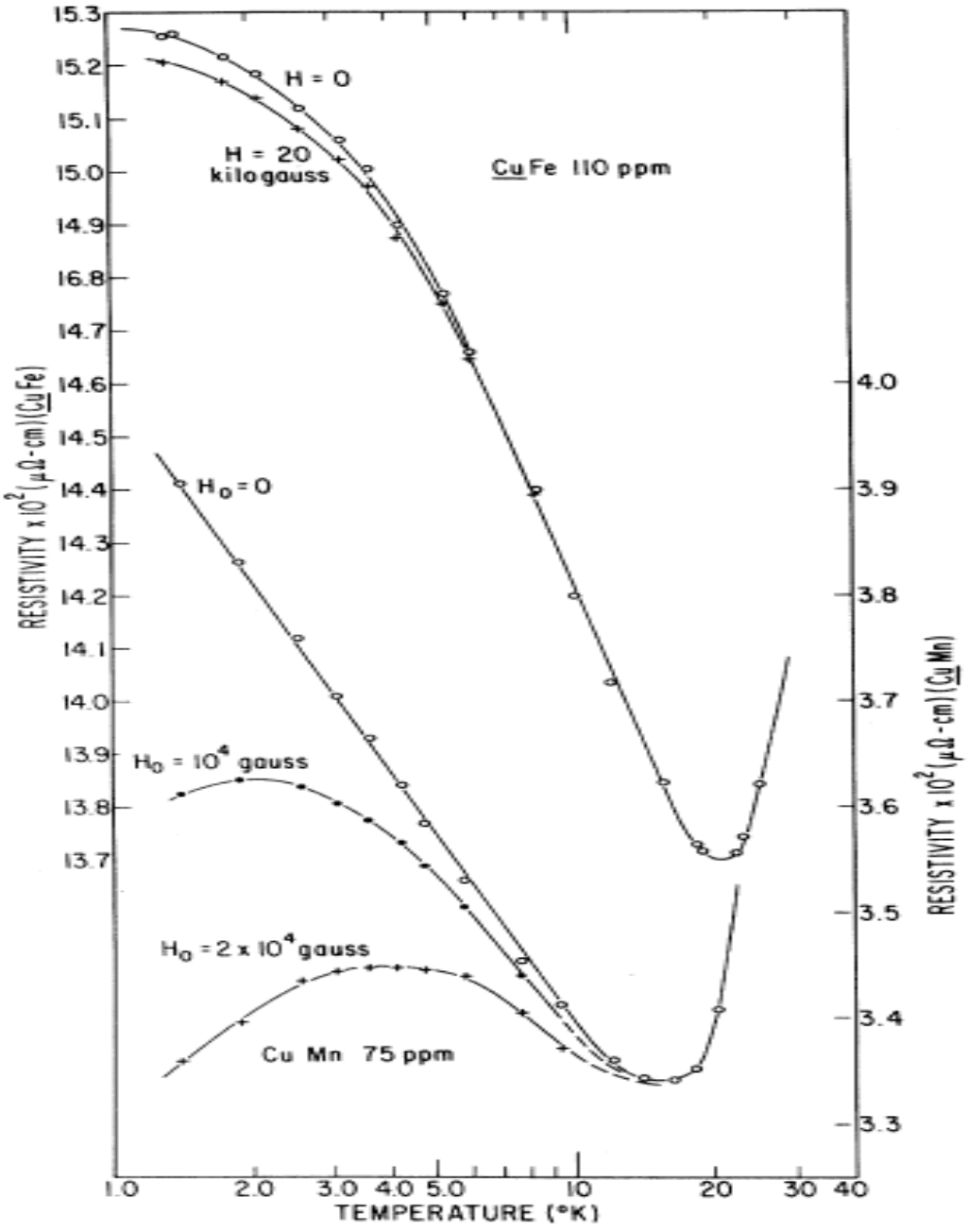

Figure 5.1 Temperature dependence of resistivity for dilute magnetic alloys CuMn and CuFe (from ref. 5.8)

The first approach is based on the assumption of an effective internal field experienced by magnetic ions in dilute alloys [5.11] [5.16] [5.17] [5.18] [5.19]. As the temperature is decreased, the internal field causes a redistribution among the Zeeman levels of the magnetic impurities and thus a suppression of the spin disorder scattering [5.20]. This suppression, combined with Kondo ln$T$ term, may cause a local maximum to appear. The internal field can be a fixed value as in a spin glass or an antiferromagnet with long range magnetic order [5.13], or can arise from short range order and be described by a symmetric probability distribution function P(H_i) [5.17][5.18][5.19] in the Marshall-Klein-Brout (M-K-B) theory. An assumption of certain forms of P(H_i) will give the relation T_{max} proportional to impurity concentration [5.18] [5.20] [5.21], a result consistent with experimental data. The most essential result of the Harrison and Klein calculation [5.21] is that the ln$T$ behavior at zero field is replaced by

$$\rho \sim \ln(T^2+H_i^2)^{1/2} \tag{5.6}$$

where H_i is the effective internal field [5.22].

The second approach to explain the resistivity maximum below the ln$T$ region is to calculate the scattering of conduction electrons by a pair of interacting magnetic impurities. This has been done in the second Born approximation with a perturbation theory up to third order for a pair of coupled spin ½ impurities [5.23]. If the coupling is strong and the distance between the pair is small, the pair acts either as spin 1 (ferromagnetic pair coupling) giving a Kondo like ln$T$ resistivity, or as spin 0 (antiferromagnetic pair coupling) giving no spin dependent resistivity at all. For intermediate coupling strength and distance, it can be shown that the absolute slope of the

ln$T$ term can be suppressed compared to the scattering by two isolated non-interacting spins, which is consistent with the experimental observation [5.24] that the absolute value of ln$T$ term decreases as the impurity concentration increases. It is also shown that the ln$T$ term is replaced by

$$\rho \sim \ ln(T^2+T_W^2)^{1/2} \tag{5.7}$$

where T_W is proportional to the coupling energy W. In the meantime, if RKKY interactions are taken as the coupling mechanism, it is possible to predict a resistivity maximum at low temperatures [5.23] [5.14]. A two-impurity Kondo effect has also been attacked by solving Green's functions with an added direct exchange term for the impurity-impurity interaction [5.25]. The essential result is that the ln$T$ term is replaced by $\ln(T^2+ T_W^2)^{1/2}$, where T_W is an energy approximately equal to the spin-spin coupling energy W. The effective Kondo temperature

$$\boldsymbol{T_K^E} = \boldsymbol{T_K^0}[1-(\boldsymbol{T_W} / \boldsymbol{T_K^0})^2]^{1/2} \tag{5.8}$$

decreases as the impurity-impurity interaction increases, where $\boldsymbol{T_K^0}$ is the single-impurity Kondo temperature. When $T_W > \boldsymbol{T_K^0}$, T_W strongly inhibits the formation of a spin-compensated state. When $T_W < \boldsymbol{T_K^0}$, the formation of the spin-compensated state is partially inhibited. The major difference with the Harrison and Klein effective field theory where H_i is zero at high temperatures, is that here T_W may be independent of temperature and has a non-zero value at high temperatures [5.25].

The third approach to explain the resistivity maximum at low temperatures is to assume a broadening of the magnetic impurity spin states [5.26] [5.27]. It was shown that this broadening Γ is sufficient to explain the decrease in the resistivity below T_M for $\Gamma > T_K$, without assuming an internal magnetic field. On the other hand, if $T_K > \Gamma$, the

maximum may not show up, as in the strongly interacting system CuFe. In the original Kondo model, the spin has only a single energy level where spin up and spin down are degenerate at zero field, therefore only elastic scattering of the conduction electrons by the spin is possible. When the broadening Γ occurs, there are both elastic and inelastic channels for scattering, where the number of possible elastic channels is small compared to the number of inelastic channels. If $T >> \Gamma$, the conduction electron of average excitation energy above the Fermi level $\varepsilon \approx T$ may take part in all inelastic scattering processes. On the other hand, if $T < \Gamma$, scattering processes with $\Gamma > \Delta E > T$ can not be excited, where ΔE is the energy transfer between the conduction electron and the local spin. In particular, for $T << \Gamma$, the conduction electron can give up only energy $\Delta E \leq T << \Gamma$ and for $T = 0$ only elastic scattering may occur. Therefore, the resistivity for $T << \Gamma$ is small relative to that for $T > \Gamma$. This effect due to 1st order perturbation theory for inelastic scattering processes, combined with usual logarithmic increase of resistivity with cooling for $T >> \Gamma$, results in a maximum at about $T \approx \Gamma$. The broadening of the magnetic impurity spin states can be accounted for by the indirect RKKY interactions between the impurity spins [5.27].

Later, the Kondo resistivity ρ_K with the impurity-impurity interaction effect was explained by assuming only the *S-d* exchange interaction, without explicit use of the RKKY interaction [5.26]. For a system of low T_K and high temperature ($T > T_m >> T_K$), the $\ln T$ dependence of ρ_K is replaced by $\ln(T^2+c^2\Delta^2)$, where c is the impurity concentration, and Δ is a constant independent of c and temperature, consistent with previous theoretical predictions [5.21][5.22][5.26].

5.1.5 The Kondo Lattice and Formation of Heavy Carriers: Heavy Fermion Metals

The resistivity of heavy fermion metals containing a periodic lattice of local *f* moments has some similarities to that of dilute magnetic alloys. Both systems show a ln*T* increases in resistivity with cooling at low temperatures [5.28] [5.29], a phenomenon usually interpreted as single-ion Kondo effect. However, why a large density of local moments in heavy fermions does not suppress this single ion Kondo behavior is still an open question. On the other hand, in contrast to dilute Kondo alloys where the resistivity saturates at its maximum value as T goes to zero, the resistivity for most heavy fermion metals shows a broad maximum, below which the resistivity rapidly falls to a very small value (a few or tens of μΩ cm) [5.29]. The low temperature resistivity follows T^2 dependence, with a coefficient proportional to the square of linear term of specific heat γ^2, a result interpreted as the formation of the coherent Fermi liquid state. The periodic lattice of *f* moments is considered to be crucial for the formation of this quantum coherent state. The crossover from the high temperature incoherent Kondo scattering state to the low temperature coherent Fermi liquid state is also evidenced by the MR and the large negative peak in Hall coefficient [5.30]. At high temperatures, negative MR is the result of the suppression of spin-flip scattering. At low temperatures, a positive MR is observed, due to the normal band effects in metals. For example, in UBe_{13} at low *T*, the zero pressure incoherent Kondo impurity scattering state evident in a negative MR can be driven to a coherent Heavy Fermi Liquid state evident in a positive MR by applying pressure [5.31].

5.1.6 Magnetic Polaron Formation in Diluted Magnetic Semiconductors and EuB_6

Compared with dilute magnetic alloys and heavy fermion systems, diluted magnetic semiconductors (DMS) can also contain local magnetic moments, and they have been described with the same or similar Hamiltonian which includes an *S-d* exchange interaction. What makes DMS extraordinary is that the carrier density is significantly lower than the local moment spin density, so spins become an integral part of the problem rather than merely a perturbation on the metallic Fermi sea [5.32].

In recent years, spintronics, where it is not only the carrier charge but also the carrier spin that carries information, has been intensively studied [5.33]. In dilute magnetic semiconductors, the coupling between the local moments and itinerant charge carriers can give rise to a band splitting effect which can be used to generate spin polarized currents in a simple metal-semiconductor-metal tunneling device as experimentally shown in EuS [5.33]. If, on the other hand, the charge carrier is localized either by disorder or by the Coulomb attraction to the acceptor/donor ion, then the coupling with local moments can lead to the formation of bound magnetic polarons (BMP). The BMP concept is commonly used to explain the conductivity and other physical properties of diluted magnetic semiconductors. A BMP is composed of a localized charge carrier with a cloud of polarized local spins within its localization radius. When the carrier moves in an electrical field, it must carry along the spin polarization of the surrounding local moment, leading to an enhanced resistivity. Polarization of the local moments via ferromagnetism or an external magnetic field decreases the scattering rate and results in a significant enhancement of the conductivity [5.33].

In II-VI semimagnetic semiconductors, such as Mn doped CdSe, the MR has two contributions, one positive and one negative. The positive component of the MR which dominates at low H and at T's above ~ 0.5 K is explained by e-e interactions in the spin-polarized universality class, and the negative component, which dominates at very low T and high H, is explained by the joint effect of spin-splitting enhancement of density of states at Fermi surface and magnetic polaron formation [5.34]. Since the magnetization of magnetic polarons is proportional to χ and magnetic polarons constitute efficient spin-flip scattering centers, the spin-flip scattering rate will be proportional to χ^2. At low temperatures, it can be larger than the thermodynamic spin fluctuation scattering rate which scales with χT [5.34].

In $Ga_{1-x}Mn_xAs$, ferromagnetism was discovered with a surprisingly high T_c up to 150K [5.35]. It is generally believed that an indirect interaction between local moments mediated by charge carriers leads to the ferromagnetism. Around the optimum doping concentration of $x \sim 0.05$, the system is a low carrier density, highly disordered metal [5.36]. The resistivity increases as T decreases, peaks around T_c and then decreases below T_c. The negative MR is also largest at T_c, which can be understood as a spin fluctuation effect. In contrast, for both the under-doped insulating and the reentrant (reentering into insulating phase, $x > \sim 0.07$) insulating samples, the MR increases as T decreases below T_c and becomes quite pronounced at low temperatures [5.36]. Three orders of magnitude change in resistance with magnetic field has been observed in the reentrant insulating samples. Magnetic polarons, or alternatively a reduction of localization length due to an increased Fermi energy with H in a spin-split band, have been proposed to account for this large negative MR [5.36]. There are two theoretical approaches starting from the

assumption either of nearly itinerant charge carriers or nearly localized charge carriers [5.37]. The first theoretical approach assumes almost free charge carriers in valence band without taking into account the disorder. It can explain the value of T_c quantitatively, but fails even on a qualitative level in explaining the insulating or strongly disordered metallic transport properties [5.37]. The other approach, which assumes almost localized charge carriers in an impurity band, seems to be a more plausible solution. The numerical mean field treatment based on this approach which includes disorder explicitly can explain the unusual magnetization curve for temperatures below T_c, i.e. a linear or concave shape, in contrast to a mean field convex shape of conventional ferromagnets [5.32]. The randomness in Mn positions is found to be crucial to this problem, and also enhances T_c significantly according to the numerical calculation. On the other hand, the experimental fact that annealing enhances T_c is considered to be due to a reduction in the number of defects, such as Mn interstitials [5.38] [5.39]. Percolating networks of bound magnetic polarons are proposed to explain the formation of the ferromagnetic state at low temperatures [5.32] [5.40]. Recently, the analytical polaron percolation theory [5.40] based on the same assumption gives similar results as the numerical calculations [5.32] in the low carrier density regime, $a_B^3 n_h << 1$, where a_B is the localization length of charge carriers and n_h is the density of the holes.

Finally, I will briefly discuss the transport properties of EuB_6 and the possibility of magnetic polaron formation above T_c in this low carrier density ($\sim 10^{20}$ cm^{-3}) compound. The resistivity of EuB_6 is metallic at high temperatures, shows a broad minimum near 100 K and increases as T is lowered [5.41]. At around 15.5 K, the resistivity peaks near T_c, then decreases by two orders of magnitude to a residual

resistivity of the order 10 μΩ cm [5.41]. Careful examination of the specific heat [5.42] and the temperature derivative of the resistivity [5.41] shows two consecutive phase transition at 12.6 K and 15.5 K (see Fig. 5.2). It is proposed that the low-T (12.6 K) transition is a bulk ferromagnetic transition, while the upper-T transition (15.5 K) corresponds to a metallization via an overlap of magnetic polarons [5.41]. From the field dependence of dρ/dT, it is clear that the maximum MR occurs at the T_M = 15.5 K transition rather than the T_c = 12.6 K transition. By subtraction of a positive quadratic field dependence from the magnetoresistance which dominates at low T and high field (classical MR), the resulting negative component of magnetoresistance, $\rho^*(H)$, can be isolated above 8K [5.41]. This negative component of MR, $\rho^*(H)$, is denoted as the magnetic MR. In the temperature range from 10 to 20K, the relative magnetic magnetoresistance ($\Delta\rho^*/\rho^*_{H=0}$) come close to -100% in high fields, i.e., a complete suppression of the zero field magnetic contribution to the resistance. For T just above 15K, $\Delta\rho^*/\rho^*$ can be shown to be a universal function of magnetization. The agreement with spin disorder scattering in low fields $\Delta\rho^*/\rho^* \sim M^2$ is reasonable [5.41]. For T well above T_M = 15.5 K and below 100K, the increasing ρ for decreasing T is thought to be the result of charge localization by means of magnetic polaron formation [5.41]. Magnetic fields suppress the resistance in this temperature range, increasing T_M, and reducing the energy barrier evident in the T-dependent scattering, all as expected for magnetic polarons formation [5.41]. More direct evidence for magnetic polaron formation above T_M come from Raman scattering experiments [5.43] where the spectra show two inelastic peaks from 15.5 K to 30K. These can be identified as spin-flip processes arising from the development of bound magnetic polarons, i.e. spin polarized

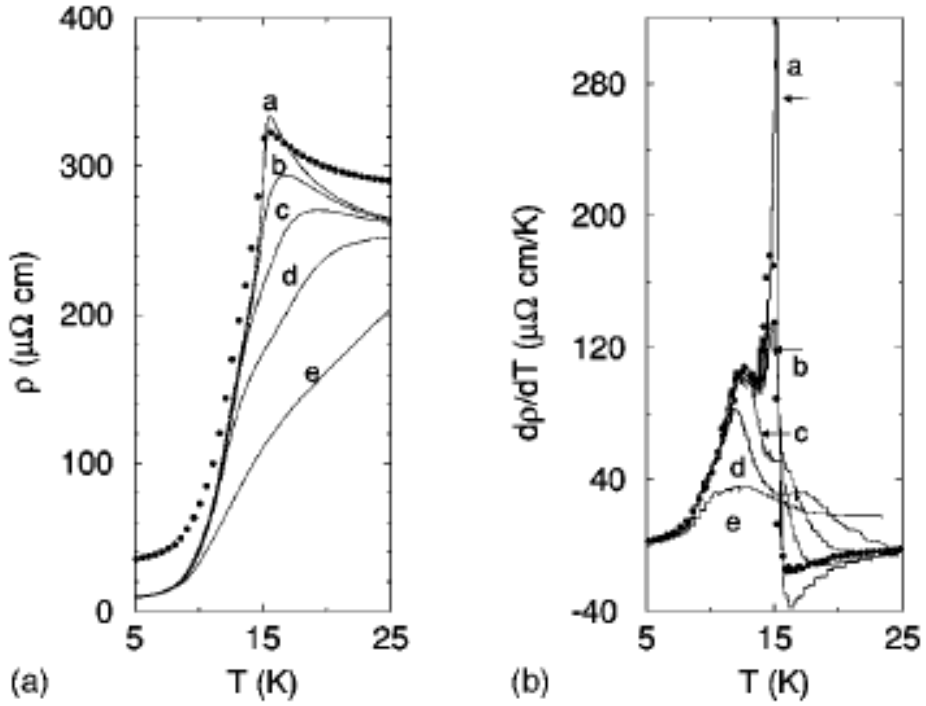

Figure 5.2 Temperature dependence of resistivity, ρ, and dρ/dT for EuB_6 (from Ref. 5.41)

(Zero field (a), 0.05 T (b), 0.1 T (c), 0.2 T (d), 0.5 T (e),
$^{153}\boldsymbol{Eu}^{11}\boldsymbol{B}_6$ --- (solid circles) different isotope of Eu and B than the naturally abundant ones)

clusters of Eu^{2+} ions formed within the Bohr orbits of localized carriers. Subsequent numerical calculations [5.44] on the spin polaron Hamiltonian reproduced the overall temperature and field dependence of the resistivity. The peak in the MR close to T_c, and the almost complete suppression of the zero field magnetic resistivity ρ^* in high fields close to T_c, are also consistent with the experimental data.

5.2 Charge Carrier Transport in $Fe_{1-x}Co_xS_2$

5.2.1 Zero Field Resistivity

In Fig 5.3 we plot the zero field resistivity vs. $T^{1.5}$ from 300K to 2K for our samples. Except for the pure sample which shows insulating behavior, all the Co-doped samples ($x \geq 0.001$) are metallic. The temperature dependence of ρ, except at the lowest temperatures, is described accurately by a $T^{1.5\pm0.2}$ dependence, a much weaker temperature dependence than a well-developed metal characterized by $\rho \sim T^3$ up to T^5 below the Debye temperature [5.1] [5.2]. Such pseudo-linear T-dependence is commonly observed in the Non-Fermi-Liquid funnel region of a generic phase diagram close to a quantum critical point (QCP) [5.45] (see Fig. 5.4 for a field driven QCP in $YbRh_2Si_2$). Quantum critical behavior is invoked to explain the linear T-dependent ρ up to 1000K in $La_{2-x}Sr_xCuO_4$ [5.46]. Another important feature is the small residual resistance ratio and the residual resistivity of the order of a milliohm centimeter, both indicating the disordered nature of these nascent metals.

As demonstrated by two typical samples in Fig. 5.5, there is a low temperature resistivity anomaly that can be separated into two classes. For low Co concentration ($x \leq 0.01$), the resistivity continues to increase as T is decreased down to our lowest temperatures. For higher Co concentration samples ($x > 0.01$), the resistivity initially

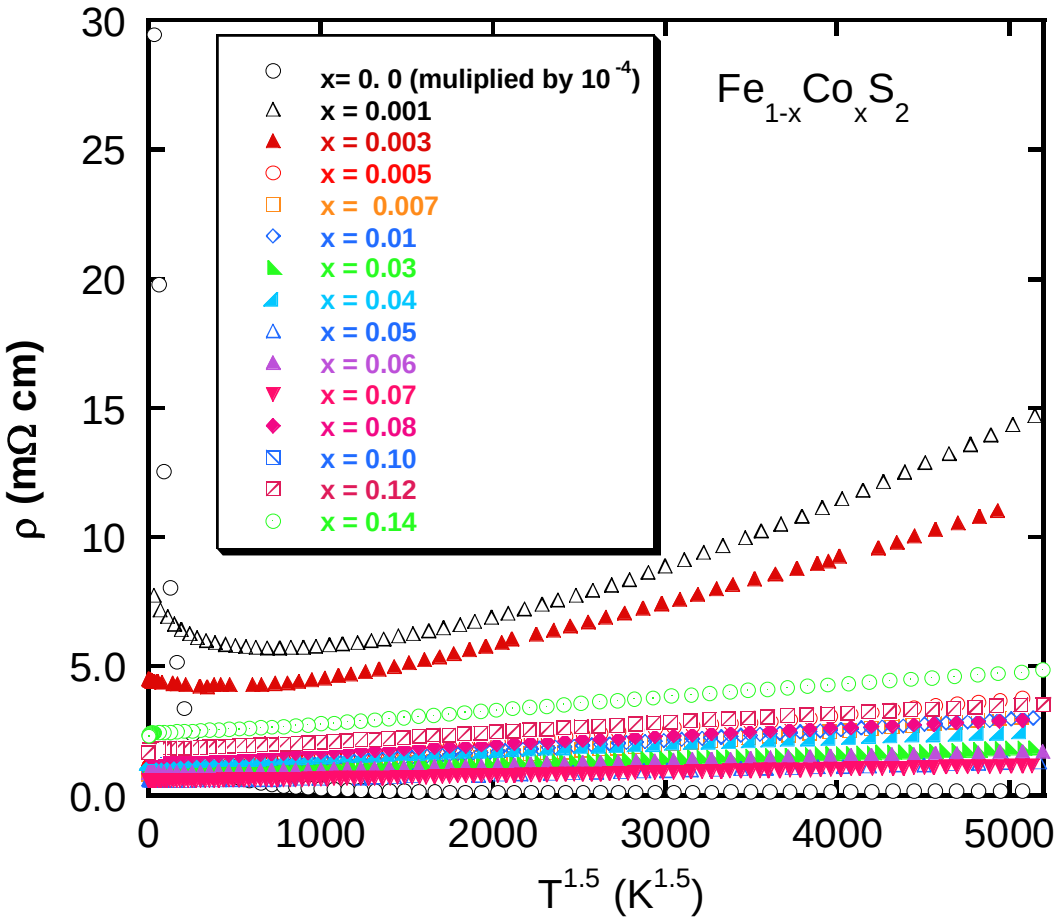

Figure 5.3 Zero field resistivity vs. $T^{1.5}$ for $Fe_{1-x}Co_xS_2$

increases as T is decreased, shows a maximum or a shoulder and then decreases as T is further decreased, indicative of a magnetic ordering.

5.2.2 Resistivity in Magnetic Field

In order to explore the mechanism for the low-T resistivity anomaly, the MR of our samples has been systematically explored. The low temperature upturn in the resistivity apparent in all samples can be suppressed by a magnetic field resulting in a negative MR. In Fig. 5.6 and 5.7, we show the T dependence of ρ for two samples, one with $x = 0.007$ and increases as T decreases in zero field, the other with $x = 0.06$ which displays a maximum before decreasing with further cooling, indicative of a magnetic ordering. We notice that the zero field ρ(T) for $x = 0.06$ is similar in shape to high field ρ(T) for $x = 0.007$, which suggests that a large effective field in the $x = 0.06$ sample is responsible for the magnetic ordering below the T_{max}. For both samples, the MR is quite large at low temperatures (10% and 35% at 1.8 K and 5T for $x = 0.007$ and 0.06 respectively), and increases in magnitude with the decreasing temperature.

The field dependence of the resistivity for various Co concentration samples is shown in Fig. 5.8, 5.9 and 5.10. In Fig. 5.8, the MR is measured for fields both perpendicular and parallel to the electrical current. The small difference, within experimental error, indicates that the MR is independent of field orientation, a phenomenon indicating the lack of orbital effects in the MR and suggesting a spin scattering nature of the negative MR in our samples. In Fig. 5.9 (a), the field dependence of the MR is plotted for the $x = 0.06$ sample. One interesting feature is that the slope of the MR versus H curves is negative and decreasing with H at high temperature well above the T_{max}, while for low temperature, well below T_{max}, this slope is negative but

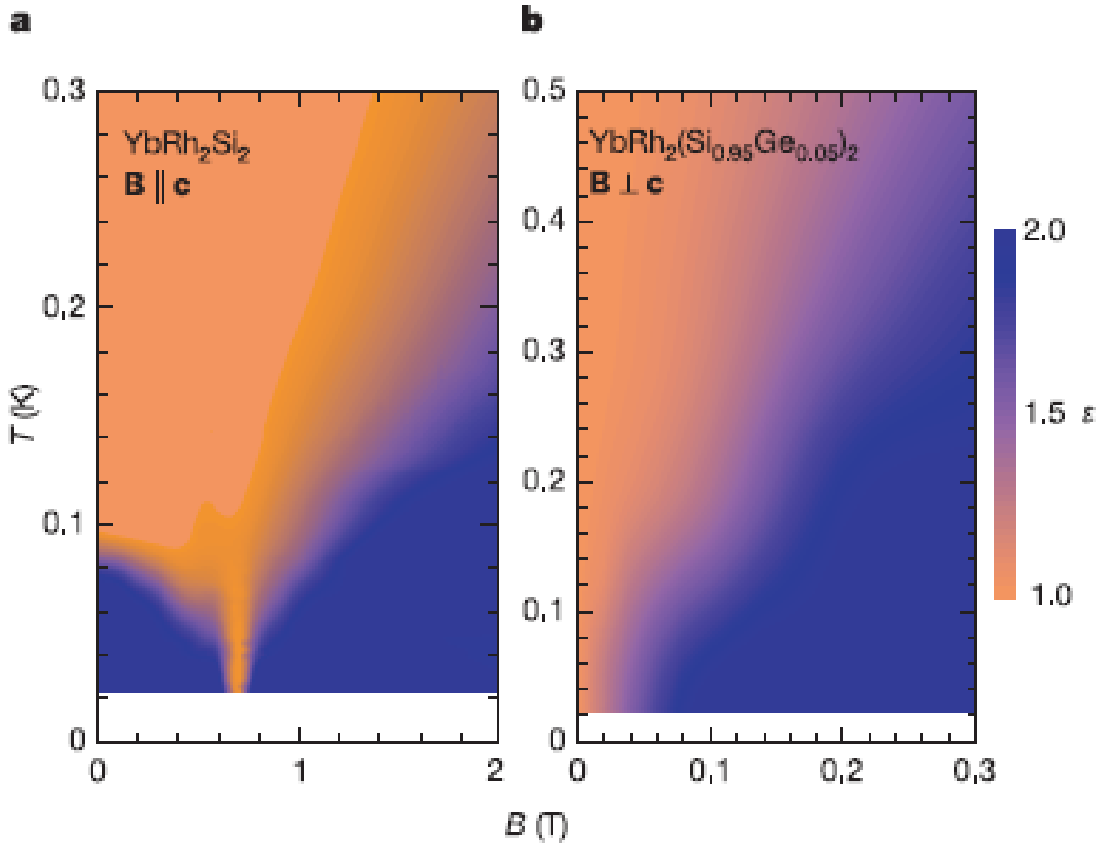

Figure 5.4 Phase diagram of resistivity exponent for $YbRh_2Si_2$ (from Ref. 5.45)

(ε is the T-dependent coefficient defined as $\rho = \rho_0 + AT^{\varepsilon}$)

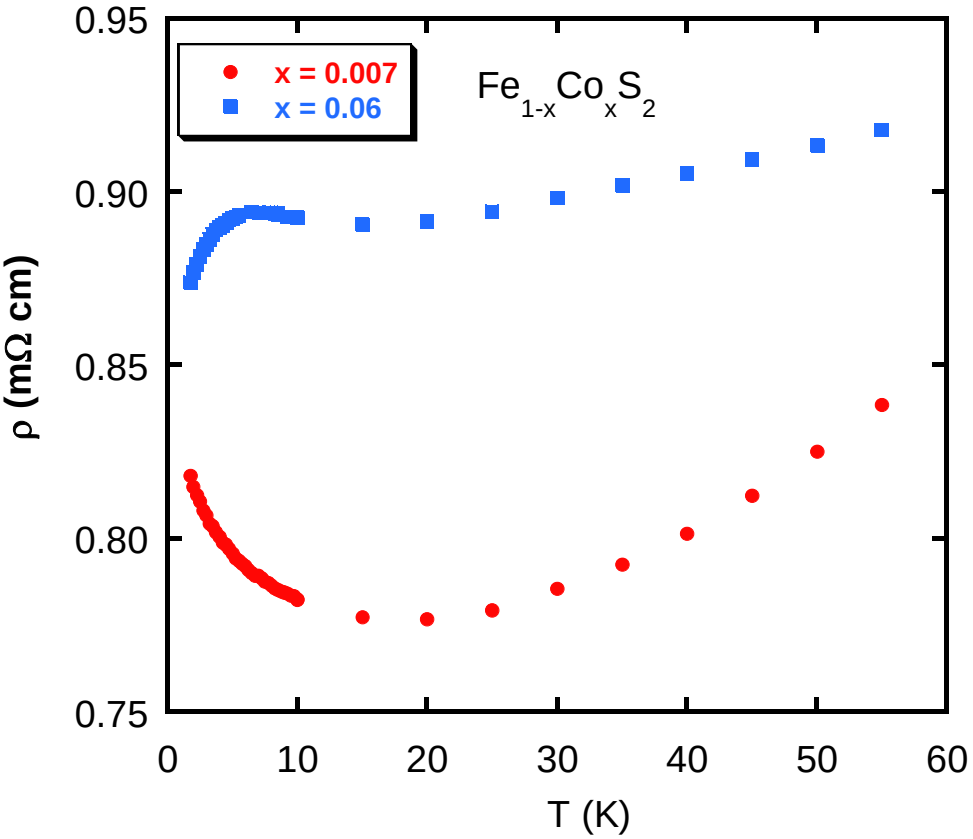

Figure 5.5 Temperature dependence of zero field resistivity for $Fe_{0.993}Co_{0.007}S_2$ and $Fe_{0.94}Co_{0.06}S_2$

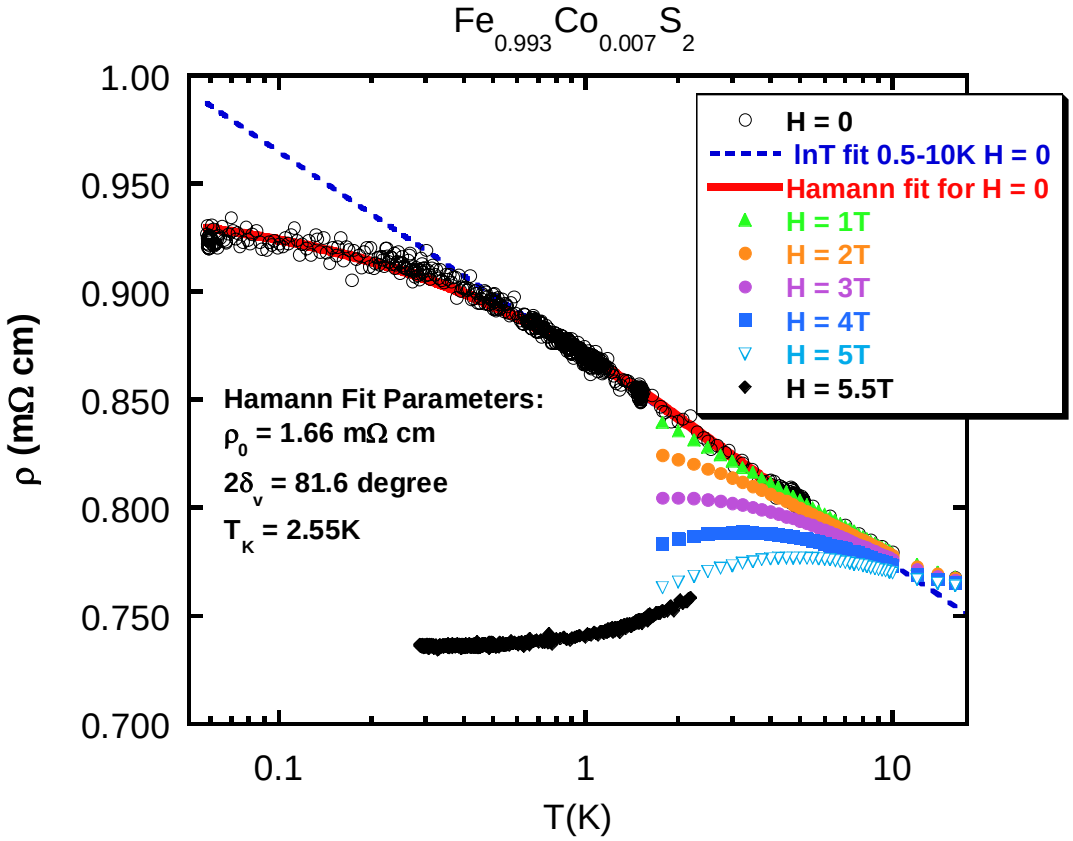

Figure 5.6 Temperature dependence of resistivity for $Fe_{0.993}Co_{0.007}S_2$ at magnetic fields indicated in the figure

(The Hamann fit [5.47] is an approximation for T dependence of single ion Kondo resistivity at $H = 0$, see equation 5.9 for details)

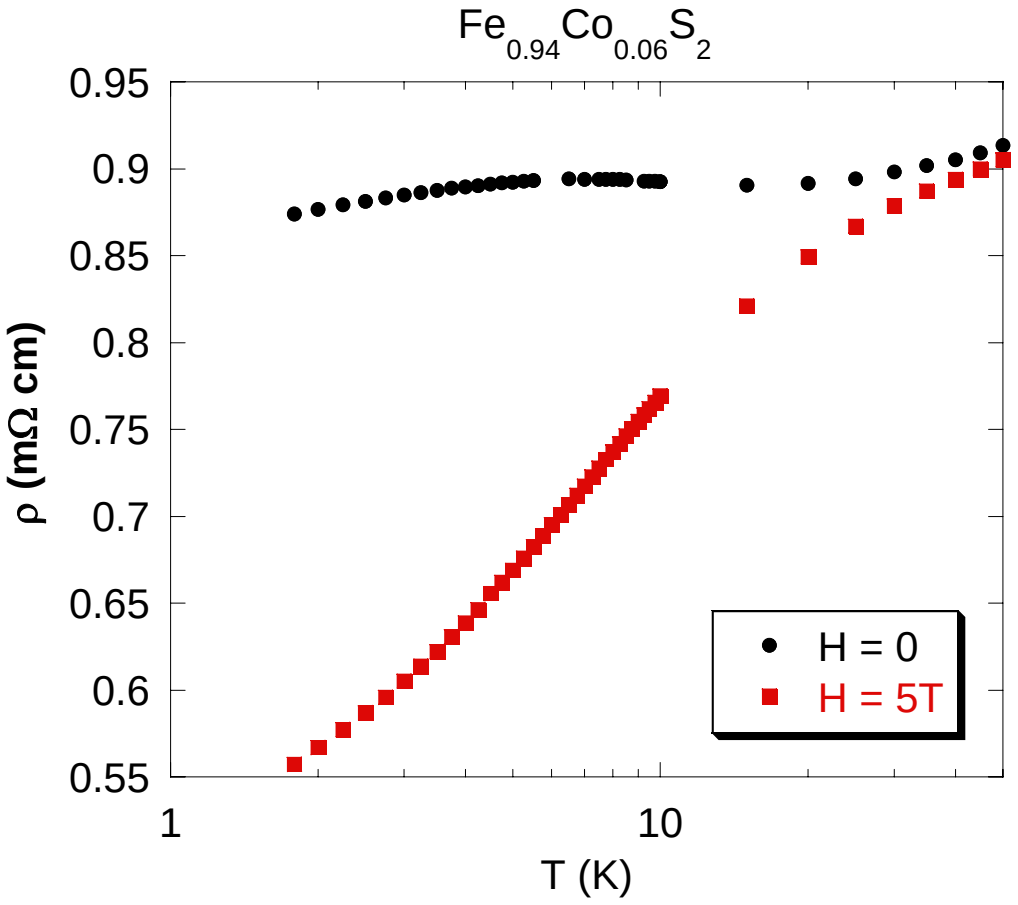

Figure 5.7 Temperature dependence of the resistivity for $Fe_{0.94}Co_{0.06}S_2$ at $H = 0$ and 5T

increasing with H. In Fig.5.9 (b), we can see the evolution of $d\rho/dH$ as T is increased for one of our $x = 0.06$ samples. The change in slope of $\rho(H)$ from low T to high T is present in all samples investigated. Note that the minimum in $d\rho/dH$ moves to lower field as T decreases suggesting H/T scaling may be possible. In Fig. 5.10 (a), the very low T (70mK) MR for both $x = 0.007$ and $x = 0.07$ samples are shown to be consistent with this description. In Fig 5.10 (b), the same data are plotted on logarithmic T scale to show that the resistivity at low-T and high-H displays a $\ln H$ dependence, consistent with single ion Kondo effect [5.10] [5.12]. We also notice that for the magnetically ordered samples the resistivity displays a similar $\ln H$ behavior in high fields as the paramagnetic samples.

The Co concentration dependence of the MR and the RRR (residual resistance ratio, the ratio of resistance between $T = 300$ K and $T = 10$ K) are plotted in Fig. 5.11. First we notice that as the Co concentration is increased from $x = 0.001$, the absolute value of the MR is small, and then increases significantly above $x > 0.03$. In the mean time, the RRR at first increases, peaks at $x \sim 0.007$, and then decreases as x increases further. The correlation between MR and the RRR for $x \geq 0.007$ is apparent in Fig. 5.12. This behavior might be telling us that both RRR and MR are caused by the same mechanism, and the $T^{1.5\pm0.2}$ dependence of the resistivity over a wide temperature range up to room temperature might be related to magnetic scattering.

5.2.3 Kondo Single Ion Scaling Analysis of MR for Low Co Concentration Samples ($x \leq 0.01$)

As shown in Fig. 5.6, for $x = 0.007$, at zero field the resistivity increases logarithmically with T from above 10K down to 0.5 K. We observed a similar logarithmic increase of the resistivity at low-T for all samples with $x \leq 0.01$. This logarithmic T-dependence along with the negative MR suggests that it may result from

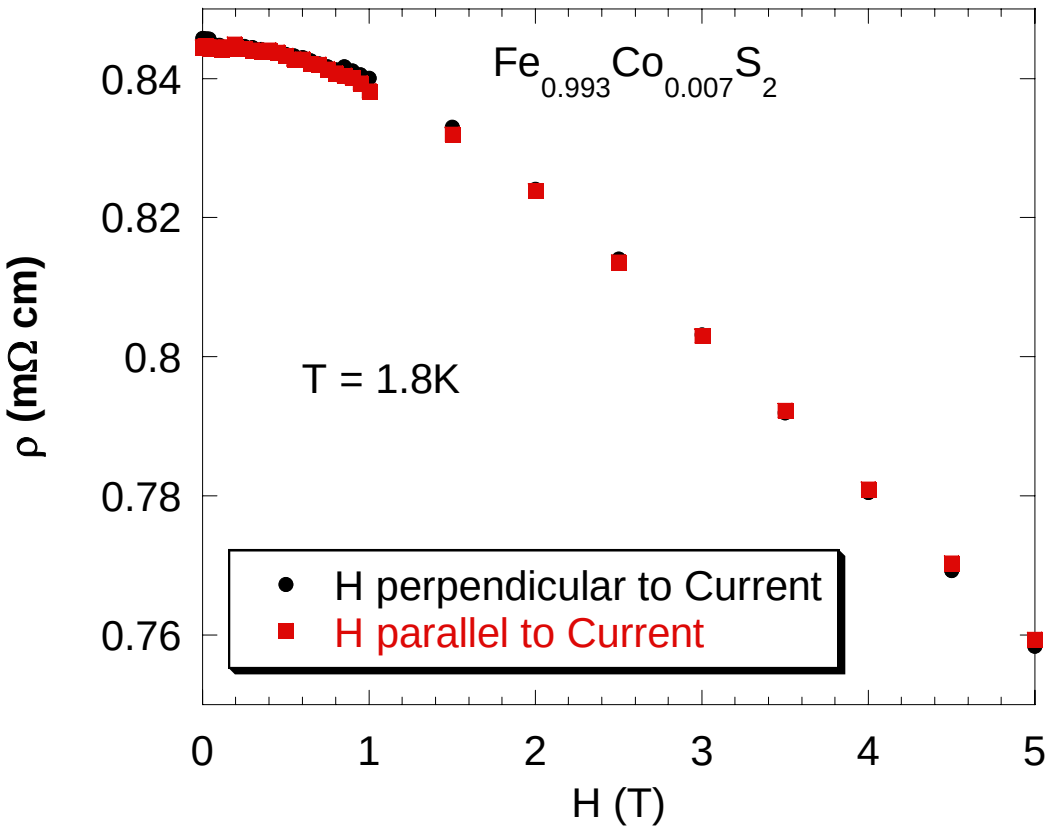

Figure 5.8 Magnetic field dependence of resistivity for $Fe_{0.993}Co_{0.007}S_2$ at $T = 1.8$ K for both parallel and perpendicular orientations

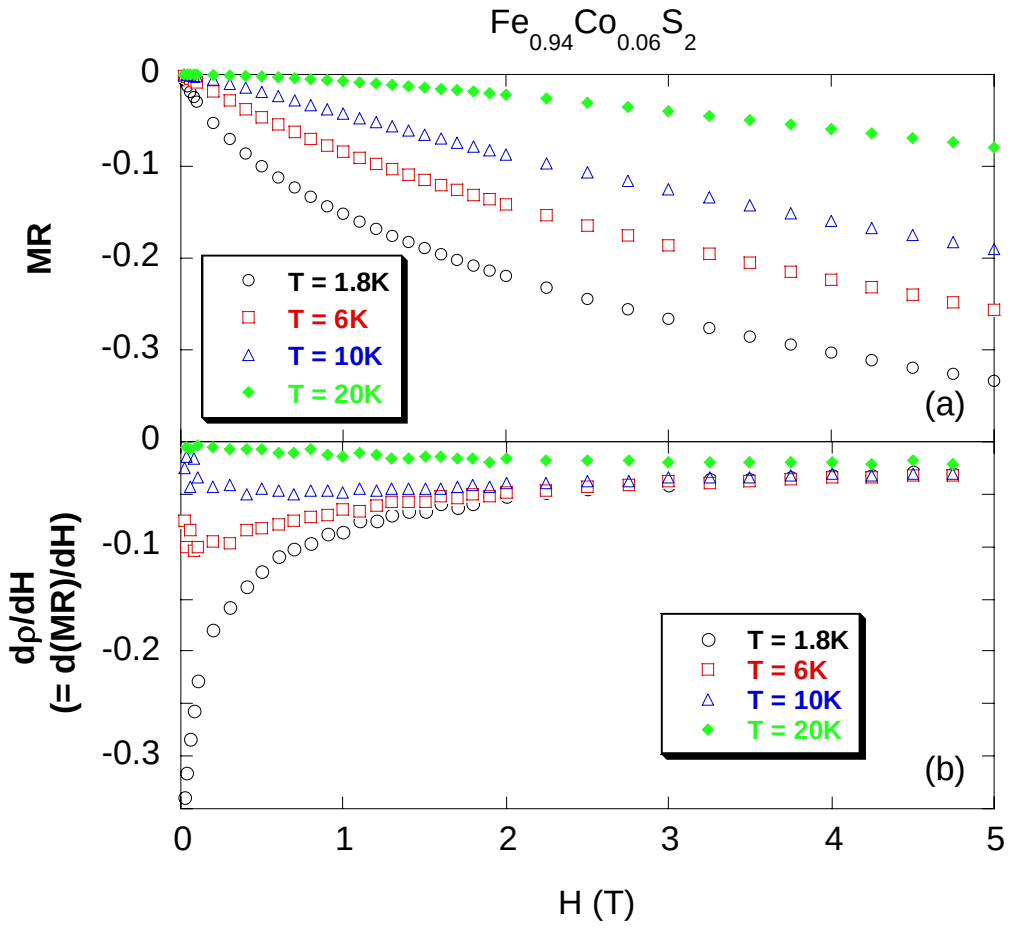

Figure 5.9 Magnetic field dependence of the MR and dρ/dH for $Fe_{0.94}Co_{0.06}S_2$ at temperatures indicated in the figure

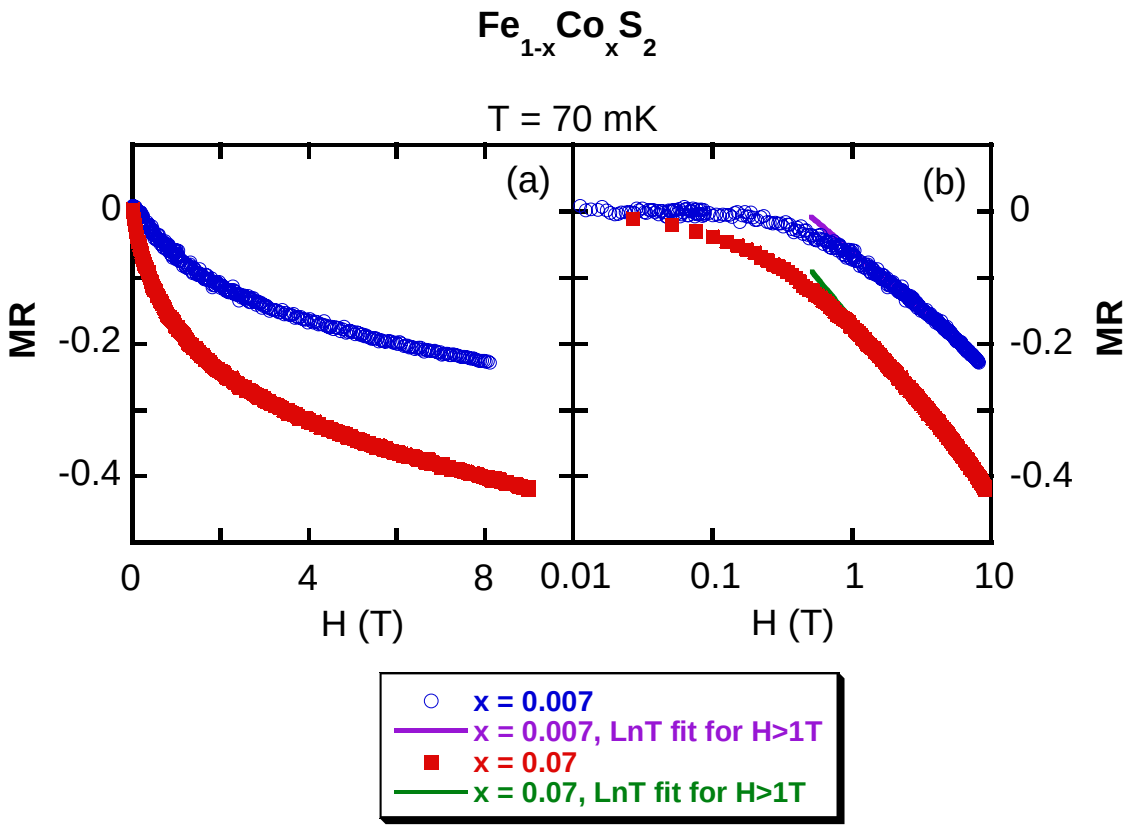

Figure 5.10 Magnetic field dependence of the MR for $Fe_{0.993}Co_{0.007}S_2$ and $Fe_{0.93}Co_{0.07}S_2$ at $T = 70$mK

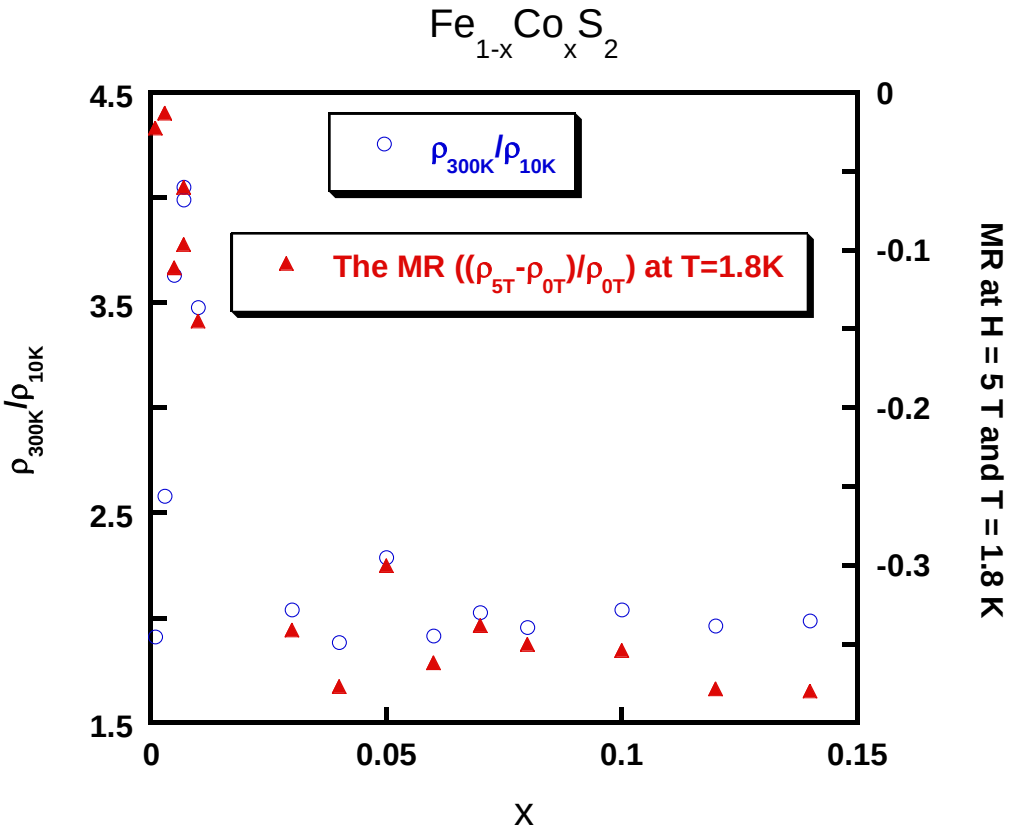

Figure 5.11 R_{300K}/R_{10K} and the MR at T = 1.8 K vs. x for $Fe_{1-x}Co_xS_2$

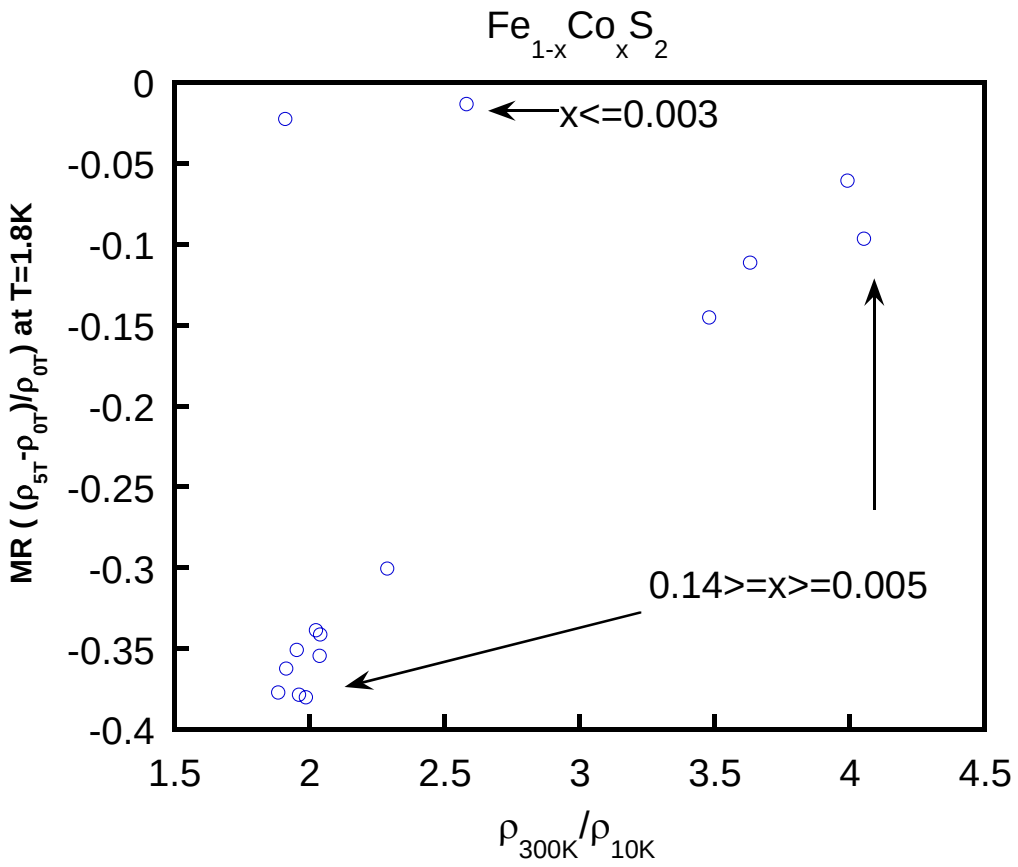

Figure 5.12 MR at T = 1.8 K vs. R_{300K}/R_{10K} for $Fe_{1-x}Co_xS_2$

the Kondo effect. In order to test this hypothesis more stringently, we fit the Hamann equation [5.47] [5.48], which is an approximate expression for Kondo effect resistivity, to the zero field resistivity data down to low T,

$$\rho_{spin}(T) = S\rho_0\left\{1 - \cos 2\delta_v \frac{\ln T/T_K}{\left[\ln^2 T/T_K + \pi^2 S(S+1)\right]^{1/2}}\right\}. \quad (5.9)$$

Here T_K is the Kondo temperature, δ_v is the phase shift due to ordinary scattering, and ρ_0 is the s-wave unitarity limit resistivity, and is given by

$$\rho_0 = mc/ne^2\hbar D(E_F) \quad , \quad (5.10)$$

where c is the impurity concentration, m and e are the electron mass and charge, respectively, and $D(E_F)$ is the density of states at the Fermi energy. ρ_0 is also related to the zero-T limit of resistivity by [5.47]

$$\rho_{spin}(T = 0K) = 2S\rho_0 \cos^2 \delta_v . \quad (5.11)$$

In the derivation of the Hamann equation, the effect of ordinary scattering is incorporated into an effective exchange scattering by replacing the exchange interaction J by $J\cos^2 \delta_v$ [5.49]. When this phase shift of ordinary scattering is taken into consideration, the resistivity increases with decreasing temperature if $J\cos(2\delta_v)$ is negative. As shown in Fig. 5.6, the fitting value for $2\delta_v$ is equal to 81.6 degrees, which immediately leads to $\cos(2\delta_v)$ = cos(81.6 degree)= 0.146. Since $\cos(2\delta_v)$ is a positive number, a negative slope of $\rho(T)$ would indicate a negative exchange interaction J as we expected for normal Kondo effect. The value for another fitting parameter, the Kondo temperature T_K (= 2.55 K), is of the same order of magnitude as, but somewhat larger than the value (1.4 K) extracted from the scaling analysis of the MR discussed below.

For Kondo systems, the single ion scaling of the MR predicts that the MR, $(\rho-\rho_{H=0})/\rho_{H=0}$, at T well above the Kondo temperature T^*, is a universal function of $H/(T+T^*)$ [5.50]. We have tested this scaling on all the samples ($x \leq 0.01$) which show a logarithmic increase of the resistivity at zero field and found that the MR scale well to this form. These scaling results are displayed in Fig. 5.13, 5.14, 5.15 and 5.16. In Fig. 5.15, we show all the H and T dependent data follow this scaling of MR for our $x = 0.007$ sample at temperatures greater than $T^* = 1.4$ K. In Fig. 5.17 for the same sample we also plot the 70mK field sweep data which do not follow the scaling function. This is reasonable since 70mK is well below the Kondo temperature $T^* = 1.4$ K, and the scaling behavior will not hold for $T < T^*$ in this model. All these scaling plots suggest that the Kondo effect is the mechanism for the negative MR of our $x \leq 0.01$ samples. However our description is phenomenological so that other mechanisms can not be completely ruled out. In Fig. 5.18, we plot the doping dependence of T^* for these paramagnetic samples, and found that T^* tends to increase with doping.

One reason that the single ion Kondo effect, as evidenced by the logarithmic increase of resistivity and the scaling of the MR above T^*, can be observed up to 1% Co concentration in our samples, in contrast to ppm impurity level in classical Kondo alloys, is most likely due to the relatively large disorder scattering in our samples. The low mean free path l will act to damp the RKKY interaction by a factor of $\exp(-r/l)$ [5.51], rendering the single impurity Kondo effect much easier to be detected. In Pd hydride with 0.2 at. % Fe impurity, the relatively large residual resistivity 15 μΩcm is thought to be responsible for the survival of single ion Kondo effect due to suppression of the RKKY interaction [5.52].

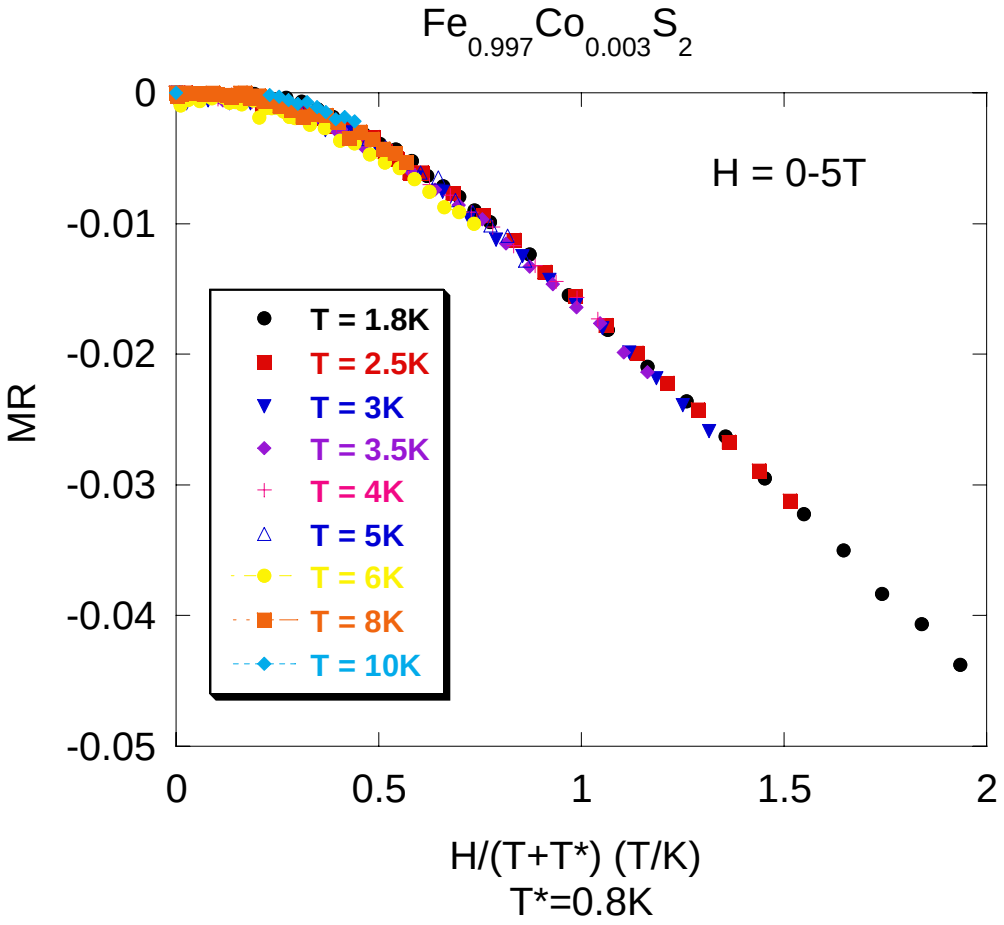

Figure 5.13 MR vs. $H/(T+T^*)$ for $Fe_{0.997}Co_{0.003}S_2$

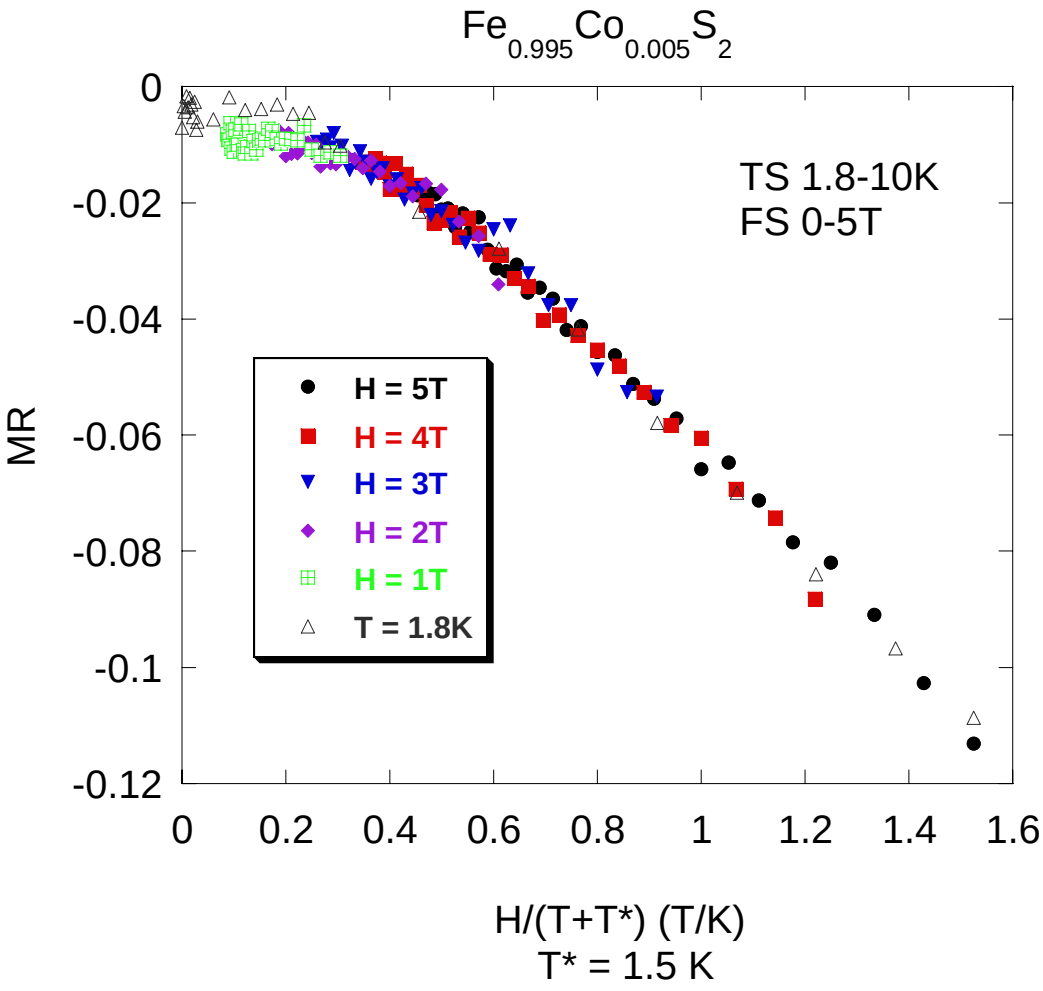

Figure 5.14 MR vs. $H/(T+T^*)$ for $Fe_{0.995}Co_{0.005}S_2$

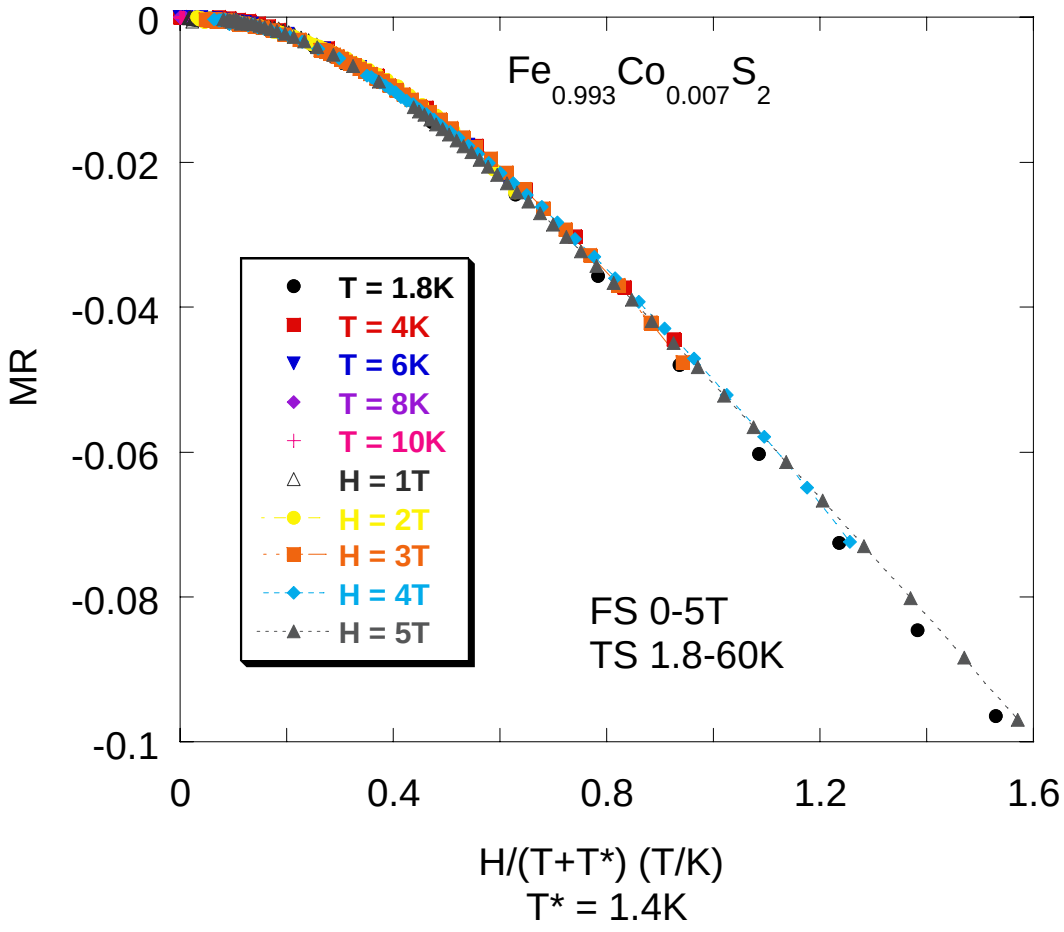

Figure 5.15 MR vs. H/(T+T*) for $Fe_{0.993}Co_{0.007}S_2$ for $T > T^*$

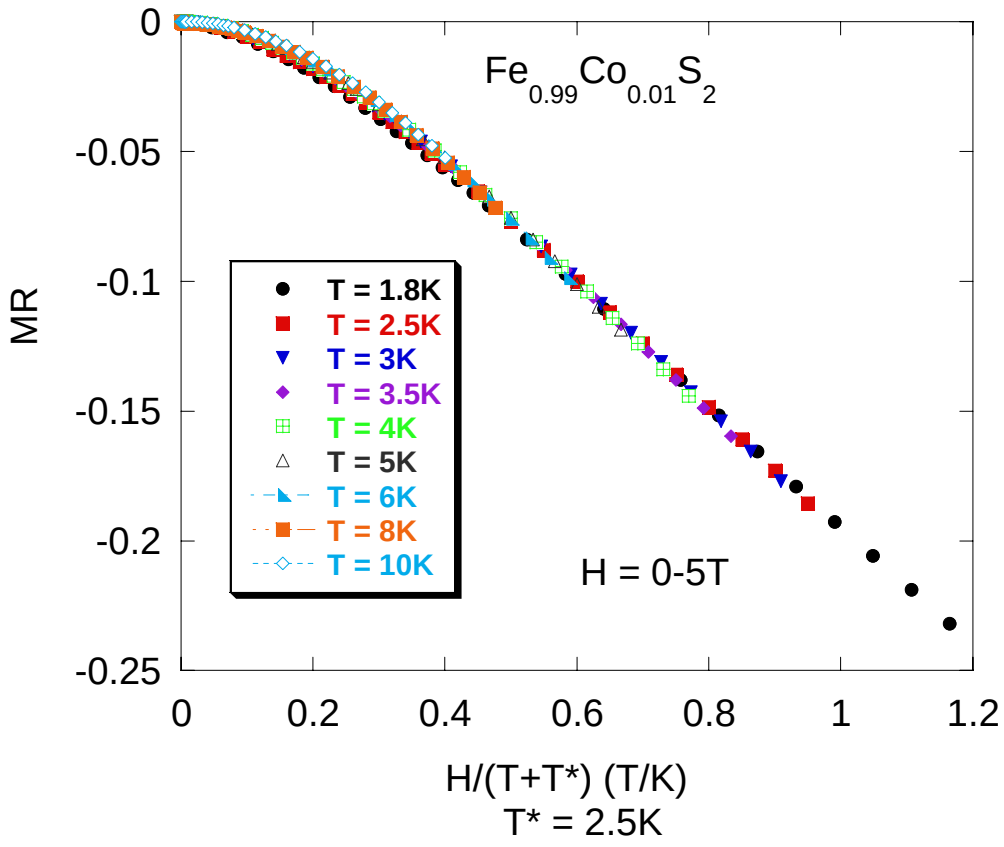

Figure 5.16 MR vs. $H/(T+T^*)$ for $Fe_{0.99}Co_{0.01}S_2$

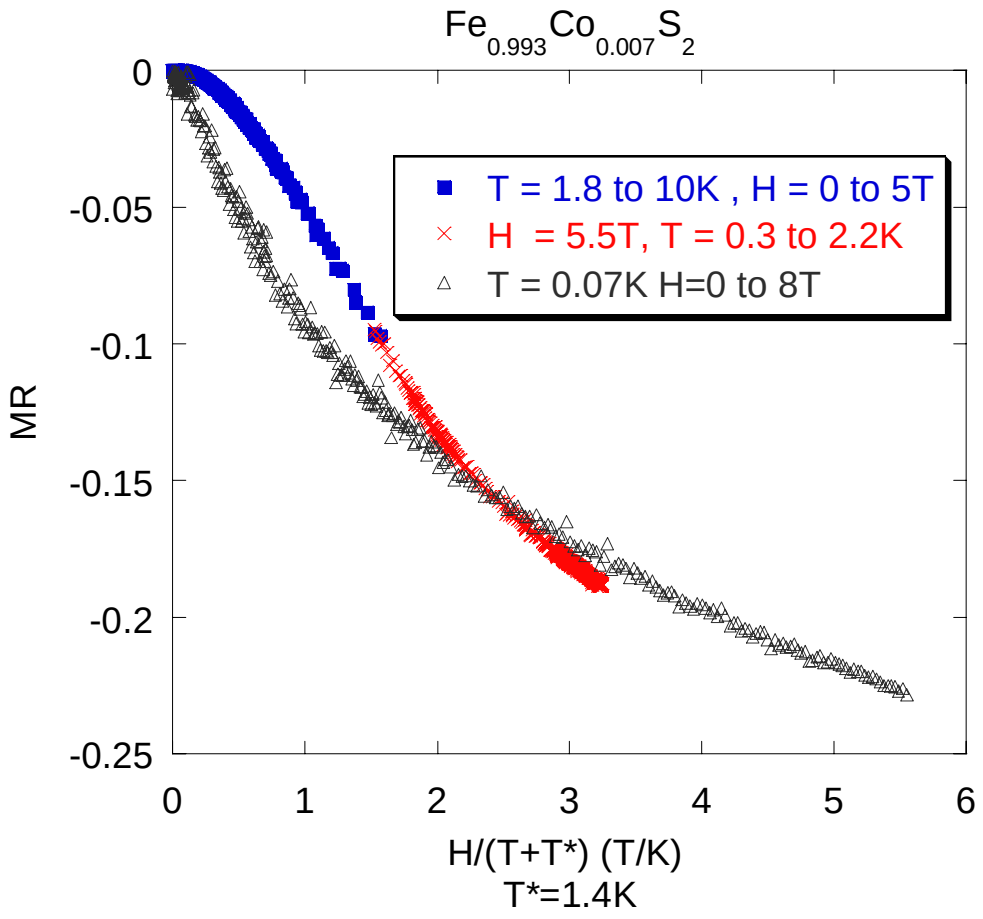

Figure 5.17 MR vs. $H/(T+T^*)$ including low-T data for $Fe_{0.993}Co_{0.007}S_2$

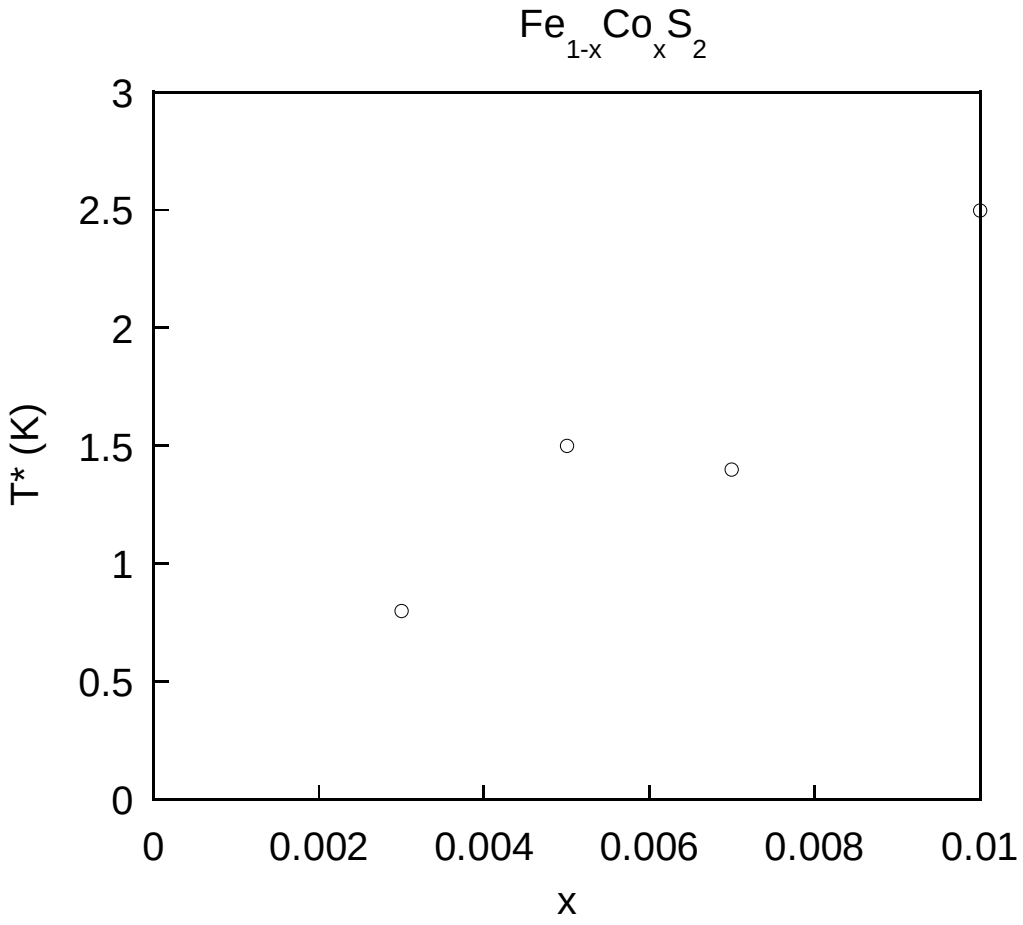

Figure 5.18 Doping dependence of the Kondo temperature for paramagnetic samples

5.3 Conclusions

For pure compound FeS_2, the resistivity displays insulating behavior as expected for a paramagnetic semiconductor. For Co doping as low as $x = 0.001$, the resistivity shows metallic behavior. The resistivity displays the $T^{1.5\pm0.2}$dependence except at the lowest temperatures, indicative of NFL behavior.

The low temperature resistivity anomaly can be separated into two classes. For $x \leq x_c$ (~ 0.01), the resistivity continues to increase as T is decreased down to our lowest temperature. For $x > x_c$, the resistivity shows a maximum or a shoulder as T is decreased indicative of a magnetic ordering.

The isotropic negative MR indicates that it is caused by a spin scattering mechanism. The field dependence of the $d\rho/dH$ changes from increasing with field behavior at low T to decreasing with field behavior at high T. The MR is larger for the more disordered, higher Co substituted samples. For $x <= 0.01$, the zero field resistance can be completely described within a single ion Kondo model as it displays a logarithmic increase with cooling and a Kondo single ion scaling in the MR. The Kondo temperature extracted from the scaling tends to increase with doping.

Chapter 6 Conclusions for $Fe_{1-x}Co_xS_2$

Cobalt substitution of iron in the paramagnet semiconductor FeS_2 results in a metallic state for $x < 0.001$. Further doping to $x_c \sim 1\%$ produces a ferromagnetic metal as evidenced by the peak in the magnetic susceptibility. The Curie temperature increases with further Co doping as determined by the susceptibility peaks and the Arrott analysis. The magnitude of the magnetic susceptibility sharply increases by more than two orders of magnitude, from our 0.7% sample to our 6% sample.

The Hall carrier density is smaller than the saturation moment, indicating the formation of local magnetic moments. Just as in the case of the doped semiconductor Si:P, where disorder leads to an inhomogeneous local density and the subsequent formation of local moments, we also propose that strong disorder leads to localized states for many of the doped charge carriers.

The logarithmic decrease with T of the zero field resistivity for $x \leq x_c$ and the isotropic negative MR are strong evidence of the Kondo effect. In fact for a sample with $x \leq x_c$, the MR follows the scaling form for single ion Kondo effect for T higher than the Kondo temperature. For $x > x_c$, the resistivity shows a maximum or a shoulder as T is decreased, most likely due to the RKKY interactions creating a FM ordering of the local moments.

For $x > x_c$, the specific heat Sommerfield coefficient, γ, increases at low temperatures with cooling, and then becomes saturated or slightly decreases to a Fermi-Liquid-like behavior. For $x \sim x_c$, γ increases as $T^{-0.69\pm0.03}$ as T is decreased from 6K to 0.1 K, a NFL behavior. NFL behavior is also evident in the $T^{1.5}$ dependence of ρ for $x > x_c$.

The rapid suppression of the magnetic susceptibility by a small magnetic field at low temperatures indicates the formation of giant spins clusters above the ferromagnetic critical temperature. The low-T rapid downturn of the inverse susceptibility for the x = 0.06 sample is a strong evidence for the formation of the Griffiths phase. A small field of 10G can recover the Curie-Weiss behavior, suggesting that the zero field susceptibility is dominated by the contributions from large spin clusters in the sample.

The Griffiths phase has been invoked by Castro Neto et al [6.1] to explain the NFL behavior in many doped Heavy Fermion compounds. In this theory, the competition between RKKY and Kondo effect in the presence of disorder and magnetic anisotropy can lead to the coexistence of two electronic fluids: one is dominated by the Kondo effect leading to quenched moments, the other is dominated by the RKKY interaction leading to a granular magnetic phase or giant spin clusters which can have large susceptibilities due to a quantum tunneling effect at low-T. The original disordered Kondo lattice problem was mapped into the random Ising model in a random transverse magnetic field. At low T, the average effect of the quantum tunneling of spin clusters of different sizes leads to the power law divergence of γ and the susceptibility, χ, with the same exponent. In our pyrite series, $Fe_{1-x}Co_xS_2$, we find that the increase in γ persists to temperatures below the T where χ saturates or peaks, indicating NFL behavior within the FM phase. We notice that NFL behavior within the FM phase had been observed before in $URu_{2-x}Re_xSi_2$ [6.2] close to a FM quantum critical point. It was argued that for the Griffiths phase model, even in the FM phase the contribution to the critical behavior from the local magnetic clusters may exceed that of the infinite cluster which describes the long range order of the FM phase, and therefore it is possible for NFL behavior to exist within the FM phase.

Chapter 7 Superconducting $LaSb_2$

7.1 Introduction

$LaSb_2$ belongs to the series of light rare earth diantimonides RSb_2 (R = La-Nd, Sm) that all form in the $SmSb_2$ crystal structure (Fig. 7.1) [7.1]. This is a highly anisotropic layered structure with alternating La/Sb layers and 2-Dimentional (2D) rectangular sheets of Sb atoms stacked along the c-axis (see Fig. 7.1 from single crystal X-ray diffraction measured by Prof. J. Y. Chan). The layered structure gives rise to the anisotropic transport and magnetic properties observed in all the compounds in this RSb_2 series [7.1]. Except for $LaSb_2$, all light rare earth diantimonides order magnetically at low temperatures [7.1]. The zero field in-plane resistivity for all the compounds are metallic, with residual resistance ratio ranging from 40 to 750 [7.1]. One interesting common feature for this series of compounds is the large linear anisotropic positive magnetoresistance (MR) at low temperatures (Fig. 7.2) [7.1]. For $LaSb_2$, the transverse MR with current in the *ab* plane can be as large as 10,000% at $H = 45$T and $T = 2$K, with no sign of saturation [7.2]. The T-dependent in-plane resistivity in a high field perpendicular to the ab plane shows a broad maximum at low T, reaching 23K at 18T (Fig. 7.2) [7.1]. For other members of this series, below the magnetic ordering temperature, the MR is steeply enhanced (see Fig. 7.3 for $NdSb_2$) [7.1]. For $PrSb_2$ at $T =$ 2K, a pressure of 11.5 kBar can decrease the zero-field resistivity by a factor of ~ 5 without changing the MR ($(\rho_H-\rho_0)/\rho_0$) [7.3].

Single crystals of $LaSb_2$ grown by Prof. D. P. Young using the metallic flux method are large flat layered plates which are malleable and easily cleaved, with typical dimensions of 5mm*5mm*0.2mm. The residual resistance ratio (RRR) can reach 70-90

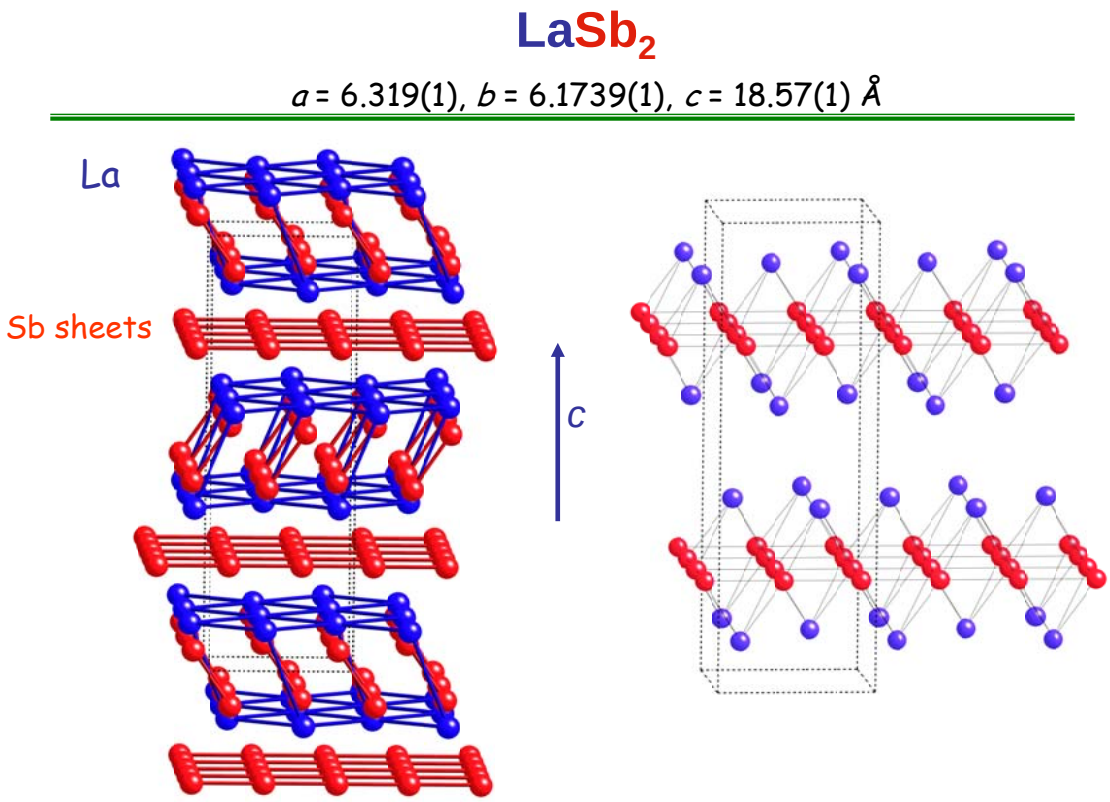

Figure 7.1 Crystal Structure of $LaSb_2$

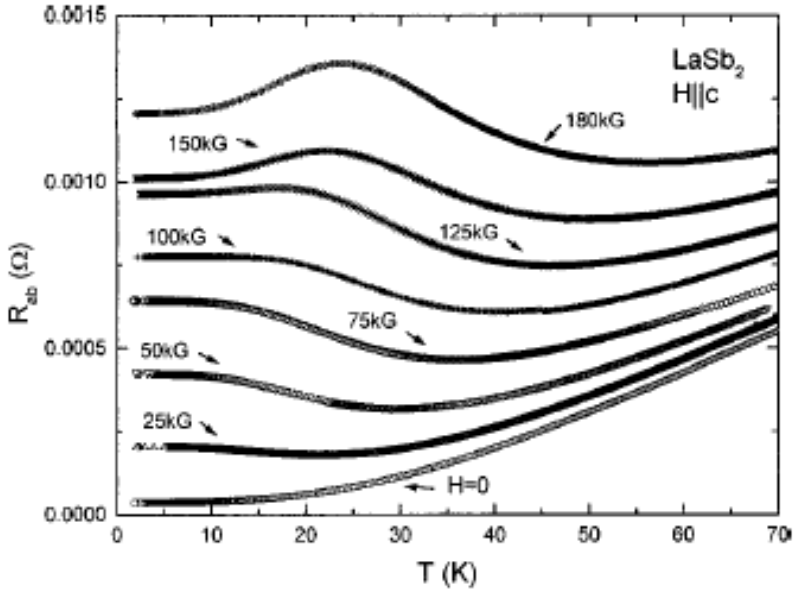

Figure 7.2 Temperature dependence of the in plane resistivity for $LaSb_2$ in zero and high field (from reference 7.1)

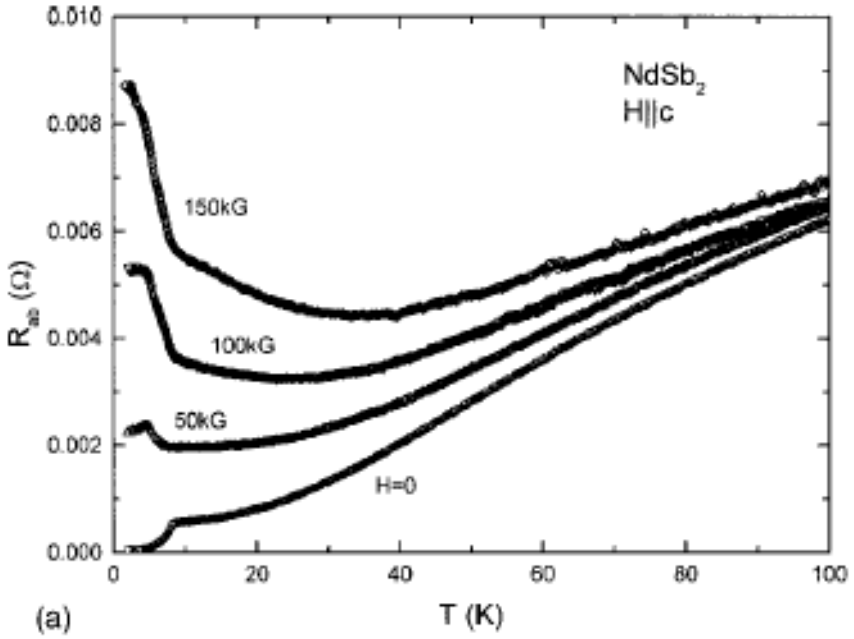

Figure 7.3 Temperature dependence of the in plane resistivity for $NdSb_2$ in zero and high field (from reference 7.2)

for in-plane currents. Early measurements showed that $LaSb_2$ becomes superconducting at $T_c = 0.4$ K [7.4]. In this chapter, I will report on our explorations of the low-T properties of $LaSb_2$, and will show that at $T \sim 2$K $LaSb_2$ is a bulk superconductor at high pressure.

7.2 Theoretical Aspects of Layered Superconductors

For superconducting multilayers separated by insulating or metallic nonsuperconducting films, a dimensional crossover from anisotropic 3D to 2D behavior has been observed when the perpendicular coherence length $\xi_\perp$ is approximately equal to the separation between the superconducting layers (or the thickness d_n of the nonsuperconducting layer). When $\xi_\perp >> d_n$, superconducting layers are well coupled and anisotropic 3D behavior is been observed [7.6]. When $\xi_\perp << d_n$, the superconducting layers are effectively decoupled. In this case, if the thickness d_s of the superconducting layer is less than the coherence length, 2D behavior will be observed, otherwise a 3D isotropic behavior is expected and observed (Fig. 7.4) [7.6]. Experimentally, the 3D to 2D crossover described by theory was observed in intercalated transition-metal dichalcogenides (TMD) [7.5], and artificially grown layered materials, for example, Nb/Ge, and Nb/Cu [7.6].

7.2.1 Anisotropic 3D Regime

For layered superconductors in the anisotropic 3D regime ($\xi_\perp >> d_n$), Lawrence and Doniach [7.6] [7.7] predicted the following behavior based on an anisotropic Ginzburg-Landau theory for different coherence lengths in fields parallel ($\xi_{//}$) and perpendicular ($\xi_\perp$) to the plane of the layers:

$$\boldsymbol{H}_{c2//}(\boldsymbol{T}) = \frac{\Phi_0}{2\pi\boldsymbol{\xi}_{//}(\boldsymbol{T})\boldsymbol{\xi}_{\perp}(\boldsymbol{T})} \tag{7.1}$$

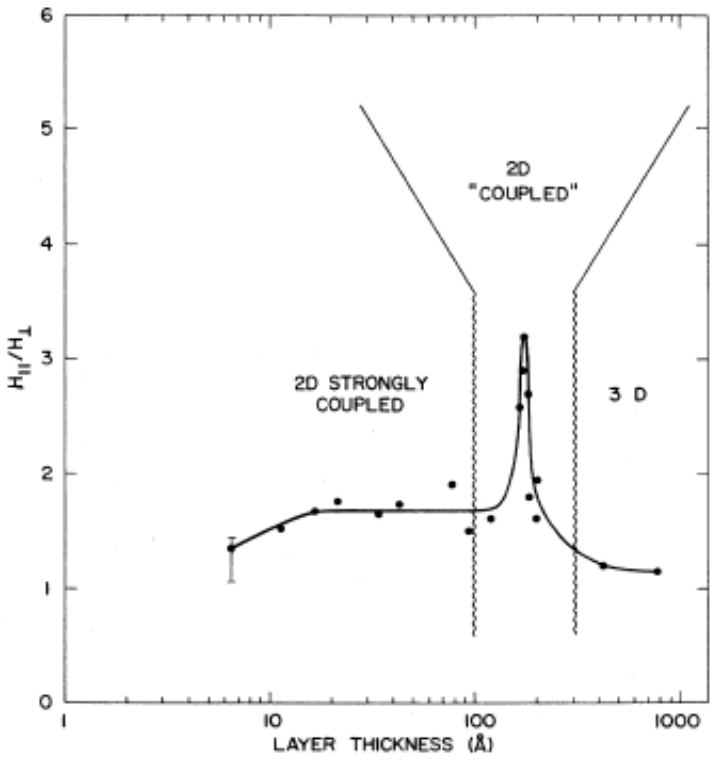

Figure 7.4 Ratio of critical fields vs. layer thickness at $T = 1.17$ K for Nb/Cu superlattices (from reference 7.6)

(Nb and Cu layers have equal thickness. “2D strongly coupled” is also called “anisotropic 3D” in the literature.)

and

$$\boldsymbol{H}_{c2\perp}(\boldsymbol{T}) = \frac{\Phi_0}{2\pi\boldsymbol{\xi}_{//}(\boldsymbol{T})^2}, \tag{7.2}$$

where Φ_0 is the flux quantum which equals to $2.0678*10^{-7}$G cm^2, and $\boldsymbol{H}_{c2//}$ and $\boldsymbol{H}_{c2\perp}$ are the upper critical fields for fields parallel and perpendicular to the plane of the layers. The angular dependence of the upper critical field is expected to be

$$\boldsymbol{H}_{c2}(\boldsymbol{\theta},\boldsymbol{T}) = \frac{\Phi_0}{2\pi\boldsymbol{\xi}_{//}^2(\boldsymbol{T})[\sin^2\boldsymbol{\theta} + (\boldsymbol{m}/\boldsymbol{M})\cos^2\boldsymbol{\theta}]^{1/2}}. \tag{7.3}$$

where θ is the angle between the direction of magnetic field and the planes, and

$$\frac{\boldsymbol{M}}{\boldsymbol{m}} = \left[\frac{\boldsymbol{H}_{c2//}(\boldsymbol{T})}{\boldsymbol{H}_{c2\perp}(\boldsymbol{T})}\right]^2 \tag{7.4}$$

is the anisotropy in the effective Ginzburg-Landau mass. $H_c(\theta)$ can also be written in the form

$$\left(\frac{\boldsymbol{H}_c(\boldsymbol{\theta})\sin\boldsymbol{\theta}}{\boldsymbol{H}_\perp}\right)^2 + \left(\frac{\boldsymbol{H}_c(\boldsymbol{\theta})\cos\boldsymbol{\theta}}{\boldsymbol{H}_{//}}\right)^2 = 1 \quad . \tag{7.5}$$

7.2.2 2D Regime

For a 2D superconducting single layer or decoupled layers in the 2D regime satisfying the relation $\xi << d_s$, the parallel and perpendicular upper critical fields have the following dependence [7.8] on the coherence length ξ:

$$\boldsymbol{H}_{c2//}(\boldsymbol{T}) = \frac{\Phi_0}{2\pi\boldsymbol{\xi}(\boldsymbol{T})\boldsymbol{d}_s/\sqrt{12}} \tag{7.6}$$

and

$$\boldsymbol{H}_{c2\perp}(\boldsymbol{T}) = \frac{\Phi_0}{2\pi\boldsymbol{\xi}(\boldsymbol{T})^2}. \tag{7.7}$$

The angular dependence of the upper critical field is given by

$$\left|\frac{\boldsymbol{H}_{c2}(\boldsymbol{\theta})\sin\boldsymbol{\theta}}{\boldsymbol{H}_{c2\perp}}\right|+\left(\frac{\boldsymbol{H}_{c2}(\boldsymbol{\theta})\cos\boldsymbol{\theta}}{\boldsymbol{H}_{c2//}}\right)^{2}=1. \tag{7.8}$$

7.2.3 Signature of the 3D-2D Crossover

3D-2D crossover can be detected in two ways: the first is to observe the angular dependence of the upper critical field $H_{c2//}(\theta)$ near $\theta = 0$, and the second to measure the T dependence of the parallel upper critical field $H_{c2//}(T)$.

For the anisotropic 3D case, from equation 7.3, close to $\theta = 0$, the slope of $H_{c2}(\theta)$ is 0. A round maximum is expected at $\theta = 0$ for the θ dependence of H_{c2} (Fig. 7.5(a)). In contrast, the 2D case, characterized by equation 7.8, has a $H_{c2}(\theta)$ slope with finite value near $\theta = 0$,

$$\left|\frac{1}{\boldsymbol{H}_{c2}}\frac{d\boldsymbol{H}_{c2}}{d\boldsymbol{\theta}}\right|_{\boldsymbol{\theta}=0}=-\frac{\boldsymbol{H}_{c2//}}{\boldsymbol{H}_{c2\perp}}. \tag{7.9}$$

Thus the θ dependence of H_{c2} is expected to display a cusp around $\theta = 0$ for 2D superconductors (Fig. 7.5(b)).

For a 3D superconductor H_{c2} is linearly dependent on T (Fig. 7.6)

$$\boldsymbol{H}_{c2}(\boldsymbol{T})\propto 1-\boldsymbol{T}/\boldsymbol{T}_{c}, \tag{7.10}$$

whereas in the 2D case, we have [7.6]

$$\boldsymbol{H}_{c2//}(\boldsymbol{T})\propto(1-\boldsymbol{T}/\boldsymbol{T}_{c})^{1/2} \tag{7.11}$$

while

$$\boldsymbol{H}_{c2\perp}(\boldsymbol{T})\propto 1-\boldsymbol{T}/\boldsymbol{T}_{c} \tag{7.12}$$

remains linear in temperature (Fig. 7.7). The signature of a 3D to 2D transition with cooling has been observed in the T-dependence of the parallel upper critical field $H_{c2//}$ (T).

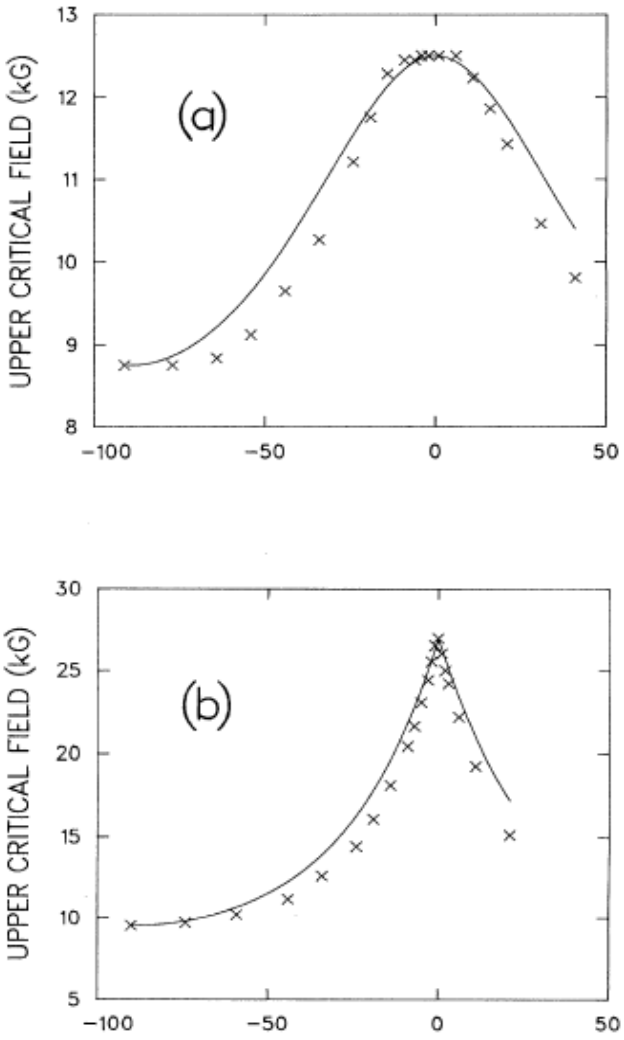

Figure 7.5 Angular dependence of critical fields for a Nb/Cu superlattice (from reference 7.6)

((a) anisotropic 3D behavior (d_{Nb} = 23A, d_{Cu} = 23 A, and T = 1.17 K) and (b) 2D behavior (d_{Nb} = 172A, d_{Cu} = 333 A, and T = 1.17 K).)

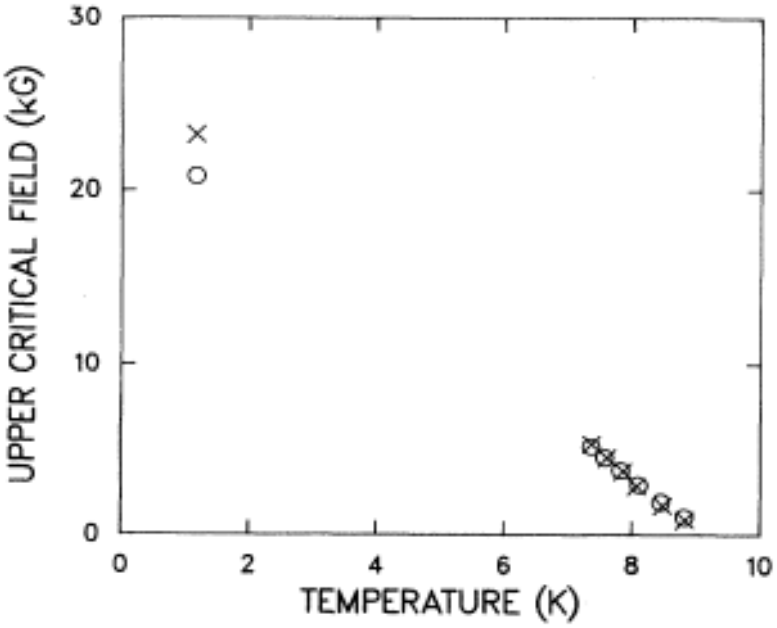

Figure 7.6 Upper critical fields for a 3D, thick Nb film (from reference 7.6)

(Cu(1500A)/Nb(8500A)/Cu(1500A)
cross for parallel field, circle for perpendicular field)

As T is decreased from T_c, the 3D linear T dependence of $H_{c2//}$ (T) close to T_c is replaced by a dramatic upturn and subsequently a tendency to saturation at low T (usually a $T^{1/2}$ behavior) (Fig. 7.8) [7.6].

7.3 Low Temperature Resistivity of $LaSb_2$

Fig. 7.9 shows the temperature dependence of the resistivity of $LaSb_2$ on the same sample for currents parallel to the *ab* plane and the *c* axis. At 1.5K, a large anisotropy in residual resistance in the order of 50 is observed which is consistent with the layered structure. Below ~ 1.5 K, the resistivity for both current (I) orientations slowly drops to zero, in an unexpected fashion for a clean crystalline material undergoing a superconducting transition. Fig. 7.10 displays the effect of transverse magnetic field on the resistivity. In Fig. 7.10(a), the field dependence of the in-plane resistivity is plotted for five temperatures below the resistive superconducting transition temperature. In Fig. 7.10(b), the c-axis resistivity is restored to the normal state by transverse fields. At T = 0.12 K the critical field H_c ~ 0.06 T, defined as the field necessary to restore full normal resistive state for I parallel to the c-axis, is in contrast to H_c ~ 0.15 T for the ab plane resistivity. Therefore, in a transverse in-plane field between 0.06 T and 0.15 T, the in-plane resistivity remains superconducting but non-zero while the resistivity perpendicular to the ab planes returns to its normal state. Perhaps a more interesting feature is for transverse in-plane fields between 0.01 T and 0.06 T, the in-plane resistivity is zero and c-axis resistivity is already non-zero. Besides the critical field H_c, we also defined two characteristic fields, H_m and H_s, for the superconducting transition as is evident in Fig. 7.10(b). H_m is defined as the field where the resistivity drops to its half value, and H_s is defined as the field where the resistivity drops to zero. In Fig. 7.11(a), the temperature

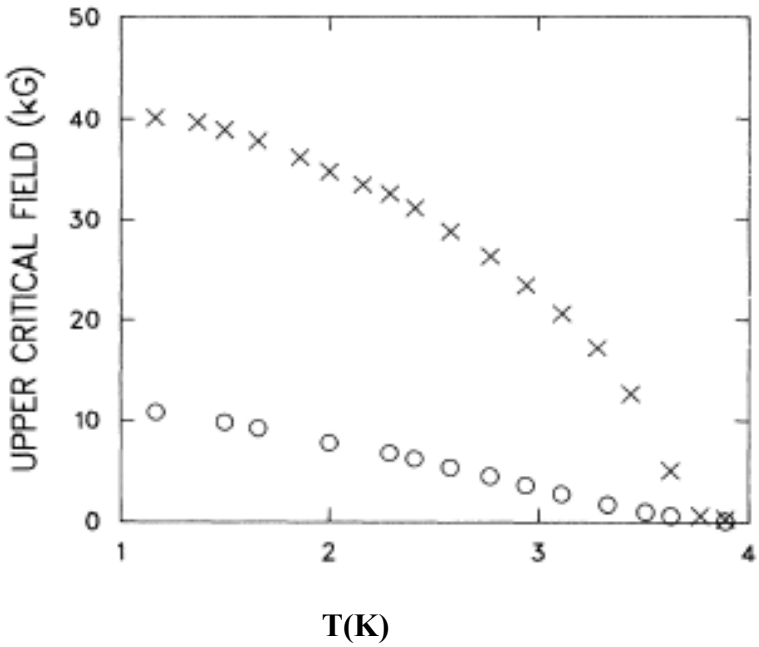

Figure 7.7 Upper critical fields for a 2D, thin Nb film (from reference 7.6)

Cu(1500A)/Nb(191A)/Cu(1500A)
(cross for parallel field, circle for perpendicular field)

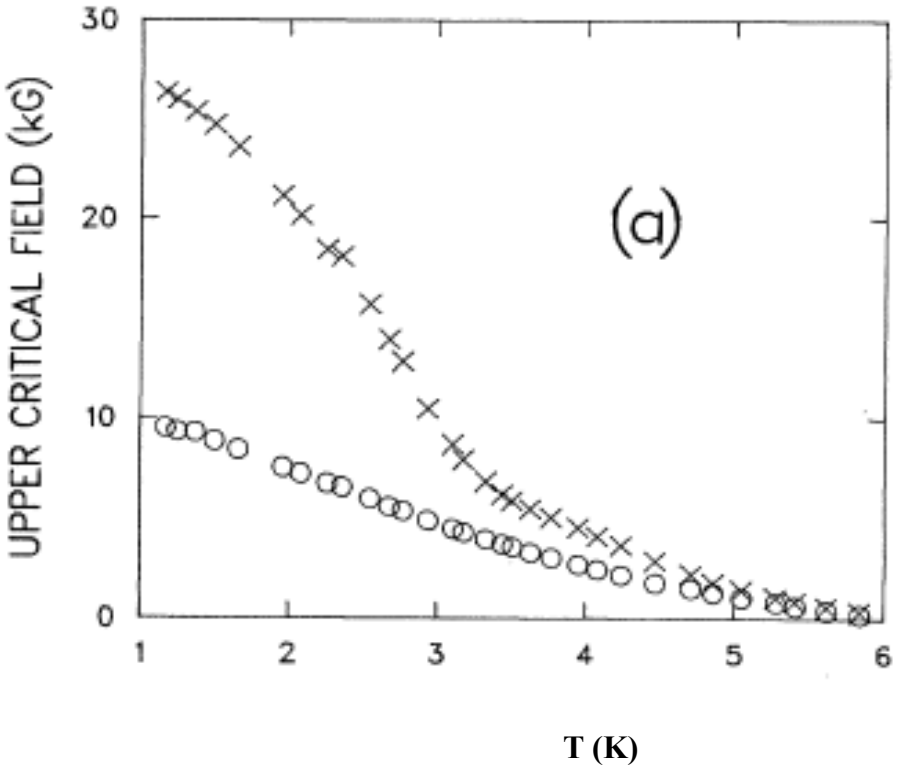

Figure 7.8 Upper critical fields for a Nb/Cu superlattice. (from reference 7.6)

(Thickness is 172A for Nb layer, and 333A for Cu layer.
cross for parallel field, circle for perpendicular field)

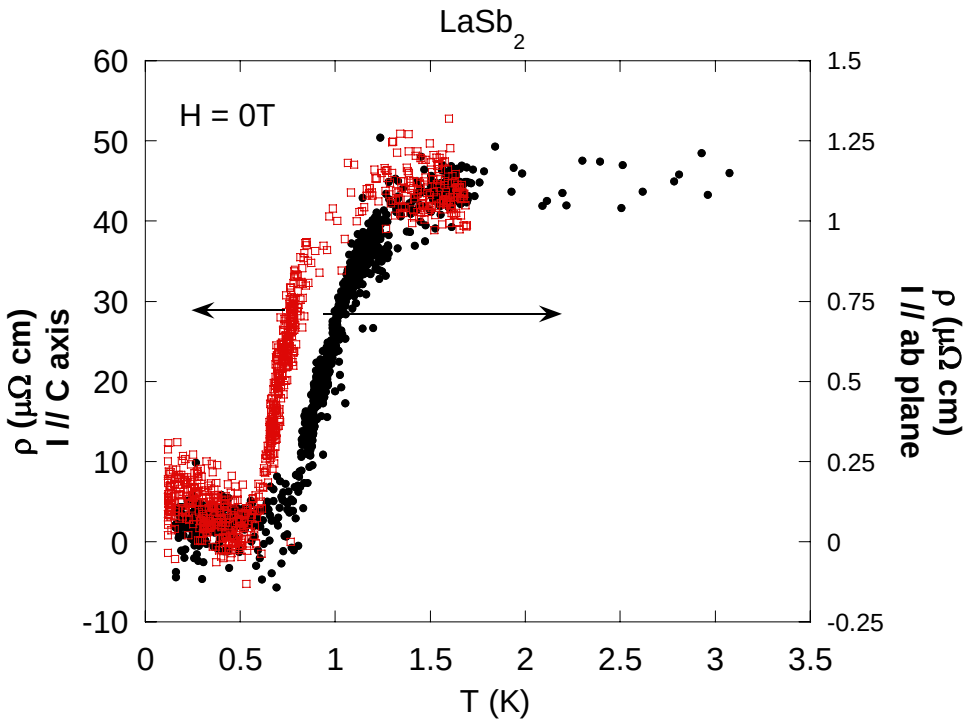

Figure 7.9 Temperature dependence of resistivity for $LaSb_2$ at low T

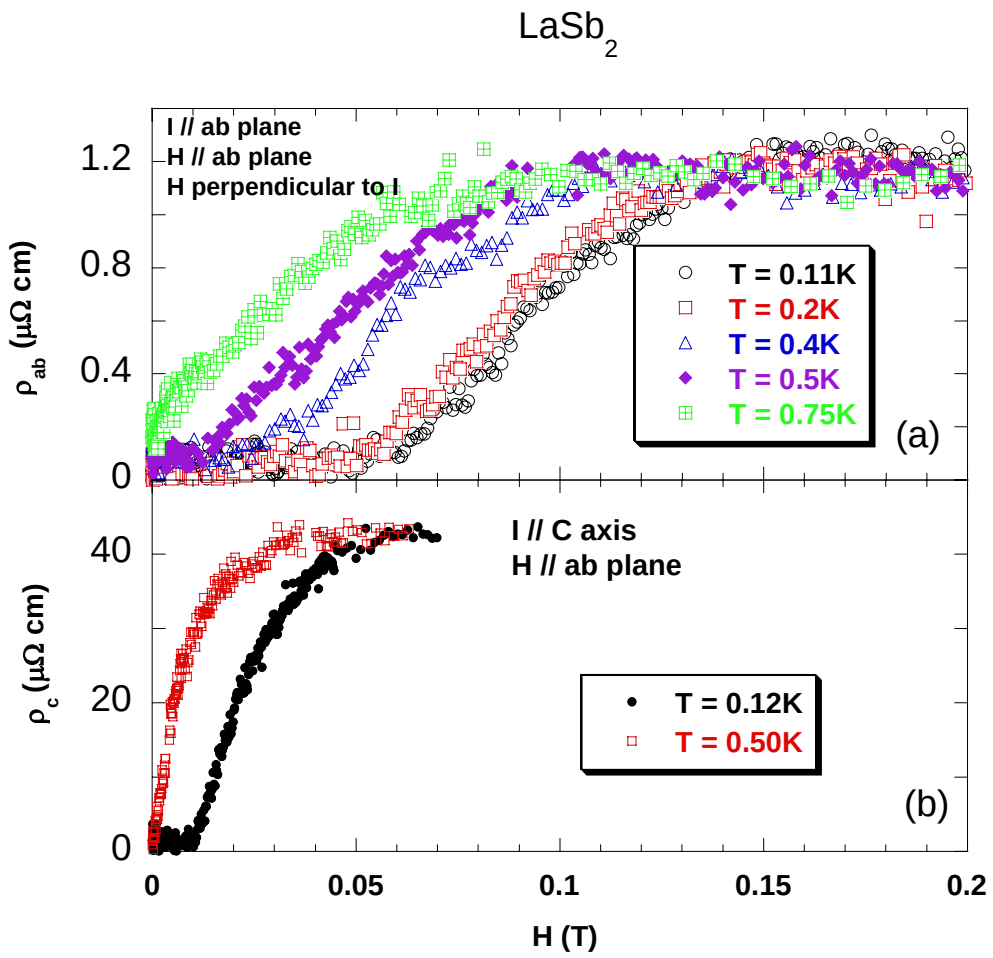

Figure 7.10 Field dependence of resistivity for $LaSb_2$ at temperatures noted in the figure

dependence of these characteristic fields appears to be linear, however, these curves do show significant curvature and may be more closely comparable to the data in Fig. 7.8. In Fig. 7.11(b), we display the temperature dependence of ratio of H_c from linear fits in the in-plane and the out-of-plane resistivity. From this figure we can see the suppression of anisotropy in H_c as T is decreased below 1K. Notice that at the base temperature $T = 0.12$ K, this ratio remains at 2.5, a value still significantly larger than 1.

The angle dependence of the resistively defined critical fields as measured by Prof. P. A. Adams for a second sample at $T = 0.1$ K is shown in Fig. 7.12. The solid line is the fit for the 2D form specified by the equation 7.8.

In addition, we have observed some sample dependence for the formation of the low-T superconducting state. For example, the c-axis resistance for a third crystal at low temperature displays only an incomplete transition at the base temperature (Fig. 7.13).

7.4 DC Magnetization at $T \sim 1.8$ K (Emergence of Superconductivity) for $LaSb_2$

The emergence of superconductivity at temperature as high as ~ 2K in zero pressure is evident in the field dependence of DC magnetization (see Fig. 7.14). At $T =$ 1.78 K, the magnitude of diamagnetism is 1.5% (0.1%) of the full Meissner effect, for perpendicular (parallel) fields respectively. The overall shape of the magnetization curves seem to suggest that this is type I superconductivity, with only a small hysteresis. However, it is also possible that $LaSb_2$ belongs to the category of clean type II superconductors such as vanadium [7.9] where little hysteresis is evident. The anisotropy is evident both in the critical field and the susceptibility. As in the low-T resistivity measurements, the critical field for H-parallel to the ab plane is larger than that perpendicular to the plane. At the same time, the in-plane diamagnetism due to the

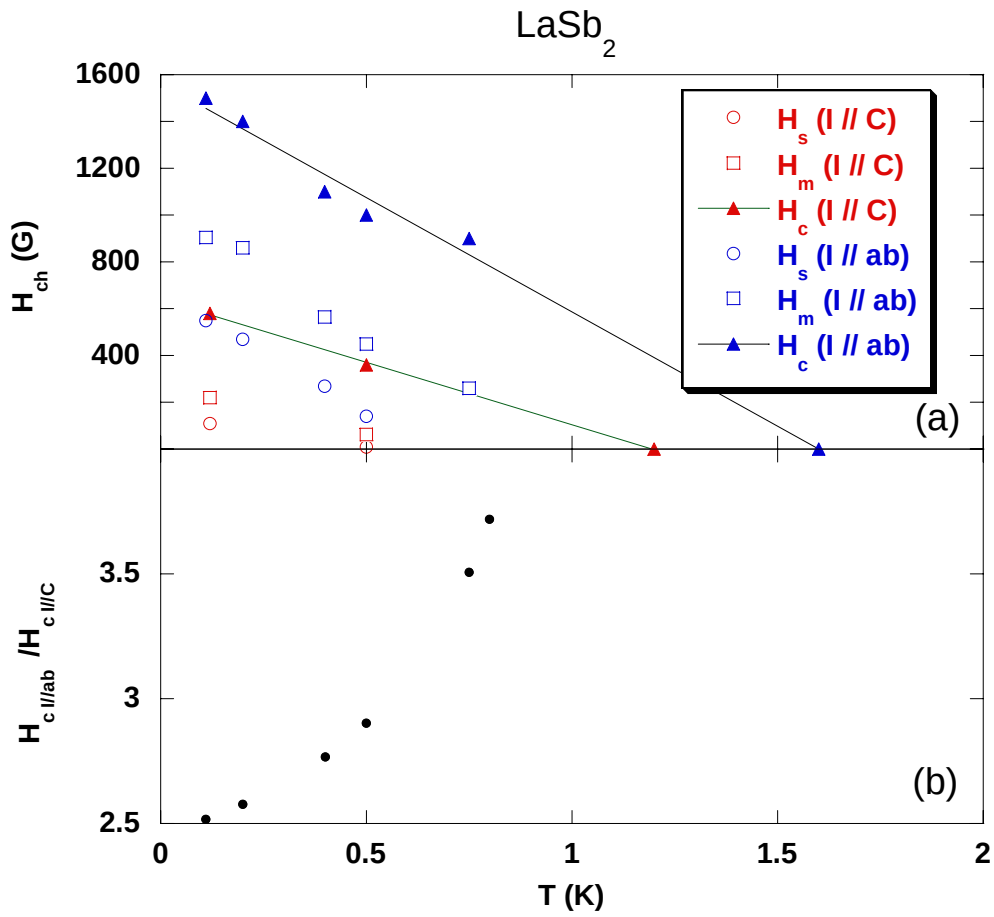

Figure 7.11 Temperature dependence of characteristic fields and anisotropy ratio of linear fits of resistivity critical fields for $LaSb_2$

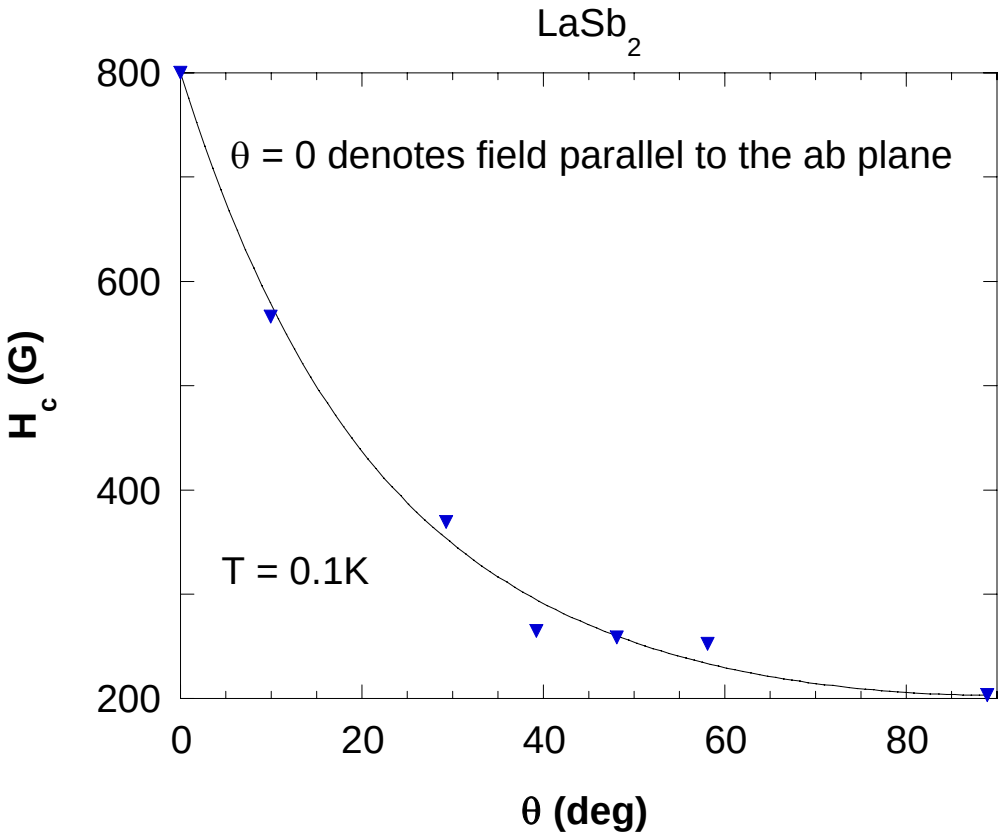

Figure 7.12 Angle dependence of the resistively defined critical field for a $LaSb_2$ crystal

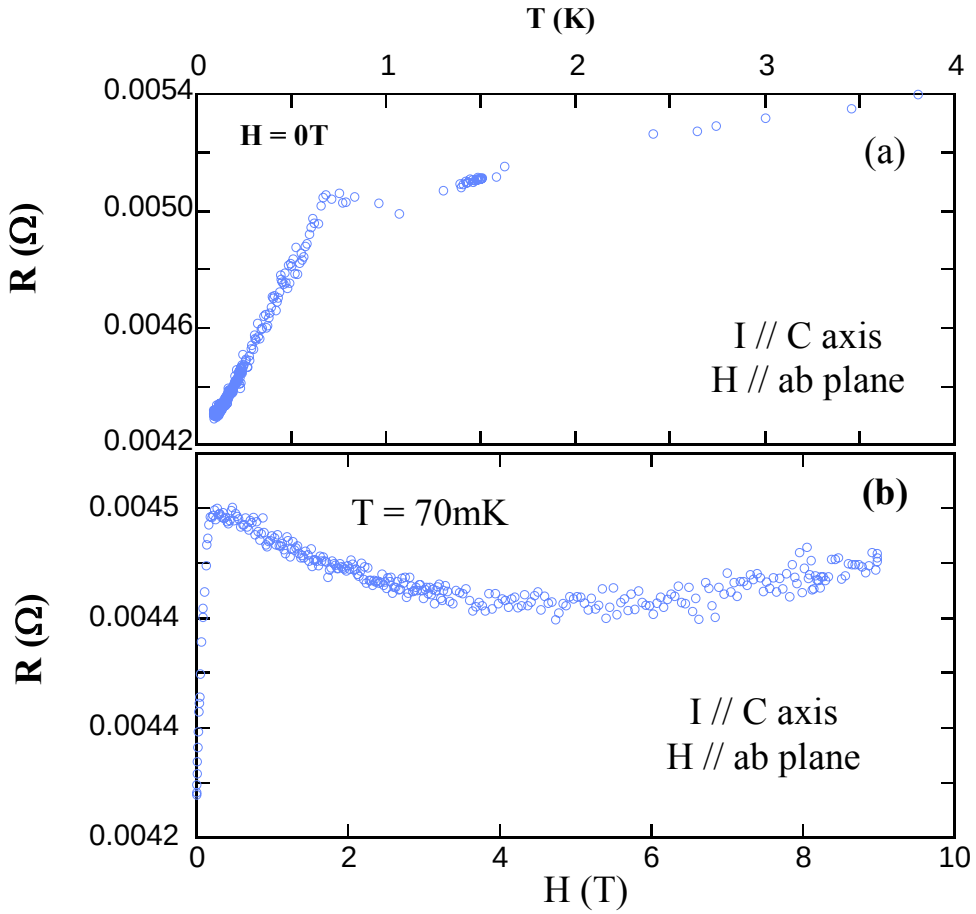

Figure 7.13 Temperature and field dependence of c-axis resistance for the 3rd $LaSb_2$ crystal

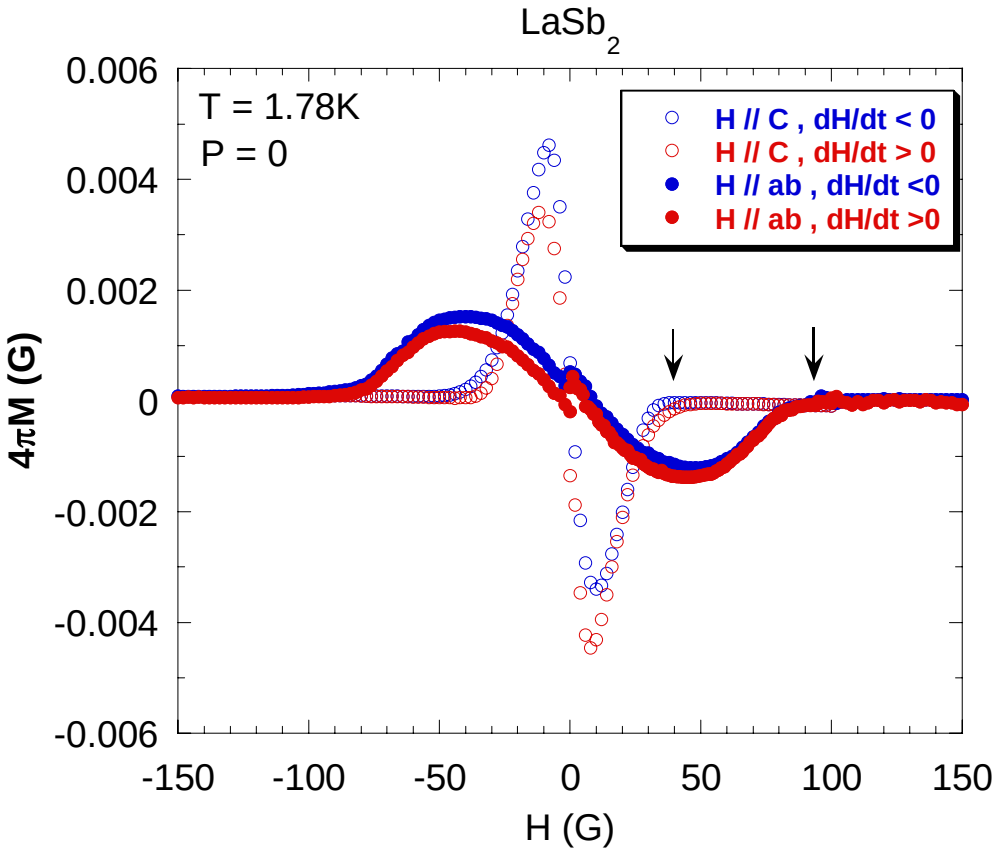

Figure 7.14 Field dependence of DC magnetization at $T = 1.78$ K for $LaSb_2$

Meissner effect is significantly smaller than (~ 1:15) that for field perpendicular to the ab plane.

There are two possible sources for the measured anisotropic susceptibility. The first is a demagnetization effect due to the finite shape of the sample, resulting in a difference between the field inside the sample and the external applied H [7.10]:

$$H_i = H_a - NM, \tag{7.13}$$

where H_i is the field inside the sample, H_a is the external applied H, and N is the demagnetization factor that is dependent on the shape of the sample and the direction of the external magnetic field. Therefore, the intrinsic $\chi_i = M/H_i$ is smaller than the experimentally measured $\chi_e = M/H_a$, according to the following relation,

$$\chi_i = \frac{\chi_e}{1 - N\chi_e}. \tag{7.14}$$

The second source for anisotropic magnetization is an intrinsic superconducting anisotropy due to the dimensionality of the sample. For instance, a superconducting thin film with thickness less than the coherence length is essentially transparent to a parallel magnetic field and has a negligible parallel Meissner effect, but has a full Meissner diamagnetic susceptibility perpendicular to the plane [7.11], as we have discussed above for 2D superconductivity.

We will show later by comparison to the high pressure data that the anisotropy ratio ~ 3.4 in susceptibility for full Meissner effect can be accounted for by a demagnetization factor ~ 0.7 (also see section 7.10.1). However, here the magnitude of measured susceptibility is small (-0.015 or 0.001 for perpendicular and parallel fields respectively), and thus according to equation 7.14, the intrinsic susceptibility is only slightly enhanced (~ 1% or ~ 0.1% increase for perpendicular and parallel fields

respectively) compared to the measured susceptibility. Both the intrinsic anisotropy ratio in the susceptibility and the anisotropic critical fields are evidence for the importance of an intrinsic superconducting anisotropy at $T = 1.8$ K and zero pressure. We propose that the anisotropy in susceptibility and critical field is the result of 2D nature of superconductivity for which the coherence length is larger than the thickness of the superconducting layers in the sample.

7.5 Low Temperature AC Susceptibility for $LaSb_2$

The low temperature ac susceptibility data was measured in a dilution refrigerator with an excitation field of 1 kHz and 0.0147 G (see section 7.9 for details of normalization). The excitation field is in the same direction as the external field. The temperature dependence of the AC susceptibility below 2K is shown in Fig. 7.15. Again, we see the anisotropy in susceptibility for parallel and perpendicular fields. We notice that the magnitude of diamagnetic susceptibility displays a precipitous increase at temperature below ~ 0.5 K, the temperature where the resistivities of some of the crystals drop to zero. If we assume that the susceptibility anisotropy measured at $T = 0.1$ K is caused entirely by the demagnetization factor with no intrinsic anisotropy, we can calculate the value of intrinsic susceptibility to be -0.75, i.e., 75% of full Meissner effect (see section 7.9.4). We also notice that the imaginary part of AC susceptibility increases sharply below ~ 0.5 K, and almost saturates at our base temperature 65mK, again an indication of emergence of bulk superconducting state.

In Fig. 7.16 and 7.17, we plot the field dependence of AC susceptibility at six temperatures for perpendicular and parallel fields respectively. It is obvious that the characteristic fields are smaller for the perpendicular field orientation. Notice that a small

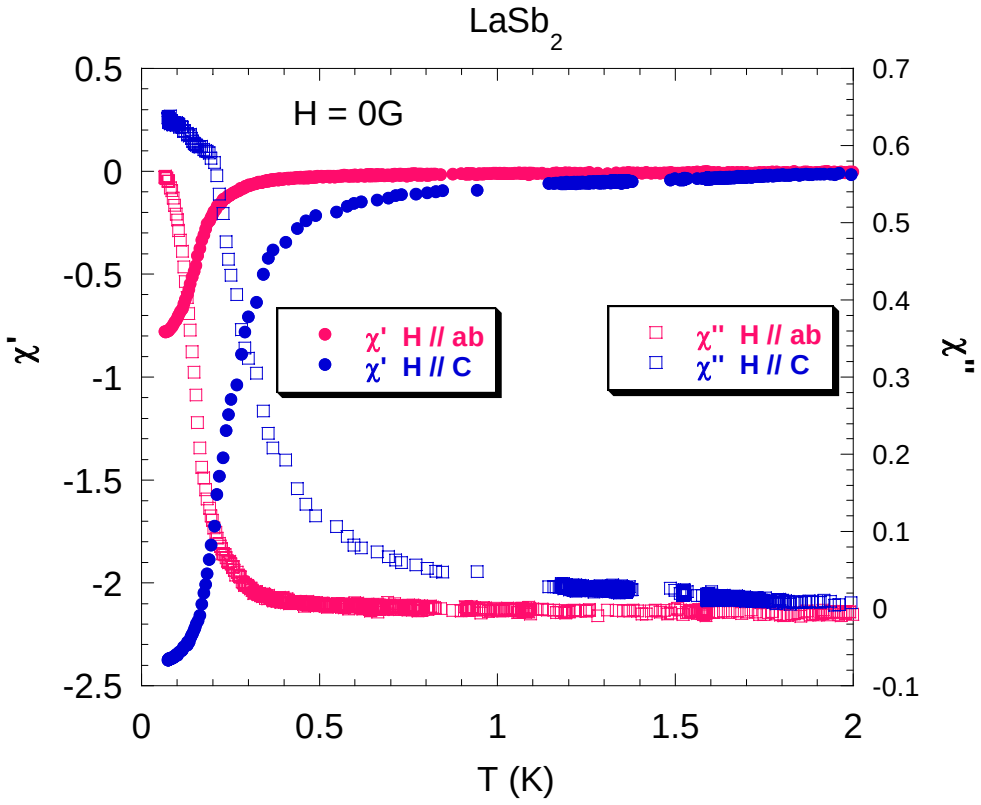

Figure 7.15 Temperature dependence of AC susceptibility below 2K for $LaSb_2$

magnetic field (< 1G) is sufficient to decrease the magnitude of susceptibility for both field orientations, which means extremely small H_{c1} and a large penetration depth. Interestingly, the imaginary part of the susceptibility at 65mK in Fig. 7.16 has a small peak feature at ±5G for field perpendicular to plane. This feature is not seen in the parallel field spectrum of the imaginary susceptibility. Later we will present similar behavior in the high pressure data.

7.6 AC Susceptibility above 1.78 K at High Pressure for $LaSb_2$

The high pressure ac susceptibility was measured in SQUID magnetometer with the probe field in the same direction of the applied external field. The magnitude of the probe field was 0.1 G and the frequency used was 1Hz.

In Fig. 7.18, we plot the T dependence of AC susceptibility in hydrostatic pressures with a probe field perpendicular to the ab plane. When the applied pressure is above ~ 2kBar, the superconducting diamagnetic signal becomes more obvious, and the superconducting transition width is significantly decreased. At 4.4 kBar the width of the transition is already ~ 0.1K and there is an observable structure. The largest negative AC susceptibility we observed is -3.4 indicating at least 90% of full Meissner effect (see section 7.10.1). This value of -3.4 is more than the expected value -1 for Meissner effect due to the demagnetization effect. Applying further pressure decreases the superconducting transition temperature below the base temperature of the SQUID magnetometer. The effect of pressure on the imaginary part of AC susceptibility is shown in Fig. 7.18(b). At low pressures ($P \leq 3.5$ kBar), a wide peak emerges around $T \sim 1.83$ K. When the pressure is increased to 4.05 kBar, the peak has grown and two maxima are clearly resolved between 1.76 K and 1.86 K. Increasing the pressure to 4.4 kBar, we

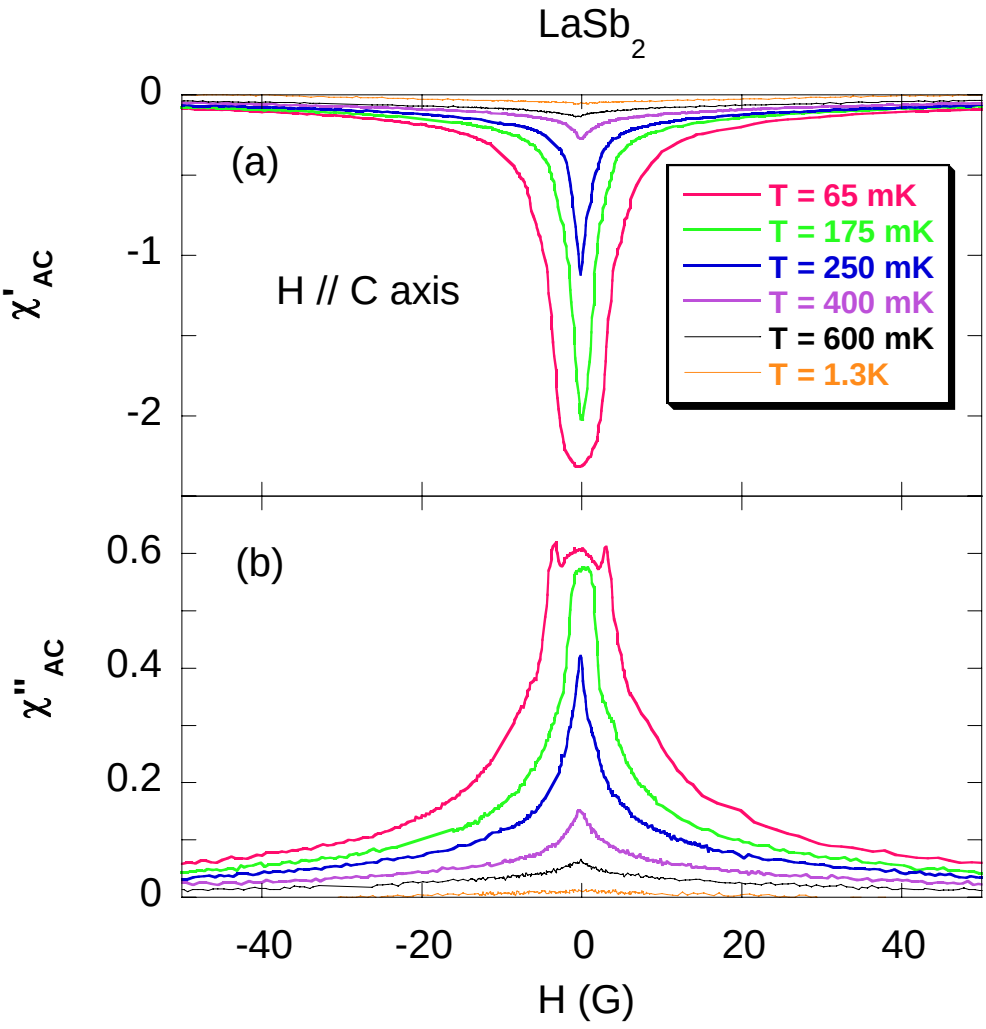

Figure 7.16 Field dependence of *H*//C axis AC susceptibility for $LaSb_2$

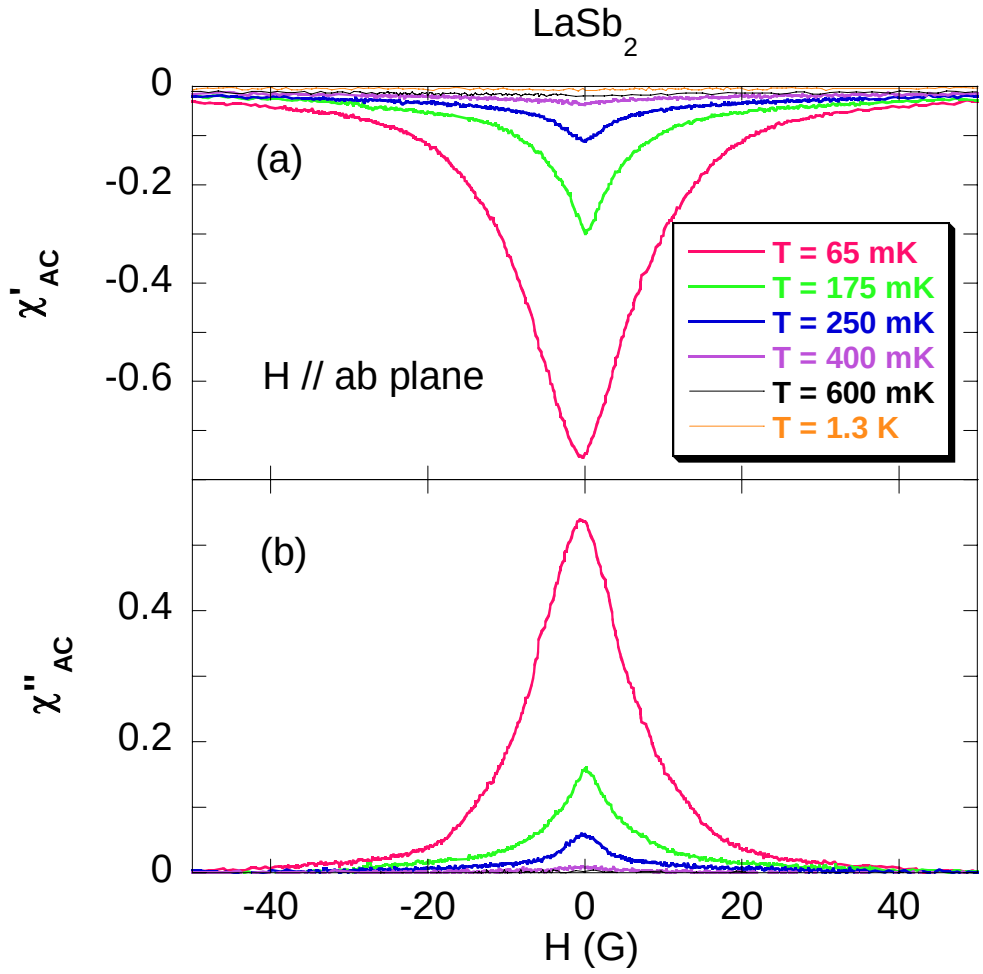

Figure 7.17 Field dependence of *H*//ab plane AC susceptibility for $LaSb_2$

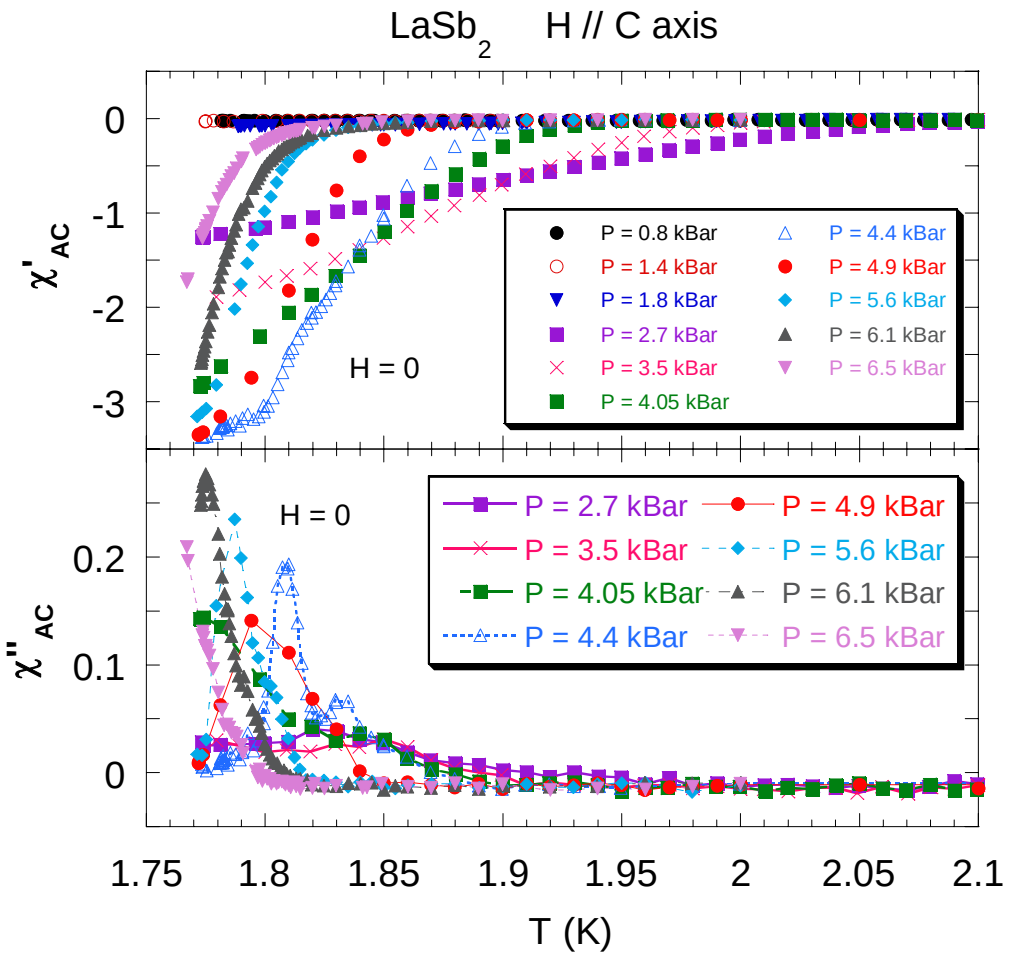

Figure 7.18 Temperature dependence of *H*//C axis AC susceptibility for $LaSb_2$ at pressures denoted in the figure

observe the full Meissner effect in χ' and two distinct peaks in χ" that have moved closer together in *T*. Applying more pressures decreases the temperatures for both peaks and brings them closer together in *T*, gradually merging the two into one low-*T* large peak. In Fig. 7.19(a), the *T* dependence of χ' is plotted with the probe field parallel to the ab plane, and we see similar increases in the diamagnetic superconducting signal with increasing pressure and the concomitant decrease in the transition width. A decrease of T_c with pressure above ~ 4.5 kBar was observed, similar to that found with *H* // c-axis. The magnitude of susceptibility is ~-1 at *P* ~ 4.6 kBar and *T* ~ 1.77 K, again an indication of full Meissner effect entering our temperature window. Note that this pressure is slightly larger than the 4.4 ± 0.1 kBar necessary to observe a full superconducting transition with *H* // c-axis. Contrary to the *H* // c-axis data χ' does not show any significant structure. In addition and in contrast to the perpendicular field orientation, we only observe a single peak in the *T* dependence of χ'' in high pressure in Fig. 7.19(b). This single peak appears at a slightly lower *T*, but close to the lower *T* peak of the *H* // c-axis χ".

In Figs. 7.20 and 7.21, the magnetic field dependence of the AC susceptibility with pressure is displayed for *T* ~ 1.78K. From the field dependence of the real part of the AC susceptibility (χ') as in Fig. 7.20(a) and 7.21(a), we observe that a small magnetic field (< 1G) is sufficient to decrease the magnitude of susceptibility for both field orientations, which means an extremely small H_{c1} and a large penetration depth. We also note that pressure decreases the upper critical field, H_{c2}, where χ' approaches zero from positive values. The field dependence of χ" is also interesting. In Fig. 7.20(b), for field parallel to the *c*-axis, at relatively low pressures (2.7 and 3.5 kBar), a small peak appears at *H* ~ 3.5 G. When the pressure is increased to 4.05 kBar, an additional larger peak

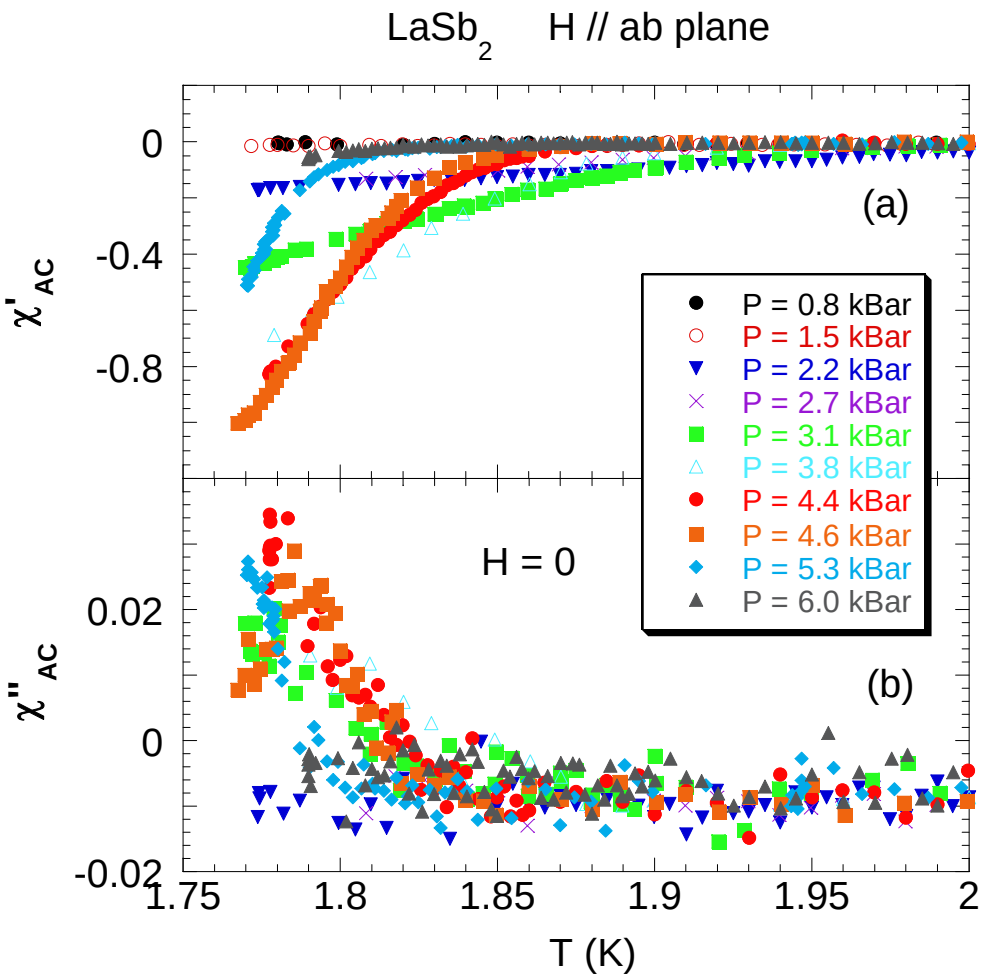

Figure 7.19 Temperature dependence of *H*//ab plane AC susceptibility for $LaSb_2$ at pressures denoted in the figure

appears around zero field, a behavior reminding us of the similar low T (65mK) zero pressure field dependence of χ" in Fig. 7.16(b). Applying further pressure to 4.4 kBar increases the size of the peaks in χ" and splits the peak field up to ~ ±1.5 G. A further increase in pressure decreases the field at which χ" peaks. The evolution of these peaks in field with pressure is consistent with the evolution of χ" with temperature and pressure as is evident in Fig. 7.18(b). Furthermore, examination of χ' in the same region of T, P and H suggests that for fields perpendicular to the ab plane the transition to superconducting state takes place in two steps. The temperature for the smaller high-T peak gradually decreases with pressure, while the peak T of the low-T larger peak increases rapidly with pressure up to 4.4 kBar. Above this pressure the peak temperatures are reduced as they gradually merge into a single structure. For fields parallel to the ab plane, in Fig. 7.21(b), we observe only a single peak for the field dependence of imaginary part of ac susceptibility χ", again consistent with single peak behavior in the T dependence (see Fig. 7.19(b)).

In Fig. 7.22(a), we plot the pressure dependence of susceptibility at T = 1.78 K and zero field for probe fields both parallel and perpendicular to the ab plane. The anisotropy in the susceptibility is more easily seen in Fig. 7.22(b), where the ratio of the two orientations is plotted against the pressure. A pressure of only 0.8 kBar is sufficient to sharply decrease the anisotropy ratio to 6 from the 15 at zero pressure. Applying further pressures gradually decreases the anisotropy ratio to ~3.4, forming a broad minimum from ~ 3 to ~ 4.5 kBar, above which the anisotropy ratio increases with pressure. The flat shape of our sample is consistent with a demagnetization effect induced anisotropy ratio of ~ 3.4 (see section 7.10.2). Therefore, we conclude that in the pressure

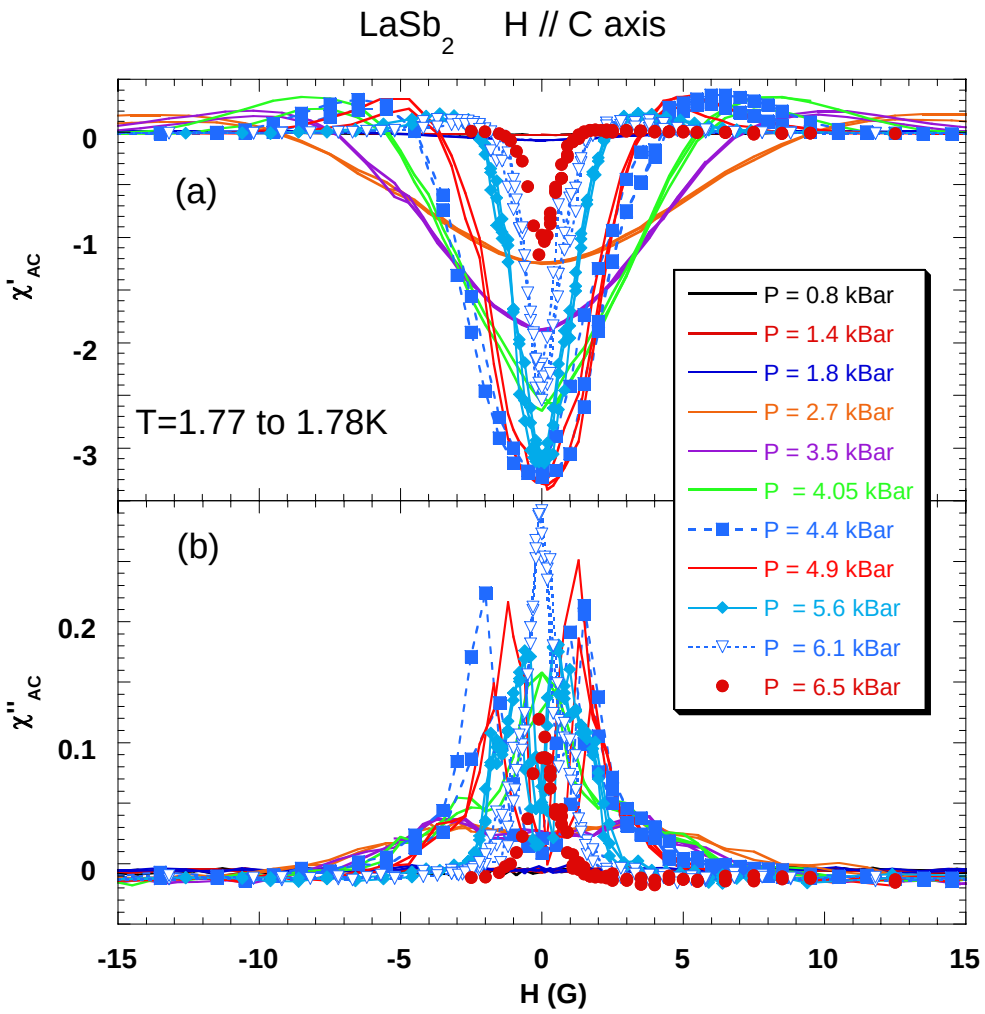

Figure 7.20 Field dependence of *H*//C axis AC susceptibility for $LaSb_2$ for applied pressures indicated in the figure

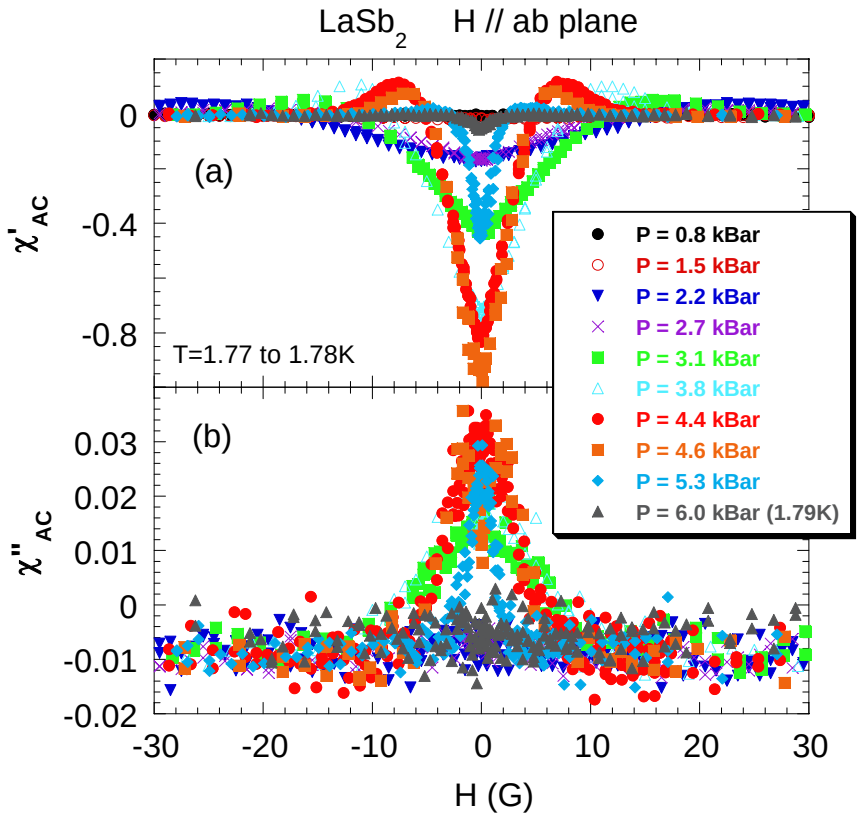

Figure 7.21 Field dependence of *H*//ab plane AC susceptibility for $LaSb_2$ for pressures as indicated in the figure

range from ~ 3 to ~ 4.5 kBar, the intrinsic susceptibility is nearly isotropic at $T = 1.78$ K. In low and high pressures when the susceptibility is small, the demagnetization factor is also small and therefore much of the anisotropy in susceptibility is intrinsic. Note that for high pressures ($P > \sim 4.5$ kBar) as in Figs. 7.18 and 7.19, T_c is slightly higher for H // c-axis than H // ab plane, and therefore large anisotropy ratio in χ' is expected, as the temperature for full Meissner effect moves below 1.78 K.

In Fig. 7.23, we display the pressure dependence of the upper critical fields for both field orientations as well as their anisotropy ratio. The salient features are the gradual suppression of critical fields for both field orientations and the suppression of the anisotropy ratio with increasing pressure. Above $P \sim 5$kBar, the anisotropy ratio approaches 1, consistent with an isotropic behavior. Note that the 3 data points for H // c-axis critical fields from 0.8 kBar to 1.8 kBar in Fig. 7.23(a) are measured in a second sample, so there is a small sample dependence in the low pressure range ($P < \sim 4.5$ kBar). The data shown in Fig. 7.20 for pressures from 0.8kbar to 1.8kBar are also measured in this second sample.

In Fig. 7.24, the temperature dependence of the susceptibility anisotropy for pressures of 2.7 kBar and 4.4 kBar is displayed. For both pressures, the anisotropy in susceptibility is suppressed by a decrease in temperature. For $P = 4.4$ kBar, the anisotropy ratio in χ' has a kink around $T = 1.81$ K, most likely related to the double peak feature in the T-dependence of χ" in perpendicular probe fields and the corresponding structure in the T-dependence of χ'.

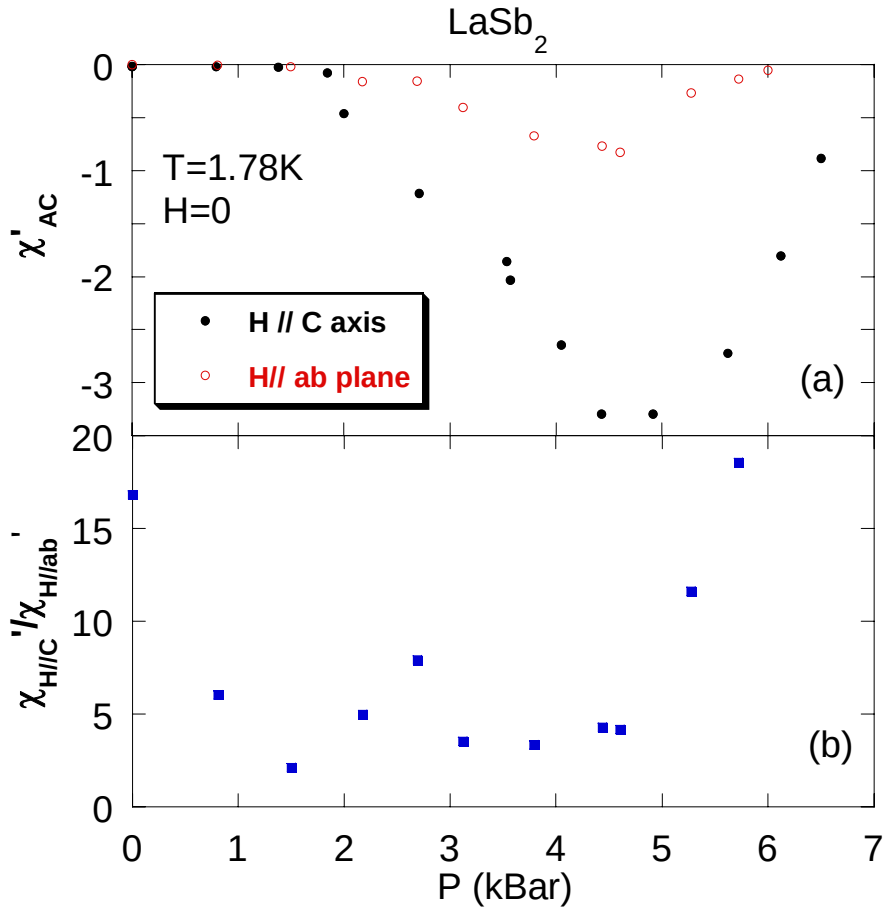

Figure 7.22 Pressure dependence of zero field AC susceptibility at $T = 1.78$ K and the anisotropy ratio for $LaSb_2$

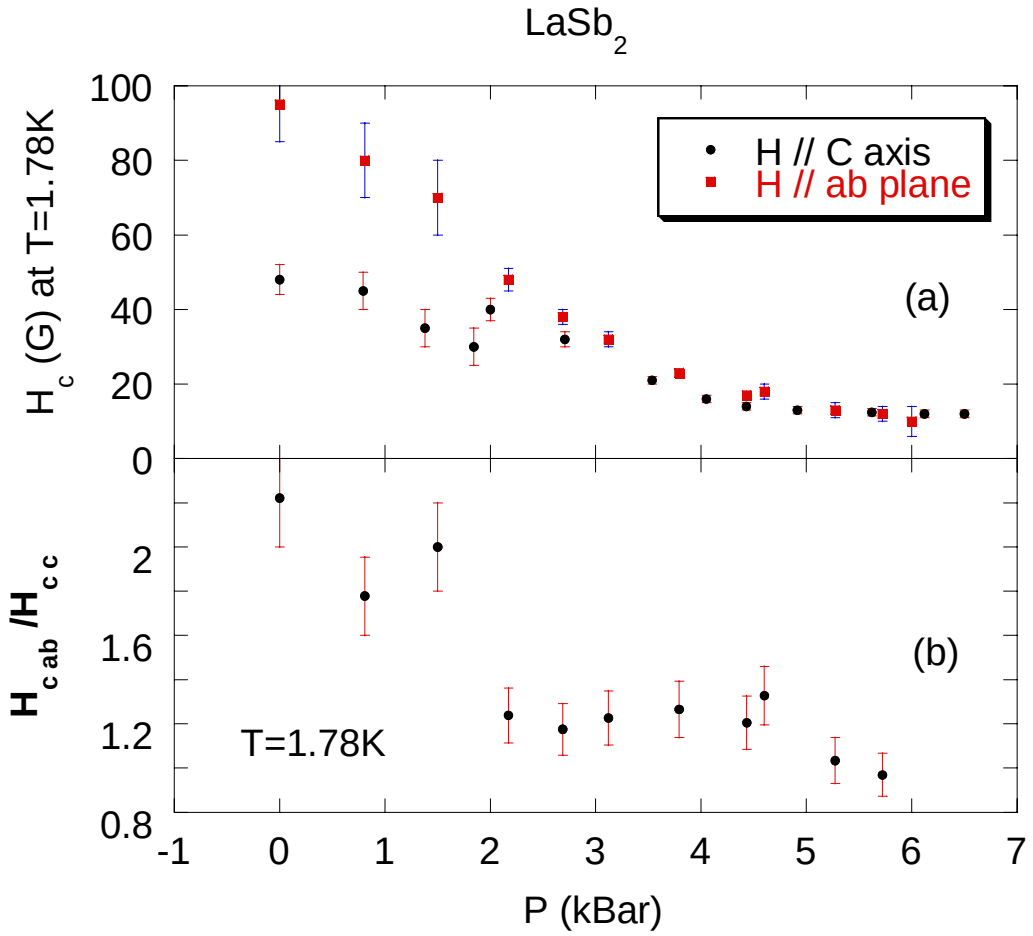

Figure 7.23 Pressure dependence of $T = 1.78$ K critical field and anisotropy ratio for $LaSb_2$

7.7 Summary and Discussion

We have studied the low temperature resistivity in zero pressure, as well as the DC magnetization, and the AC susceptibility in zero and high pressures in $LaSb_2$, a metal with a highly layered structure. At zero pressure, both the resistivity and susceptibility data confirm that superconductivity starts to emerge at $T \sim 2$K with anisotropic critical fields and a tiny (thousands of full Meissner effect) anisotropic diamagnetic effect. When temperature is cooled down below ~ 0.5 K, for some samples, the resistivity drops to zero and the real part of the AC susceptibility, χ', precipitously drops with a simultaneously sharp increase of χ". At $T = 65$mK, the magnitude of χ' for both field orientations (-2.37 for H // c-axis and -0.78 for H // ab plane) leads to estimated -75% of the full Meissner effect (see section 7.9.4). Interestingly, these values are comparable to the values of χ' at $T = 1.78$ K in the pressure range between 3.5 kBar and 4 kBar. The structure (side peaks and the middle peak) in the field dependence of χ" for $T = 65$mK and H // c-axis at zero pressure is also similar to the behavior for $P = 4.05$ kBar and $T = 1.78$ K. In addition, for zero pressure at $T \sim 0.2$ K, χ" displays a kink as in Fig. 7.15 similar to high pressure data. All these features strongly suggest that at zero pressure the sample starts to become partially superconducting at $T \sim 2$K. As T is cooled down to 0.2 K, characterized by a kink in χ", the sample finishes being partially superconducting and starts to go into a fully superconducting state. Cooling down also decreases the anisotropy ratio in the critical field (Fig. 7.11(b)) and χ', which suggests that the initial partially superconducting state is 2D in nature and the final state would be an isotropic 3D at a temperature below our base temperature of 65mK. A tentative phase diagram in the H-T space for zero pressure

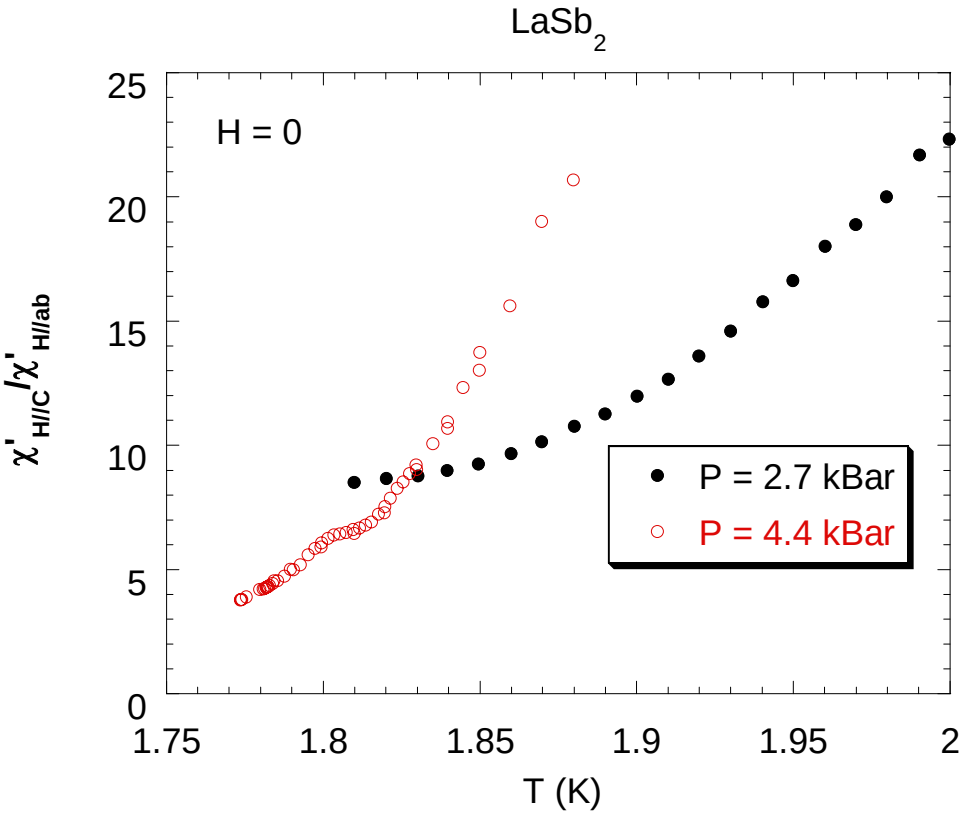

Figure 7.24 Temperature dependence of AC susceptibility anisotropy at $P = 2.7$ kBar and 4.4 kBar for $LaSb_2$

is drawn in Fig. 7.25. Because a low-T maximum in χ" is not found down to 65mK at zero field, we denote the low-T-H state as the onset of 3D superconducting state.

Applying pressure significantly reduces the superconducting transition width, and at the same time reduces the critical field anisotropy and the χ' anisotropy. When the pressure reaches ~ 4.5 kBar, a sharp isotropic, full (at least 90% of, see section 7.10.1) Meissner effect can be observed for both field orientations at $T \sim 1.8$ K. Further increasing pressure tends to decrease T_c. A tentative P-T space phase diagram is plotted in Fig. 7.26 from AC susceptibility data. As is more evident in the inset, at $P \geq 4$ kBar an isotropic 3D superconducting state can be experimentally accessed, in contrast to the zero pressure low-T incomplete 3D superconducting transition.

7.8 Suggestions for Future Work to Detect Possible CDW States in $LaSb_2$

$LaSb_2$ shares many properties with quasi-2D transition metal dichalcogenides (TMD) [7.12] such as TaS_2, $TaSe_2$, NbS_2 and $NbSe_2$. Both $LaSb_2$ and TMD have layered structure and a low-T superconducting state with an extremely small lower critical field H_{c1} [7.13]. In Fig. 7.27, we can observe that a small field 0.5G can significantly suppress the Meissner effect for 2H-TaS_2. And in Fig. 7.28, we notice that magnetization curve departs from a linear dependence with a small applied field, a similar behavior to $LaSb_2$. One interesting property of TMD when intercalated with organic molecules is the precursor effect of superconductivity. In Fig. 7.29, we see the anisotropic diamagnetism at temperature as high as 35K in $TaS_2(pyridine)_{1/2}$ [7.14].

TMD materials are driven into the charge density wave (CDW) state by a mechanism which is distinct from the Fermi Surface nesting found in 1D CDW compounds. In TMD, a 2D energy band with saddle points was proposed to be

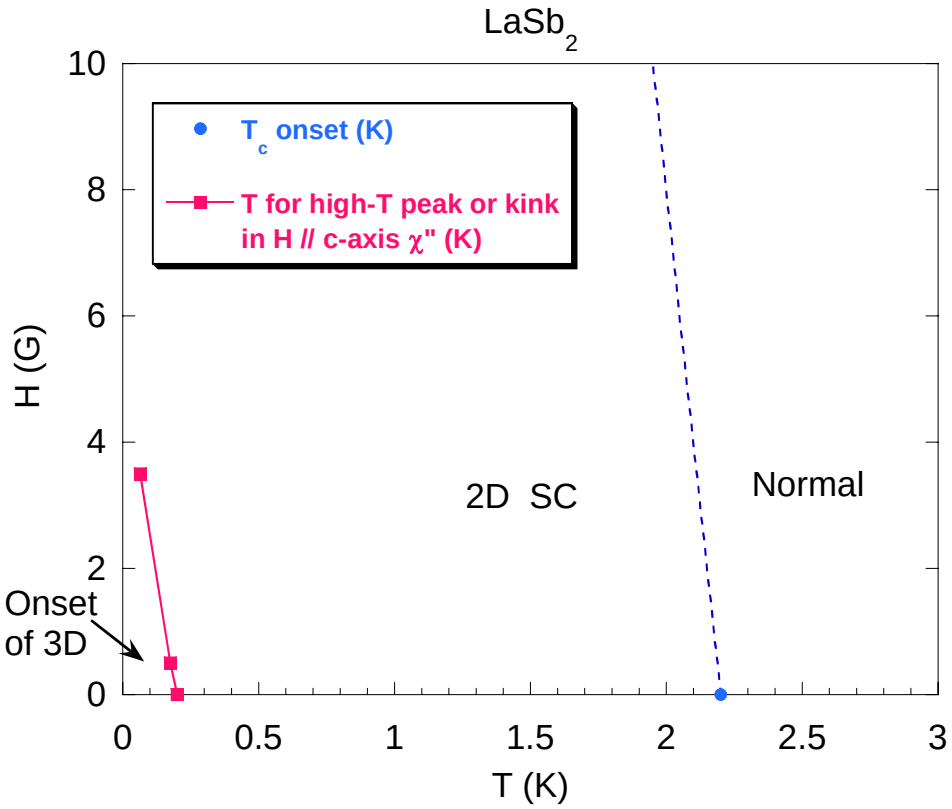

Figure 7.25 The tentative phase diagram in *H-T* space at zero Pressure

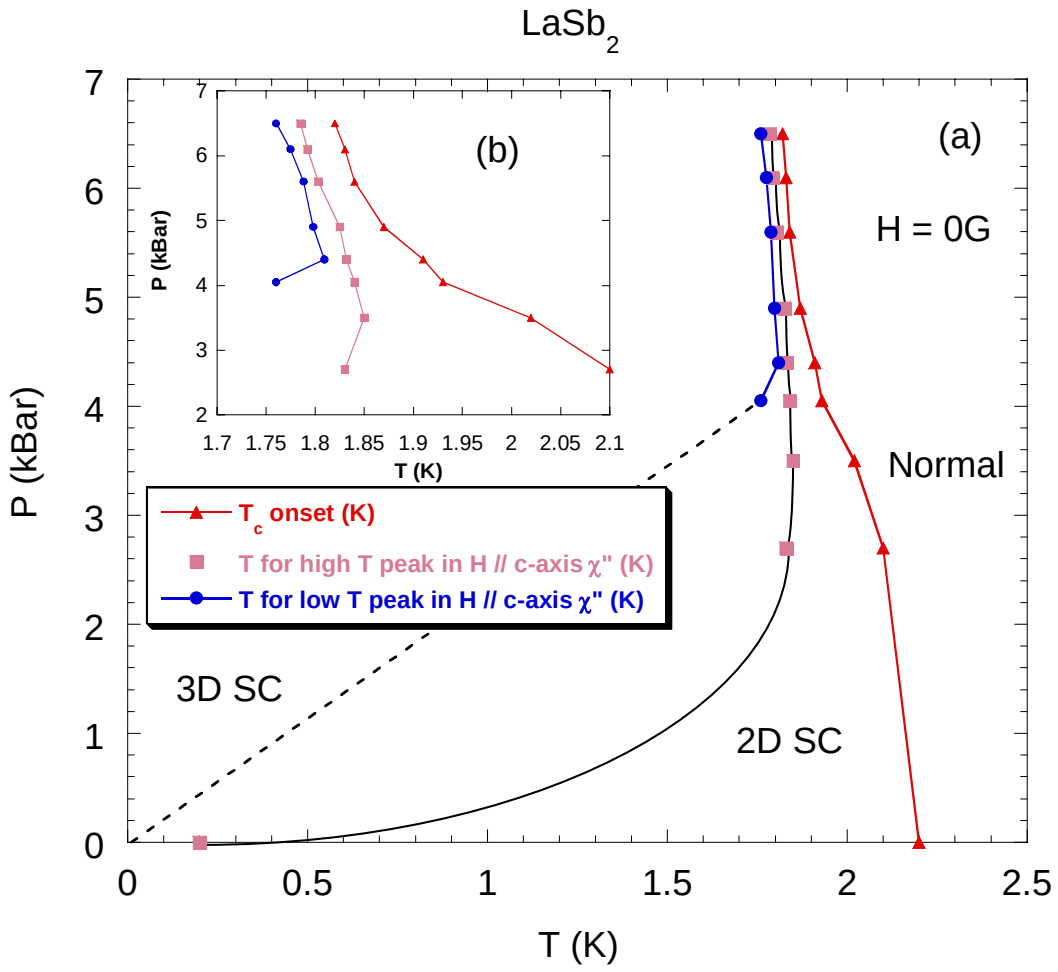

Figure 7.26 Pressure dependence of superconducting transition temperatures from *H* //c-axis AC susceptibility and the tentative phase diagram in *P*-*T* space**.**

(Inset is the blow-up of high *T* and *P* region)

responsible for CDW formation [7.15]. In this model large areas of Fermi surface are not truncated and the material can still be a metal. Later, a unified microscopic theory was proposed for coexistence and competition of CDW and superconducting ground states [7.16]. This theory predicts that the competition of superconductivity and CDW order is dependent on the lattice constant ratio a/c [7.16]. Increasing a/c tends to decreases T_{cdw} and increases T_c, consistent with experimental results in intercalated TMD [7.16] (see Fig. 7.30).

For $LaSb_2$, one neutron diffraction experiment showed that in addiction to the primary phase peaks, there appear broad peaks that are very weak at room temperature and very strong at 10K. These new peaks show anomalous broadening with cooling. However, these data have proven difficult to repeat and the reason why remains unknown. On the other hand, the Angle-Resolved Photoemission Spectroscopy (ARPES) data show no evidence of an enhancement in the density of states (DOS) near the Fermi energy E_F as T is cooled from 300K to 140K, implying that a CDW state does not form within this T range [7.17]. However, ARPES usually only detects the surface state of the sample, and therefore it is possible that the change in bulk state DOS has not been probed.

To unambiguously determine the existence of CDW state, we propose to measure resistivity, magnetic susceptibility, and neutron scattering in high pressure at temperatures from 2K to 300K. Because in pressures equal or above ~ 4.5 kBar the superconducting transition width is very small, the physical properties measured at or above this pressure may be more easily interpreted and hopefully the existence of CDW state and its relation to superconductivity and large linear MR can be elucidated.

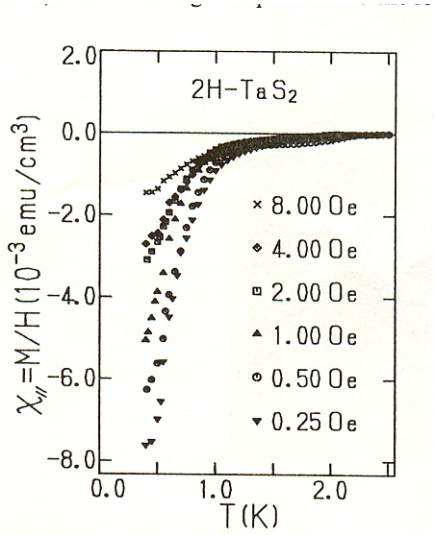

Figure 7.27 Temperature dependence of susceptibility for 2H-TaS_2 at fields indicated in the figure (from Ref. 7.13)

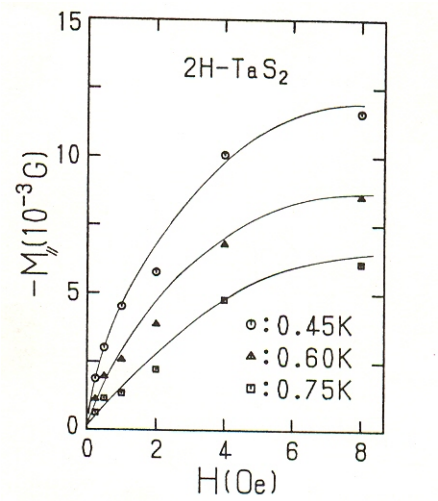

Figure 7.28 Field dependence of susceptibility for 2H-TaS_2 at temperatures indicated in the figure (from Ref. 7.13)

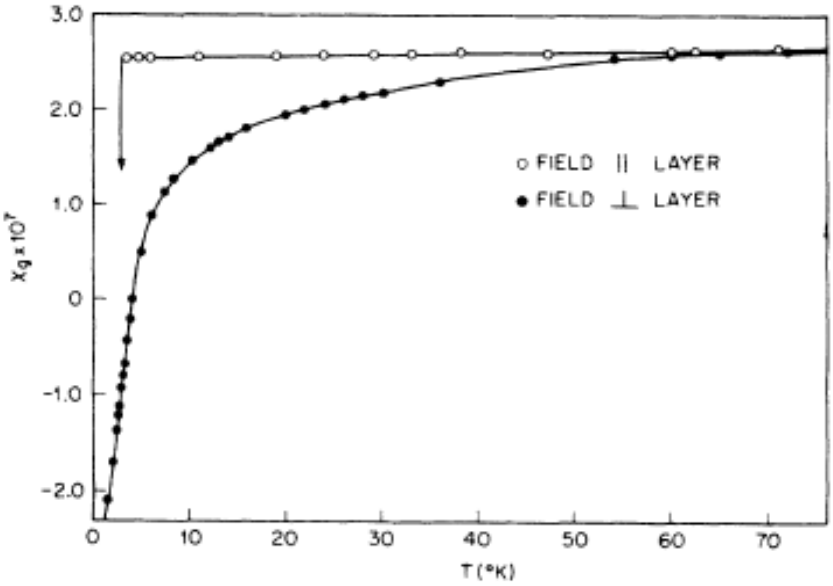

Figure 7.29 Temperature dependence of magnetic susceptibility of TaS_2 (pyridine)$_{1/2}$ (from Ref. 7.14)

x_g represents the magnetic susceptibility per gram of TaS_2 (pyridine)$_{1/2}$

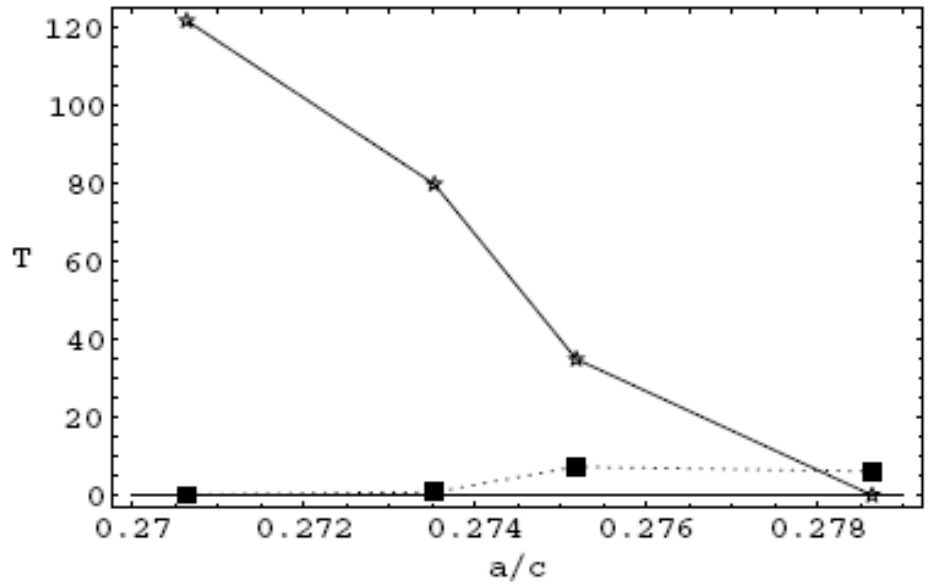

Figure 7.30 Phase diagram of TMD. From left to right: $TaSe_2$, TaS_2, $NbSe_2$ and NbS_2. (from Ref. 7.16)

(Stars: T_{CDW}; filled squares: T_c. a is the in-plane lattice spacing and c is the interplane spacing)

7.9 Normalization of AC Susceptibility Measured in Dilution Refrigerator

7.9.1 EMF Generated in the Astatic Secondary Coil

Inside the dilution refrigerator, we measured the AC susceptibility by an apparatus which consists of a primary coil and a secondary balanced astatic coil sitting inside the primary coil. The secondary astatic coil is made up of one clockwise and one anticlockwise coil section which are connected to each other serially. The clockwise and anticlockwise coil sections are made as similar as possible in geometry. An AC current of 1kHz and $5*10^{-6}$ A is driven through the primary coil to generate sinusoidal magnetic field in the secondary coil and subsequently an EMF with the same frequency.

A single crystal sample is put inside one half of the secondary coil which lies inside the primary coil. From classical electromagnetic theory, we can deduce the following equations [7.18]. The first equation is for the EMF ε_2 generated in the secondary coil,

$$\boldsymbol{\varepsilon}_2 = -\boldsymbol{M}_{21}\frac{\boldsymbol{di}_1}{\boldsymbol{dt}} = -\boldsymbol{N}_2\frac{\boldsymbol{d}\Phi_2}{\boldsymbol{dt}}, \tag{7.15}$$

where M_{21} is the mutual induction coefficient from the primary to secondary coil, i_1 is the current in the primary coil, Φ_2 is the magnetic flux through one single turn of the secondary coil, and N_2 is the number of turns in the secondary coil. We also have,

$$\Phi_2 = \int \boldsymbol{B}\bullet\boldsymbol{dA}_2 = \mu_0(1+\chi)\int \boldsymbol{H}\bullet\boldsymbol{dA}_2 = \mu_0(1+\chi)\boldsymbol{H}(\pi\boldsymbol{R}_2^2), \tag{7.16}$$

and

$$\boldsymbol{H} = \boldsymbol{n}_1\boldsymbol{i}_1 = \frac{\boldsymbol{N}_1}{\boldsymbol{L}_1}\boldsymbol{i}_1. \tag{7.17}$$

Here χ is the magnetic susceptibility of the sample, R_2 is the radius of the secondary coil, and n_1 is the number of turns per unit length in the primary coil. Due to the balanced

astatic nature of the secondary coil, the generated EMF will be cancelled if no sample is present. Taking this into account, and then combining equation 7.15 to 7.17, we can get

$$\varepsilon_2 = -N_2 \mu_0 \chi (\pi R_2^2) n_1 \frac{di_1}{dt} = V_s n_1 n_2 \mu_0 \chi \frac{di_1}{dt}, \qquad (7.18)$$

where V_s is the volume of the sample, n_1 and n_2 are the number of turns per unit length in the primary and secondary coil respectively. From this equation, we can see that the generated EMF in the secondary coil is proportional to susceptibility χ and the volume of the sample.

7.9.2 Normalization from Susceptibility of Superconducting Cd

We measured separately a Cd single crystal sample inside our secondary coil under the same conditions (the same current through primary coil, 5e-6 A and 1kHz) in order to normalize our low-T susceptibility data in $LaSb_2$. The Cd sample is prepared by stacking 6 pieces of Cd in the shape of square thin plates. The geometries of the 6 pieces are as follows:

Table 7.1 Geometry of Cd crystals

Piece	Width (mm)	Length (mm)	Thickness (mm)	Volume (mm^3)
1	0.51	0.57	0.194	0.056
2	0.35	0.50	0.18	0.032
3	0.33	0.53	0.20	0.035
4	0.46	0.38	0.19	0.034
5	0.40	0.38	0.22	0.034
6	0.70	0.36	0.161	0.041
Total	2.75	2.72	1.15	0.232
Average	0.46	0.45		

To estimate the demagnetization factor, we use the following equations [7.19] appropriate for a prolate ($a = b$) ellipsoidal sample with $c \approx a$:

$$\delta = \frac{4}{15}\left(1 - \frac{a}{c}\right), \qquad N_c = \frac{1}{3} - \delta, \qquad N_{ab} = \frac{1}{3} + \frac{1}{2}\delta \quad . \tag{7.19}$$

Here N_{ab} and N_c are the demagnetization factors for the direction in width (or length) and thickness respectively. In our case for Cd, $c/a = 1.15/0.45 = 2.6$, therefore, $N_c = 0.169$.

With the demagnetization factor calculated, we can calculate the expected value for the change in susceptibility at the superconducting transition of Cd. Since the relation between the measured value of susceptibility χ_m and the intrinsic value of susceptibility χ_i is [7.10]

$$\chi_m = \frac{\chi_i}{1 + N\chi_i}, \tag{7.20}$$

and χ_i is equal to -1 in MKS units for a full Meissener effect in Cd at the superconducting transition, we have $\chi_m = \frac{-1}{1 - 0.169} = -1.203$ in MKS units, or $\chi_m = -1.203/4\pi = -0.096$ in Gaussian units.

The measured value of the EMF jump for the Cd superconducting transition is $2.44*10^{-7}$ V (see Fig. 7.31). Therefore, the normalization factor is $1.203/2.44*10^{-7}$ (1/V) for the Cd sample of volume $2.32*10^{-4}$ cm^3.

Next, we need to calculate the volume of our $LaSb_2$ sample. We measured the mass of the $LaSb_2$ sample as 2.8 +/- 0.1mg (with additional 1.0 mg GE Varnish). This is converted to $8.1*10^{-6}$ moles. We multiply the number of moles by the molar density, 0.01834 moles/cm^3, to find that the volume of the sample is $4.4*10^{-4}$ cm^3. Given similar shapes of the $LaSb_2$ and Cd sample, the normalization factor should be

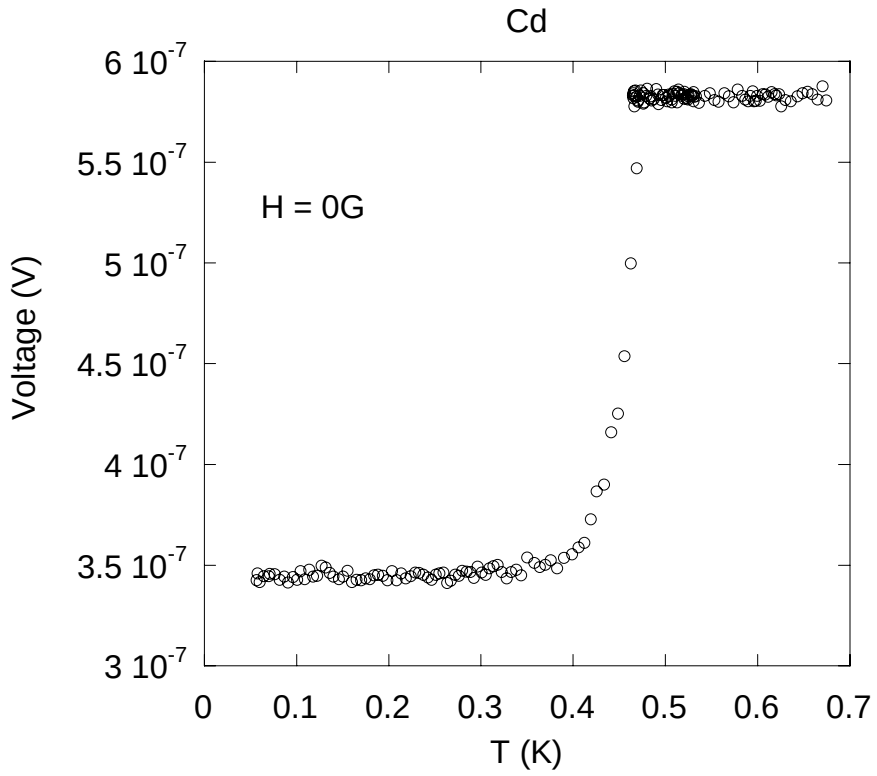

Figure 7.31 Superconducting AC susceptibility jump for Cd sample measured in a Dilution Refrigerator

(The volume of the Cd sample is 2.32e-4 cm^3)

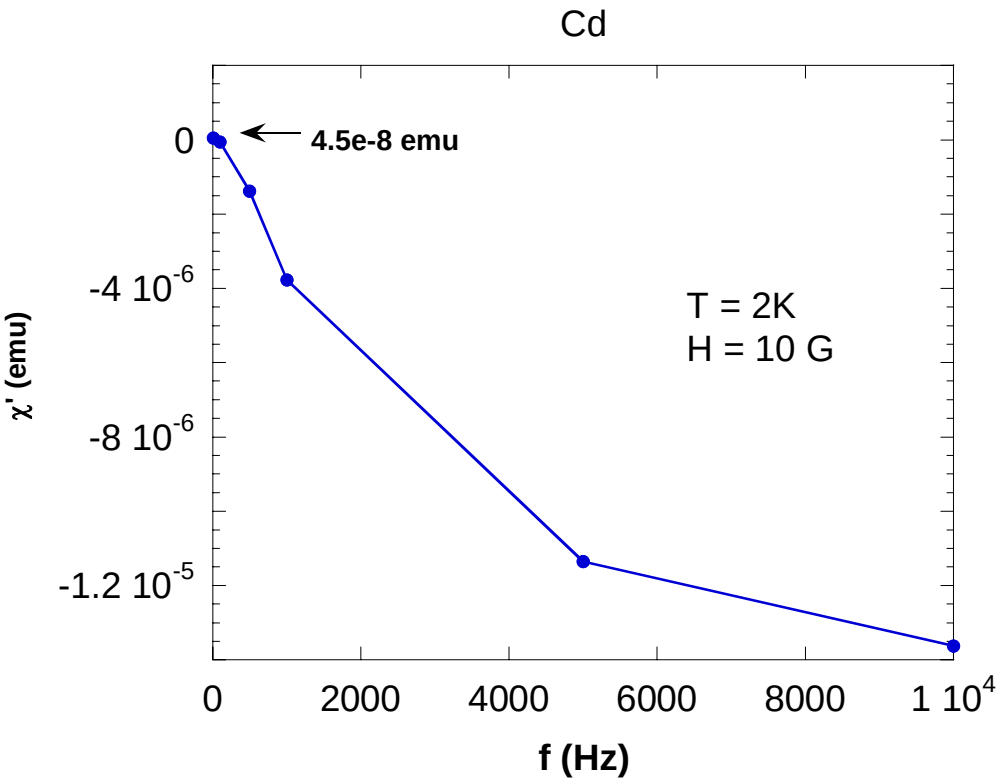

Figure 7.32 Frequency dependence of diamagnetic susceptibility for normal state of Cd measured in a Quantum Design PPMS

(The mass of the sample is 1.7 mg)

$\frac{1.203}{2.44\times10^{-7}} * \frac{2.32\times10^{-4}}{4.4\times10^{-4}} = 2.6\times10^{6}$ (1/V). The measured EMF voltage is multiplied by this value to get the susceptibility in MKS unit for our $LaSb_2$ samples.

7.9.3 Correction Due to High Frequency Normal State Diamagnetic Signal in Cd (above T_c)

Due to the skin effect, high frequency magnetic fields are reduced in the interior of a good metal [7.1], resulting in possible diamagnetic signal above T_c in our Cd sample (see Fig. 7.32). We measured the normal state contribution to diamagnetism for a Cd sample cut from the same crystal and with similar shape which was composed of 5 flat plates. We found that the diamagnetic susceptibility is -0.242 for f = 1kHz above T_c (Fig. 7.33). This normal state diamagnetism need to be taken into account in the AC susceptibility normalization.

The 5 pieces of Cd sample have the following geometry:

Table 7.2 Geometry of 2nd Cd crystal samples

Piece	Width (mm)	Length (mm)	Thickness (mm)	Volume (mm^3)
1	0.45	0.50	0.20	0.045
2	0.38	0.50	0.20	0.038
3	0.35	0.53	0.20	0.0371
4	0.50	0.50	0.23	0.0575
5	0.33	0.43	0.20	0.0284
Total				0.206

The mass of the sample measured is 1.7mg. Since the density for Cd at room temperature is 8.65g/cm^3, the volume is 1.7e-3/8.65 cm^3, or 1.965e-4 cm^3. From Fig. 7.27, we can see that the trend of the normal state diamagnetic susceptibility of Cd is toward saturation at T less than 2k. We can estimate that at $T \sim 0.5$ k, the diamagnetic susceptibility is -3.78

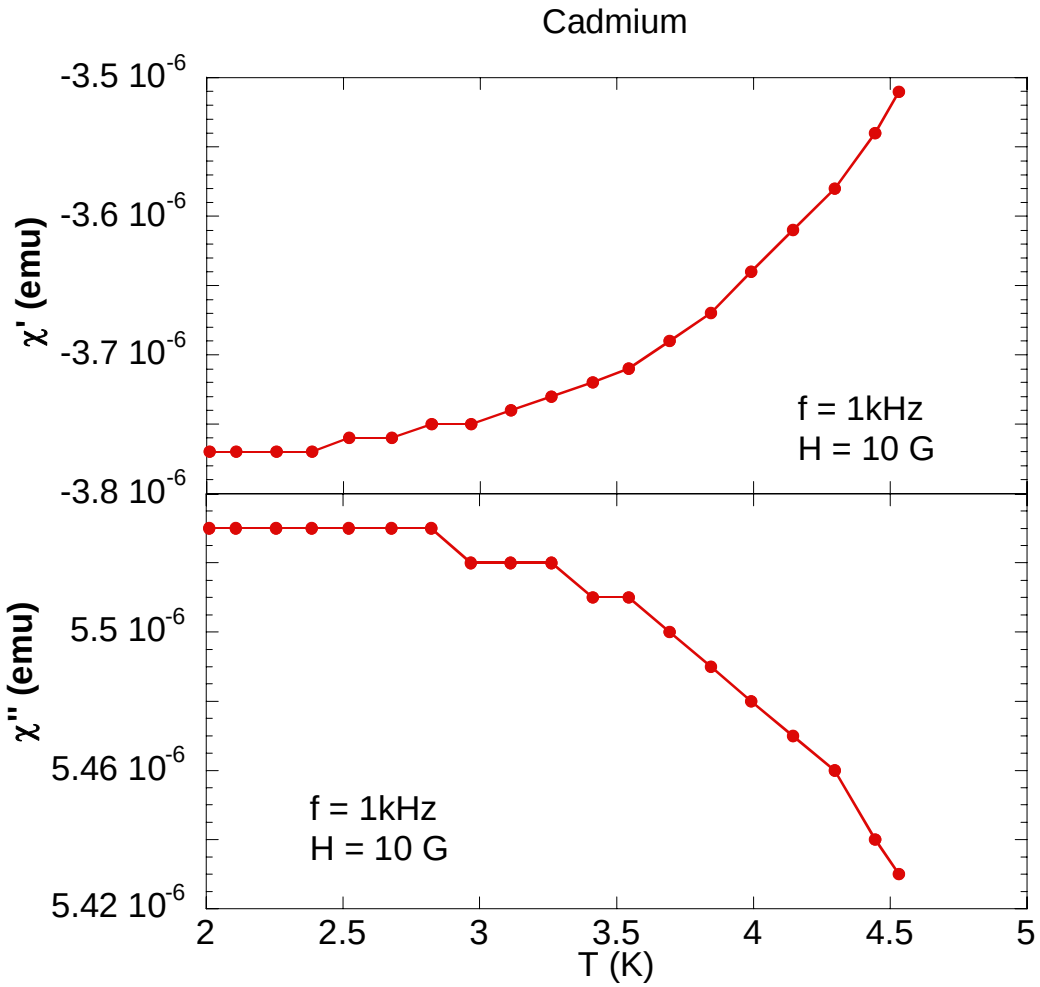

Figure 7.33 High Frequency diamagnetic susceptibility for normal state of Cd measured in a Quantum Design PPMS

(The mass of the sample is 1.7 mg)

emu per 1.965e-4 cm^3, or -0.01924 in Gaussian units. Multiplying this value by 4π, we can get the value for normal state diamagnetic susceptibility of -0.242 in MKS units.

Taking this into consideration, the normalization factor obtained in the previous section $2.6*10^6$ (1/V) should be multiplied by (1-0.242). Therefore, *the final normalization factor should be* $1.97*10^6$ (1/V). We multiplied the measured EMF voltage by this factor to normalize the susceptibility in MKS units for our $LaSb_2$ samples.

7.9.4 Estimate of Percentage of Full Meissener Effect at T = 65mK

After the normalization of ac susceptibility data, we find a χ_c = -2.37 for H // c-axis and χ_{ab} = -0.78 for H // ab plane at T = 65mK. If we assume that susceptibility is intrinsically isotropic at T = 65mK, i.e. the difference in susceptibility is caused entirely by the demagnetization factor, we can calculate the intrinsic χ_i and the demagnetization factor N. From equation 7.20, we find that

$$N = \frac{\chi_i - \chi_m}{\chi_i \chi_m} \quad . \tag{7.21}$$

Since for a prolate ($a = b$) ellipsoidal sample,

$$N_c + 2N_{ab} = 1, \tag{7.22}$$

we have

$$\frac{\chi_i - \chi_c}{\chi_i \times \chi_c} + 2 \times \frac{\chi_i - \chi_{ab}}{\chi_i \times \chi_{ab}} = 1, \tag{7.23}$$

or

$$\frac{\chi_i - (-2.37)}{\chi_i \times (-2.37)} + 2 \times \frac{\chi_i - (-0.78)}{\chi_i \times (-0.78)} = 1. \tag{7.24}$$

From equation 7.24, we calculate the value for intrinsic susceptibility value -0.75, i.e., 75 ± 1% of full Meissner effect. From equation 7.21, the demagnetization factor for c-axis is (-0.75+2.37) / (0.75*2.37) = 0.91.

7.10 Estimate of Demagnetization Factor for the Sample Used for Susceptibility Measurement in Pressure Cell

7.10.1 Estimate Based on the Magnitude of High Pressure *H* // C-axis Susceptibility

The largest diamagnetic susceptibility for *H* // c-axis we measured at $T \sim 1.77$ K is -3.4 at pressures of 4.4 and 4.9 kBar. If we assume a full Meissner effect is reached, i.e., an intrinsic susceptibility -1, we can estimate the value of the demagnetization factor. From equation 7.21, the demagnetization factor for c-axis is (-1+3.4)/3.4 = -2.4/3.4 = 0.706.

On the other hand, if we assume the sample has a prolate ($a = b$) ellipsoidal shape, from the value -1.002 of the largest diamagnetic susceptibility for *H* // ab plane, and equation 7.22, we can get the intrinsic susceptibility χ_i by

$$\frac{\chi_i - (-3.4)}{\chi_i \times (-3.4)} + 2 \times \frac{\chi_i - (-0.1.002)}{\chi_i \times (-1.002)} = 1. \qquad (25)$$

χ_i is calculated to be -0.912, i.e. 91.2% of full Meissner effect. The demagnetization factor for *H* // c-axis is (3.4-0.912) / (3.4*0.912) = 0.802 from equation 7.21.

7.10.2 Estimate of Demagnetization Factor from Sample Geometry

The sample has the shape of a plate with c-axis thickness smaller than the width and length. Unfortunately, the sample was destroyed when it was taken out of the pressure cell after measurement was completed. A reasonable estimate of the geometry is 0.1cm*0.1cm*0.0328cm, which amounts to a volume of $3.28*10^{-4}$ cm^3, consistent with measured mass of 2.3 mg. Using equation 7.19, I estimate the demagnetization factor for

H // c-axis to be 0.88, which is larger than the values we calculated based on measured susceptibility by ~10%.

References

[1.1] S. A. Wolf, et al., Science 294, 1488 (2001)

[1.2] M. Baibch, et al., Phys. Rev. Lett. 61, 2472 (1988)

[1.3] H. Ohno, Science 281, 951 (1998)

[1.4] H. S. Jarrett, et al, Phys. Rev. Lett. 21, 617 (1968)

[1.5] G. L. Zhao, et al, Phys. Rev. B 48, 15781 (1993)

[1.6] V. Eyert, et al, Phys. Rev. B 57, 6350 (1998)

[1.7] I. I. Mazin, Appl. Phys. Lett. 77, 3000 (2000)

[1.8] G. R. Stewart, Rev. Mod. Phys. 73, 797 (2001)

[1.9] A. H. Castro Neto, et al, Phys. Rev. Lett. 81, 3531 (1998)

[1.10] M.C. Andrade, et al, Phys. Rev. Lett. 81, 5620 (1998)

[1.11] J. Deisenhofer, et al, Phys. Rev. Lett. 95, 257202 (2005)

[1.12] M. B. Salamon, et al, Phys. Rev. Lett 88, 197203 (2002)

[1.13] M. B. Salamon, et al, Phys. Rev. B 68, 014411 (2003)

[1.14] V. M. Galitski, et al, Phys. Rev. Lett. 92, 177203 (2004)

[2.1] R. Bachmann, et al, Rev. Sci. Instrum. 43, 205 (1972)

[2.2] P. F. Sullivan, et al, Phys. Rev. Lett. 173, 679 (1968)

[2.3] G.R. Stewart, et al, Rev. Sci. Instrum. 54, 1 (1982)

[2.4] R.J. Schutz, et al, Rev. Sci. Instrum. 45, 548 (1974)

[2.5] see e.g. F. Pobell, *Matter and Methods at low Temperatures*, Springer-Verlag, 1992

[2.6] N. F. Mott, Philos. Mag. 19, 635 (1969); V. Ambagaokar, et al, Phys. Rev. B 4, 2612 (1972)

[2.7] N. D. Mathur, nature 394, 39 (1998)

[2.8] R. H. McKenzie, Science 65, 820 (1997)

[2.9] K. Murata, et al., Rev. Sci. Instrum. 68(6), 2490 (1997)

[2.10] K. Koyama, et al, Rev. Sci. Instrum. 69(8) 3009 (1998)

[2.11] K. Kamishima, et al, Rev. Sci. Instrum. 72(2) 1472 (2001)

[2.12] S. A. Carter, et al, Phys. Rev. B. 49, 7898 (1994)

[2.13] R. J. Bouchard, Mat. Res. Bull. 3, 563-570 (1968)

[3.1] see e.g. N. W. Ashcroft, et al, *Solid State Physics* (1976); C. Kittel, *Introduction to Solid State Physics* (1996)

[3.2] see e.g. T. Moriya, *Spin Fluctuations in Itinerant Electron Magnetism* (1985)

[3.3] K. Ishimoto, et al., J. Phys. Soc. Jpn 61, 2503 (1992)

[3.4] S. Kawarazaki, et al., J. Phys. Soc. Jpn 41, 1971 (1976)

[3.5] K. Ishimoto, et al., Physica B 213 & 214, 381 (1995)

[3.6] N. Rama, et al, Phys. Rev. B 70, 224424 (2004)

[3.7] A. Arrott, et al, Phys. Rev. Lett. 19, 786 (1967)

[3.8] D. M. Edwards, et al, Proc. Roy. Soc. A. 303, 127-137 (1968)

[3.9] G. R. Steward, Rev. Mod. Phys. 73, 797 (2001)

[3.10] A. H. Castro Neto, et al, Phys. Rev. Lett. 81, 3531 (1998)

[3.11] M. C. Andrade, et al, Phys. Rev. Lett. 81, 5620 (1998)

[3.12] J. Deisenhofer, et al, Phys. Rev. Lett. 95, 257202 (2005)

[3.13] M. B. Salamon, et al, Phys. Rev. Lett 88, 197203 (2002)

[3.14] M. B. Salamon, et al, Phys. Rev. B 68 014411 (2003)

[3.15] V. M. Galitski, et al, Phys. Rev. Lett. 92,177203 (2004).

[3.16] R. B. Griffiths, Phys. Rev. Lett. 23, 17 (1969)

[3.17] A. J. Bray, J. Phys. C: Solid State Phys. 15, L765 (1982)

[3.18] A. J. Bray, Phys. Rev. Lett.59, 586 (1987)

[3.19] E. Miranda, Rep. On Prog. In Phys. (2005)

[4.1] see e.g. N.W. Ashcroft, et al, *Solid State Physics* (1976); C. Kittel, *Introduction to Solid State Physics* (1996)

[4.2] see e.g. T. Moriya, *Spin Fluctuations in Itinerant Electron Magnetism* (1985)

[4.3] see e.g. F. Pobell, *Matter and Methods at low temperatures* (1992)

[4.4] A. M. Finkel'shtein, Sov. Phys. JETP 59, 97(1983)

[4.5] C. Castellani, et al, Phys. Rev. Lett 59, 323 (1987)

[4.6] P. A. Lee, et al, Rev. Mod. Phys. 57, 287 (1985)

[4.7] M.A. Paalanen, et al, Physica B 169, 223 (1991)

[4.8] T. F. RosenBaum, et al, Phys. Rev. B 27, 7509 (1983)

[4.9] R. N. Bhatt, et al, Phys. Rev. Lett., 48, 344 (1982)

[4.10] M. Laker, et al, Phys. Rev. Lett. 63, 648 (1989)

[4.11] M. Laker, et al, Phys. Rev. B, 50, 17064 (1994)

[4.12] C. Kasl, et al, Phys. Rev. B, 58, 13510 (1998)

[4.13] M.A. Pallanen, et al, Phys. Rev. Lett., 61, 597

[4.14] see e.g. A. C. Hewson, *the Kondo Problem to Heavy Fermion*, Cambridge University Press (1993)

[4.15] G. R. Stewart, Rev. Mod. Phys. 56, 755 (1984)

[4.16] G. R. Stewart, et al, Phys. Rev. B, 37, 3344 (1988)

[4.17] J. S. Kim, et al, Phys. Rev. B, 64, 134524 (2001)

[4.18] B. Andraka, et al, Phys. Rev. B, 39, 6420 (1989)

[4.19] A. S. Edelstein, Phys. Rev. B, 37, 3808 (1988)

[4.20] J. W. Kim, et al, Phys. Rev. B, 47, 2890 (1993)

[4.21] G. R. Stewart, Rev. Mod. Phys. 73,797 (2001)

[4.22] Sondhi, et al, Rev. Mod. Phys. 69, 315 (1997)

[4.23] M. Nicklas, et al, Phys. Rev. Lett., 82, 4268 (1999)

[4.24] A. H. Castro Neto, et al, Phys. Rev. Lett. 81, 3531 (1998)

[4.25] E. D. Bauer, et al, Phys. Rev. lett. 94. 046401-1 (2005)

[4.26] R. B. Griffiths, Phys. Rev. lett. 23,17 (1969)

[4.27] W. F. Brinkman, and T. M. Rice, Phys. Rev. B 2, 4302 (1970)

[4.28] H. V. Löhneysen, et al, Phys. Rev. Lett. 72, 3262 (1994)

[4.29] S. R. Julian, et al., Physica (Amsterdam) 259B–261B, 928 (1999)

[5.1] see e.g. N. W. Ashcroft, et al, *Solid State Physics* (1976)

[5.2] see e.g. C. Kittel, *Introduction to Solid State Physics* (1996)

[5.3] P. A. Lee, et al, Rev. Mod. Phys. 57, 284 (1985)

[5.4] T. F. Rosenbaum, et al, Phys. Rev. B 27, 7509 (1983)

[5.5] J. F. Ditusa, et al, Phys. Rev. B 58, 10288 (1998)

[5.6] see e.g. T. Moriya, *Spin Fluctuations in itinerant electron magnetism* (1985)

[5.7] J. Kondo, Solid State Physics 23, 184 (1969)

[5.8] P. Monod, Phys. Rev. Lett. 19, 1113 (1967)

[5.9] M. B. Monod, et al, Phys. Rev. 170, 552 (1968)

[5.10] R. A. Weiner, et al, Phys. Rev. B 3, 145 (1971)

[5.11] A. A. Abrikosov, Physics 2, 61 (1965)

[5.12] M. D. Daybell, et al, Phys. Rev. Lett. 20, 195 (1968)

[5.13] J. W. Loram, et al, Phys. Rev. B 3, 953 (1971)

[5.14] K. Matho, et al, Phys. Rev. B 5, 1899 (1972)

[5.15] M. Strauss, et al, Phys. Rev. B, 17, 1424 (1978)

[5.16] K. Yosida, Phys. Rev. 107, 396 (1957)

[5.17] W. Mashall, Phys. Rev. 118, 1520 (1960)

[5.18] M. W. Klein, et al, Phys. Rev. 132, 2412 (1963)

[5.19] M. W. Klein, Phys. Rev. 136, A1156 (1964)

[5.20] S. D. Silverstein, Phys. Rev. Lett. 16, 466 (1966)

[5.21] R. Harrison, et al, Rhys. Rev. 154, 540 (1967)

[5.22] Y. C. Tsay, et al, Phys. Rev. B, 7, 352 (1973)

[5.23] M. T. Beal-Monod, Phys. Rev. 178, 874 (1969)

[5.24] M.D. Daybell, et al, Rev. Mod. Phys. 40, 380 (1968)

[5.25] Y. C. Tsay, et al, Phys. Rev. B, 7, 352 (1973)

[5.26] I. Reiss, et al, Phys. Rev. B 4, 4099 (1971)

[5.27] I. Reiss, et al, Phys. Rev. B 8, 3467 (1973)

[5.28] see e.g. Hewson, *The Kondo Problem to Heavy Fermions,* Cambridge University Press, 1992

[5.29] G. R. Stewart, Rev. Mod. Phys. 56,755 (1984)

[5.30] T. Penney, et al., Phys. Rev. B, 34, 5959 (1986)

[5.31] M. C. Aronson, et al, Phys. Rev. Lett. 63, 2311 (1989)

[5.32] R. N. Bhatt, et al., J. of Superconductivity: Incorporating Novel Magnetism, 15, 71 (2002)

[5.33] S. Von Molnar, et al, J. Magn. Magn. Mater. 242, 13 (2002)

[5.34] T. Dietl, et al., Physica Scripta, Vol. T14, 29 (1986)

[5.35] H. Ohno, Science 281, 951 (1998)

[5.36] H. Ohno, J. Magn. Magn. Mater. 200, 110 (1999)

[5.37] A. Kaminsiki, et al, Phys. Rev. Lett. 88, 247202 (2002)

[5.38] K. M. Yu, et al, Phys. Rev. B 65, 201303 (2002)

[5.39] A. H. MacDonald, et al, Nature Materials, 4, 195 (2005)

[5.40] S. Das. Sarma, et al, Sold State Comm. 127,99 (2003)

[5.41] S. Sullow, et al, Phys. Rev. B 62, 11626 (2000)

[5.42] L. Degiorgi, et al, Phys. Rev. Lett. 79, 5134 (1997)

[5.43] P. Nyhus, et al, Phys. Rev. B 56, 2717 (1997)

[5.44] J. Chatterjee, et al, Phys. Rev. B 69, 134423 (2004)

[5.45] J. Custers, et al, Nature, 424, 524 (2003)

[5.46] H. Takagi, et al, Phys. Rev. Lett. 69, 2975 (1992)

[5.47] J. S. Schiling, Advances in Physics 28, 5, 657 (1979) p.668

[5.48] D. R. Hamann, Phys. Rev. 158, 570 (1967)

[5.49] J. Kondo, Phys. Rev. 169, 437 (1968)

[5.50] B. Andraka, et al, Phys. Rev. B 49, 12359 (1994)

[5.51] see e.g. D. C. Mattis, *The Theory of Magnetism* (Harper and Row, New York, 1965), p. 195

[5.52] J. A. Mydosh, Phys. Rev. Lett. 33, 1562 (1974)

[6.1] A. H. Castro Neto, et al, Phys. Rev. Lett. 81, 3531 (1998)

[6.2] E. D. Bauer, et al, Phys. Rev. lett. 94. 046401-1 (2005)

[7.1] S.L. Bud'ko, et al., Phys. Rev. B 57, 13624 (1998)

[7.2] D. P. Young, et al, Applied Physics Letter 82, 21, 3713 (2003)

[7.3] G. Oomi, et al, Physica B 230 (1997)

[7.4] F. Hullinger, et al, J. Less-Common Met. 55, 103 (1977)

[7.5] R. V. Coleman, et al, Phys. Rev. B, 27, 125 (1983)

[7.6] S. Cornell, et al, Phys. Rev. B, 29, 4915 (1984); I. Banerjee, et al, Phys. Rev. B 28, 5037 (1983)

[7.7] W. E. Lawrence and S. Doniach, in Proc. 12th Int. Conf. Low Temp. Phys., edited by E. Kanda (Academic, Kyoto, 1971), p.361.

[7.8] M. Tinkham, Phys. Rev. 129, 3413 (1963)

[7.9] S. T. Sekula, et al, Phys. Rev. B 5, 904–911 (1972)

[7.10] see e.g. S. Blundell, *Magnetism in Condensed Matter*, Oxford University Press, P.5.

[7.11] see e.g. M. Tinkham, Introduction to Superconductivity, 2nd ed. (McGraw-Hill, New York, 1996)

[7.12] A. H. Neto, Phys. Rev. Lett. 86, 4382 (2001)

[7.13] T. H. Geballe, Phys. Rev. Lett 27, 314 (1971)

[7.14] J. A. Wilson, et al, Phys. Rev. Lett 32, 882 (1974)

[7.15] S. Nagata, J.Phys.Chem.Solids 53, 10, 1259 (1992), S. Nagata, J.Phys.Chem.Solids 54, 8,895 (1993)

[7.16] T. M. Rice, et al, Phys. Rev. Lett 35, 120 (1975)

[7.17] A. I. Acatrinei, et al, J. Phys: Condens. Matter 15, L511 (2003)

[7.18] see e.g. J.D. Jackson, *Classical Electrodynamics*, 2nd edition, John Wiley & Sons, Inc. (1975)

[7.19] see e.g. F. Pobel, *Matter and Methods at low Temperatures*, Springer-Verlag, (1992)

Vita

Song Guo was born in November 1969, in Xuzhou, Jiansu province, China. He started to be interested in mathematics, physics and chemistry when attending the Hefei No.1 High School. In 1987, he went to the Physics Department of Beijing Normal University for undergraduate study. In 1992, he graduated with a Bachelor of Science degree in physics and then worked as an assistant engineer in the institute of microelectronics in Anhui. In 1998, he came to Louisiana State University for graduate studies in physics. In 2000, he started to do research in the experimental condensed matter physics with his advisor John F. DiTusa. He will graduate with a Doctor of Philosophy degree in physics in August of 2006.